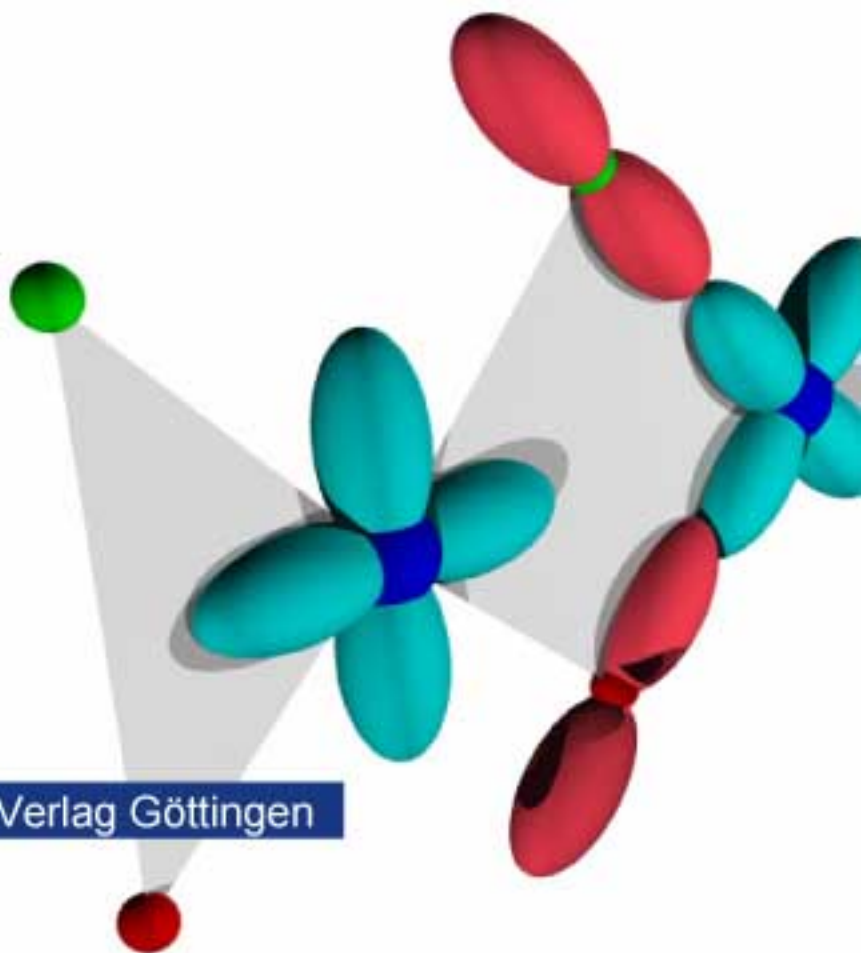




Dmitry Zakharov

# Exchange and Relaxation in Spin Chains



Cuvillier Verlag Göttingen

# Exchange and Relaxation in Spin Chains



Dissertation zur Erlangung des Grades eines  
Doktors der Naturwissenschaften  
(Dr. rer. nat.)

vorgelegt beim  
Fachbereich Physik der  
Universität Augsburg

VON  
**Dmitry Zakharov**

Augsburg 2007

Gedruckt mit Unterstützung des Deutschen Akademischen Austauschdienstes

Referent: Prof. Dr. Alois Loidl  
Koreferent: Prof. Dr. Armin Reller

Tag der Einreichung: 04. April 2007  
Tag der Prüfung: 04. Juli 2007

# Contents

<b>1. Introduction</b>	<b>1</b>
<b>2. Microscopic Theory of Superexchange</b>	<b>3</b>
2.1. Exchange Mechanisms . . . . .	4
2.1.1. Direct Exchange Interaction . . . . .	4
2.1.2. Indirect Exchange Mechanisms . . . . .	6
2.2. Isotropic Exchange Interaction . . . . .	8
2.2.1. Classical Concept: Antiferromagnetic Spin Ordering . . . . .	8
2.2.2. Ferromagnetic Superexchange . . . . .	9
2.2.3. Quantum Interference of Superexchange Interactions . . . . .	10
2.2.4. Exchange at Small Charge-Transfer Energy . . . . .	12
2.2.5. Double Exchange: Extreme Case of Free Charge Transfer . . . . .	14
2.3. Anisotropic Exchange Interaction . . . . .	15
2.3.1. Antisymmetric Part of Anisotropic Exchange . . . . .	15
2.3.2. Symmetric Anisotropic Exchange Interaction . . . . .	18
<b>3. Physics of Low-Dimensional Systems</b>	<b>23</b>
3.1. Spin Chains . . . . .	23
3.1.1. Spin-Peierls Transition . . . . .	24
3.1.2. Magnetic and Thermal Properties . . . . .	26
3.2. Spin Ladders . . . . .	28
<b>4. Electron Spin Resonance Spectroscopy</b>	<b>31</b>
4.1. Resonance Effect . . . . .	31
4.1.1. Zeeman Effect . . . . .	31
4.1.2. Bloch Equations . . . . .	33
4.2. Measured Quantities . . . . .	34
4.2.1. Resonance Field . . . . .	34
4.2.2. Linewidth and Lineshape . . . . .	35
4.2.3. ESR Intensity . . . . .	36
4.3. Experimental Setup . . . . .	37
4.4. Spin Relaxation Mechanisms . . . . .	39
4.4.1. The Kubo-Tomita Formula . . . . .	39

4.4.2.	Main Sources of the Line Broadening . . . . .	40
4.5.	ESR in Low-Dimensional Spin Systems . . . . .	41
4.5.1.	Spin Diffusion at High Temperatures . . . . .	42
4.5.2.	Low-Temperature Field-Theory Approach . . . . .	42
4.5.3.	Crossover Temperature Regime . . . . .	44
4.6.	Other Experimental Techniques . . . . .	46
<b>5.</b>	<b>Symmetric Ring Exchange in <math>\alpha'</math>-<math>\text{NaV}_2\text{O}_5</math></b>	<b>49</b>
5.1.	Sample Characterization . . . . .	49
5.1.1.	Crystal Structure . . . . .	49
5.1.2.	Charge Ordering Phenomenon . . . . .	51
5.1.3.	Magnetic and Thermodynamic Properties . . . . .	53
5.2.	ESR in $\alpha'$ - $\text{NaV}_2\text{O}_5$ . . . . .	54
5.2.1.	Resonance Spectra . . . . .	54
5.2.2.	Analysis of the $\mathbf{g}$ Tensor . . . . .	55
5.2.3.	ESR Linewidth . . . . .	57
5.3.	Analysis of Relaxation Mechanisms . . . . .	58
5.3.1.	Exchange Pathways . . . . .	60
5.3.2.	Symmetric Anisotropic Exchange in $\alpha'$ - $\text{NaV}_2\text{O}_5$ . . . . .	61
5.4.	Summary . . . . .	65
<b>6.</b>	<b>Superexchange Competition in <math>\text{TiOCl}</math></b>	<b>67</b>
6.1.	Sample Characterization . . . . .	67
6.1.1.	Crystal Structure . . . . .	67
6.1.2.	Magnetic and Thermal Properties . . . . .	69
6.1.3.	Fluctuations in the High-Temperature Phase . . . . .	71
6.2.	ESR in $\text{TiOCl}$ . . . . .	71
6.2.1.	Resonance Spectra and Absorption Intensity . . . . .	73
6.2.2.	$g$ -Factor and ESR Linewidth . . . . .	73
6.3.	Crystal-Field Splittings of $\text{Ti}^{3+}$ . . . . .	76
6.4.	Spin Relaxation in $\text{TiOCl}$ . . . . .	78
6.4.1.	Symmetric Anisotropic Exchange . . . . .	79
6.4.2.	Dzyaloshinsky-Moriya Interaction . . . . .	82
6.4.3.	Competition of Relaxation Mechanisms . . . . .	84
6.5.	Summary . . . . .	88
<b>7.</b>	<b>Multi-Spin Chains in <math>\eta</math>-<math>\text{Na}_{9/7}\text{V}_2\text{O}_5</math></b>	<b>89</b>
7.1.	Crystal Structure . . . . .	89
7.2.	ESR in $\eta$ - $\text{Na}_{9/7}\text{V}_2\text{O}_5$ . . . . .	90
7.2.1.	Experimental Survey . . . . .	90
7.2.2.	Splittings of Crystal-Field Levels . . . . .	93

---

7.2.3. Exchange Interactions . . . . .	94
7.2.4. Analysis of the Linewidth . . . . .	96
7.3. Charge Fluctuations . . . . .	97
7.3.1. Cross-Relaxation via a Mixed Valence Fragment $V^{4.5+\delta}-V^{4.5-\delta}$ . . . . .	97
7.3.2. Changes in Dielectric Conductivity . . . . .	101
7.3.3. Specific Heat Measurements . . . . .	102
7.4. Exotic Low-Temperature Ground State of $\eta\text{-Na}_{9/7}\text{V}_2\text{O}_5$ . . . . .	103
7.5. Summary . . . . .	108
<b>8. Conclusions and Perspectives</b>	<b>111</b>
<b>Appendix</b>	
<b>A. Canonical-Transformations Perturbation Method</b>	<b>113</b>
<b>B. Angular Overlap Model and the Program Package CAMMAG</b>	<b>119</b>
<b>C. Kubo-Tomita Approach and Method of Moments</b>	<b>121</b>
C.1. Second Moment of Dzyaloshinsky-Moriya Interaction . . . . .	121
C.2. Second Moment of Symmetric Anisotropic Exchange . . . . .	122
<b>Bibliography</b>	<b>123</b>
<b>List of Publications</b>	<b>139</b>
<b>Acknowledgements</b>	<b>141</b>
<b>Curriculum Vitae</b>	<b>143</b>



# 1. Introduction

The effective dimensionality and electron correlations determine the properties of interacting electron systems. Furthermore, correlation effects increase as the number of effective dimensions decreases: for example, in three-dimensional metallic systems, the low-energy electronic states behave as Fermi liquid quasiparticles, whereas in one dimension, even weak interactions break the quasiparticles into collective excitations. The concept of a Luttinger liquid [Tomonaga'50, Luttinger'63] has recently been established as vital to our understanding of the behavior of one-dimensional quantum systems. This concept has led to a number of theoretical breakthroughs, in particular, this theory characterizes the low-energy excitation spectrum as consisting entirely of *independent* spin and charge density fluctuations. Over the last decade its descriptive power has been confirmed experimentally, when high quality quantum wires have been fabricated displaying all characteristic Luttinger liquid properties [Bockrath'99, Ishii'03].

The variety of exotic ground states, new phases of matter and quantum effects dominating thermal fluctuations are only some of the phenomena that the low-dimensional systems offer to enrich solid state physics. Moreover, the theoretical treatment is sufficiently simplified in a reduced dimension allowing to solve many theoretical models exactly. For more than 30 years the experimental realization of (quasi-)low-dimensional compounds is not a real problem anymore: anisotropy of exchange coupling obtained in organic spin systems reaches the values of  $10^4:1$  [Dietz'71]. It has also to be mentioned that the huge fundamental work made in the field of low-dimensional systems is of great importance in three-dimensional systems as well. One of the recent examples is given by the three-dimensional cubic system  $\text{Tl}_2\text{Ru}_2\text{O}_7$  which has been supposed to evolve into a one-dimensional spin-one system with a spin gap below  $T = 120$  K [Lee'06]. The appearance of the gap was predicted by Haldane in 1983 as an inherent property of integer spin chain systems [Haldane'83]. But low-dimensional systems are not only interesting from a fundamental physics point-of-view. They offer unique opportunities for practical applications, for example building of quantum computers, high-capacious data-storage elements and superconductors. Therefore, understanding the properties of low-dimensional spin systems is one of the central problems in quantum magnetism.

Nevertheless, despite the fact that the field of low-dimensional magnetism developed into one of the most active areas of today's solid state physics, the number of unexplained phenomena tends to increase with time. Their understanding needs a more detailed study of the physics underlying these phenomena. In this thesis we will characterize the spin relaxation mechanisms in one-dimensional spin systems using the electron spin resonance



spectroscopy. This technique allows to directly access the spin of interest and gain information on its relaxation processes and, in particular, on the exchange interaction with its neighbors. The systems chosen for the present study are all structurally different but reveal a clear one-dimensional character in their magnetic properties. In spite of structural differences, we will show the close similarity of their relaxation behavior and identify the dominant sources of spin relaxation common in all compounds.

Two of the systems investigated are the members of the sodium-vanadium bronze series  $\text{Na}_x\text{V}_2\text{O}_5$  which acquired a paradigmatic status. The possibility to tune the vanadium valence between  $\text{V}^{4+}$  ( $3d^1$ ) and  $\text{V}^{5+}$  ( $3d^0$ ) allows the realization of a variety of spin-1/2 systems with strong quantum effects. Moreover, the rich structural chemistry of these systems, where the V ions can occur in pyramidal, tetrahedral, or octahedral coordination, gives rise to the formation of very interesting chain-like and ladder-like structures.  $\beta\text{-Na}_{1/3}\text{V}_2\text{O}_5$  which shows a metal-to-insulator transition and superconductivity under pressure is only one member of this series. This study focuses on two other compounds with higher Na concentration:  $\alpha'\text{-NaV}_2\text{O}_5$  and  $\eta\text{-Na}_{9/7}\text{V}_2\text{O}_5$ . The former system reveals charge ordering phenomena [Grenier'02] and has been intensively studied during the last decade. The latter one came only recently into the focus of interest and we will show that its ground state can be understood in terms of exotic spin objects.

Strictly speaking, both of these systems are not ideal spin chains.  $\alpha'\text{-NaV}_2\text{O}_5$  represents a prototypical two-leg spin-ladder system, and  $\eta\text{-Na}_{9/7}\text{V}_2\text{O}_5$  can be described as a zigzag-like chain. In order to make this study more conclusive, a linear spin chain compound,  $\text{TiOCl}$ , was considered as well. The properties of this system are even more exciting.  $\text{TiOCl}$  exhibits a spin-Peierls-like dimerization [Pytte'74] with the highest transition temperature known at the moment [Shaz'05] and undergoes a metal-to-insulator transition under pressure [Kuntscher'06]. Furthermore, electron doped  $\text{TiOCl}$  has been suggested to exhibit unconventional superconductivity with a  $T_C$  of about room temperature [Craco'06].

The course of this thesis is the following: First, we give an introduction to the microscopical theory of superexchange in Chapter 2, including the generalized schemas of the Dzyaloshinsky-Moriya and the pseudodipolar exchange. In Chapter 3, we briefly review the properties of low-dimensional systems necessary for the following analysis. The basic ideas of electron spin resonance spectroscopy in concentrated spin systems are given in Chapter 4. In the following Chapters we consider three spin-chain systems:  $\alpha'\text{-NaV}_2\text{O}_5$ , where the spin relaxation can be explained by only one type of exchange interaction is treated first, in Chapter 5. The next Chapter deals with the more involved situation in  $\text{TiOCl}$ . Chapter 7 treats then the  $\eta\text{-Na}_{9/7}\text{V}_2\text{O}_5$  system. The electron spin resonance data in this compound are even richer in features, but are crucial in determining the nature of the low-temperature ground state. Chapter 8 is devoted to conclusions. It is followed finally by an Appendix which contains the explicit derivation of exchange constants in terms of a perturbation theory.

## 2. Microscopic Theory of Superexchange

Exchange interaction, the major source of magnetic ordering in solids, constitutes the head stone of the theory of magnetism. The concept of exchange coupling arose in 1927 with the Heitler-London theory of the chemical bonds [Heitler'27], and was at once applied by Heisenberg [Heisenberg'28] to the theory of ferromagnetism. The Heisenberg model of exchange interaction became the foundation for most of the current theoretical treatments of cooperative magnetic phenomena. The principal feature of this model is the assumption that the interaction  $\mathcal{H}_{\text{iso}}$  between two magnetic atoms  $a$  and  $b$  in a crystal can be expressed as  $\mathcal{H}_{\text{iso}} = J(\mathbf{S}_a \cdot \mathbf{S}_b)$ , where  $J$  is an exchange integral and  $\mathbf{S}_\alpha$  is the spin operator for the respective atom. Obviously, the sign and magnitude of  $J$  are extremely important in determining the transition temperatures, the magnetic structures, and indeed practically all of the fundamental magnetic properties of a crystal. But this model does not account for any anisotropic effects.

Generally, the exchange interaction

$$\mathcal{H}_{\text{ex}} = \sum_{ij} J_{ij} S_{a,i} S_{b,j} \quad (i, j = \{x, y, z\}) \quad (2.1)$$

contains two anisotropic terms as well

$$\mathcal{H}_{\text{ex}} = J(\mathbf{S}_a \cdot \mathbf{S}_b) + \frac{1}{2} \sum_{ij} D_{ij} (S_{a,i} S_{b,j} + S_{a,j} S_{b,i}) + (\mathbf{d} \cdot [\mathbf{S}_a \times \mathbf{S}_b]). \quad (2.2)$$

The second term describes the *symmetric* anisotropic exchange and the third term – the *Dzyaloshinsky-Moriya (antisymmetric)* interaction. Both of them are considerably smaller than the isotropic Heisenberg exchange (the first term), but have a profound impact on the magnetic properties of crystals. Among others, they produce canted spin arrangements and can even lead to phase transitions in the systems of lower dimension, as for instance the Berezinsky-Kosterlitz-Thouless transition in two-dimensional lattice. Moreover, the anisotropic parts of exchange interaction seem to be the origin of magnetism-induced ferroelectricity. A particular importance they get in spin-1/2 systems, where they represent the only one source of anisotropy.<sup>1</sup>

<sup>1</sup> (i) Double exchange interaction which cannot be written using spin variables is beyond the scope of this work and will only be mentioned briefly in chapter 2.2.5.

(ii) In case  $\mathbf{S} > 1/2$ , this equation may only be the leading term of a series expansion with respect to the total spin operators  $\mathbf{S}_a$  and  $\mathbf{S}_b$ , in which higher terms such as biquadratic  $(S_{a,i} S_{b,j})^2$  occur.

In spite of the remarkable success in the general theory of cooperative phenomena, any rigorous treatment of exchange interactions in three-dimensional systems lies behind the classical statistical theory. But the difficulties of quantum-mechanical treatment can be overcome in a lower dimension: The recent field-theory calculation of the spin-1/2 quantum antiferromagnetic chain by Oshikawa and Affleck [Oshikawa'02] gives an unique opportunity to study the exchange interactions in spin chain compounds using the rigorous theoretical basis. On the other hand, the large isotropic exchange ( $J/k_B \sim 10^2$  K) characteristic for one-dimensional spin systems serves as a background for comparatively small anisotropic contributions and makes it difficult to access them by means of magnetic susceptibility or by inelastic neutron scattering. But the spin-spin relaxation, measured by the electron spin resonance spectroscopy, is driven primarily by the local fields produced by the anisotropic parts only. That makes the electron spin resonance an ideal tool to study these fine effects.

One of the main purposes of this thesis is to investigate the influence of the exchange interaction on the spin relaxation in low-dimensional systems both from the experimental and the theoretical side. In this chapter we will discuss a theoretical approach, which allows to estimate their magnitude microscopically and allows in the most ocular (and correct) way to deal with the exchange interactions.

## 2.1. Exchange Mechanisms

Spin exchange correlations may only occur if the wave functions of the electron of interest have a non negligible overlap. In case of direct overlap of the orbitals of neighboring magnetic ions one speaks about *direct exchange*.

### 2.1.1. Direct Exchange Interaction

The Hamiltonian of direct exchange between the ions  $a$  and  $b$  has generally the form [Eremin'72]

$$\mathcal{H}_{\text{dir}} = -\frac{1}{2}(\mathcal{H}\mathcal{P} + \mathcal{P}\mathcal{H}) + \frac{1}{2}\left(\sum \mathcal{H}|\psi_1\psi_2\rangle\langle\psi_1\psi_2|\mathcal{P} + \sum \mathcal{P}|\psi_1\psi_2\rangle\langle\psi_1\psi_2|\mathcal{H}\right). \quad (2.3)$$

---

Theoretical [Anderson'59, Gondaira'66] as well as experimental [Harris'63] estimates of this contribution give the value, which is two orders of magnitude smaller than the bilinear part (2.1). In this work we will concern only  $S = 1/2$  systems for which this expression is fully correct. The quantities entering into Eq. (2.2) are

$$J = \frac{1}{3} \sum_i J_{ii}, \quad D_{ij} = J_{ij}^{\text{sym}} - J\delta_{ij}, \quad J_{ij}^{\text{sym}} = \frac{1}{2}(J_{ij} + J_{ji});$$

$$d_x = \frac{1}{2} J_{yz}^{\text{asym}}, \quad d_y = \frac{1}{2} J_{zx}^{\text{asym}}, \quad d_z = \frac{1}{2} J_{xy}^{\text{asym}}, \quad J_{ij}^{\text{asym}} = \frac{1}{2}(J_{ij} - J_{ji}).$$

Here  $|\psi_1\psi_2\rangle \equiv |\psi_1\rangle|\psi_2\rangle$  means the product of the wave functions of interacting electrons, the permutation operator  $\mathcal{P} = \sum_{ij} \mathcal{P}_{ij}$  interchanges two electrons  $i$  and  $j$ . Let us discuss the case of one electron on each site (see Fig. 2.1). The total Hamiltonian then reads

$$\mathcal{H} = \frac{p_1^2}{2m} + \frac{p_2^2}{2m} - \frac{Z_a e^2}{r_{a1}} - \frac{Z_b e^2}{r_{b2}} - \frac{Z_b e^2}{r_{b1}} - \frac{Z_a e^2}{r_{a2}} + \frac{e^2}{r_{12}}. \quad (2.4)$$

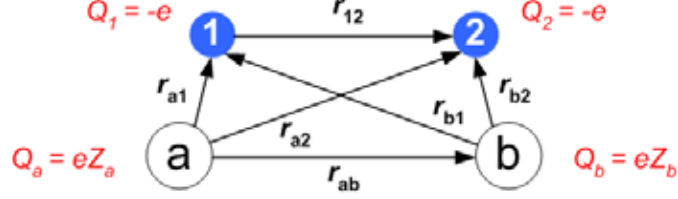


Figure 2.1.: Schematic representation of two interacting electrons 1 and 2 belonging to the ions  $a$  and  $b$ , respectively.

In terms of spin operators the Hamiltonian of direct exchange between two electrons in the states  $\eta$  and  $\zeta$  reads

$$\mathcal{H}_{\text{dir}}^{\eta\zeta} = J_{\eta\zeta}^{\text{dir}} \left[ \frac{1}{2} + 2(\mathbf{s}_\eta \cdot \mathbf{s}_\zeta) \right], \quad (2.5)$$

where the parameter  $J_{\eta\zeta}^{\text{dir}}$  is determined by [Schastnev'75]

$$J_{\eta\zeta}^{\text{dir}} = -\langle \eta_1 \zeta_2 | \frac{e^2}{r_{12}} | \eta_2 \zeta_1 \rangle + 2\text{Re} \langle \eta | \zeta \rangle \langle \eta | \frac{p^2}{2m} | \zeta \rangle - |\langle \eta | \zeta \rangle|^2 \left[ \varepsilon_\eta + \varepsilon_\zeta - \langle \eta | U_2 | \eta \rangle - \langle \zeta | U_1 | \zeta \rangle + \langle \eta_1 \zeta_2 | \frac{e^2}{r_{12}} | \eta_1 \zeta_2 \rangle \right]. \quad (2.6)$$

$S_{\eta\zeta} \equiv \langle \eta | \zeta \rangle$  represents the overlap integral.  $U_1$  and  $U_2$  are the Coulomb energies of electrons in the field of the other atoms,  $\varepsilon_\eta$  and  $\varepsilon_\zeta$  – the Hartree-Fock energies of the electrons in the states  $\eta$  and  $\zeta$ , respectively:

$$U_2 = -\frac{Z_b e^2}{r_{b1}} + \langle \zeta_2 | \frac{e^2}{r_{12}} | \zeta_2 \rangle, \quad \varepsilon_\eta | \eta_1 \rangle \equiv \left( \frac{p_1^2}{2m} - \frac{Z_a e^2}{r_{a1}} \right) | \eta_1 \rangle. \quad (2.7)$$

The first term in Eq. (2.6) represents the *potential exchange* as introduced by Anderson [Anderson'59]. It is always negative and favors a *ferromagnetic* spin alignment. Detailed calculations show [Freeman'61, Freeman'62] that  $J_{\eta\zeta}^{\text{dir}}$  is negative only in case of zero overlap of the neighboring orbitals  $S_{\eta\zeta} = 0$ , otherwise the last two terms in Eq. (2.6) will dominate and lead to an antiferromagnetic coupling.

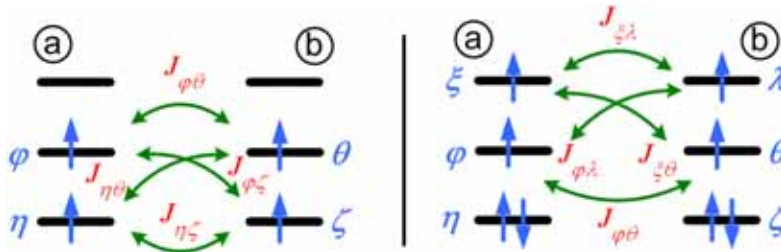


Figure 2.2.: Channel model of exchange interaction [Eremin'77]. The exchange coupling of each pair of spins  $J_{\alpha\alpha'}$  is supposed to be mutually independent that allows their algebraical summation (2.9).

The microscopical expression (2.6) corresponds to the exchange between a pair of spins. In case of several electrons on one site the exchange operator is usually approximated by the sum of individual exchange integrals  $J_{\eta\zeta}^{\text{dir}}$  depicted in Fig. 2.2:  $\mathcal{H}_{\text{dir}} = \sum \mathcal{H}_{\text{dir}}^{\eta\zeta}$ . For detailed discussion of this 'channel model' we refer to [Eremin'77, Eremin'80]. Here we will consider only the case of interacting ions in the ground state what is usually the case in magnetic resonance measurements. According to Hund's rule they possess the maximal spin value  $\mathbf{s}_\eta = \frac{1}{2S_a} \mathbf{S}_a$ ,  $\mathbf{s}_\zeta = \frac{1}{2S_b} \mathbf{S}_b$ , and, hence, the spin dependent part of the Hamiltonian of direct exchange reads

$$\mathcal{H}_{\text{dir}} = J^{\text{dir}} (\mathbf{S}_a \cdot \mathbf{S}_b), \quad (2.8)$$

where the effective exchange integral is given by

$$J^{\text{dir}} = \frac{1}{2S_a S_b} \sum_{\eta\zeta} J_{\eta\zeta}^{\text{dir}}. \quad (2.9)$$

The exchange integral (2.9) scales with the overlap squared and decreases exponentially with the distance  $r$  between the spins. Therefore, direct exchange plays a large role only for radicals [Musin'76] and in case of  $90^\circ$  metal-ligand-metal exchange geometry. For  $3d$ -ions it becomes negligible already at  $r \sim 2.7 - 3 \text{ \AA}$ . In practice, magnetic ions  $a$  and  $b$  are always separated by diamagnetic ions  $c$ , so that no appreciable direct overlap is to be expected in this case. That led Kramers [Kramers'34] to propose that a strong admixture of the cation's and intermediate anion's wave functions could be invoked to couple the cations *indirectly*.

### 2.1.2. Indirect Exchange Mechanisms

It is tempting to assume, by analogy with the case of direct exchange, that exchange coupling in case of three-center system  $a - c - b$  will be proportional to the product of the overlap integrals  $J_{\eta\zeta} \propto S_{\eta\kappa}^2 S_{\kappa\zeta}^2$  ( $\kappa$  is the state of the intermediate diamagnetic

ion  $c$ ). This contribution referred as Yamashita-Kondo's mechanism is nevertheless only marginal because the overlap integrals  $S_{\eta\kappa}$  are usually small compared to the covalency parameters (i. e. hopping integrals  $t_{\eta\kappa}$ , see Eq. A.17).

The hopping integrals  $t_{\eta\kappa}$  characterize the kinetic energy of electrons or their desire to delocalize. Whenever their repulsion predominates and prevents metallic conduction, the tendency to delocalize can gain energy by spreading electrons into nonorthogonal overlapping orbitals, naturally leading to the antiferromagnetic spin ordering. This problem was first considered by Kramers who developed a unique method of handling configuration interactions [Kramers'34]. The idea by Kramers is displayed in Fig. 2.3(i). The excited configuration in which an electron has been removed from the nonmagnetic center  $c$  and placed on  $a$  leaves an unpaired spin on  $c$  and  $b$  leading to a spin coupling due to the direct overlap of these charge densities. The magnitude of this type of indirect exchange can be estimated as  $J_{\eta\zeta} \propto t_{\eta\kappa}^2 S_{\kappa\zeta}^2$ .

Twenty years later Pratt [Pratt'55] could show that such polarization effects cannot produce the actual antiferromagnetic spin-ordering and proposed another scheme shown in Fig. 2.3(ii): two electrons of the diamagnetic ion are simultaneously transferred to the magnetic ions providing an antiferromagnetic coupling. An attempt to compare the effectiveness of all possible mechanisms of superexchange was made by Yamashita and Kondo [Yamashita'58], but it was not possible to single out the most efficient one. In 1959, Anderson [Anderson'59] simplified and unified the various mechanisms giving rise to superexchange interaction. He showed that the superexchange mechanism, where the ionic configuration  $a^+b^-$  is obtained (see Fig. 2.4), strongly dominates all others. On the one hand, the energy of this ionic state is higher than the energy of the unperturbed state by an amount  $U = \Delta_{ab}$ , corresponding to the average electrostatic repulsion energy for two electrons on the same site. On the other hand, the system gains kinetic energy  $J_{\eta\zeta} \propto t_{\eta\kappa}^2 t_{\kappa\zeta}^2$ . This delocalization stabilizes the singlet configuration, because the two

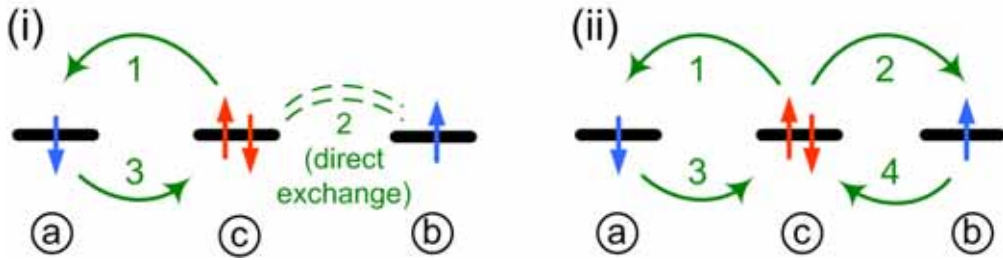


Figure 2.3.: Schematic representation of the indirect exchange between two magnetic ions  $a$  and  $b$  via a diamagnetic ion  $c$  proposed by (i) Kramers in 1934 [Kramers'34] and (ii) Pratt in 1955 [Pratt'55]. The green arrows denote the virtual hoppings of electrons. Numeration corresponds to the sequence of the electron transfers.

electrons at site  $b$  must necessarily pair up. Anderson’s approach to the theory of superexchange interactions has become classical and will be considered in more detail in the next section.

## 2.2. Isotropic Exchange Interaction

The following consideration generalizes Anderson’s approach [Anderson’59] by accounting directly for the states of an intermediate ion. It is based on the method of canonical transformations which allows in a natural way to derive the constants of exchange interactions using a perturbation theory. The detailed description of this method can be found in appendix A. Here we will only use the results of these calculations, which are needed to discuss the underlying physical processes.

First, let us introduce some notations:  $a_{\eta}^+(a_{\eta'})$  and  $b_{\zeta}^+(b_{\zeta'})$  are the creation (annihilation) operators of electrons on the magnetic ions,  $c_{\kappa}^+(c_{\kappa'})$  – on the intervening diamagnetic ions. With  $\eta, \varphi, \xi$  we denote the orbital and spin states of the magnetic ion  $a$  [ $\eta \equiv (n_{\eta} l_{\eta} m_{\eta} s_{\eta})$ ] and with  $\zeta, \theta, \lambda$  the corresponding states of the magnetic ion  $b$ . The letters  $\kappa, \rho$  signify the one-electron states of the diamagnetic ion  $c$ .

### 2.2.1. Classical Concept: Antiferromagnetic Spin Ordering

The most effective mechanism of the isotropic superexchange between two magnetic ions  $a$  and  $b$  via the intervening ion  $c$  as first described by Anderson [Anderson’59] is illustrated in Fig. 2.4. By counting the involved electronic hopping processes, it becomes evident that this mechanism corresponds to the fourth order of perturbation theory with respect to the energy of the electron hoppings.

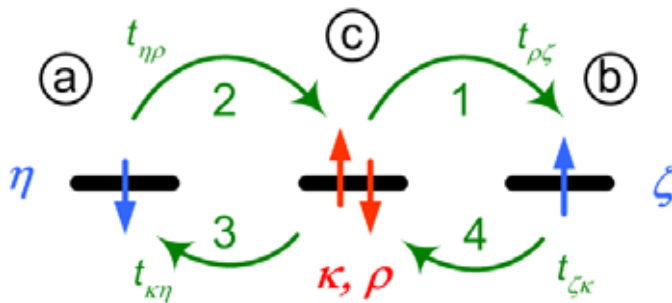


Figure 2.4.: Schematic representation of the "superexchange" between two magnetic ions  $a$  and  $b$  via a diamagnetic ion  $c$  proposed by Anderson [Anderson’59]. The green arrows denote the virtual hoppings of electrons. The Greek letters denote the orbital states of an electron on the corresponding ion.

Consequently, this process can be described by the Hamiltonian (A.22), which is derived in the appendix. Here, we add a factor of two to this Hamiltonian

$$\mathcal{H}_{\text{kin}} = 2 \cdot \frac{t_{\eta\rho}t_{\rho\zeta}t_{\zeta\kappa}t_{\kappa\eta}}{\Delta_{ac}^2\Delta_{ab}} \left( -\frac{1}{2} + 2(\mathbf{s}_\eta \cdot \mathbf{s}_\zeta) \right), \quad (2.10)$$

because we also take into account the electron transfer from site  $a$  to site  $b$ . Moreover,  $t_{\eta\rho}$  denotes the *hopping (transfer) integral* between the orbital states  $\eta$  and  $\rho$ ,  $\Delta_{ab} \sim U$  and  $\Delta_{ac}$  are the electron transfer energies from ion  $a$  to the cation  $b$  and to the anion  $c$ , respectively. The expression (2.10) represents the *kinetic exchange* in Anderson's notation and was considered to be intrinsically *antiferromagnetic*. This type of exchange constitutes an *isotropic antiferromagnetic exchange interaction*

$$\mathcal{H}_{\text{iso}}^{\eta\zeta} = J_{\eta\zeta} (\mathbf{s}_\eta \cdot \mathbf{s}_\zeta) \longrightarrow \mathcal{H}_{\text{iso}} = J (\mathbf{S}_a \cdot \mathbf{S}_b), \quad (2.11)$$

where the constant of isotropic exchange is given by

$$J_{\eta\zeta} = 4 \cdot \frac{t_{\eta\rho}t_{\rho\zeta}t_{\zeta\kappa}t_{\kappa\eta}}{\Delta_{ac}^2\Delta_{ab}} \quad \text{and} \quad J = \frac{1}{4S_a S_b} \sum_{\eta\zeta} J_{\eta\zeta}. \quad (2.12)$$

The direct exchange (2.8) is also isotropic, but negligible as compared to the kinetic exchange because of the large distance between the interacting ions. It is worth noting, that the isotropic exchange is strongly antiferromagnetic only in case of  $180^\circ$  bond geometry (all three ions are lying on a straight line). The deviations of the bond angle  $\theta$  from  $180^\circ$  can be described by introducing geometrical factors like, for example,  $t(\theta) \propto -t_\sigma \cos\theta - t_\pi \sin\theta$ . As we will discuss in the following, competition and quantum-interference effects between different exchange paths can occur in some cases and can lead to a strong *ferromagnetic* coupling of spins [Bencini'90, Krug'02].

### 2.2.2. Ferromagnetic Superexchange

Following Anderson, ferromagnetic coupling can be obtained considering two major processes: (i) potential exchange and (ii) transfer of the electron to the unoccupied orbital of the neighboring ion. The indirect potential exchange is, as a matter of fact, of the same nature as the corresponding direct process. It describes the electrostatic energy of the system as a spin-spin interaction in the basis of one-electron wave functions. Anderson's treatment allows to separate the part of the interaction containing the spreading of the orbitals of the  $d$ -electrons into the neighboring ions by the modification of the local wave functions. The exchange effect then appears as a consequence of the direct overlap of the new longer-ranging orbitals. But this process only plays a minor role compared to the following one.

The second mechanism is shown schematically on the left side of Fig. 2.5. This is a fifth-order effect of transfer together with the internal exchange coupling  $V_{mm'}^{(1)} = J_H$  (see



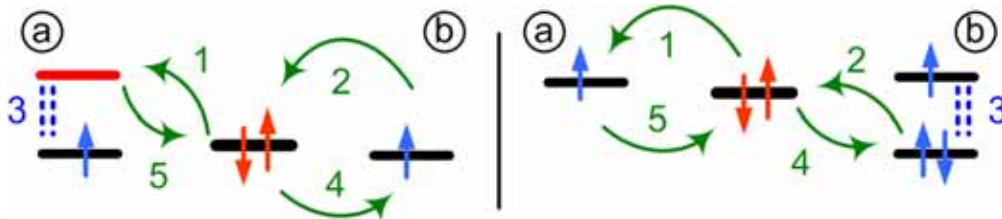


Figure 2.5.: Two possible mechanisms favoring ferromagnetic exchange. Left: transfer of an electron to the empty orbital state of the neighboring ion, the spins will be aligned parallel in accordance with the Hund's rule. Right: Scheme of the electron transfer from the fully-filled orbital state of ion  $b$  into the half-filled orbital of ion  $a$ , the ferromagnetic configuration will be minimized due to the Pauli principle as well as the Hund's rule.

appendix A). Therefore, its order of magnitude in comparison with the antiferromagnetic isotropic exchange (2.11) can be estimated as

$$J^{\text{FM}} \approx -J \cdot \frac{J_H}{\Delta_{ab}}. \quad (2.13)$$

Here,  $J_H$  represents the matrix element of the Coulomb interaction on the involved pair of orbitals. E.g.  $J_H(d_{xy}, d_{x^2-y^2}) = C$ ,  $J_H(d_{xy}, d_{yz}) = J_H(d_{xy}, d_{xz}) = 3B + C$ ,  $J_H(d_{xy}, d_{3z^2-r^2}) = 4B + C$  [Griffith'71], where  $B$  and  $C$  are the Racah parameters. Anderson estimated  $J_H/\Delta_{ab}$  to be about  $0.1 \div 0.2$  and supposed that this interaction is negligible in comparison with the potential exchange [Anderson'59]. However, the analysis of experimental data has shown the importance of this mechanism for formation of the magnetic structure in many dielectrics: Goodenough [Goodenough'58] has emphasized the key role of empty and filled orbitals, and proposed two processes depicted in Fig. 2.5 for the formation of the ferromagnetic ground state. In the following we will give some examples in which the exchange coupling between the excited states and the ground states exceeds in orders of magnitude the exchange between ground states only, favoring a ferromagnetic coupling of spins.

### 2.2.3. Quantum Interference of Superexchange Interactions

As described above the traditional approach to superexchange in dielectrics is based on the three-centre (metal-ligand-metal) model [Anderson'63]. It is assumed tacitly that the resulting interaction is the algebraical sum of all contributions from the bridging ligands. In this chapter we would like to emphasize that, in general, superexchange is *not* additive. In fact, an interference occurs in superexchange via two or more intermediate ions, which can suppress as well as amplify Anderson's conventional superexchange.

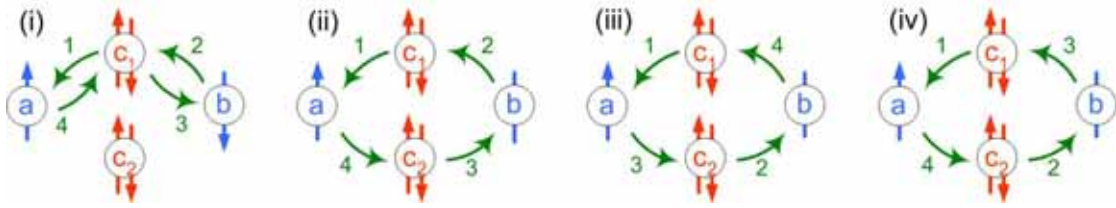


Figure 2.6.: Electron-transfer schemes illustrating various superexchange mechanisms via anions  $c_1$  and  $c_2$  between cations  $a$  and  $b$ . (i), (ii), (iii) and (iv) refer to transfer sequences.

This statement is easily to substantiate in terms of the 'four centers - six electrons' model. Various sequences of one-electron transfers responsible for superexchange between magnetic ions  $a$  and  $b$  via the diamagnetic ions  $c_1$  and  $c_2$  are shown in Fig. 2.6. The scheme (i) describes Anderson's additive superexchange through several ligands [Anderson'63]. Three other sequences correspond to essentially four-centre exchange mechanisms. All the mechanisms specified contribute naturally to the fourth-order perturbation and therefore their effect should be of the same order of magnitude.

The looped exchange of the type (ii) is the interference process to the usual Anderson's exchange (i). If the product of all transfer integrals is positive, it provides an antiferromagnetic contribution. Correspondingly, the contribution becomes ferromagnetic, if the product is negative. Note that if the ligands  $c_1$  and  $c_2$  are equivalent, this contribution doubles as well as completely suppresses the Anderson type of exchange [Eremin'82a].

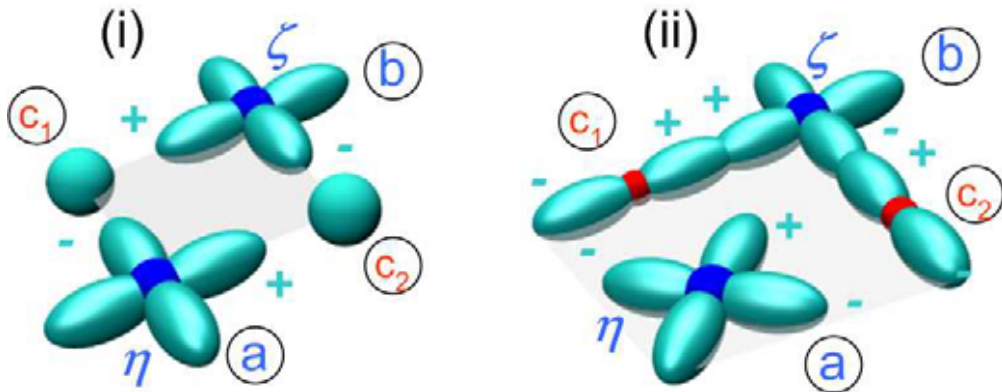


Figure 2.7.: Schemes of overlapping orbitals having (i) the same and (ii) different symmetries in the case of two bridging ligands. In the former case the product of transfer integrals for ring-like processes is positive favoring antiferromagnetic coupling, in the latter one it is negative providing a ferromagnetic contribution.

These two extreme cases are shown in Fig. 2.7(i) and (ii), respectively. This effect is called *quantum interference* of superexchange interaction.

Two other types of exchange processes shown in Fig. 2.6(iii),(iv) are not reducible to the exchange looped paths. They should be rather called the interference processes with regard to Pratt's mechanism shown in Fig. 2.3(ii). However, with the transfer energy of two electrons from one ligand being higher than the transfer energy of electrons from different ligands, mechanisms (iii) and (iv) of Fig. 2.6 dominate the Pratt's exchange mechanism. The effective Hamiltonian of this type of exchange has the form [Eremin'82b]

$$\mathcal{H}^{(\text{iii,iv})} = \sum \frac{1}{|\Delta_{\eta^-\kappa^+\rho^+\zeta^-}|} \left( \frac{t'_{\eta\rho} t_{\zeta\kappa}}{\Delta_{\zeta\kappa}} + \frac{t'_{\zeta\kappa} t_{\eta\rho}}{\Delta_{\eta\rho}} \right) \left( \frac{t'_{\rho\zeta'} t_{\kappa\eta'}}{\Delta_{\kappa\eta'}} + \frac{t'_{\kappa\eta'} t_{\rho\zeta'}}{\Delta_{\rho\zeta'}} \right) \cdot a_{\eta'} a_{\eta}^+ b_{\zeta'} b_{\zeta}^+, \quad (2.14)$$

where  $\rho$  and  $\kappa$  belong to different anions. Using (2.14) one can conclude that the exchange in the case Fig. 2.7(ii) is ferromagnetic and estimate the exchange constant as  $J_{xy,x^2-y^2} \sim -3(\Delta_{\pi} + \Delta_{\sigma})/(\Delta_{\pi}\Delta_{\sigma})^2 \cdot t_{\pi}^2 (t'_{\sigma})^2$ . Exact calculations showed that this contribution is considerable and amounts e.g. for the  $\text{Cu}^{2+}$  dimers [Voronkova'83] to  $J_{xy,x^2-y^2}/k_B \approx -475$  K.

### 2.2.4. Exchange at Small Charge-Transfer Energy

In the previous chapters we focused on the cases when the isotropic exchange interaction leads to the ferromagnetic coupling of spins. Let us now discuss a further generalization of the classical Anderson's *one electron per site* theory [Anderson'63] and show that in multi-electron systems the kinetic exchange is essentially antiferromagnetic only, if the charge transfer energies exceed by far the inter-term splittings. If this condition is not fulfilled, the averaging of the transfer energies over all configurations is not justified anymore (in other words, the energy denominator in Eq. (A.18) cannot be factored out). That affects the spin-dependent part of the exchange Hamiltonian which from the standard Anderson's form (Eq. 2.10) is transformed to [Eremin'80, Eremin'81]

$$\mathcal{H}_{\text{ex}}^{(\text{sm},\Delta)} \propto 1 - \frac{\bar{S}_a(\bar{S}_a + 1) - S_a(S_a + 1) - \frac{3}{4}}{S_a(S_a + 1)} \cdot \frac{\bar{S}_b(\bar{S}_b + 1) - S_b(S_b + 1) - \frac{3}{4}}{S_b(S_b + 1)} (\mathbf{S}_a \cdot \mathbf{S}_b), \quad (2.15)$$

where  $S_k$  and  $\bar{S}_k$  denote the spin of the ion  $k$  in the ground and excited (with charge transfer) states, respectively. This factor depends on the particular type of excitation. Since we are interested in one-electron transfer, possible excited spin states are  $\bar{S}_k = S_k \pm 1/2$ . Therefore, there are only four types of spin operators corresponding to the charge transfer processes illustrated in Fig. 2.8.

The first process corresponds to the Anderson's exchange, and the spin operators in the last three terms have an unusual form. The type of magnetic ordering due to kinetic exchange depends now on competing contributions. The second and the third type of the exchange processes favor a ferromagnetic coupling, whereas the other ones are

No	$\bar{S}_a$	$\bar{S}_b$	operator	illustration
(i)	$S_a - \frac{1}{2}$	$S_b - \frac{1}{2}$	$1 - \frac{(S_a \cdot S_b)}{S_a S_b}$	
(ii)	$S_a - \frac{1}{2}$	$S_b + \frac{1}{2}$	$1 + \frac{(S_a \cdot S_b)}{S_a(S_b + 1)}$	
(iii)	$S_a + \frac{1}{2}$	$S_b - \frac{1}{2}$	$1 + \frac{(S_a \cdot S_b)}{(S_a + 1)S_b}$	
(iv)	$S_a + \frac{1}{2}$	$S_b + \frac{1}{2}$	$1 - \frac{(S_a \cdot S_b)}{(S_a + 1)(S_b + 1)}$	

Figure 2.8.: Four possible types of one-electron charge transfer.  $\bar{S}_a$  and  $\bar{S}_b$  represent the change of the total spin of the ions  $a$  and  $b$ , respectively. In the fourth column the corresponding spin part (2.15) of the exchange Hamiltonian is given.

responsible for antiferromagnetic spin alignment. The resulting coupling is determined by the first term only in the case of  $180^\circ$  exchange between equivalent ions with half-filled orbitals. Otherwise, couplings of other types may contribute, and the exchange may become ferromagnetic. This conclusion agrees with numerous experimental data.

Let us consider an example of  $\text{Cu}^{2+}$ - $\text{Mn}^{2+}$  pair in  $\text{KZnF}_3$  in order to clarify the previous discussion. Exchange coupling between the ions in the ground state has been found to be antiferromagnetic  $J/k_B \approx 187$  K, whereas  $\text{Mn}^{2+}$  excitation to the  ${}^4A_1$  state results in ferromagnetic exchange  $\bar{J}/k_B \approx -144(\pm 7)$  K [Ferguson'71]. Ferromagnetism in the excited state cannot be rationalized within the traditional exchange theory frame. In particular, the Goodenough-Kanamory rules are obviously violated in this case. The pair under consideration is characterized by a relatively low charge-transfer energy ( $\Delta_{ab} \approx 5$  eV), which is of the same order of magnitude with the energy of the  ${}^4A_1$  state (3 eV). Therefore, the exchange interaction should be analyzed using Eq. (2.15) rather than Eq. (2.10). The quantitative analysis [Eremin'80] explained the negative  $\bar{J}$  by showing that the  $\text{Mn}^{2+}$  ion being in a state of lower than maximum multiplicity gives rise to the exchange process  $\bar{S}_{\text{Cu}} = S_{\text{Cu}} - 1/2$ ,  $\bar{S}_{\text{Mn}} = S_{\text{Mn}} + 1/2$  (case 2 in Fig. 2.8), which is intrinsically ferromagnetic.

### 2.2.5. Double Exchange: Extreme Case of Free Charge Transfer

Having considered the exchange coupling at low energy of transfer, let us discuss shortly the limiting case of free charge transfer. Zener [Zener'51] has shown for the first time that the indirect coupling of incomplete  $d$ -shells via conducting electrons is ferromagnetic. This mechanism called *double exchange* is explained in Fig. 2.9 by the example of a  $Mn^{4+}$ - $Mn^{3+}$  pair.

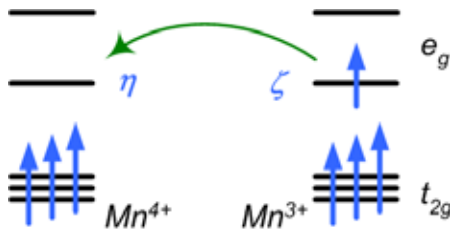


Figure 2.9.: The double-exchange schema by the example of a  $Mn^{4+}$ - $Mn^{3+}$  pair. Both manganese ions are in the spin state with highest multiplicity in compliance with Hund's rule. Since the  $e_g$  electron carries its spin unchanged as it wanders from one ion to another, the energy of the pair will be lower when the spins of both ions are parallel.

The first semiclassical consideration of double exchange was performed by Anderson and Hasegawa [Anderson'55] in terms of a pure spin model. They concluded that this exchange results in the equidistant energy spectra  $E_S \propto -|J_{DE}|(S+1/2)$ . The quantum-mechanical treatment of it can be found in [Karpenko'76]. The double exchange is *kinematic* and therefore cannot be written in form of an effective spin-Hamiltonian as an interaction of spin or orbital moments. But using the Eq. (A.14) we can easily write its Hamiltonian in the second quantization representation:

$$\mathcal{H}_{DE} = \sum t_{\zeta\eta'} b_{\zeta}^{\dagger} a_{\eta'} + \frac{1}{2} \sum \left( \frac{1}{\Delta_{\kappa\zeta}} + \frac{1}{\Delta_{\kappa\eta}} \right) t_{\zeta\kappa} t_{\kappa\eta'} b_{\zeta}^{\dagger} a_{\eta'} + \text{h.c.} \quad (2.16)$$

The first term here corresponds to the direct hopping of an electron from one magnetic ion to another, the second – to the cascade transfer via intermediate anions. The typical values of the exchange constant  $J_{DE} \approx t_{\alpha\alpha'}^2 / \Delta_{\alpha\alpha'}$  are usually about 0.1 eV.

This indirect coupling involving *real* electron transfer should not be confused with the superexchange. The double exchange is inherently degenerate owing to the presence of the magnetic ions of two charges. Therefore, this mechanism is linked inseparably with the electrical conductivity, which is not the case for superexchange. Since we are interested in dielectric materials, we will not account for double exchange in the present work.

## 2.3. Anisotropic Exchange Interaction

The isotropic exchange interaction, which was discussed so far, does not depend on the direction of spins with respect to the crystal axes. Exchange interaction becomes anisotropic when the exchange Hamiltonian includes the spin-orbit (SO) coupling. Due to SO coupling the excited orbital states are always admixed to the ground state of the electron making it sensitive to the local crystal environment. This admixture can be accounted for in terms of the given perturbation expansion (for details see appendix A) by including an additional  $V^{(1)}$  term acting on one site ( $k$ ) – the SO coupling

$$\mathcal{H}_{LS}^{(k)} = \lambda_k (\mathbf{l}_k \cdot \mathbf{s}_k) \quad (2.17)$$

besides four hopping terms (2.10). The SO coupling constant  $\lambda$  is of the order of  $10^2$  K [Abragam'70]. The resulting fifth- or higher order effect will be notably smaller as compared to the four-order isotropic exchange (2.11) but nevertheless makes a profound impact on magnetism and relaxation dynamics of many compounds.

Taking into account a single on-site excitation due to the SO interaction results in the so-called *Dzyaloshinsky-Moriya (antisymmetric) anisotropic exchange* interaction. The effect of two excitation due to SO coupling is symmetric in the spin variables and, therefore, is called *symmetric (pseudo-dipole) anisotropic exchange*.

### 2.3.1. Antisymmetric Part of Anisotropic Exchange

The combination of the on-site SO coupling  $\mathcal{H}_{LS}$  and isotropic exchange  $\mathcal{H}_{\text{iso}}$  can be expressed by the effective Hamiltonian

$$\mathcal{H}_{\text{eff}}^{(5)} = - \sum_{m'} \frac{|\mathcal{H}_{LS}^{(a)} + \mathcal{H}_{LS}^{(b)}|m'\rangle \langle m'|\mathcal{H}_{\text{iso}}| + |\mathcal{H}_{\text{iso}}|m'\rangle \langle m'|\mathcal{H}_{LS}^{(a)} + \mathcal{H}_{LS}^{(b)}|}{\Delta_{mm'}}, \quad (2.18)$$

where  $m$  and  $m'$  are the ground and the excited states involved into the exchange process, respectively. The term of this Hamiltonian, which is quadratic with respect to the spin variables, can be expressed as a cross-product of spin operators

$$(\mathbf{l}_a \cdot \mathbf{s}_a)(\mathbf{s}_a \cdot \mathbf{s}_b) = \frac{1}{4}(\mathbf{l}_a \cdot \mathbf{s}_b) + i(\mathbf{l}_a[\mathbf{s}_a \times \mathbf{s}_b]). \quad (2.19)$$

Therefore, the effective contribution of (2.18) to the exchange interaction is given by

$$\mathcal{H}_{\text{DM}} = \mathbf{d} \cdot [\mathbf{S}_a \times \mathbf{S}_b] \quad (2.20)$$

with [Eremin'UP]

$$d_j = \frac{1}{2S_a S_b} \frac{i}{\Delta_{\eta\zeta}} \left( \frac{1}{\Delta_{\kappa\eta} \Delta_{\rho\eta}} + \frac{1}{\Delta_{\kappa\zeta} \Delta_{\rho\zeta}} \right) \left( t_{\zeta\rho} t_{\rho\eta} \frac{\langle \eta | \lambda_a l_j | \varphi \rangle}{\Delta_{\eta\varphi}} t_{\varphi\kappa} t_{\kappa\zeta} - t_{\eta\kappa} t_{\kappa\zeta} \frac{\langle \zeta | \lambda_b l_j | \theta \rangle}{\Delta_{\zeta\theta}} t_{\theta\rho} t_{\rho\eta} \right), \quad (2.21)$$

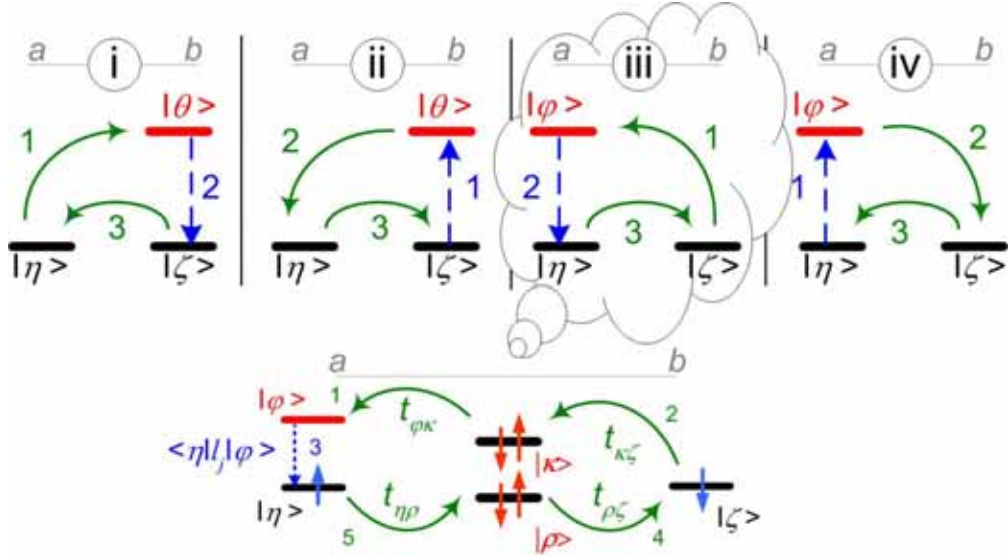


Figure 2.10.: Possible pathways of the DM interaction between the spins in the  $\eta$  and  $\zeta$  states on the ions  $a$  and  $b$ , respectively, via the excited orbital states  $\varphi$  and  $\theta$ . The transition due to the SO coupling is represented by the blue dashed line, the electron hoppings with the transfer integral  $t_{\alpha\alpha'}$  – by the solid green lines.

where  $j = \{x, y, z\}$ ,  $t_{\alpha\alpha'}$  are the effective hopping integrals between the states  $|\alpha\rangle$ ,  $|\alpha'\rangle$  and a sum over all states of an intermediate ion ( $|\kappa\rangle$ ,  $|\rho\rangle$ ) is implied. We also assumed that the charge-transfer energy  $\Delta_{ab} \equiv \Delta_{\eta\zeta}$  from site  $a$  to site  $b$  is large compared to the crystal-field splittings  $\Delta_{cf} \equiv \Delta_{\eta\varphi}, \Delta_{\zeta\theta}$  and the energy of the charge transfer to the intermediate ion  $\Delta_{ac} \equiv \Delta_{\kappa\eta}, \Delta_{\rho\eta} \dots$ . These virtual hopping processes are displayed schematically in Fig. 2.10, where e.g. the frame (iii) corresponds to the first term of Eq. (2.21): the electron on site  $b$  is transferred to the empty state  $\varphi$  at site  $a$  and interacts via SO coupling with the electron in the corresponding ground state  $\eta$ . Then, one of the electrons hops to the initial state  $\zeta$ .

The existence of this kind of anisotropic interaction was pointed out by Dzyaloshinsky [Dzyaloshinski'58] on the basis of symmetry analysis and the microscopic derivation of the interaction was done by Moriya [Moriya'60]. Therefore, this interaction is called the *antisymmetric exchange interaction of Dzyaloshinsky-Moriya* (DM). When the point bisecting the straight line connected two interacting ions is not a center of inversion one can expect that the Dzyaloshinsky-Moriya vector  $\mathbf{d} \neq 0$ . A very useful rule to determine the direction of the DM vector has been given by Keffer [Keffer'62, Moskvin'77]:  $\mathbf{d}_{ab}$  is an axial vector perpendicular to the plane spanned by the interacting magnetic ions  $a$ ,

$b$  and the intermediate diamagnetic ion  $c$

$$\mathbf{d}_{ab} = d_c \cdot [\mathbf{n}_{ac} \times \mathbf{n}_{bc}], \quad (2.22)$$

where the unit vectors  $\mathbf{n}_{ac}$  and  $\mathbf{n}_{bc}$  connect the spins  $a$  and  $b$  with the bridging ion  $c$ , respectively, as it is shown in Fig. 2.11. Note that  $d_c$  is a numerical parameter dependent on the distance between the ions but not on the bond angle. The information about the bond geometry is contained now only in the so-called "geometrical factor"  $\mathbf{G}_c = [\mathbf{n}_{ac} \times \mathbf{n}_{bc}]$  which can be easily calculated.

The rough estimation of the strength of DM interaction using ESR can be obtained in the following way: Let us consider e.g. a  $\text{Cu}^{2+}$  ion placed in an octahedron with a strong tetragonal distortion along the  $z$ -axis and estimate the magnitude of the DM vector  $d_z$  along the  $z$  axis. Knowing the ground state  $\eta = d_{x^2-y^2}$  and the corresponding excited one  $\varphi = d_{xy}$  of a hole in such an environment, the expression (2.21) can be simplified in this case as

$$d_z \simeq 2i \frac{\lambda \langle \eta | l_z | \varphi \rangle}{\Delta_{\eta\varphi}} \cdot 4 \frac{t_{\varphi\kappa} t_{\kappa\zeta} t_{\zeta\rho} t_{\rho\eta}}{\Delta_{ac}^2 \Delta_{ab}} = \frac{4\lambda}{\Delta_{\eta\varphi}} \cdot J_{\varphi\zeta\eta} = \frac{4\lambda}{\Delta_{\eta\varphi}} \cdot J_{\eta\zeta\eta} \frac{t_{\varphi\kappa}}{t_{\eta\kappa}} = \frac{4\lambda}{\Delta_{\eta\varphi}} \cdot J \frac{t_{\varphi\kappa}}{t_{\eta\kappa}}, \quad (2.23)$$

where we used  $\langle \eta | l_z | \varphi \rangle = \langle d_{x^2-y^2} | l_z | d_{xy} \rangle = -2i$  and the definition (2.12) of the exchange integral. The hopping integrals of an electron to the diamagnetic ion from the ground and excited orbital of the magnetic ion are denoted by  $t_{\eta\kappa}$  and  $t_{\varphi\kappa}$ , respectively (see Fig. 2.10). The value of the  $g$  factor along the  $z$  axis gives us the possibility to estimate  $\lambda/\Delta_{\eta\varphi}$  by [Abragam'70]

$$g_z = 2 - 8 \frac{\lambda}{\Delta_{\eta\varphi}} \quad \rightarrow \quad \frac{\lambda}{\Delta_{\eta\varphi}} = \frac{2 - g_z}{8} \simeq \frac{1}{4} \frac{\Delta g}{g}, \quad (2.24)$$

where we have used  $g = 2$  as the  $g$ -factor for the free electron value and  $\Delta g$  denotes the deviation of the experimental  $g$ -value from the pure spin value.

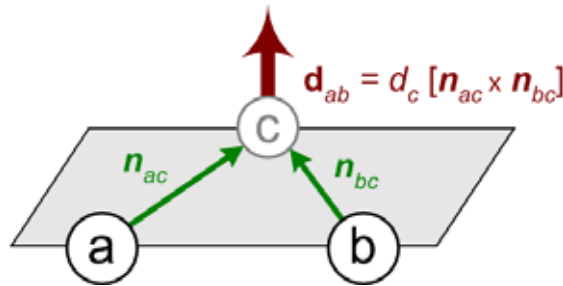


Figure 2.11.: Direction of the DM vector for the interaction between the ions  $a$  and  $b$  via the intermediate ion  $c$  following Keffer [Keffer'62].



Hence, the magnitude of the Dzyaloshinsky-Moriya vector can be estimated as

$$|\mathbf{d}| = d_z \simeq \frac{\Delta g}{g} \cdot J \frac{t_{\varphi\kappa}}{t_{\eta\kappa}}. \quad (2.25)$$

The well-known expression by Moriya [Moriya'60]

$$|\mathbf{d}| \approx \frac{\Delta g}{g} \cdot J, \quad (2.26)$$

( $J$  is the integral of the usual isotropic exchange) can be obtained then using the assumption of the equal hopping integrals between the ground  $t_{\eta\kappa}$  and excited  $t_{\varphi\kappa}$  levels (see Fig. 2.10). Despite the fact that this assumption is not justified in general case [Moskvin'77], it was widely used by many authors and, consequently, the DM interaction was accepted to be the dominant source of anisotropy [Ikebe'71, Yamada'89, Kato'05]. In section 4.5.3 we give several experimental examples, where the DM interaction plays only a minor role in spin relaxation. These findings are in accordance with recent theoretical investigations [Choukroun'01, Oshikawa'02] which strongly support that the symmetric and the antisymmetric part of the anisotropic exchange in low-dimensional transition metal compounds are at least of equal importance.

### 2.3.2. Symmetric Anisotropic Exchange Interaction

Let us consider now the next order of perturbation theory taking into account four virtual electron transfer and *two* times the effect of SO coupling. As we will show later, in case of orbital order and reduced dimensionality this type of exchange can dominate all other anisotropic spin-relaxation mechanisms. Proceeding just as described in the previous section, we rewrite the general Hamiltonian

$$\mathcal{H}_{\text{eff}}^{(6)} = \sum_{m'm''} \frac{|\mathcal{H}_{LS}^{(a)}|m''\rangle \langle m''|\mathcal{H}_{\text{iso}}|m'\rangle \langle m'|\mathcal{H}_{LS}^{(a)}|}{\Delta_{mm'}\Delta_{mm''}}, \quad (2.27)$$

considering only the terms which are quadratic in the spin variables,

$$(\mathbf{l}_a \cdot \mathbf{s}_a)(\mathbf{s}_a \cdot \mathbf{s}_b)(\mathbf{l}_a \cdot \mathbf{s}_a) \longrightarrow \frac{1}{4} \sum_{ij} l_{a,i} l_{a,j} (s_{a,i} s_{b,j} + s_{a,j} s_{b,i}) \quad (2.28)$$

as

$$\mathcal{H}_{\text{AE}}^{(i)} = \frac{\lambda_a^2}{8S_a S_b} \sum \frac{\langle \eta | l_i | \varphi \rangle}{\Delta_{\eta\varphi}} \frac{t_{\varphi\rho} t_{\rho\zeta} t_{\zeta\kappa} t_{\kappa\xi}}{\Delta_{ac}^2 \Delta_{ab}} \frac{\langle \xi | l_j | \eta \rangle}{\Delta_{\eta\varphi}} (S_{a,i} S_{b,j} + S_{a,j} S_{b,i}). \quad (2.29)$$

Introducing the exchange parameter  $D$  of the AE this expression can be written in the form

$$\mathcal{H}_{\text{AE}} = \mathbf{S}_a \cdot D \cdot \mathbf{S}_b. \quad (2.30)$$

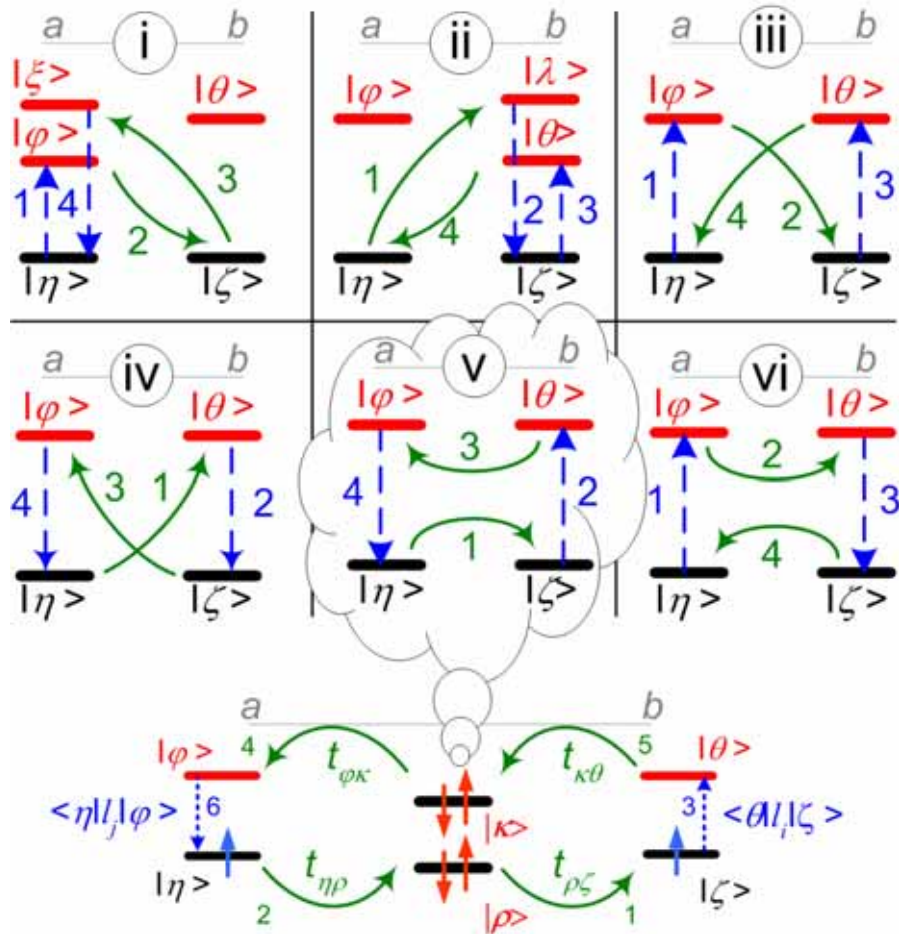


Figure 2.12.: Possible paths for the symmetric anisotropic exchange between two sites  $a$  (with ground state  $|\eta\rangle$ , excited states  $|\varphi\rangle$ ,  $|\xi\rangle$ ) and  $b$  ( $|\zeta\rangle$  and  $|\theta\rangle$ ,  $|\lambda\rangle$ , respectively). Solid arrows correspond to the effective hopping integrals, dashed arrows indicate the matrix elements of the spin-orbit coupling. The process of type (v) is represented in more detail at the bottom, where all hopping integrals  $t_{\alpha\alpha'}$  and matrix elements of SO coupling  $\langle \alpha | l_i | \alpha' \rangle$  are explicitly indicated.

Being a tensor of second rank,  $D$  does not allow for a simple graphical illustration.

This process was considered first by Bleaney and Bowers in 1952 [Bleaney'52] in case of one electron placed on each site. The schematic graphical representation of this process is given in Fig. 2.12(i). This picture represents the conventional symmetric anisotropic exchange (AE) process [Bleaney'52, Yosida'96]: electron at site  $a$  is excited via SO coupling from the ground state  $\eta$  into the state  $\varphi$ , is transferred to the ground state  $\zeta$  at site  $b$  and then retraces its steps returning to the initial state. It is obvious that the SO coupling can take place on the ion  $b$  as well. That case is represented in Fig. 2.12(ii), the respective Hamiltonian can be obtained from (2.29) by substituting  $\{a, \eta, \varphi, \xi\} \rightarrow \{b, \zeta, \theta, \lambda\}$ .

All other processes shown in Fig. 2.12 were pointed out by Eremin *et al.* [Eremin'05]. All such combinations of the interaction operators lead to the effective symmetric anisotropic exchange as well. The general expression for the exchange constant of AE between the ions  $a$  and  $b$  then reads

$$\begin{aligned}
 D_{ij}(\eta \rightarrow \zeta) = & \frac{1}{2\Delta_{ab}\Delta_{ac}^2} \left( \frac{\langle \eta | \lambda_a l_i | \varphi \rangle}{\Delta_{\eta\varphi}} t_{\varphi\rho} t_{\rho\zeta} t_{\zeta\kappa} t_{\kappa\xi} \frac{\langle \xi | \lambda_a l_j | \eta \rangle}{\Delta_{\eta\varphi}} + \right. \\
 & + t_{\varphi\rho} t_{\rho\lambda} \frac{\langle \lambda | \lambda_b l_i | \zeta \rangle}{\Delta_{\zeta\lambda}} \frac{\langle \zeta | \lambda_b l_j | \theta \rangle}{\Delta_{\zeta\theta}} t_{\theta\kappa} t_{\kappa\eta} + \frac{\langle \eta | \lambda_a l_i | \varphi \rangle}{\Delta_{\eta\varphi}} t_{\varphi\rho} t_{\rho\zeta} \frac{\langle \zeta | \lambda_b l_j | \theta \rangle}{\Delta_{\zeta\theta}} t_{\theta\kappa} t_{\kappa\eta} + \\
 & + t_{\eta\rho} t_{\rho\theta} \frac{\langle \theta | \lambda_b l_i | \zeta \rangle}{\Delta_{\zeta\theta}} t_{\zeta\kappa} t_{\kappa\varphi} \frac{\langle \varphi | \lambda_a l_j | \eta \rangle}{\Delta_{\eta\varphi}} + t_{\eta\rho} t_{\rho\zeta} \frac{\langle \zeta | \lambda_b l_i | \theta \rangle}{\Delta_{\zeta\theta}} t_{\theta\kappa} t_{\kappa\varphi} \frac{\langle \varphi | \lambda_a l_j | \eta \rangle}{\Delta_{\eta\varphi}} + \\
 & \left. + \frac{\langle \eta | \lambda_a l_i | \varphi \rangle}{\Delta_{\eta\varphi}} t_{\varphi\rho} t_{\rho\theta} \frac{\langle \theta | \lambda_b l_j | \zeta \rangle}{\Delta_{\zeta\theta}} t_{\zeta\kappa} t_{\kappa\eta} \right). \quad (2.31)
 \end{aligned}$$

Here  $S_a = S_b = 1/2$  and the sum over all possible excited states is implied. The exchange constant  $D_{ij}(\zeta \rightarrow \eta)$  for the reverse processes  $b \rightarrow a$  has the same magnitude in case of equal ions  $a$  and  $b$ .

The Moriya relation [Moriya'60] for  $D \sim (\Delta g/g)^2 J$  implies that the transfer integrals in the ground and excited states are of the same order of magnitude, i.e.  $D \propto t_{\eta\zeta}^2$ . Here, we would like to emphasize that the actual transfer integrals which enter into expression (2.31) are given by

$$D^{(i-iv)} \propto t_{\varphi\zeta}^2, \quad D^{(v,vi)} \propto t_{\zeta\eta} t_{\theta\varphi}. \quad (2.32)$$

These terms can deviate considerable from  $t_{\eta\zeta}$ . For example, in case of two bridging ions (no  $90^\circ$ -exchange) shown in Fig. 2.7(ii) the transfer integral in the excited state  $t_{\varphi\zeta} = t_{xy, x^2-y^2}$  exceeds the transfer integral in the ground state  $t_{\eta\zeta} = t_{x^2-y^2, x^2-y^2}$  by orders of magnitude. Moreover, the exchange in the excited state is strongly ferromagnetic clearly showing that the approximate relation  $D \sim (\Delta g/g)^2 J$  neither gives the correct order of magnitude nor the right sign of the interaction.

The generalization of the classical AE schema is of particular importance in the case of spin-chain systems. This is related to the fact that in linear chain systems the overlap between the ground and excited states is negligible  $t_{\varphi\zeta} \approx 0$ . Therefore, the 'ring-exchange'

processes [Fig. 2.12(v,vi)] containing the electron transfer between the states with the same symmetry play a major role.

The foregoing discussion shows that estimations of exchange parameters, especially in low-dimensional systems, demand special care. For a reliable estimation microscopic considerations of involved orbital states and exchange paths are necessary. In the following such an analysis will be presented for several low-dimensional systems, which evidence that AE constitutes one of the main sources of spin relaxation.



## 3. Physics of Low-Dimensional Systems

The field of low-dimensional magnetism can be traced back some 80 years ago. In 1925, Ernst Ising [Ising'25] tried to provide a microscopic justification for Weiss' molecular field theory in one-dimensional (1D) case; in 1931, Hans-Albrecht Bethe [Bethe'31] suggested a method to calculate the exact quantum mechanical ground state of the antiferromagnetic Heisenberg chain [Heisenberg'28]. Both papers were actually not to the complete satisfaction of their authors: The 1D Ising model failed to show any spontaneous order and Bethe did not succeed to extend the method to cover three-dimensional (3D) lattices. In spite of this not very promising beginning, the field of low-dimensional magnetism developed into one of the most active areas of today's solid state physics. Theorists are attracted by the possibility to find exact solutions using the advantage of lower dimension [Mermin'66, Baxter'71], experimentalist are excited by exotic properties of low-dimensional systems.

A low-dimensional system is one where the motion of microscopic degrees-of-freedom, such as electrons, phonons, or photons, is restricted from exploring the full three dimensions of our world. Physics in low-dimensional systems is often different than in three dimensions and the interest in these systems is constantly quickened by the discovery of their new unusual properties. In the mid eighties it was the high-temperature superconductivity which turned out to be intimately connected to the strong magnetic fluctuations which are possible in low-dimensional materials. Further progress of material science triggered interest in spin ladders, objects staying "in between" one and two dimensions [Dagotto'96]. At present many of these phenomena remain unexplained and it seems certain to say that low-dimensional magnetism will be an active area of research good for surprises in many years to come.

In this chapter we will discuss the general features of quantum chains and ladders. The spin-Peierls transition as well as magnetic and thermal properties of spin chains will be described in more detail because they are necessary for the analysis of the systems investigated in the present work.

### 3.1. Spin Chains

A one-dimensional line of spins is known as a *spin chain*. Spin chains can be approximately realized in crystals, if the crystal structure is such as to keep the spins from the different chains reasonably far apart. The single ion anisotropy due to the crystal field may constrain the spins to lie parallel or antiparallel to a particular direction  $z$  (Ising

spins), or in a fixed plane  $xy$  (XY spins), or leave them free to point in any direction (Heisenberg spins). The corresponding Hamiltonians read

$$\mathcal{H}_{\text{Ising}} = \sum_{i,j} J_{ij} S_{i,z} S_{j,z}, \quad (3.1)$$

$$\mathcal{H}_{\text{XY}} = \sum_{i,j} J_{ij} [S_{i,x} S_{j,x} + S_{i,y} S_{j,y}], \quad (3.2)$$

$$\mathcal{H}_{\text{Heisenberg}} = \sum_{i,j} J_{ij} \mathbf{S}_i \cdot \mathbf{S}_j. \quad (3.3)$$

Very often these systems show three-dimensional long range order at low temperatures, because there are always some small interchain interactions which couple the chains together. For example,  $\text{KCuF}_3$  shows 3D long range magnetic order below 39 K, nevertheless, there is a wide region of temperatures above the crossover to a 3D region, where the magnetic behavior is that of a 1D system.

The properties of spin chains depend strongly on the value of spin. For example, integer-spin Heisenberg AFM systems have a gap in the excitation spectrum [Haldane'83], the magnitude of which is inversely proportional to the spin value, whereas uniform half-spin chains are gapless. In the present work we will deal only with  $S = \frac{1}{2}$  systems, which will be considered in the following in more detail. What makes these chains interesting is not their ordering (according to the Mermin-Wagner theorem [Mermin'66], there cannot be any antiferromagnetic (AFM) long range order at finite temperature), but their excitations. In 3D Heisenberg magnets the excitations are  $S = 1$  magnons, which are bosons. In Heisenberg spin chain, the excitations are known as *spinons*. They have  $S = \frac{1}{2}$  and are fermions. The dispersion relation is given by

$$\hbar\omega = \pi |J \sin(ka)|, \quad (3.4)$$

where  $a$  and  $k$  are the lattice constant and wave vector, both measured along the chain direction, respectively. Equation (3.4) corresponds to the thin blue line in Fig. 3.1(ii). One can see that a  $S = \frac{1}{2}$  antiferromagnetic chain is generally gapless. But it is susceptible to an analogous kind of instability that occurs in one-dimensional metals which can open up a gap. This occurs at the *spin-Peierls transition* [Pytte'74].

### 3.1.1. Spin-Peierls Transition

The driving force of this intrinsic lattice instability is the magnetoelastic coupling between the one-dimensional electronic structure and the three-dimensional lattice vibrations (phonons). This coupling arises because the exchange energy of the chains is a function of the separation between the adjacent lattice sites and a distortion of the lattice influences the magnetic energy of the system.

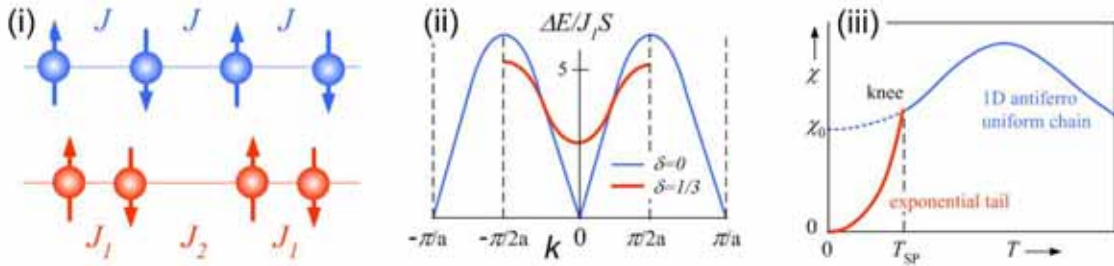


Figure 3.1.: **(i)**: Schematic representation of an uniform (above) and an alternating  $J_{1,2} = J(1 \pm \delta)$  (below) chain. **(ii)**: Dispersion curves for a  $S = 1/2$  Heisenberg antiferromagnetic chain with  $\delta = 0$  (the blue thin line) and  $\delta = 1/3$  (the red bold line) [Bonner'82]. Note that in the later case only excitations with gap occur. **(iii)**: Characteristic zero-field susceptibility for a system showing a spin-Peierls transition. Above the transition the system behaves as an assembly of uniform Heisenberg antiferromagnetic chains (for details see Fig. 3.2(i)). Below the transition,  $T_{SP}$ ,  $\chi$  drops sharply, going exponentially to zero, whereas the uniform curve, now shown dashed, continues on to a nonzero value,  $\chi_0$ .

The name spin-Peierls reflects the similarity with the Peierls distortion in 1D metals [Peierls'55]: an instability associated with the fact that the periodic modulation of the electron density charge with wave vector  $q = 2k_F$  opens a gap at the Fermi surface and leads to a lowering of the total energy. Then the gained electronic energy outweighs the elastic energy cost of the dimerization which can occur spontaneously.

Above the transition temperature  $T_{SP}$ , there is a uniform antiferromagnetic nearest-neighbour exchange in each chain. Below  $T_{SP}$  there is an elastic distortion resulting in a dimerization, and, hence, two unequal alternating exchange constants  $J_{1,2} = J(1 \pm \delta)$  (see Fig. 3.1(i)). The dimerization increases progressively as the temperature is lowered and reaches a maximum at zero temperature. The alternating chain possesses an energy gap  $\Delta$  between the singlet ground state  $S = 0$  and the lowest lying band of triplet excited states. Thus the magnetic susceptibility  $\chi(T)$  shows a knee at  $T_{SP}$ , with a rather abrupt fall of  $\chi$  below  $T_{SP}$ , corresponding to the opening of the gap (Fig. 3.1(iii)). While the normal Peierls distortion occurs at  $T_P \sim E_F/k_B \cdot \exp(-1/\lambda)$ , where  $\lambda$  is the electron-phonon coupling constant, the spin-Peierls transition will occur at  $T_{SP} \sim |J|/k_B \cdot \exp(-1/\lambda)$ , where  $J$  is the exchange interaction between the adjacent spins. Since  $J/k_B \sim 10^2$  K and the Fermi energy  $E_F/k_B \sim 10^3$  K,  $T_{SP}$  is always small in comparison with  $T_P$ . In the framework of the mean field theory [Grüner'94, Bray'75]

$$\chi(T) \propto e^{-\Delta(T)/T}, \quad \frac{|\Delta(T)|}{|\Delta(0)|} = 1.74 \left(1 - \frac{T}{T_{SP}}\right)^{1/2}, \quad \frac{2\Delta(0)}{k_B T_{SP}} = 3.53, \quad (3.5)$$



$T_{\text{SP}} = 3.73 |J|/k_{\text{B}} \cdot \exp(-1/\lambda)$  and  $\delta = 0.61 \cdot \Delta(T)/J$ . However, it should be stressed at this point that serious deviations from the mean field treatment can be expected because of the low-dimensional character of the materials of interest and the relatively short coherence lengths which result from the high transition temperatures. The quantum-mechanical treatment of the spin subsystem [Cross'79] results in quite different predictions for the transition temperature and the gap value

$$T_{\text{SP}} = 0.8 \frac{|J|}{k_{\text{B}}} \lambda, \quad \Delta(0) \sim \delta^{2/3} J^{1/3}. \quad (3.6)$$

Nevertheless, the thermodynamic properties such as the specific heat and susceptibility were shown to be roughly the same as the mean field values. For small  $H < H_c \approx 1.45 T_{\text{SP}}(0)/g\mu_{\text{B}}$  the transition temperature was predicted to scale with the magnetic field squared  $T_{\text{SP}}(H)/T_{\text{SP}}(0) \approx 1 - 0.11 (g\mu_{\text{B}}H/T_{\text{SP}}(0))^2$  [Bulaevskii'78].

Very often the antiferromagnetic chains become three-dimensionally ordered at low temperature due to the interchain coupling. Only in a small number of materials the spin-phonon coupling is able to dominate the interchain spin-spin coupling and allows the formation of a spin-Peierls ground state. Examples of such materials include a number of organic systems such as MEM(TCNQ)<sub>2</sub> ( $T_{\text{SP}} = 18$  K) [vanBodegom'81] and TTF-CuS<sub>4</sub>C<sub>4</sub>(CF<sub>3</sub>)<sub>4</sub> ( $T_{\text{SP}} = 12$  K) [Bray'75] and an inorganic system CuGeO<sub>3</sub> ( $T_{\text{SP}} = 14$  K) [Hase'93]. A candidate for the second inorganic system is TiOCl showing the spin-Peierls-like transition to a non-magnetic state below  $T_{\text{c1}} = 67$  K. This system will be considered in Chapter 6 in more detail.

### 3.1.2. Magnetic and Thermal Properties

Let us return to the case of uniform  $S = \frac{1}{2}$  chains and consider basic theoretical results concerning their magnetic and thermal properties. One of the most important works is represented by the numerical calculation of chains up to  $N = 11$  atoms made by Jill Bonner and Michael Fisher [Bonner'64]. The behavior of infinite chains was estimated by extrapolation which was shown to be accurate at  $T \geq \frac{1}{4}J/k_{\text{B}}$ . The calculated temperature dependence of the spin susceptibility of an uniform AFM Heisenberg chain is depicted in Fig. 3.2(i) by the dashed line. The solid line in the same Figure represents the prediction of a low-temperature field-theoretical treatment [Eggert'94]. Both curves coincide at high temperatures and can be fitted by an expression [Estes'78]

$$\chi(x) = \frac{Ng^2\mu_{\text{B}}^2}{k_{\text{B}}T} \frac{0.25 + 0.074975x + 0.075235x^2}{1 + 0.9931x + 0.172135x^2 + 0.757825x^3} \quad (3.7)$$

with  $x \equiv |J|/k_{\text{B}}T$ . This curve coincides perfectly with the Bonner-Fisher curve for all  $T > 0.04J/k_{\text{B}}$  (see the thin blue line in Fig. 3.2(i)). The limiting susceptibility for infinite chains displays a rounded maximum of height

$$\chi_{\text{max}} = 0.147 \frac{Ng^2\mu_{\text{B}}^2}{|J|} \quad \text{at} \quad T_{\text{max}} = 0.641 \frac{|J|}{k_{\text{B}}}, \quad (3.8)$$

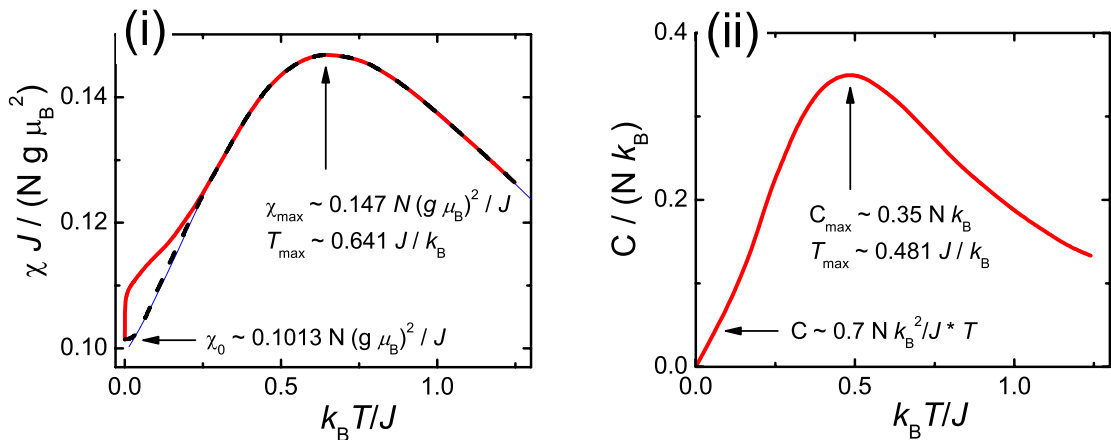


Figure 3.2.: **(i)**: The dashed black curve: estimated temperature dependence of susceptibility for an infinite  $N = \infty$  AFM Heisenberg chain based on the numerical results for  $N \leq 11$  by Bonner and Fisher [Bonner'64], the solid thick red line:  $\chi(T)$  obtained using the Bethe ansatz and field-theory methods [Eggert'94]. The blue thin line corresponds to the fit using Eq. (3.7). **(ii)**: Estimated variation with temperature of specific heat for infinite antiferromagnetic Heisenberg chains taken from [Bonner'64].

decreasing at high temperatures as  $\chi \propto 1/T$ . The situation at low temperatures as zero is approached is more complicated. Bonner and Fisher predict the low-temperature behavior with higher uncertainty about 5% in the range  $T < \frac{1}{4}|J|/k_B$ . The highly accurate results, obtained using the Bethe ansatz [Griffiths'63] and field-theory methods [Eggert'94], showed the presence of an inflection point at  $T \approx 0.087|J|/k_B$  in the temperature dependence of the susceptibility with the slope of  $\chi(T)$  approaching  $\infty$  as  $T \rightarrow 0$  (the solid line in Fig. 3.2(i)). Nevertheless, the value at  $T = 0$

$$\chi_0 = \frac{1}{\pi^2} \frac{N g^2 \mu_B^2}{|J|} \approx 0.101322 \frac{N g^2 \mu_B^2}{|J|} \quad (3.9)$$

was shown to coincide with the Bonner-Fisher prediction.

The profound work by Bonner and Fisher [Bonner'64] covers the variation of the specific heat  $C$  with temperature as well. Fig. 3.2(ii) displays the expected behavior of  $C$  for an antiferromagnetic  $S = \frac{1}{2}$  Heisenberg spin chain. The maximum

$$C_{\max} = 0.35 N k_B \quad \text{at} \quad T_{\max} = 0.481 \frac{|J|}{k_B} \quad (3.10)$$

lies again in the well defined region  $T \geq \frac{1}{4}|J|/k_B$ , and the calculated behavior at low

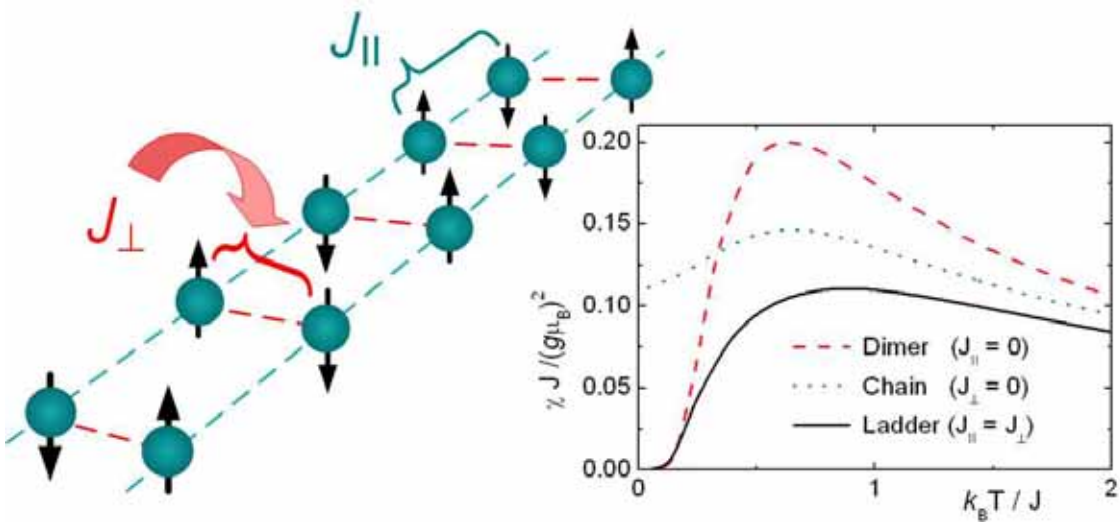


Figure 3.3.: Schematic sketch of a two-leg spin ladder. The inset shows the temperature dependencies of the susceptibility in a spin chain, a dimer and a ladder system with  $J_{\parallel} = J_{\perp}$  [Johnston'00, Barnes'94].

temperatures reads

$$C(T < \frac{|J|}{10k_B}) = 0.7 N k_B \frac{k_B T}{|J|}. \quad (3.11)$$

## 3.2. Spin Ladders

The spin ladder systems serve as a bridge between one- and two-dimensional spin systems. Consider two parallel spin chains with bonds between them such that the interchain coupling  $J_{\perp}$  is of comparable strength to the intrachain coupling  $J_{\parallel}$ . Such a system is known as a two-leg *spin ladder* (see Fig. 3.3). It has a finite gap in the excitation spectrum, which is easy to see in the 'strong-rung' limit in which  $J_{\perp} \gg J_{\parallel}$ . In this case the ground state consists simply of spin singlets along each rung of the ladder. To create an excitation, you must promote a rung-singlet into a rung-triplet, hence the energy gap  $\Delta \sim J_{\perp}$ . Exact calculations give, e.g. in the case  $J_{\perp} = J_{\parallel}$ ,  $\Delta \approx J_{\perp}/2$  [White'94, Troyer'94]. It is believed that a gap appears as soon as  $J_{\perp}$  is non-zero, no matter how small it is. In particular, the inset of Fig. 3.3 shows that the susceptibility of a ladder with  $J_{\perp} = J_{\parallel}$  coincides at low temperatures  $T \ll J/k_B$  with the dimer one [Bleaney'52]

$$\chi_{\text{Dimer}}(T) = \frac{N g^2 \mu_B^2}{k_B T} \cdot \frac{1}{3 + \exp(J/k_B T)}. \quad (3.12)$$

There is an interesting feature associated with ladder systems, when more than two

legs are coupled. Namely, the ladders with an even number of legs have a spin gap, while odd-leg ladders are gapless, which is a quantum manifestation of the fact that an even number of half-integer spins can be arranged into a spin singlet. The model systems for the  $n$ -leg ladders are  $\text{Sr}_{n-1}\text{Cu}_{n+1}\text{O}_{2n}$  compounds [Dagotto'96]. With increasing number of legs we arrive at two dimensions, but the magnitude of the spin gap goes to zero. This is an indication why only few two-dimensional systems exhibiting the spin gap are known.

The interest in spin ladders derives mainly from the fact they have a gap in their excitation spectrum, they can become superconducting (e.g.  $\text{Sr}_{14-x}\text{Ca}_x\text{Cu}_{24}\text{O}_{21}$ ), and yet are simple well defined systems which theorists can try to model. Hence, these systems may shed light on the problem of high- $T_c$  superconductivity. The ladder system considered in this work,  $\text{NaV}_2\text{O}_5$ , undergoes, however, another type of phase transition, charge ordering, which will be considered in Sec. 5.1.2 in more detail.



## 4. Electron Spin Resonance Spectroscopy

E. K. Zavoiski first observed electron spin resonance (ESR) in 1944 [Zavoiski'45]. His proposal was to measure paramagnetic relaxation, which was an important subject in magnetism at that time, using a resonance phenomenon in a frequency region of MHz. Later, however, the ESR technique has become mainly used for the spectroscopy of magnetic ions in the microwave region due to the progress of microwave techniques and theoretical developments of magnetic resonance. Its application now is not only to physics of magnetism but also to a variety of scientific fields like chemistry, biology, geology and anthropology [Kawamori'02].

Often, the terms Electron Paramagnetic Resonance (EPR) and (Anti)FerroMagnetic Resonance (A)FMR are used depending on the magnetic state of the sample. EPR experiments that were intensively performed during the 1950's contributed to establish spin-Hamiltonians and relaxation mechanisms of diluted transition-metal ions [Abragam'70, Pake'73] that are still important concepts in magnetism. The relaxation mechanisms were discussed phenomenologically by Bloch [Bloch'46], microscopically by Van Vleck [vanVleck'48] and Anderson [Anderson'53] and summarized in a general theory by Kubo and Tomita [Kubo'54]. FMR was investigated mainly for interests in the spin wave relaxation mechanism and AFMR contributed to study of anisotropic energy of magnetic materials [Rado'63]. In the last decades the interest was turned to the investigation of magnetically concentrated systems in the paramagnetic regime. A very useful review on the development of ESR experiments and theory before the year 1990 is provided by Bencini and Gatteschi [Bencini'90].

In the following only a short introduction to the magnetic resonance of exchange coupled spins will be given, necessary to understand the results presented in this work. A particular emphasis will be put on the effect of the anisotropic exchange interaction on the ESR absorption in low-dimensional systems. Starting from the Zeeman interaction of a single spin we will describe the quantities measured by ESR and turn finally to the theoretical approaches which are necessary for a description of the ESR linewidth.

### 4.1. Resonance Effect

#### 4.1.1. Zeeman Effect

An electron spin  $\mathbf{S}$  interacts via its magnetic moment  $\boldsymbol{\mu} = -g\mu_B\mathbf{S}$  with an external static magnetic field  $\mathbf{H}$ , resulting in an equidistant splitting of the  $2S+1$  spin eigenstates, which

#### 4. Electron Spin Resonance Spectroscopy

---

is known as Zeeman effect. The corresponding Hamiltonian is given by

$$\mathcal{H}_Z = -\boldsymbol{\mu} \cdot \mathbf{H} = g\mu_B \mathbf{S} \cdot \mathbf{H} = g\mu_B H S_z \quad (4.1)$$

where  $\mu_B = (e\hbar)/(2mc)$  denotes the Bohr magneton with elementary charge  $e$ , electron mass  $m$ , Planck's constant  $\hbar$ , and light velocity  $c$ . Here CGS units are used to be compatible with the majority of ESR literature. For a free electron the  $g$  value is  $g = 2.0023$ . Choosing the direction of the static field along the  $z$  axis, the eigen energies read

$$E_{m_S} = g\mu_B H m_S, \quad -S \leq m_S \leq S. \quad (4.2)$$

A magnetic microwave field  $\mathbf{h} \cos(\omega t)$  of frequency  $\nu = \omega/(2\pi)$  and amplitude  $h \ll H$  applied transversal to the static field, e.g. along the  $x$  direction, results in a perturbation

$$\mathcal{H}_{\text{MW}} = g\mu_B h \cos(\omega t) \cdot S_x = g\mu_B h \cos(\omega t) \cdot \frac{1}{2}(S_+ + S_-). \quad (4.3)$$

The spin operators  $S_+ = S_x + iS_y$  and  $S_- = S_x - iS_y$  increase respectively decrease the magnetic quantum number  $m_S$  by 1 and, therefore, induce dipolar transitions  $\Delta m_S = \pm 1$  between neighboring Zeeman levels, if the microwave energy equals the corresponding energy difference (see Fig. 4.1(i)). Resonance absorption takes place at the Larmor frequency

$$\omega_L = g\mu_B H / \hbar = \gamma H. \quad (4.4)$$

Another association of the Larmor frequency is obtained from the equation of motion of the spin operator in the Heisenberg picture:

$$\frac{d\mathbf{S}}{dt} = \frac{i}{\hbar} [\mathcal{H}_Z, \mathbf{S}] = -\gamma [\mathbf{S} \times \mathbf{H}]. \quad (4.5)$$

The spin feels a torque from the magnetic field and, hence, precesses with the Larmor frequency around the field direction like a mechanical gyroscope in the gravitation field.

Experimentally, in continuous-wave ESR the microwave frequency  $\omega$  is kept constant and the external magnetic field  $H$  is changed continuously (for details see Sec. 4.3). By detecting the power absorbed by the sample as a function of the magnetic field, the resonance spectra (Fig. 4.1(ii)) are recorded when sweeping through the resonance condition  $H_{\text{res}} = \frac{\hbar}{g\mu_B} \omega$ . One observes not a  $\delta$ -peak but an absorption line with a finite width. That arises due to interactions of spins with their surroundings. The experimentally observed ESR line shapes in a large variety of materials can often be fitted by a Lorentzian line shape. A simple phenomenological derivation of such a line shape can be given using the modified Bloch equations.

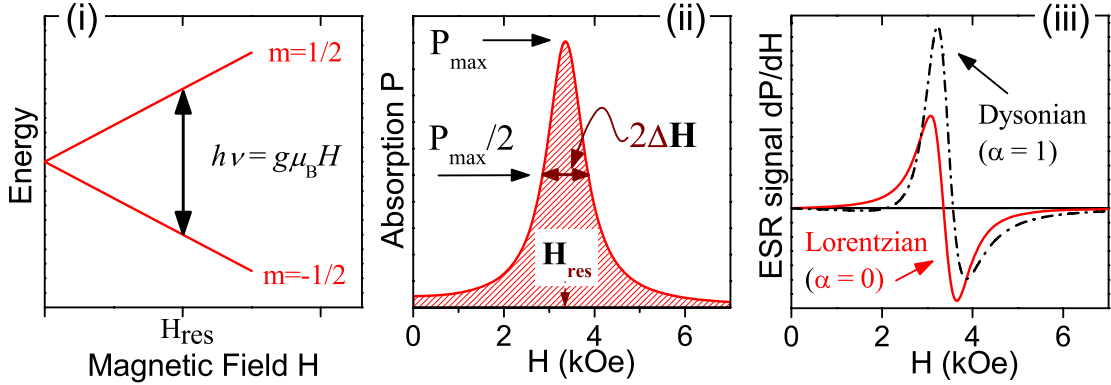


Figure 4.1.: (i): Zeeman splitting and resonance condition of a spin  $S = 1/2$  in a magnetic field  $H$ . (ii): Lorentzian lineshape generated using Eq. (4.14) with  $\alpha = 0$ ,  $H_{\text{res}} = 3360$  Oe and  $\Delta H = 500$  Oe. (iii): Comparison of the field derivatives of Lorentzian ( $\alpha = 0$ ) and Dysonian ( $\alpha = 1$ ) lineshapes generated using Eq. (4.15) with the same parameters  $H_{\text{res}} = 3360$  Oe and  $\Delta H = 500$  Oe.

#### 4.1.2. Bloch Equations

Let's consider a system of  $N$  spins with magnetic moments  $\mu_i$  interacting with each other and the crystal lattice. The dynamics of the magnetization  $\mathbf{M} = \sum_i \mu_i / N$  may then be approximated by a set of modified Bloch equations, where the equilibrium state of the magnetization is always parallel to the momentary magnetic field  $\mathbf{H}_{\text{ges}}$  [Krug'97, Barnes'81]:

$$\frac{d}{dt} M_z = -\gamma [\mathbf{M} \times \mathbf{H}_{\text{ges}}]_z - \frac{(\mathbf{M} - \chi_0 \mathbf{H}_{\text{ges}})_z}{T_1}, \quad (4.6)$$

$$\frac{d}{dt} M_{x,y} = -\gamma [\mathbf{M} \times \mathbf{H}_{\text{ges}}]_{x,y} - \frac{(\mathbf{M} - \chi_0 \mathbf{H}_{\text{ges}})_{x,y}}{T_2}, \quad (4.7)$$

with  $\mathbf{H}_{\text{ges}} = \mathbf{H} + \mathbf{h}$ . In comparison with the equation of motion for a single spin given by Eq. (4.5), a second term appears in the above Bloch equations that accounts for the relaxation phenomena occurring due to the interaction of the spins with their surroundings in a crystal. In momentary equilibrium the magnetization is given by  $\chi_0 \mathbf{H}_{\text{ges}}$  and, since we assume  $h \ll H$ , the magnetization  $\mathbf{M}_0 \simeq \chi_0 \mathbf{H}$  is parallel to the constant magnetic field  $\mathbf{H}$ . The changes in the occupation of the Zeeman levels induced by the microwave field  $\mathbf{h}$  drive the system out of equilibrium and, hence, relaxation processes occur to restore this state. One distinguishes between the longitudinal or spin-lattice relaxation time  $T_1$ , where the spin system relaxes by transferring energy to the lattice, and the transversal or spin-spin relaxation time  $T_2$ , which describes all relaxation



phenomena that tend to destroy the coherence of the spin components rotating in the  $(xy)$ -plane. Note, however, that this strict distinction between  $T_1$  and  $T_2$  is not possible, usually. By using  $\mathbf{h} = \hbar e^{i\omega t}$  and  $M_+ = M_x + iM_y$  the linearized equation of motion for the transversal component is given by

$$\frac{d}{dt}M_+ = \left(i\omega_L - \frac{1}{T_2}\right) \cdot (M_+ - \chi_0 \hbar e^{i\omega t}). \quad (4.8)$$

A solution can be obtained by the ansatz  $M_+ = \chi(\omega)\hbar e^{i\omega t}$  and the corresponding complex susceptibility  $\chi(\omega) = \chi' - i\chi''$  reads:

$$\chi(\omega) = \chi_0 \left(1 + \frac{\omega(\omega_L - \omega)}{(\omega_L - \omega)^2 + (1/T_2)^2} - i \frac{\omega/T_2}{(\omega_L - \omega)^2 + (1/T_2)^2}\right) \quad (4.9)$$

Experimentally, the static magnetic field  $H = \omega_L/\gamma$  is varied at a constant microwave frequency and one derives

$$P_{\text{abs}}(H) = \frac{1}{2}\omega h^2 V \chi''_{xx}(\omega) \propto \frac{\Delta H}{(H - H_{\text{res}})^2 + \Delta H^2}, \quad (4.10)$$

a Lorentzian lineshape at the resonance field  $H_{\text{res}} = \omega/\gamma$  with half-width-at-half-maximum linewidth  $\Delta H = 1/\gamma T_2$ , which is related to the peak-to-peak linewidth by  $\Delta H_{\text{pp}} = \frac{2}{\sqrt{3}}\Delta H$ .

## 4.2. Measured Quantities

Eq. (4.10) contains all basic quantities measured by ESR: the position of the resonance line  $H_{\text{res}}$ , its width  $\Delta H$  and the absorbed power  $P_{\text{abs}}(H)$ . In this section we will consider each of them in detail and will discuss which information they allow to obtain.

### 4.2.1. Resonance Field

Recalling the resonance condition  $\hbar\omega = g\mu_B H$  (Eq. 4.4) with the microwave frequency  $\omega$  and magnetic field  $H$ , one has to take into account that local magnetic fields  $H_{\text{loc}}$  will be present at the spin's site in addition to the external magnetic field  $H_{\text{ext}}$ . Hence, the fit parameter  $H_{\text{res}} = H_{\text{ext}} + H_{\text{loc}}$  or the resulting effective  $g$ -factor  $g_{\text{eff}}$  and its shift  $\Delta g$  with regard to the  $g$ -factor of the free electron  $g_e = 2.0023$

$$g_{\text{eff}} = \frac{\hbar\omega}{\mu_B H_{\text{res}}}, \quad \Delta g = g_{\text{eff}} - g_e \quad (4.11)$$

provide a measure for local fields at the spin's site. For strongly exchange coupled systems, where these local fields are assumed to originate from perturbations  $\mathcal{H}_{\text{int}}$  that are small compared to the Zeeman  $\mathcal{H}_Z$  and exchange  $\mathcal{H}_{\text{iso}}$  energies (see Sec. 4.4.1), the

standard formula to calculate the shift of the resonance in linear response theory is given by the first moment of the absorption which has been derived by Nagata and Tazuke [Nagata'72]

$$\Delta\omega = \frac{1}{2\hbar^2} \frac{\langle [S^-, [S^+, \mathcal{H}_{\text{int}}]] \rangle}{\langle S^z \rangle}, \quad (4.12)$$

where the expectation value  $\langle \dots \rangle$  is defined with respect to the full Hamiltonian  $\mathcal{H}$ .

A very useful tool for describing the  $\mathbf{g}$  tensor is represented by a program package *CAMMAG* based on the angular overlap model (AOM). Using the local symmetry data and several ligand-field parameters the program calculates the eigenenergies of the spin on different crystal-field levels together with the principal values of the  $\mathbf{g}$  tensor. Moreover, the comparison with the experimentally determined values allows to estimate the reduction of the spin-orbit coupling due to covalency of the metal-ligand bonds. A more detailed description of AOM can be found in appendix B.

#### 4.2.2. Linewidth and Lineshape

The line width  $\Delta H$  is a measure of spin relaxation processes. To evaluate this quantity rigorously, a quantum-mechanical treatment is necessary. The corresponding theories have been developed by Kubo and Tomita [Kubo'54] and Mori and Kawasaki [Mori'62] about 50 years ago. The discussion of these results and of possible spin-relaxation mechanisms in concentrated spin systems will be given in section 4.4. Here, we will consider a phenomenological approach that allow to describe the non-Lorentzian lineshape (4.10) often observed in a large variety of materials:

In the case of semiconductors and metals the skin effect drives electric and magnetic microwave components out of phase and leads to an admixture of dispersion (given by  $\chi'$ ) into the absorption spectra as derived by Dyson [Dyson'55]. With  $\alpha$  denoting the dispersion-to-absorption ratio the Dysonian lineshape is given by:

$$P_{\text{abs}}(H) \propto \frac{\Delta H + \alpha(H - H_{\text{res}})}{(H - H_{\text{res}})^2 + \Delta H^2}. \quad (4.13)$$

For samples which are small compared to the skin depth one expects a symmetric absorption spectrum ( $\alpha = 0$ ), whereas absorption and dispersion are of equal strength for samples larger than the skin depth yielding an asymmetric resonance line ( $\alpha = 1$ ) shown in Fig. 4.1(iii) [Barnes'81].

If the linewidth  $\Delta H$  is of the same order of magnitude as the resonance field  $H_{\text{res}}$ , both circular components of the exciting linearly polarized microwave field  $\mathbf{h}$  have to be taken into account. Therefore, the resonance at the reversed magnetic field  $-H_{\text{res}}$  has to be included into the fit formula for the ESR spectra:

$$P_{\text{abs}}(H) \propto \frac{\Delta H + \alpha(H - H_{\text{res}})}{(H - H_{\text{res}})^2 + \Delta H^2} + \frac{\Delta H - \alpha(H + H_{\text{res}})}{(H + H_{\text{res}})^2 + \Delta H^2}. \quad (4.14)$$

Usually, the field-derivative of the absorption line is observed in the experiment due to the use of lock-in technique (Fig. 4.1(iii)). Therefore, the following fit formula has been used to evaluate the ESR spectra:

$$\frac{dP}{dH} = A \cdot \left( \frac{-2x + \alpha(1 - x^2)}{(1 + x^2)^2} + \frac{-2y - \alpha(1 - y^2)}{(1 + y^2)^2} \right) + C + B \cdot H \quad (4.15)$$

with  $x = \frac{H - H_{\text{res}}}{\Delta H}$ ,  $y = \frac{H + H_{\text{res}}}{\Delta H}$ .

The linear term  $C + B \cdot H$  takes into account the effects of oscillations of the cavity due to the modulation of the external magnetic field.

Although or because this asymmetric lineshape allows to evaluate the resonance spectra of a large variety of different materials, one has to be extremely careful with the interpretation and use of the asymmetry parameter  $\alpha$  as a free fitting parameter, especially, because sometimes  $\alpha > 1$  or even negative values occur:

- (i) The resonance field  $H_{\text{res}}$  and  $\alpha$  strongly depend on each other as it is illustrated in Fig. 4.1(iii) for the case of a purely Lorentzian lineshape ( $\alpha = 0$ ) and a Dysonian lineshape ( $\alpha = 1$ ). Therefore, variations in the resonance field always have to be cross-checked with corresponding features in  $\alpha$  and the resistivity.
- (ii) Asymmetric Dysonian lineshapes rather than Lorentzian ones have been observed in low-dimensional compounds. An additional contribution to the asymmetry of the resonance line can arise from the fact that  $\Delta H$  is of the same order of magnitude as  $H_{\text{res}}$ , because then not only the overlap with the resonance at  $-H_{\text{res}}$  but the usually neglected nondiagonal elements of the dynamic susceptibility influence the lineshape [Benner'83]. A more rigorous treatment of this analysis of the asymmetry of ESR spectra has only recently attracted again attention from theorists [Maeda'03, Choukroun'03].
- (iii) In anisotropic polycrystalline samples the superposition of Lorentzian lines can also account for the Dysonian lineshape.

### 4.2.3. ESR Intensity

The ESR intensity  $I_{\text{ESR}}$

$$I_{\text{ESR}} = \int_0^{\infty} P_{\text{abs}}(H) dH \propto \chi_0 \quad (4.16)$$

is a measure for the static spin susceptibility  $\chi_0$  of the system. In the case of a Lorentzian lineshape given by Eq. (4.10) one obtains  $I_{\text{ESR}} = A \cdot \Delta H^2$ . If a small admixture of dispersion ( $\alpha \gtrsim 0$ ) is present in the resonance spectra, one has to correct the absorptive

part resulting in  $I_{\text{ESR}} = A \cdot \Delta H^2 \cdot \sqrt{1 + \alpha^2}$ . In the case of metallic samples where  $\alpha$  approaches 1, the skin depth has to be taken into account to estimate the necessary volume correction.

Absolute values for the spin susceptibility measured by ESR can only be obtained by comparison with the intensity of a reference compound the linewidth of which is of the same order of magnitude. Thus, the effective moments can be obtained by ESR and compared to *dc*-susceptibility measurements.

An important difference between  $I_{\text{ESR}}$  and *dc*-susceptibility  $\chi_0$  in the case of 3d transition metal ions in solids is the following. For these ions the orbital angular momentum is quenched in the ground state, which is realized by the crystal-field splitting [Yosida'96]. Nonetheless, the magnetic field polarizes the orbitals and imparts an induced paramagnetism to the ground state. This effect is no more than the second-order perturbation of the Zeeman energy  $\mathcal{H}_Z = \mu_B(\mathbf{L} + 2\mathbf{S}) \cdot \mathbf{H}$  for the orbital angular momentum. This gives a temperature independent (anisotropic) paramagnetic susceptibility, which is called the *Van Vleck orbital paramagnetism*. The Van Vleck orbital paramagnetism gives a non-negligible contribution to the *dc*-susceptibility, if the energy of the excited states is not too high and can be calculated as

$$\chi_i^{(\text{VV})} \approx 2 \left( \frac{2\mu_B}{\hbar} \right)^2 \sum_{n \neq 0} \frac{|\langle n | L_i | 0 \rangle|^2}{E_n - E_0}, \quad (4.17)$$

presuming  $E_n - E_0 \gg k_B T$  [Emin'91]. The ESR intensity  $I_{\text{ESR}}$  measures the splitting of the ground state only and, thus, does not contain the van Vleck contribution.

### 4.3. Experimental Setup

The ESR measurements were performed using a Bruker ELEXSYS 500 CW spectrometer working at X-band ( $\nu \sim 9.3$  GHz) and Q-band ( $\nu \sim 34$  GHz) frequencies. The experimental setup is shown in Fig. 4.2. As microwave generator a Dual Gunn-oscillator bridge is used. The resonator (Bruker ER4102ST) is a TE102 rectangular cavity with an eigenfrequency of 9.48 GHz. A water cooled electromagnet allows for field sweeps up to 18 kG. The microwave diode detects the power absorption  $P_{\text{abs}}$  of the samples from the magnetic microwave field  $h$  as function of the static magnetic field  $H$  applied perpendicular to microwave field (Faraday configuration). The reference power keeps the diode current in the operating regime of 200  $\mu\text{A}$ . To improve the signal-to-noise ratio, one records the field derivative of the absorption  $dP_{\text{abs}}/dH$  by means of the lock-in technique with field modulation on the frequency of 100 kHz.

For the measurements in the temperature range from 3.8 K to 300 K an Oxford Instruments ESR900 continuous flow cryostat for liquid He was used. The liquid He is supplied from a Dewar through an insulated transfer tube. It flows through a heat exchanger where the helium is evaporated and heated up to the required temperature

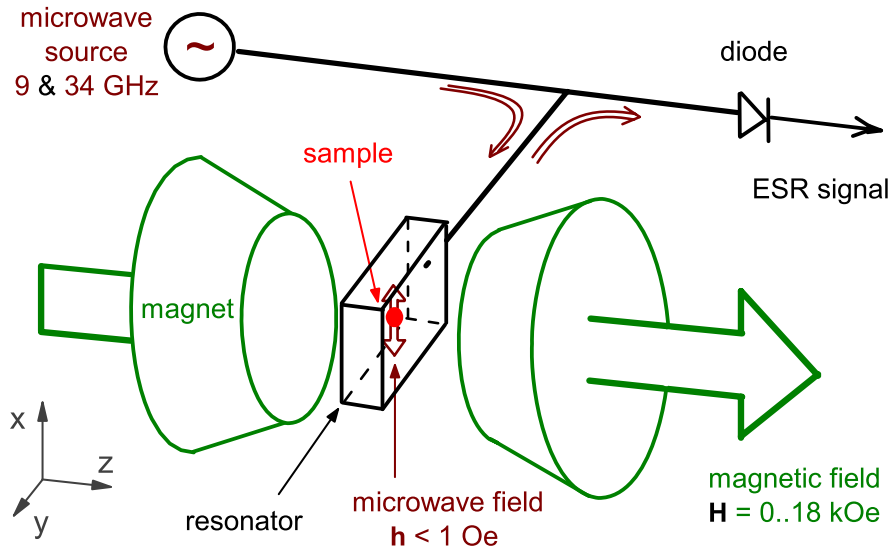


Figure 4.2.: Schematic sketch of the ESR setup: The incoming microwave (the wine lines) induces magnetic dipole transitions at the site of the sample (the red point) centered in the cavity. The reflected power of the microwave is measured on a diode as a function of the external magnetic field  $H$  (green).

and then supplied to the sample space. The heater is mounted on the heat exchanger and is used with a temperature controller ITC 501 (Oxford Instruments) to balance the cooling power of the cryogen and to control the temperature of the gas before it reaches the sample space. The temperature is measured by a thermocouple with liquid nitrogen as reference temperature.

Additionally, for the measurements in the temperature range from 110 K to 700 K a Bruker Digital ER4131VT Control System was used. The Digital temperature Control System ER4131VT makes use of liquid (110 ÷ 700 K) or gaseous (300 ÷ 600 K) nitrogen as coolant.

The spectrometer is equipped with a computer-controlled goniometer (resolution about  $0.125^\circ$ ), which allows high-precision recording of angular dependent spectra in single crystals.

At low-temperatures  $T < 300 \text{ K}$  the samples were mounted into a small tube from Suprasil glass and fixed with paraffin. At measurements above room temperature NaCl powder was used to fix the sample. Some measurements of the angle and temperature dependence were not possible inside a small glass tube due to the size of the single crystal. In this case the crystal was glued from outside on a particularly flattened glass tube using GE Varnish (General Electrics).

## 4.4. Spin Relaxation Mechanisms

The theory of ESR line broadening and exchange narrowing was initially developed by van Vleck [vanVleck'48] and treated more generally by Anderson and Weiss [Anderson'53], and by Kubo and Tomita (KT) [Kubo'54]. Here, we will restrict the discussion to the result of the KT approach, the details of this theoretical treatment can be found in [Oshikawa'02, Deisenhofer'05].

### 4.4.1. The Kubo-Tomita Formula

The spin Hamiltonian is given by

$$\mathcal{H} = \mathcal{H}_Z + \mathcal{H}_{\text{iso}} + \mathcal{H}_{\text{int}}, \quad (4.18)$$

where  $\mathcal{H}_Z = -(g/\hbar)\mu_B H S_z$  denotes the Zeeman interaction for the total spin operator  $S_z = \sum_i S_{i,z}$  and  $\mathcal{H}_{\text{iso}}$  the isotropic Heisenberg exchange  $J \sum_{(i,j)} \mathbf{S}_i \cdot \mathbf{S}_j$  between spins at sites  $i$  and  $j$ . These two terms leave the line completely sharp, and the linewidth in the system is determined only by the symmetry-breaking anisotropic interactions represented by  $\mathcal{H}_{\text{int}}$ . Assuming that these interactions can be treated as small perturbations with regard to the isotropic exchange, the final KT formula for the linewidth can be written as follows:

$$\Delta H_{\text{KT}}(T) = \frac{\chi_0(T)}{\chi(T)} \Delta H_\infty \quad (4.19)$$

with the Curie susceptibility  $\chi_0 = C/T$ , where  $C = Ng^2\mu_B^2 S(S+1)/3k_B$  denotes the Curie constant, and the measured *dc*-susceptibility  $\chi(T)$ , which accounts to a large extent for the temperature dependence in the paramagnetic regime [Huber'99]. Given the fact that  $\chi_0(T)/\chi(T) \rightarrow 1$  for  $T \rightarrow \infty$ , the temperature independent parameter  $\Delta H_\infty$  can be identified with the high-temperature limit of the ESR linewidth. The KT approach is a high-temperature approximation and its assumptions can be justified for temperatures  $T \gg J/k_B$ , where  $\Delta H_\infty$  can be calculated explicitly in the infinite-temperature limit by

$$\Delta H_\infty \sim \frac{1}{J} \langle [\mathcal{H}_{\text{int}}, S^+] [\mathcal{H}_{\text{int}}, S^-] \rangle_\infty, \quad (4.20)$$

where  $S^+$  denotes the total spin of the system and  $\langle \dots \rangle_\infty$  is the expectation value with respect to the density matrix at infinite temperatures  $\rho_\infty = \mathbf{1}/\text{Tr } \mathbf{1}$ . The appearance of the isotropic exchange coupling  $J$  in the denominator arises due to the assumption that  $J$  determines the time-scale of the exponential decay of the spin correlations in a three-dimensional magnet. This phenomenon is the so called *exchange narrowing* derived by Anderson and Weiss using the method of moments to calculate the linewidth [Anderson'53]. Therefore, the KT formula is often written as

$$\Delta H_\infty \approx \frac{\hbar^2}{g\mu_B} \frac{M_2}{J} \quad \text{with} \quad M_2 = \frac{1}{\hbar^2} \frac{\langle [\mathcal{H}, S^+] [\mathcal{H}, S^-] \rangle_\infty}{\langle S^+ S^- \rangle}. \quad (4.21)$$

where  $M_2 = \langle (\nu - \nu_{\text{res}})^2 \rangle$  is the second moment of the absorption line.

Due to the fact that these results are obtained in the high-temperature approximation, when all states are equally populated, additional considerations are necessary concerning the temperature regime, where this approximation fails. In strongly exchange-coupled systems this approximation is only valid at temperatures exceeding the exchange-integral value  $J$ . For three dimensional magnets this restriction is not very severe, because at temperatures  $k_B T \sim J$  long-range order is established. Only on approaching magnetic order in the regime of critical fluctuations the temperature dependence of second moment and exchange frequency have to be treated with care. However, in one-dimensional magnets long-range order, if it exists, is established only due to the weak inter-chain interactions at  $k_B T \ll J$ . Thus, there is a wide temperature range in the paramagnetic state where antiferromagnetic correlations have to be taken into account. This case will be considered in Sec. 4.5 in more detail.

#### 4.4.2. Main Sources of the Line Broadening

Before we will turn to the particular case of low-dimensional systems, let us discuss the major line broadening sources in strongly exchange coupled systems and compare their magnitudes in the high-temperature limit using Eq. (4.21). An example how the second moment can be expressed via the parameters of the corresponding interaction is given in appendix C.

Usually, one of the most important origins is represented by the *crystal field*  $\mathcal{H}_{\text{CF}} = \mathbf{S}_a \cdot D_{\text{cf}} \cdot \mathbf{S}_a$ . But this single-ion source of anisotropy is absent for  $S=1/2$  systems that constitute the topic of this work. The further perturbation which should always be taken into account is the *anisotropic Zeeman interaction*  $\mathcal{H}_{\text{AZ}} = \mu_B \mathbf{S} \cdot \mathbf{g} \cdot \mathbf{H}$ . It arises, if the magnetic lattice contains inequivalent sites with different  $g$  tensors, each of them gives an absorption line in different field due to difference in the Zeeman energies. However, for sufficiently strong exchange interaction the spectrum narrows into one single line with a linewidth [Pilawa'97]

$$\Delta H_{\text{AZ}}(\text{kOe}) \approx \frac{g \mu_B H_{\text{res}}^2}{|J'|} \left( \frac{\Delta g}{g} \right)^2 \approx 6.7 \frac{g [H_{\text{res}}(10^4 \text{ Oe})]^2}{J'(\text{K})} \left( \frac{\Delta g}{g} \right)^2, \quad (4.22)$$

Note that for the anisotropic Zeeman interaction the exchange constant  $J'$  between two places with different  $g$  values ( $\Delta g = g_1 - g_2$ ) is responsible for the narrowing. If it is the case for the sites with a weak exchange coupling (e.g. from the neighboring chains in a quasi-one-dimensional material) this broadening can be considerable, at least at Q-band ESR frequencies. An estimation using  $J'/k_B = 3 \text{ K}$ ,  $\Delta g \sim 0.4$  results in  $\Delta H_{\text{AZ}}(f \approx 9 \text{ GHz}) \sim 10 \text{ Oe}$  and  $\Delta H_{\text{AZ}}(f \approx 34 \text{ GHz}) \sim 10^2 \text{ Oe}$  for X- and Q-band frequencies, respectively.

Other sources of the line broadening are narrowed by the isotropic exchange  $J$  which can be very large in low-dimensional materials ( $J/k_B \sim 10 - 10^3 \text{ K}$ ). For this reason, all

sources involving the nuclear spins (the hyperfine interaction, the nuclear Zeeman effect, the nuclear quadrupolar coupling) can usually be neglected. It should be nevertheless noted that the *hyperfine* coupling  $\mathcal{H}_{\text{HF}} = \mathbf{S} \cdot A_{\text{hf}} \cdot \mathbf{I}$ , the largest of this interactions, can become remarkable if the isotropic exchange  $J$  is suppressed, e.g. in the low-temperature dimerised phase. Then the resulting linewidth can be estimated as  $\Delta H_{\text{HF}} \sim \frac{1}{g\mu_{\text{B}}} A^2/J$ , where  $A$  denotes the hyperfine constant (see e.g. [Altshuler'64]).

The *dipole-dipole interaction* is one of the most important line broadening sources in magnetically diluted systems. It describes the mutual influence of the spins by their locally generated magnetic dipolar fields:

$$\mathcal{H}_{\text{DD}} = g^2 \mu_{\text{B}}^2 \sum_{a>b} \frac{1}{r_{ab}^3} \left\{ \mathbf{S}_a \cdot \mathbf{S}_b - 3 \left( \mathbf{S}_a \cdot \frac{\mathbf{r}_{ab}}{r_{ab}} \right) \left( \mathbf{S}_b \cdot \frac{\mathbf{r}_{ab}}{r_{ab}} \right) \right\}, \quad (4.23)$$

where the vector  $\mathbf{r}_{ab}$  connects the sites  $a$  and  $b$  at the distance  $r_{ab}$ . Neglecting the geometrical factors the corresponding high-temperature linewidth is of the order

$$\Delta H_{\text{DD}} \sim \frac{g^3 \mu_{\text{B}}^3 N_{\text{nn}}^2}{J r_{\text{nn}}^6}, \quad (4.24)$$

with the number  $N_{\text{nn}}$  of nearest-neighbor spins at distance  $r_{\text{nn}}$ . For  $r_{\text{nn}} = 4 \text{ \AA}$ ,  $N_{\text{nn}} = 6$ ,  $J/k_{\text{B}} = 10 \text{ K}$  this contribution is only about  $\Delta H_{\text{DD}} \sim 40 \text{ Oe}$  and overwhelmed by the broadening due to *anisotropic exchange interactions* [Pilawa'97, Yamada'98]. Estimations of their magnitude result in values at least two orders of magnitudes higher than for the other sources of line broadening. A detailed theoretical description of anisotropic spin-spin interactions has already been given in Chapter 2.3. In the following we will give several experimental examples which show that the constants of anisotropic exchange can reach values of about several Kelvin which corresponds to a linewidth of about  $10 - 10^3 \text{ Oe}$  assuming  $J/k_{\text{B}} \sim 100 \text{ K}$ .

## 4.5. ESR in Low-Dimensional Spin Systems

Low-dimensional magnetic materials have been an interesting object for ESR since the initial stage of development. Especially, the one-dimensional magnetic systems that are supposed to have no magnetic ordering at finite temperature theoretically, but show short-range order below the temperature corresponding to the main exchange interaction, attracted much attention. The corresponding concepts developed in 1970's for ESR of one-dimensional magnets were the Long-Time-Tail of the relaxation proposed by Dietz *et al.* [Dietz'71] (see the next section) and the anomalous  $g$ -shift calculated by Nagata and Tazuke [Nagata'72] (see Sec. 4.2.1). Subsequently, the questions of EPR have been considered as almost solved. Recently, however, new type of low-dimensional materials that show interesting quantum effects<sup>1</sup> have been found and ESR became again an

<sup>1</sup> e.g. spin-Peierls transition in  $\text{CuGeO}_3$  [Hase'93] and charge ordering in  $\text{NaV}_2\text{O}_5$  [Isobe'96]



important tool to investigate them. In particular, ESR can give an unique information on the anisotropic part of exchange interactions in such a system, what represents the main topic of this work.

#### 4.5.1. Spin Diffusion at High Temperatures

An expansion of the ESR-linewidth theory to the case of one-dimensional systems is a very difficult task up to now (cf. [Bencini'90] and references therein). Besides the question how to treat appropriately the temperature regime  $k_B T < J$ , even in the high-temperature approximation the general problem appears that the spin correlations do not decay fast enough.

It is qualitatively clear that, if the inter-chain exchange  $J'$  is very small, the spin excitations remain on a single chain for a long time. The ESR line shape will no longer be Lorentzian, but will lie somewhere between a Gaussian and a Lorentzian, reflecting the diffusive behavior of the spins along the chain. A self-consistent theory [Hennessey'73, Reiter'75, Lagendijk'77] gives in the range  $0.001 < J'/J < 0.05$  the estimate for the linewidth

$$\Delta H \sim \frac{\hbar^2}{g\mu_B} \frac{M_2}{J'(J'/J)^{1/3}}. \quad (4.25)$$

Since  $J'/J \ll 1$ , the  $1/3$  exponent has a large effect, making the linewidth much larger than predicted by the Kubo-Tomita formula (4.21).

This effect was experimentally observed in several quasi-one-dimensional compounds [Hennessey'73, Lagendijk'77], for example, in tetramethylammonium manganese trichloride TMMC [Dietz'71, Cheung'78], where  $J'$  is more than four orders of magnitude smaller than  $J$ . But in the quasi one-dimensional transition-metal oxides treated in the present work, the inter-chain exchange  $J'$  is usually only about one or two orders of magnitude smaller than the intra-chain exchange  $J$ , for example in  $\text{NaV}_2\text{O}_5$   $J'/J \approx 0.03 - 0.16$  [Smolinski'98, Suaud'00, Gros'05]. The inter-chain exchange of that magnitude almost recovers the Lorentzian shape of the ESR line with renormalized linewidth (Eq. 4.25). Thus, for quasi-one dimensional systems with sufficiently strong inter-chain interaction  $J'$ , the Kubo-Tomita approach works at least in the high-temperature approximation  $k_B T \gg J$ , but the experimentally observed linewidth may exceed the expected value estimated from Eq. (4.21).

#### 4.5.2. Low-Temperature Field-Theory Approach

An expansion of the ESR-linewidth theory to the case of low-dimensional systems at temperatures  $k_B T < J$  was performed e.g. by Soos [Soos'77] who included the temperature dependence of the spin-correlation functions within the traditional formalism. Recently, Oshikawa and Affleck [Oshikawa'02] used field-theory methods to derive the temperature dependence of the ESR linewidth in the spin-1/2 quantum antiferromagnetic chain at

low temperatures  $T \ll J/k_B$ . One relevant result of these papers is that, if the ESR linewidth is due to a single anisotropic interaction, then the temperature dependence of the linewidth is an isotropic function. This means that for all temperatures the relative anisotropy of the ESR linewidth  $\Delta H$  should be the same as in the high-temperature approximation  $T \rightarrow \infty$ , i.e.

$$\Delta H(T, \vartheta, \varphi) = F(T) \cdot \Delta H(\vartheta, \varphi)|_{T \rightarrow \infty}. \quad (4.26)$$

The isotropic function  $F(T)$  approaches unity at high temperatures  $T \gg J/k_B$ .

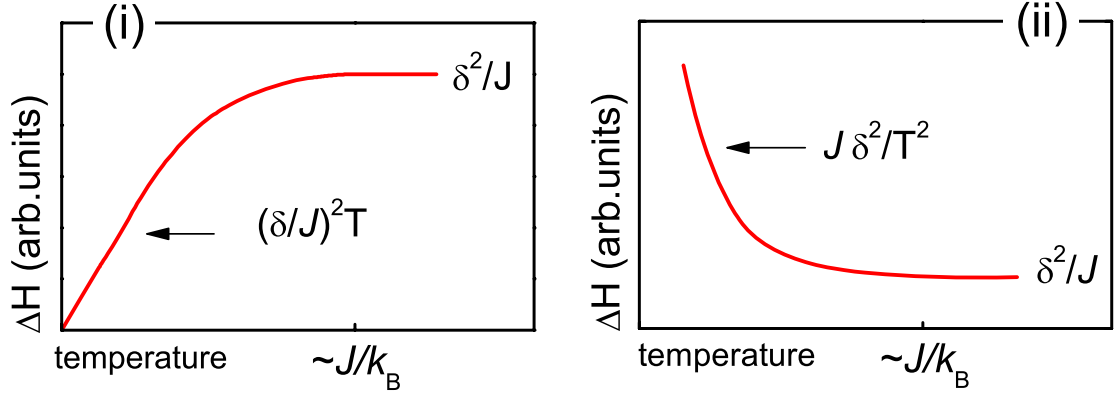


Figure 4.3.: Temperature dependence of the linewidth taken from Oshikawa and Affleck [Oshikawa'02] for relaxation via (i) symmetric anisotropic exchange or (ii) staggered Dzyaloshinsky-Moriya interaction. The relevant exchange constants are denoted by  $\delta$ .

The behavior of the function  $F(T)$  at finite temperatures depends on the origin of the anisotropic interaction which causes the line broadening (see Fig. 4.3). For the case of symmetric anisotropic exchange interaction,  $F(T)$  was predicted to increase linearly with increasing temperature at  $k_B T \ll J$  and to saturate at high temperatures  $k_B T \gg J$ , while for the staggered Dzyaloshinsky-Moriya interaction with  $\mathbf{d}_j = (-1)^j \mathbf{d}$  a divergence  $\propto 1/T^2$  is expected at low temperatures [Oshikawa'02]. The exact temperature dependence of  $F(T)$  is unknown and in Fig. 4.3 only the simplest possible scenario is illustrated. However, Eqs. (4.19) and (4.26) allow us to write down a simple expression for the normalized linewidth

$$\frac{\Delta H(T, \vartheta, \varphi)}{\Delta H(T, \mathbf{H} \parallel \mathbf{1})} = \frac{\Delta H(\vartheta, \varphi)|_{T \rightarrow \infty}}{\Delta H(\mathbf{H} \parallel \mathbf{1})|_{T \rightarrow \infty}} = \frac{M_2(\vartheta, \varphi)|_{T \rightarrow \infty}}{M_2(\mathbf{H} \parallel \mathbf{1})|_{T \rightarrow \infty}}. \quad (4.27)$$

Here  $\mathbf{1}$  is some fixed direction. As it follows from Eq. (4.27), the normalized linewidth should be temperature independent as long as only one type of interaction is responsible for it. It is also free from the uncertainty in the definition of the exchange frequency  $\omega_{\text{ex}}$ .

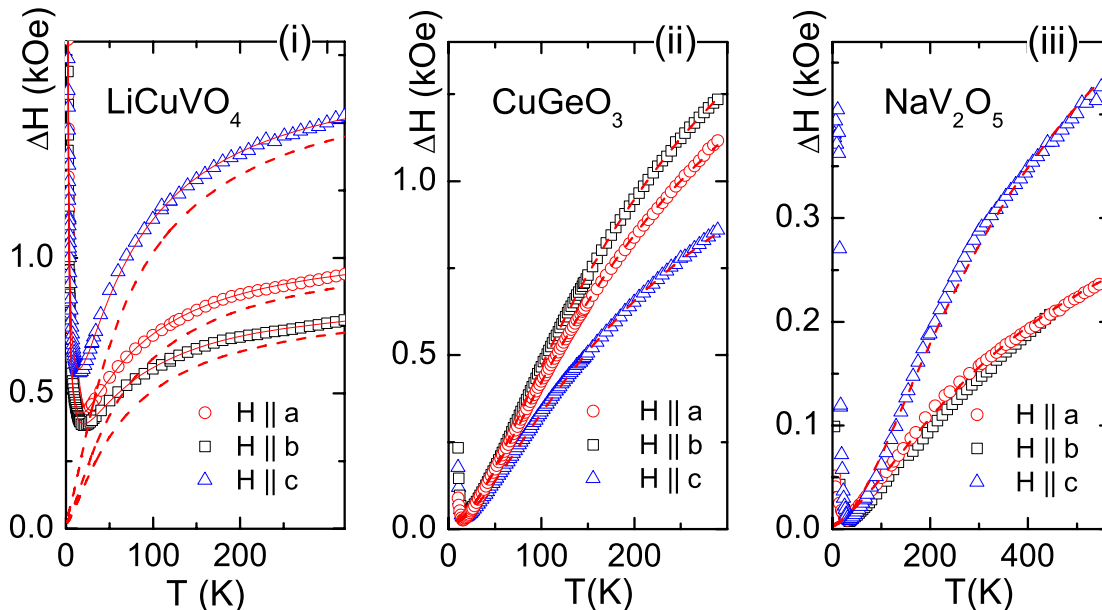


Figure 4.4.: Temperature dependence of the linewidth  $\Delta H$  for the external field applied along the three orthorhombic crystal axes in  $\text{LiCuVO}_4$ ,  $\text{CuGeO}_3$  and  $\text{NaV}_2\text{O}_5$ . The dashed lines fit  $\Delta H(T)$  by Eq. (4.28) with (i)  $\text{LiCuVO}_4$ :  $C_1 = 60 \pm 5$  K ( $J/k_B = 45$  K) and  $C_2 = 15 \pm 5$  K without (with, shown by the solid line) a critical contribution  $(T - T_N)^{-\alpha}$ , where  $\alpha = 0.55 \pm 0.05$ ; (ii)  $\text{CuGeO}_3$ :  $C_1 = 235 \pm 5$  K ( $J/k_B = 120$  K) and  $C_2 = 40 \pm 2$  K; (iii)  $\text{NaV}_2\text{O}_5$ :  $C_1 = 420 \pm 20$  K ( $J/k_B = 578$  K) and  $C_2 = 80 \pm 10$  K.

The price for this simplicity is that we can obtain only ratios of microscopic Hamiltonian parameters, once we express second moments in (4.27).

### 4.5.3. Crossover Temperature Regime

There are no theoretical predictions at the moment for the temperature dependence of the ESR linewidth at temperatures intermediate between the regions covered by Oshikawa-Affleck's calculations  $T \ll J/k_B$  on one side and by the Kubo-Tomita theory  $T > J/k_B$  from other side. Fig. 4.3 represents only the simplest possible variant of this crossover. However, the scenario given in Fig. 4.3 can be confirmed by experimental investigation of the variety of one-dimensional spin systems.

Fig. 4.4 displays the temperature dependence of ESR linewidth in three quasi-one-dimensional systems: the spin-chain compound  $\text{LiCuVO}_4$  [Krug'02], the double-chain system  $\text{CuGeO}_3$  [Eremina'03] and the spin-ladder system  $\text{NaV}_2\text{O}_5$  [Lohmann'00]. For

all compounds the linewidth increases monotonously with increasing temperature in the paramagnetic regime and approaches saturation in the high-temperature limit. Differences appear only at low temperatures, where the linewidth increases again below the spin-Peierls transition in  $\text{CuGeO}_3$  and below the charge-order transition in  $\text{NaV}_2\text{O}_5$ , because the singlet formation inhibits the exchange narrowing of the residual magnetic centers, but diverges already for  $T < 20$  K in  $\text{LiCuVO}_4$  due to the critical spin fluctuations on approaching magnetic order.

In all three compounds it is possible to parametrize the temperature dependence of the linewidth above the transition into the ground state by the empirical expression [Eremina'03]

$$\Delta H_{\text{KvN}}(T) = \Delta H(\infty) \exp\left(-\frac{C_1}{T + C_2}\right), \quad (4.28)$$

where  $\Delta H(\infty)$ ,  $C_1$ , and  $C_2$  are treated as fitting parameters. For  $\text{LiCuVO}_4$  an additional critical divergence at  $T_N$  has been added typical for the onset of magnetic order. Note that the parameter  $C_1$  corresponds to the order of magnitude of the isotropic exchange constant. This is reasonable, because the parameter  $C_1$  indicates the transition from the strongly correlated one-dimensional regime at low temperatures  $T \ll J/k_B$  to the purely paramagnetic regime  $T \gg J/k_B$ , where the high-temperature approximation is valid. The parameter  $C_2$  indicates the influence of the low-temperature phase-transition on the line broadening. But it is necessary to recall that this purely empirical parametrization has no underlying microscopic picture, yet.

Nevertheless, the general feature of the observed temperature dependence, i.e. an approximately linear increase at temperatures small compared to the exchange constant

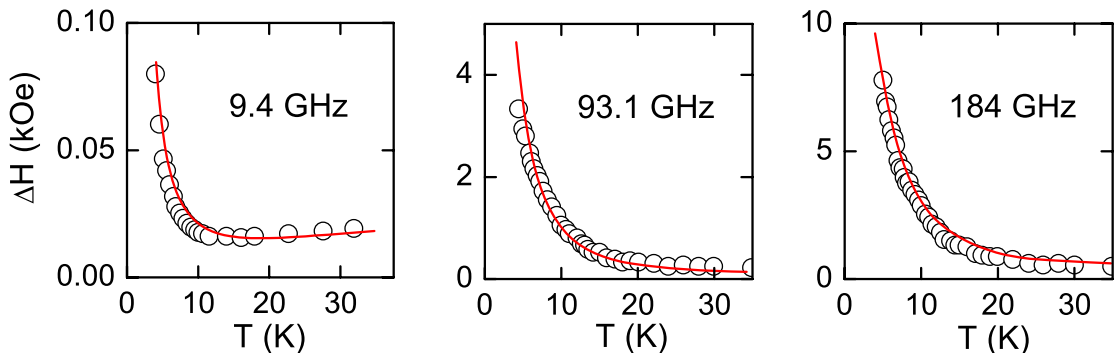


Figure 4.5.: The temperature dependence of the ESR linewidth in  $[\text{PM-Cu}(\text{NO}_3)_2(\text{H}_2\text{O})_2]_n$  taken from Zvyagin *et al.* [Zvyagin'05]. The experimental points coincide with theoretical predictions by Oshikawa and Affleck [Oshikawa'02] (solid lines) for the dominant relaxation via DM interaction.

$T \ll J/k_B$  but large compared to any phase-transition temperature and a saturation behavior in the high-temperature regime  $T \gg J/k_B$  coincides with the theoretically expected temperature dependence for the case of dominant relaxation via AE.

The theoretical expectations in case of dominant relaxation via DM interaction were recently confirmed experimentally by Zvyagin *et al.* [Zvyagin'05]. The multifrequency ESR study of copper pyrimidine dinitrate, a spin-1/2 antiferromagnetic chain, has shown an excellent quantitative agreement between the theoretical predictions and experiment (see Fig. 4.5) confirming both the temperature  $\propto 1/T^2$  and the field  $\propto H^2$  dependence of  $\Delta H$  due to the staggered DM interaction.

## 4.6. Other Experimental Techniques

The use of a resonant cavity provides the highest sensitivity of ESR spectroscopy. But with one cavity only a single frequency can be investigated. E.g. the X- and Q-band setups used in the present work allow the measurements at  $\nu_{\text{ESR}} \approx 9.3$  and 34 GHz, respectively. To go beyond these limits, additional experimental techniques have to be used.

An alternative method is given by the *quasi-optical technique* where the electromagnetic wave, generated by a monochromatic source, propagates through "free space" (i.e. is unguided in contrast to ESR) and is detected by a suitable detector after passing (or being reflected by) the sample. The experimental arrangement used in this work is similar to that of a Mach-Zehnder interferometer. This setup allows the measurement of the frequency dependence of both the transmission and the phase shift of a monochromatic electromagnetic beam through the sample. The frequency range 40-1100 GHz is covered continuously by ten tuneable narrow-band backward-wave oscillators.

At frequencies lower than  $\nu_{\text{ESR}}$  the broadband *dielectric spectroscopy* was used in the present work [Lunkenheimer'00]. By dielectric spectroscopy, dynamic processes can be detected that involve the reorientation of dipolar entities or the displacement of charged entities. Relaxation processes of such entities occur if they are subjected to an electric field  $E$  changing with time. In the region of some  $\mu\text{Hz}$  up to several MHz, essentially the capacitance and conductance can be measured. The sample has to be prepared in this case as a capacitor. Then the frequency-response analyzer (Novocontrol  $\alpha$ -analyzer) measures directly the sample voltage and the sample current using lock-in techniques. Between 1 MHz and about 10 GHz, the coaxial reflection method is best suited. Here the sample is connected to the end of a coaxial line, thereby bridging inner and outer conductor. The impedance analyzer (Agilent E 4991A) measures, after a proper calibration, the complex reflection coefficient.

The results of both quasi-optical and dielectric spectroscopy measurements are usually presented by the complex dielectric permittivity  $\varepsilon^* = \varepsilon' - i\varepsilon''$ .<sup>2</sup> The temperature and

<sup>2</sup>  $\varepsilon^*$  can be defined by  $D^*(\nu) = \varepsilon^* \varepsilon_0 E^*(\nu)$  with  $D^*$  the dielectric displacement,  $E^*$  the electric field

frequency dependence of the conductivity can be calculated as  $\sigma(T, \nu) = 2\pi\nu\varepsilon_0\varepsilon''(T, \nu)$ , where  $\varepsilon_0$  is the permittivity of vacuum. The exceptionally broad frequency window, accessible with quasi-optical and dielectric spectroscopy, makes them powerful tools to describe the charge dynamics and relaxation mechanisms.

A further important experimental method used in the present work is the measurement of the *magnetic susceptibility*  $\chi = M/H$ , where  $M$  is the magnetization of a sample in an external magnetic field  $H$ . This technique helps to reveal information, for example, about the electronic structure, interactions between neighboring ions or the character of a transition between two phases of the material. In this work we used a superconducting quantum interference device (SQUID), the probably most sensitive device available for measuring magnetic fields. This magnetometer is capable of resolving changes in magnetic field that approach  $10^{-15}$  tesla, yet can operate in fields as large as 7 tesla. The operating range of temperatures is 1.9 - 400 K. To avoid confusions, we will give the relation of the used CGS units to the corresponding SI ones:  $1 \text{ emu/mol} = 4\pi \cdot 10^{-6} \text{ m}^3/\text{mol}$ .

The *specific-heat* data were obtained by the adiabatic calorimetry. This method directly follows the classical definition of heat capacity  $C_p = \lim_{dT \rightarrow 0} (dQ/dT)_p$ , where  $dQ$  is the heat input that causes a subsequent temperature rise  $dT$  in the sample. The Physical Property Measurement System (PPMS) from Quantum Design allows to measure very small samples (with the mass larger than 1 mg) fully automatically in the broad temperature range 1.9 - 300 K. The specific heat is governed by the manner in which the internal energy is distributed in the system and allows to address a wide range of phenomena. For example, in solid materials the phonons (lattice vibrations) provide the main contribution to the specific heat, in metals the thermal energy of electrons can be measured. The magnetic contribution, which is important for this study, is related to the thermal excitations of spin waves to higher energy states. The corresponding theoretical predictions for the case of spin chains can be found in section 3.1.2.

---

and  $\varepsilon_0$  the permittivity of vacuum. Here the star superscripts denote the use of complex quantities, a common practice to include phase information in frequency-dependent quantities. The real part  $\varepsilon'$  is the frequency dependent dielectric constant. The imaginary part  $\varepsilon''$  is proportional to the part of  $D'$  that is out of phase with the electric field with a phase difference of  $\pi/2$ . It is proportional to the 'loss' of energy from the applied field into the sample (in fact this energy is dissipated into heat) and therefore denoted as dielectric loss.



## 5. Symmetric Ring Exchange in $\alpha'$ - $\text{NaV}_2\text{O}_5$

In recent years  $\alpha'$ - $\text{NaV}_2\text{O}_5$  has raised a great deal of interest as being the second inorganic compound, after  $\text{CuGeO}_3$ , where a quantum antiferromagnetic state is achieved at the expense of a lattice distortion [Isobe'96]. However, the subsequent investigations [Ohama'99] have shown that  $\text{NaV}_2\text{O}_5$  cannot be considered as a conventional spin-Peierls compound and much efforts have been provided to understand the mechanism of the spin-gap formation and the nature of this phase transition.

In this chapter we will discuss the ESR results that can contribute to the determination of the spin-gap, the isotropic exchange constant, the crystal-field splitting schema and, most importantly, to the estimation of the anisotropic parts of the exchange interaction. We will reveal an unconventional nature of this spin-spin interaction and a strong increase of inter-ladder anisotropic exchange on approaching the phase transition.

### 5.1. Sample Characterization

The single crystals were grown in a two step process [Lohmann'97]: First pellets of a nearly stoichiometric mixture of high purity  $\text{NaVO}_3$  and  $\text{VO}_2$  were pressed and heated in an evacuated quartz tube at  $620^\circ\text{C}$  for four days. Then the material was heated above the melting temperature and, in a temperature gradient, was cooled down at a cooling rate of  $7^\circ\text{C}/\text{h}$ . The crystal used in this work was characterized by Debye-Scherrer x-ray diffraction and Laue diffraction, which showed the material to be single phase.

#### 5.1.1. Crystal Structure

A phase transition occurs in  $\alpha'$ - $\text{NaV}_2\text{O}_5$  at  $T_{\text{CO}} \approx 34$  K. The charge redistribution taking place at this temperature affects dramatically all physical properties of this system. In order to lay the basis for the following discussion of this phenomenon, let us discuss first the crystal structure of this compound and its changes at  $T_{\text{CO}}$ .

According to the recent crystallographic investigations [vonSchnering'98, Smolinski'98], at high temperatures the structure is centrosymmetric with the space group  $D_{2h}^{13} - Pmmn$  (lattice parameters  $a = 11.325$  Å,  $b = 3.611$  Å, and  $c = 4.806$  Å) with all V atoms crystallographically equivalent at room temperature. In Fig. 5.1(i) we show the ion arrangement for  $\text{NaV}_2\text{O}_5$ . The high-temperature structure can be seen as a set of layers of two-leg vanadium ladders running along the  $b$  direction with the rungs along the  $a$



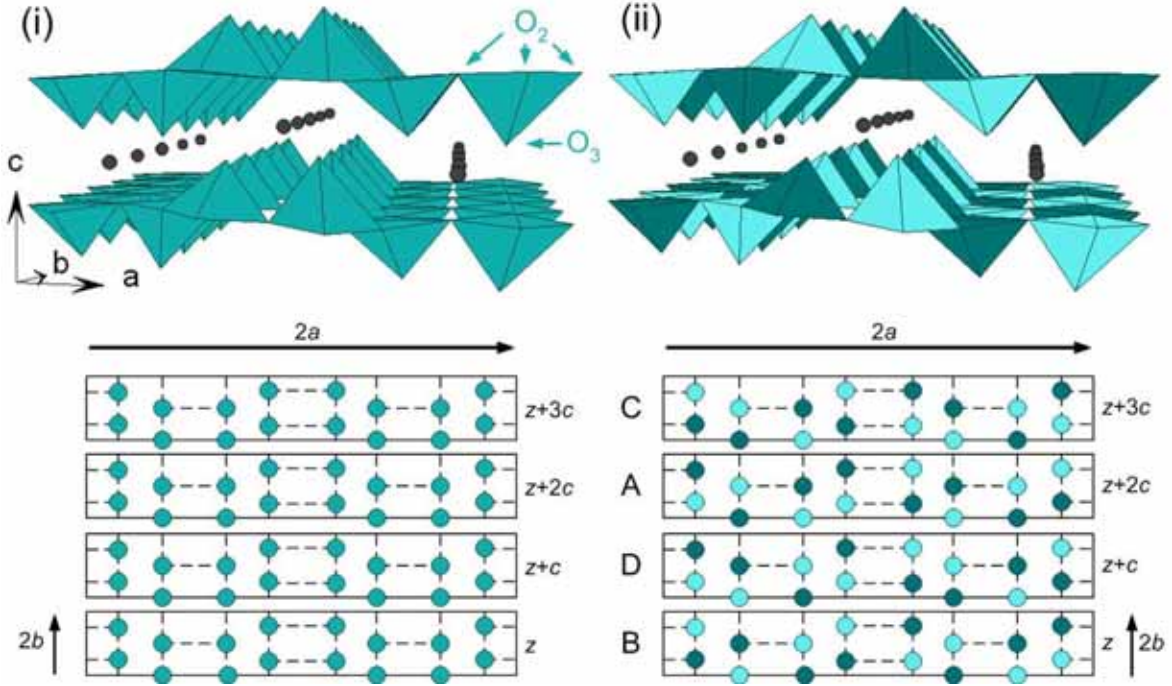


Figure 5.1.: Crystal structure of  $\alpha'$ - $\text{NaV}_2\text{O}_5$  at high temperatures  $T > T_{\text{CO}}$  (i) and in the charge-ordered phase (ii). Oxygen pyramids around V ions and rows of Na ions are shown. At the bottom of each picture the schematic representation of V atoms arrangement is given. At  $T > T_{\text{CO}}$  all V have the equal valence  $+4.5$  (the cyan circles/pyramids), at  $T < T_{\text{CO}}$  the zigzag-like charge redistribution takes place into  $\text{V}^{4+}$  (light cyan) and  $\text{V}^{5+}$  (dark cyan). With large probability, the low-temperature crystal structure consists of layers with different charge arrangements (A-D) stacking along the  $c$  direction [Grenier'02].

direction. The V ions are located inside oxygen squared-base pyramids whose corners shared with neighboring pyramids. The cations  $\text{Na}^+$  are located between the layers.

This compound is a mixed-valence system with an average valence of  $\text{V}^{4.5+}$  ( $3d^{1/2}$ ) and can be considered as a quarter-filled two-leg ladder system. The ladders running along the crystallographic  $b$  axis are responsible for the one-dimensional character of this compound observed in magnetic susceptibility measurements (Sec. 5.1.3). Each  $d$  electron, supplied by the two V ions forming a rung of the ladder, is not attached to a particular V site but is shared in a V-O-V molecular bonding orbital along the rung.

At  $T_{\text{CO}}$  the crystal structure changes and a lattice distortion with a supercell of  $2a \times 2b \times 4c$  results. The refinement of the low-temperature crystal structure is strongly

hindered by the large size of the supercell, including 16 unit cells, and, therefore, by the large number of atoms necessary to consider. Most likely, it belongs to the space group  $Fmm2$  and contains stacking faults separating regions corresponding to the four possible patterns of zigzag-like *charge ordering* in each layer (Fig. 5.1(ii)) [Grenier'02].

Nevertheless, no matter how the real low-temperature structure looks like exactly, the *zigzag* form of the local charge order in each separate ladder seems to be an established fact. It is confirmed by a number of experiments and theoretical calculations, part of that will be discussed in the following section.

### 5.1.2. Charge Ordering Phenomenon

A long range order of different metal oxidation states in a crystal lattice may be important to the mechanism of superconductivity, colossal magnetoresistances and other phenomena in oxides. However, there is still little known about physics underlying this effect. First envisaged over 70 years ago [Wigner'34], charge order (CO) has been firmly evidenced by neutron diffraction studies only in the last decade. These results clearly show that in all cases CO is far from complete, lying for the most of materials in the range  $\%CO = 20 - 60\%$  [Attfield'06, Goto'03].<sup>1</sup> But no correlations of  $\%CO$  with  $T_{CO}$ , type of magnetic ordering, average oxidation state or structural frustration of CO have been evident. First theoretical attempts to gain some insight into the various ground states were made from calculation of the Madelung energy of the assembly of charged ions. But electron-lattice coupling seems to dominate over pure electron-electron repulsions, enabling, in particular, CO states to be switched and tuned by internal lattice effects and external fields. At present a microscopical description of this phenomenon is still lacking.

Whatever the reason for this phase transition and the reduced charge separation could be, CO occurs in  $\alpha'$ - $\text{NaV}_2\text{O}_5$  at  $T_{CO} \approx 34$  K. In particular the  $^{51}\text{V}$  NMR results, which gave just one line for  $T > T_{CO}$  show the presence of two inequivalent  $\text{V}^{4+}$  and  $\text{V}^{5+}$  below the transition temperature [Sawa'02]. More precisely, the real charge separation between these two sites, calculated using the bond valence sum method [Attfield'06], amounts to

<sup>1</sup> Here the idealised CO formula was used [Attfield'06]

$$\%CO = \frac{V_2 - V_1}{V_2 + V_1} \frac{F_H + F_L}{F_H - F_L} \cdot 100\%,$$

where  $F_H$  and  $F_L$  are the formal valences in the higher and lower states (e.g.  $F_H = 5$  for  $\text{V}^{5+}$  and  $F_L = 4$  for  $\text{V}^{4+}$ ).  $V_1$  and  $V_2$  are the lower and higher bond valence sums calculated from experimental bond distances  $d_i$  from each metal site to the coordinating ligand ion

$$V_n = \sum_i \exp\left(\frac{d_n - d_i}{B}\right).$$

$B$  is a global constant and  $d_n$  is the bond valence parameter for the metal in an assumed oxidation state  $n$ .

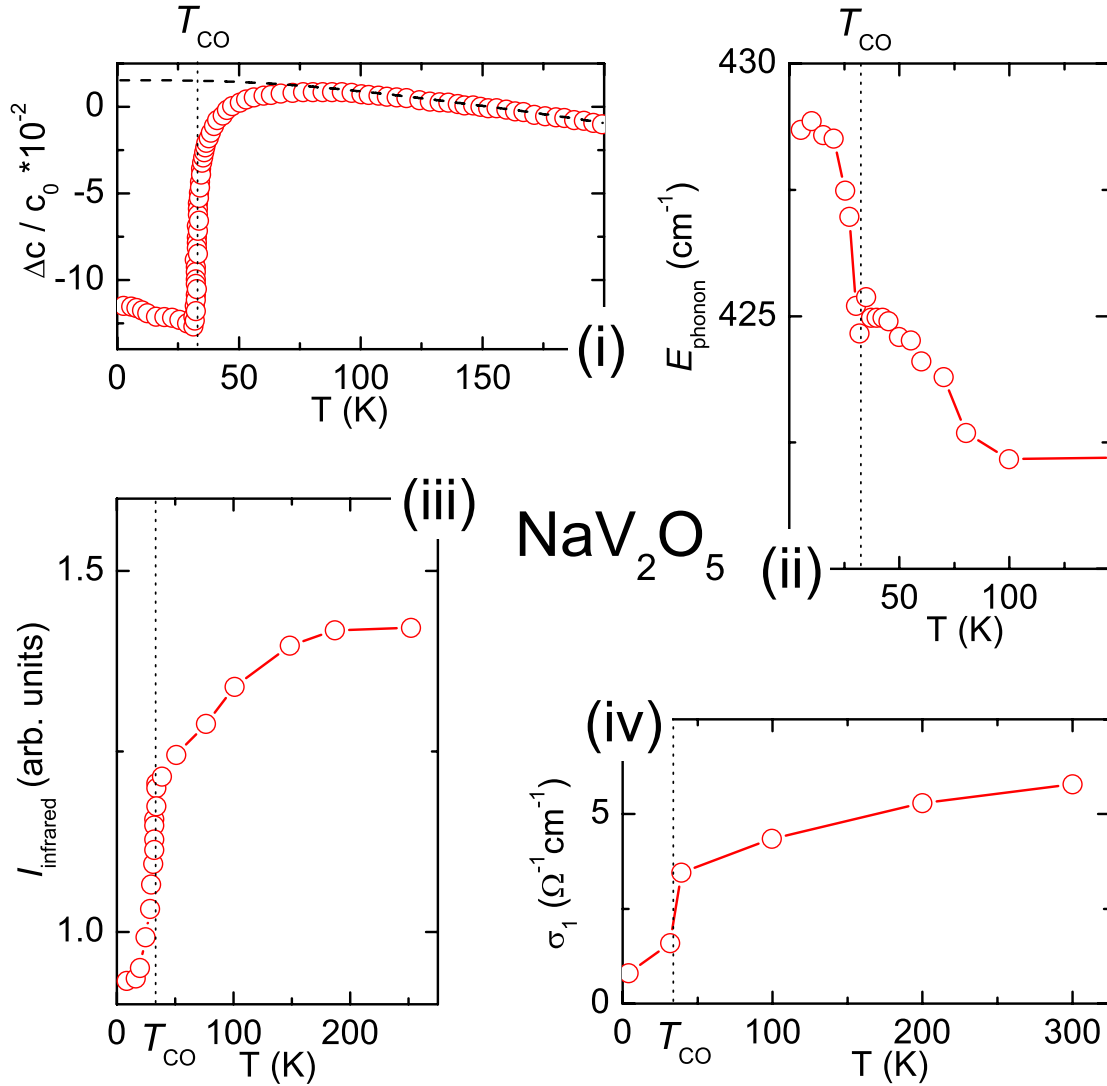


Figure 5.2.: **(i)**: Temperature dependence of the relative sound velocity of the  $c_{66}$  mode (propagation along the  $b$  axis with polarization along the  $a$  axis), the dash line indicates the background [Schwenk'99]. **(ii)**: Temperature dependence of the energy of the  $422\text{ cm}^{-1}$  Raman mode in  $(bb)$  light polarization, taken from [Fischer'99]. **(iii)**: Temperature dependence of the integrated intensity of the far-infrared absorption  $I = \int_1^{12\text{ THz}} \beta(\nu) d\nu$ ,  $\beta$  being the absorption coefficient [Smirnov'99]. **(iv)**: Temperature dependence of the optical conductivity at  $\omega = 115\text{ cm}^{-1}$  for  $E \perp$  chain [Damascelli'00]. All quantities mark the onset of charge-ordering fluctuations in  $\alpha'$ - $\text{NaV}_2\text{O}_5$  at temperatures far above  $T_{\text{CO}} \approx 34\text{ K}$  (shown by the black dot lines).

$\%CO \approx 59\%$  (corresponding to  $V^{4.2+}$  and  $V^{4.8+}$  [Grenier'01]).

The symmetry analysis [Goto'03] of the enlarged unit cell in the ordered region favors a zigzag structure of CO depicted in Fig. 5.1(ii), in accordance with the calculations based on the Hartree approximation for both on-site and intersite Coulomb interactions [Seo'98]. This CO pattern is corroborated by the results of X-ray diffraction [Grenier'02] and by neutron-scattering experiments [Grenier'01], where the occurrence of two magnon branches along the  $a$  axis was observed.

A very powerful method for the investigation of the lattice effects related to the CO is represented by the ultrasonic measurement of the elastic constants. Due to coupling to charge-ordering modes they allow to draw conclusions not only about the CO pattern but also about the onset and development of charge fluctuations. Fig. 5.2(i) shows that in  $\alpha'$ - $NaV_2O_5$  the softening of the  $c_{66}$  mode starts to develop already at  $T \sim 100$  K [Schwenk'99]. The very broad temperature region of preexisting CO fluctuations (Fig. 5.2(ii)) was revealed also by the frequency shift of the  $422\text{ cm}^{-1}$  mode in Raman scattering [Fischer'99] and by the change of the refractive index at different infrared frequencies [Smirnov'99] (Fig. 5.2(iii)). Moreover, the optical investigation in the range  $4\text{ meV} - 4\text{ eV}$  [Damascelli'00] provided direct evidences for a charge disproportionated electronic state at  $T \gg T_{CO}$ . The strong increase of CO fluctuations affects apparently also the low-temperature magnetic and thermodynamic properties that will be discussed in the next section.

### 5.1.3. Magnetic and Thermodynamic Properties

Fig. 5.3(i) displays the temperature dependence of  $I_{ESR}$  up to 650 K [Hemberger'98]. The absolute value was determined by comparing the room-temperature value of the ESR data to SQUID measurements on the same single crystal.  $I_{ESR}(T)$  is preferable to  $\chi_{SQUID}$  in this case because of the small mass of the single crystals. The Bonner-Fisher curve (Eq. 3.7) adequately describes the ESR data at  $T > 250$  K assuming the exchange constant  $J = 578$  K, somewhat larger than  $J^{(Isobe)} = 560$  K obtained from susceptibility measurements by Isobe and Ueda [Isobe'96]. Also the maximum value  $\chi_{\max}^{(BF)} \approx 4 \cdot 10^{-4}$  emu/mol predicted by Eq. (3.8) is in good agreement with the experimentally observed value  $\chi_{\max}^{(exp)} \approx 4.2 \cdot 10^{-4}$  emu/mol. This kind of behavior allows to conclude, that  $\alpha'$ - $NaV_2O_5$  is a good 1D spin system at high temperatures.

At  $T < 200$  K significant deviations from the expected behavior are observed resulting in a considerable exponential drop of susceptibility at  $T_{CO} \approx 34$  K. The gap value  $\Delta/k_B \approx 98$  K coincides well with published results giving  $\Delta/k_B \approx 90 \pm 20$  K [Vasilev'97, Luther'98, Fujii'97]. This result indicates significant deviations from the weak-coupling limit  $2\Delta(0)/(k_B T_{CO}) = 3.53$  (Eq. 3.5) and yields a ratio  $2\Delta(0)/(k_B T_{CO}) = 5.9$ .

The heat capacity also shows an anomaly at  $T_{CO} \approx 34$  K. Fig. 5.3(ii) shows this peak with the background line. The background was obtained using two contributions: the linear Bonner-Fisher term calculated from the exchange interaction (Eq. 3.11) and the

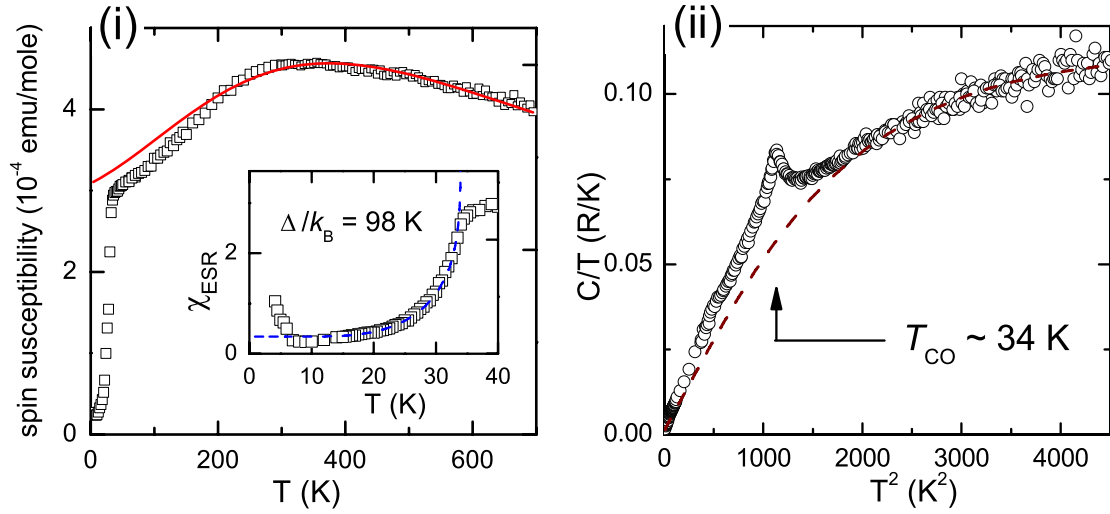


Figure 5.3.: (i): Temperature dependence of the ESR intensity (spin susceptibility) in single-crystalline  $\alpha'$ - $\text{NaV}_2\text{O}_5$  (open squares) as compared to the predictions of the Bonner-Fisher model (solid red line). Inset: Spin susceptibility at low temperatures around  $T_{\text{CO}} \approx 34$  K, the solid line represents a mean-field fit (Eq. 3.5) with a gap of 98 K. (ii): Heat capacity in  $\text{NaV}_2\text{O}_5$  plotted as  $C/T$  vs.  $T^2$ . The dashed wine line is a sum of a phonon term and a small linear magnetic contribution as predicted by the Bonner-Fisher model [Hemberger'98].

Debye  $T^3$ -term (with  $\Theta_D = 281$  K and the number of degrees of freedom  $N = 15$ ). Note that the obtained specific-heat anomaly  $\Delta C \approx 14Rk_B T_{\text{CO}}/J$  strongly exceeds the value expected in mean-field approximation  $\Delta C \approx Rk_B T_{\text{CO}}/J$  just as the gap value.

## 5.2. ESR in $\alpha'$ - $\text{NaV}_2\text{O}_5$

Having already discussed the intensity of the ESR signal (Fig. 5.3(i)) we will introduce further ESR results in this section, analyzing the temperature and angular dependencies of the resonance field as well as of the linewidth. Let us start with presenting the ESR spectra in  $\alpha'$ - $\text{NaV}_2\text{O}_5$ .

### 5.2.1. Resonance Spectra

Resonance spectra for the paramagnetic regime are presented in Fig. 5.4, illustrating their evolution with temperature as well as the angular dependence with respect to the direction of the external magnetic field. The spectra consist of one exchange narrowed

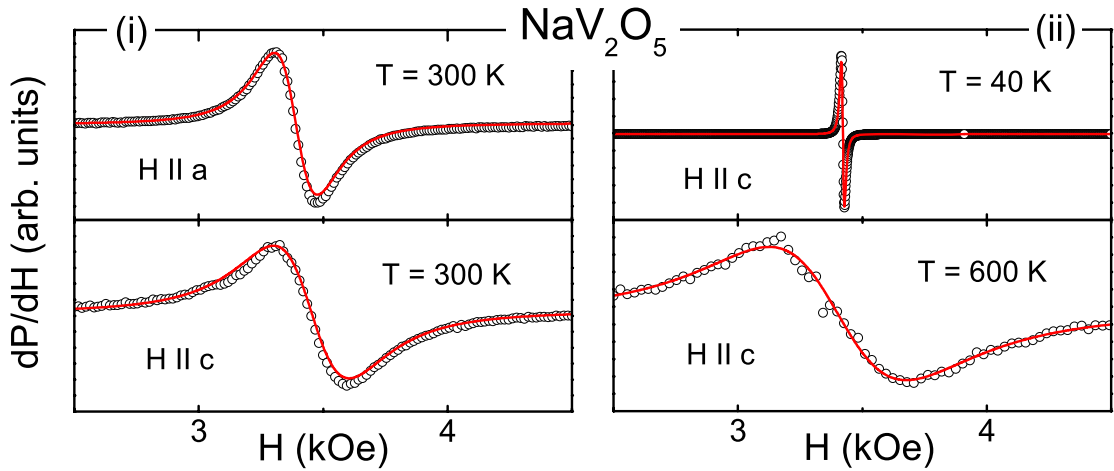


Figure 5.4.: ESR spectra of  $\alpha'$ - $\text{NaV}_2\text{O}_5$ . **(i)**: two different orientations at room temperature. **(ii)**: temperature evolution of the ESR spectrum from a temperature near the phase transition  $T = 40$  K to the one of the highest measured temperature  $T = 600$  K. Solid lines represent fits using Lorentzian line shape.

resonance line, nearly symmetric with respect to the resonance field. In the whole temperature range they can be described using a single Lorentzian line shape (solid lines in Fig. 5.4), i. e. by Eq. (4.13) with  $\alpha = 0$ .

The absorption line appears at a magnetic field of 3430 Oe which corresponds to the effective  $g$  value of about 2, characteristic for spin systems with only small contribution from orbital moments. The angular and temperature dependencies of the resonance field will be discussed in the next section.

### 5.2.2. Analysis of the $g$ Tensor

Fig. 5.5(i) shows that the  $g$ -factors in  $\alpha'$ - $\text{NaV}_2\text{O}_5$  are almost temperature independent. They can be described using anisotropic  $g$  values  $g_c \approx 1.93$ ,  $g_a \approx g_b \approx 1.97$ , characteristic of  $\text{V}^{4+}$  ions in strong octahedral fields [Abragam'70].

Note that these values were obtained at X-band frequencies ( $\nu \sim 9.3$  GHz). Using higher Q-band frequencies ( $\nu \sim 34$  GHz) allows to get more reliable data. In particular, an angular dependence of the  $g$  factor in the  $(ac)$ -plane measured at  $T = 50$  K is given in Fig. 5.5(ii). In the following we will describe the angular dependence of the  $g$  factor and calculate the energy level scheme of the  $\text{V}^{4+}$  ion in  $\alpha'$ - $\text{NaV}_2\text{O}_5$  in terms of the angular overlap model (Sec. 4.2.1) using the improved  $g$  values  $g_c \approx 1.918(4)$ ,  $g_a \approx g_b \approx 1.969(3)$ .

The magnetic ion in the system under consideration is placed in a  $\text{VO}_5$  pyramid. The necessary crystallographic data can be taken from [Carpy'75] and the spin-orbit coupling

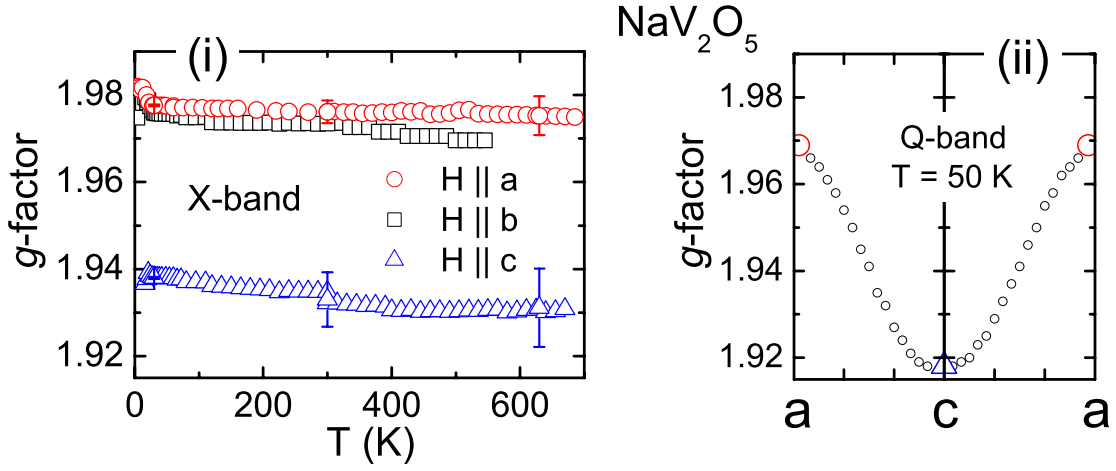


Figure 5.5.: **(i)**: Temperature dependencies of the effective  $g$ -factors in  $\alpha'$ - $\text{NaV}_2\text{O}_5$  measured at X-band frequency ( $\nu \approx 9.34$  GHz). **(ii)**: An angular dependence of the  $g$  factor at  $T = 50$  K in the  $(ac)$ -plane measured at Q-band frequency ( $\nu \approx 34$  GHz).

Table 5.1.: Left column: Observed and calculated  $g$  tensors in  $\text{NaV}_2\text{O}_5$ . Right column: Relative energies of the  $d$  orbital states calculated by means of the AOM model as well as using the LDA+ $U$  approximation from [Yaresko'00].

		Orbital state	$E_{\text{AOM}}$ [eV]	$E_{\text{LDA}+U}$ [eV]
	Experiment			
$g_a$	1.970(3)	$d_{3z^2-r^2}$	3.78	$2.2 \div 4.4$
$g_b$	1.970(3)	$d_{x^2-y^2}$	2.41	$0.7 \div 4.4$
$g_c$	1.918(4)	$d_{xz}$	1.03	$0.8 \div 1.8$
		$d_{yz}$	0.98	$0.7 \div 1.6$
		$d_{xy}$	0	$-0.3 \div 0.3$

Table 5.2.: Angular overlap model parameters for the  $[\text{V}^{4+}\text{O}_5]$  complex in  $\alpha'$ - $\text{NaV}_2\text{O}_5$ .

$\lambda$ [ $\text{cm}^{-1}$ ]	$e_\sigma(\text{O}_3)$	$e_\pi(\text{O}_3)$	$e_\sigma(\text{O}_2)$	$e_\pi(\text{O}_2)$	[ $10^3 \text{ cm}^{-1}$ ]	$k_x$	$k_y$	$k_z$
190	32	8	12	3		0.65	0.65	1

constant for a free  $\text{V}^{4+}$  ion is equal to  $\lambda_{\text{fi}} = 248 \text{ cm}^{-1}$  [Abragam'70]. In order to reduce the number of parameters we will distinguish two types of ligands: apical oxygen ions  $\text{O}_3$  located above the basal plane and oxygen ions  $\text{O}_2$ , which form the basal quadrangles of the  $\text{VO}_5$  pyramids (see Fig. 5.1). The average metal-ligand distance amounts to  $1.54 \text{ \AA}$  and  $1.87 \text{ \AA}$ , respectively. Assuming the variation of  $e_\sigma$  as a function of bond distance  $e_\sigma \sim r^{-5.2}$  we obtain

$$e_\sigma(\text{O}_2) = \left(\frac{1.87}{1.54}\right)^{-5} e_\sigma(\text{O}_3) \approx 0.38 \cdot e_\sigma(\text{O}_3). \quad (5.1)$$

Then, for the  $e_\pi$  bounding parameters one has

$$e_\pi(\text{O}_3) = \frac{e_\sigma(\text{O}_3)}{4}; \quad e_\pi(\text{O}_2) = \frac{e_\sigma(\text{O}_2)}{4} = 0.095 \cdot e_\sigma(\text{O}_3) \approx \frac{e_\sigma(\text{O}_3)}{10}. \quad (5.2)$$

The given set of parameters allows to describe the anisotropy of the  $g$ -factor very well (see the left side of Table 5.1). Note that the distribution of electrons in the  $(xy)$ -plane, i. e. the plane of the ladders, plays an important role in  $\text{NaV}_2\text{O}_5$  and results in the strong reduction of SO interaction  $k_{x,y} < 1$ . The calculated relative energies of the orbital states are listed on the right side of Table 5.1. For comparison, the results of the band calculations [Yaresko'00] are also given. The quantitative coincidence is clearly seen although our calculations can give only the "centre of mass" for the energy of the electron on the respective band.

### 5.2.3. ESR Linewidth

At  $T < 500 \text{ K}$  the linewidth in  $\alpha'$ - $\text{NaV}_2\text{O}_5$  increases monotonously from a value of  $10 \text{ Oe}$  at  $T_{\text{CO}} \approx 34 \text{ K}$  up to several hundreds  $\text{Oe}$  above room temperature (Fig. 5.6(i)). In section 4.5.3 it was shown that this saturating behavior (Eq. 4.28) is related to the dominant spin relaxation via symmetric anisotropic exchange. Below  $T_{\text{CO}}$  the ESR line strongly broadens due to the weakening of the exchange narrowing on dimerization of the majority of spins leaving only weakly interacting residual magnetic moments. At high temperatures<sup>3</sup>  $T > 500 \text{ K}$  a peculiar change from a negative to positive curvature is observed at about  $600 \text{ K}$ , which is displayed in Fig. 5.6(i). This increase can be described by adding an exponential term to the spin-chain contribution (Eq. 4.28)

$$\begin{aligned} \Delta H(T) &= \Delta H_{\text{KvN}}(T) + \Delta H_{\text{exp}}(T) = \\ &= \Delta H_{\text{KvN}}(\infty) \exp\left(-\frac{C_1}{T + C_2}\right) + \Delta H_{\text{exp}}(\infty) \exp\left(-\frac{\Delta_{\text{ESR}}}{k_{\text{B}}T}\right). \end{aligned} \quad (5.3)$$

<sup>2</sup> That is consistent with the measurements of the pressure dependence of the electronic spectra of most of the metal oxides (see [Figgis'00] and App. B).

<sup>3</sup> The measurement at  $T > 600 \text{ K}$  were performed using a high-temperature ESR set-up in Lousanne in collaboration with Prof. László Forró and Dr. Titusz Feher.



$\Delta_{ESR} = 0.4$  eV and the parameters used for  $\Delta H_{KvN}$  are given in the caption of Fig. 4.4. The exponential nature of the additional contribution is highlighted in Fig. 5.6(ii), where only the contribution  $\Delta H_{\text{exp}}(T)$  is plotted in Arrhenius representation.

The similar temperature behavior of dielectric conductivity depicted in the same figure allows to speculate about the reasons of that broadening. The Arrhenius law of the conductivity  $\sigma \propto \exp(-\Delta_\sigma/(2k_B T))$  indicates the thermal activation of charge carriers into a level with an activation energy  $\Delta_\sigma \approx 0.86$  eV. The experimental charge-transfer gap is nevertheless considerably larger and amounts to about 3 eV [Damascelli'00]. At the same time a strong electronic absorption is observed in both optical reflectivity and conductivity at the energy  $\Delta \sim 1.1 \pm 0.4$  eV [Damascelli'00]. Moreover, this gap value is very close to the energy of the first almost degenerate crystal-field levels  $xz$  and  $yz$ , calculated in Sec. 5.2.2. This might indicate the involvement of excited orbital states in this relaxation process. It is also worth noting at this point, that in  $\text{CuSb}_2\text{O}_6$  a similar temperature dependence of the linewidth with  $\Delta_{ESR}^{(\text{CuSb}_2\text{O}_6)} = 0.13$  eV was observed and explained in terms of a thermally activated dynamic Jahn-Teller process [Heinrich'03]. However, a rigorous theoretical treatment of this effect has not yet been undertaken. To finally decide about the origin of the high-temperature relaxation, additional theoretical efforts as well as structural investigations at these temperatures are necessary.

The probably most peculiar feature of the low-temperature ESR linewidth data is a crossover at about 60 K, emphasized in Fig. 5.6(iii). At higher temperatures  $\Delta H$  reaches its maximum for  $H \parallel c$  with  $\Delta H_c/\Delta H_{a,b} \sim 1.8$ . The crossover results in the broadest spectra for  $H \parallel a$  at  $T_{\text{CO}} < T < 60$  K (Figs. 5.7(i,ii)). It is related to the change of the spin relaxation mechanism, in particular, to the increase of inter-ladder anisotropic exchange. In order to understand this effect let us discuss first all relaxation mechanisms and exchange paths involved.

### 5.3. Analysis of Relaxation Mechanisms

All possible origins for the line broadening  $\Delta H$  in low-dimensional spin systems were considered in Sec. 4.4.2. In accordance with those estimations, single-ion, dipolar, hyperfine and spin-lattice relaxation were shown to be less important in  $\text{NaV}_2\text{O}_5$  ([Yamada'98, Zvyagin'01, Hemberger'98]). The anisotropic Zeeman-effect is not relevant, because of nearly equivalent  $g$  tensors for all vanadium sites. Therefore, only two sources remain to account for the broadening of the ESR spectra in  $\alpha'$ - $\text{NaV}_2\text{O}_5$  – the symmetric anisotropic exchange (AE) and the antisymmetric Dzyaloshinsky-Moriya exchange (DM) interaction.

These contributions have been already estimated and discussed by Yamada *et al.* [Yamada'98] on the basis of the conventional approach suggested by Moriya [Moriya'60]. But in view of recent theoretical results [Choukroun'01, Oshikawa'02] discussed in section 2.3, such conventional estimations have to be taken with care. In particular, the DM interaction was found to produce a divergence in the temperature dependence of

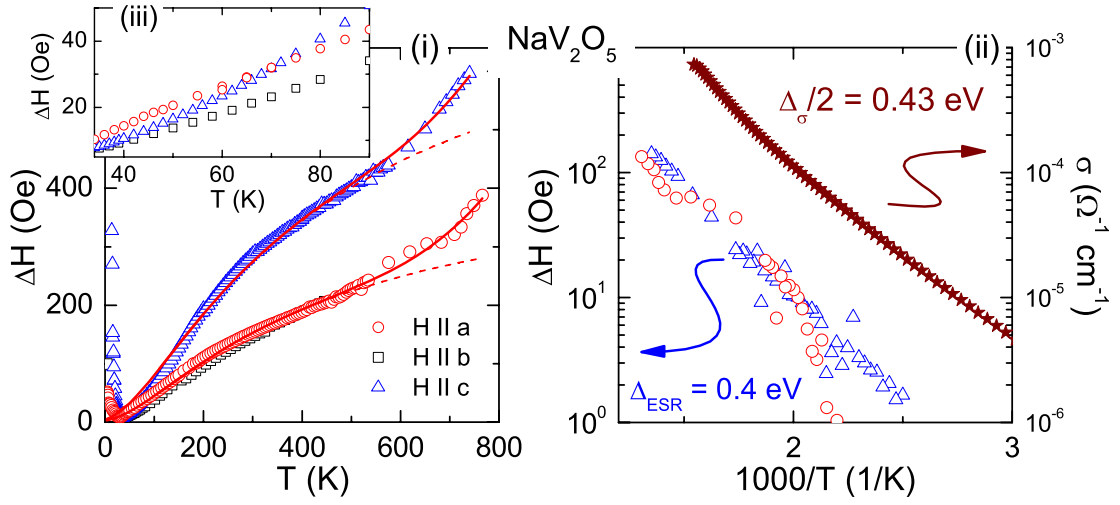


Figure 5.6.: (i): Temperature dependence of the ESR linewidth in  $\alpha'$ - $\text{NaV}_2\text{O}_5$ . The fit by Eq. (5.3) is shown by a solid red line, the  $\Delta H_{KvN}(T)$  contribution is emphasized by a dash line. (ii): Reduced contribution  $\Delta H_{\text{exp}}(T) = \Delta H(T) - \Delta H_{KvN}(T)$  compared to conductivity as Arrhenius plot. (iii): Inset emphasizes a crossover of  $\Delta H_a$  and  $\Delta H_c$  at low temperatures.

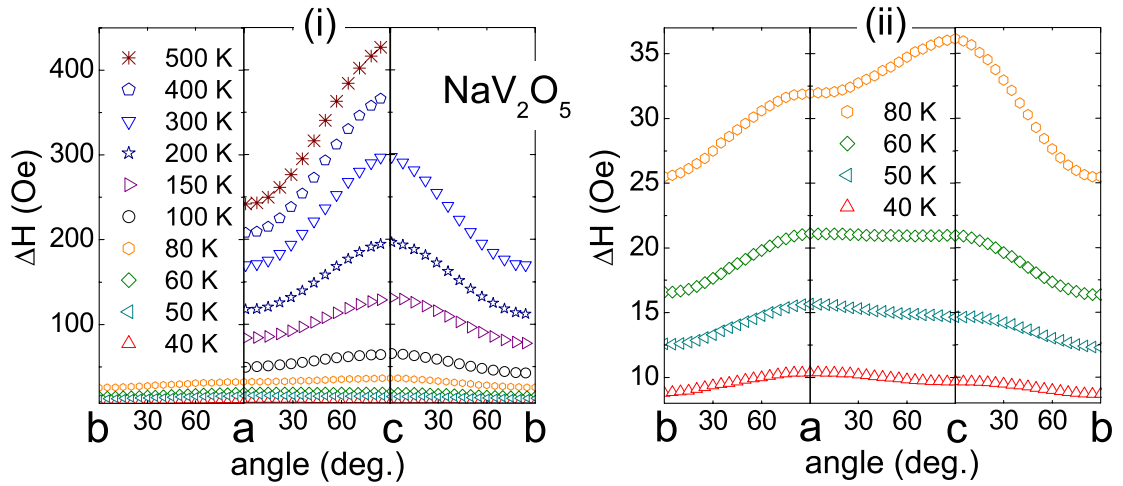


Figure 5.7.: Angular dependence of the ESR-linewidth in  $\alpha'$ - $\text{NaV}_2\text{O}_5$  at different temperatures.

the linewidth  $\Delta H_{\text{DM}} \propto T^{-2}$  for  $T \ll J/k_B$ . This is in contrast to the monotonic increase of  $\Delta H$  with increasing temperature in  $\text{NaV}_2\text{O}_5$ . Such a behavior, however, is in agreement with the theoretical expectation for a dominant AE [Oshikawa'02]. Experimental investigations of related compounds (see sections 4.5.3 and 5.3.2) corroborate this expectation, too. In the following we will provide detailed microscopical estimations of this term in  $\alpha'$ - $\text{NaV}_2\text{O}_5$  and show that the angular and temperature dependencies of  $\Delta H$  can be completely described in terms of this relaxation mechanism, only.

### 5.3.1. Exchange Pathways

It is important to recall that  $\text{NaV}_2\text{O}_5$  contains quarter-filled spin-ladders where each rung consists of two vanadium ions sharing one electron. Hence, the ground-state wave function is built by the superposition of two neighboring  $3d_{xy}$  orbitals hybridized with the intermediate oxygen  $2p_y$  orbital on the same rung, as depicted in Fig 5.8(i). Note that the conventional AE processes shown in Fig. 2.12(i-iv) do not contribute to the symmetric anisotropic exchange within one ladder due to the orthogonality of the involved wave functions. Therefore we will concentrate now on 'ring-exchange' processes (Fig. 2.12(v,vi)), that involve exchange between orbital levels with the same symmetry. In particular, the superexchange between the ground states  $|\eta\rangle = c_l |d_{xy}\rangle - c_r |d_{xy}\rangle$  and  $|\zeta\rangle = c'_l |d_{xy}\rangle - c'_r |d_{xy}\rangle$  on the neighboring rungs A and A' is transferred via  $\pi$  bonds with the interconnecting oxygen  $2p_x$  orbitals, as it is illustrated in Fig. 5.8(i). Most relevant for the symmetric anisotropic exchange is the strong antiferromagnetic superexchange between the excited states  $|\varphi\rangle = c_l |d_{x^2-y^2}\rangle - c_r |d_{x^2-y^2}\rangle$  and  $|\theta\rangle = c'_l |d_{x^2-y^2}\rangle - c'_r |d_{x^2-y^2}\rangle$  transferred via  $\sigma$  bonds with the oxygen  $2p_y$  orbitals (Fig. 5.8(ii)). Here  $c_l$ ,  $c_r$  and  $c'_l$ ,  $c'_r$  denote the distribution coefficients of the wave functions for the left ( $l$ ) and right ( $r$ ) vanadium site on rung A and neighboring rung A', respectively.

Thus, the ring AE process in  $\text{NaV}_2\text{O}_5$  can be described as follows: The electron e.g. couples from the  $|\eta\rangle$  ground state to the  $|\varphi\rangle$  excited state via spin-orbit coupling  $\mathcal{H}_{\text{LS}}$  (Eq. 2.17) by  $l_z$ , is transferred ( $t'_\sigma$ ) to the excited  $|\theta\rangle$  state of the neighboring rung, couples via  $\mathcal{H}_{\text{LS}}$  to the corresponding  $|\zeta\rangle$  ground state and returns ( $t_\pi$ ) to the starting orbital. Due to the spin-orbit coupling between  $3d_{xy}$  and  $3d_{x^2-y^2}$  states via the  $z$  component of the orbital momentum  $\langle d_{x^2-y^2} | l_z | d_{xy} \rangle = -2i$ , the only non zero matrix element of the symmetric AE is given by

$$D_{zz}^{\text{intra}} = 8\lambda^2 \frac{t_\pi t'_\sigma}{\Delta_{x^2-y^2,xy}^2 \Delta_{AA'}} [c_l^* c'_l + c_r^* c'_r]^2. \quad (5.4)$$

Here '\*' denotes the complex conjugation. True to literature, the crystal field splitting amounts to about  $\Delta_{x^2-y^2,xy} \approx 0.36$  eV [Ohama'97, Mazurenko'02] and for the charge-transfer energy between neighboring rungs on finds  $\Delta_{AA'} = 3$  eV [Golubchik'97]. The hopping integral  $t'_\sigma$  between the excited states is difficult to estimate, but as a lower boundary one can approximate it by the hopping integral between the ground states

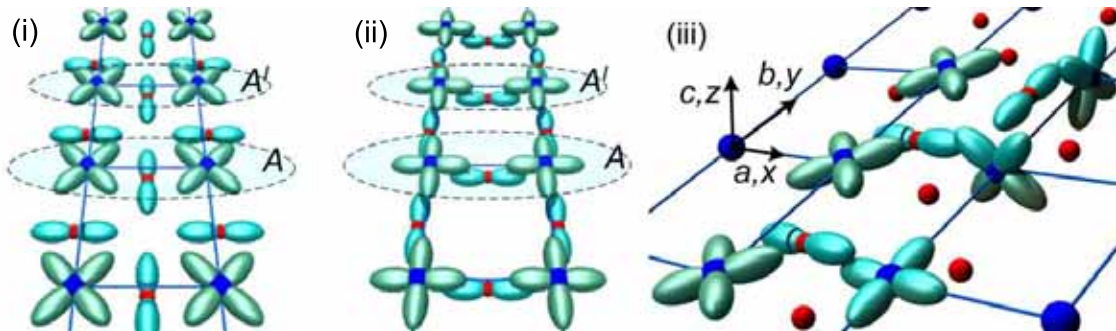


Figure 5.8.: Schematic pathways of the exchange coupling in NaV<sub>2</sub>O<sub>5</sub> (blue big spheres: V, red small spheres: O) *y* axis running along the chains. **(i)**: In the ground state the electron occupies the  $d_{xy}$  orbital. **(ii)**: Anisotropic spin-spin coupling via excited V  $d_{x^2-y^2}$  states. **(iii)**: Inter ladder coupling.

$t'_\sigma \approx t_\pi = 0.17$  eV [Smolinski'98]. Using the free ion value of the spin-orbit coupling  $\lambda = 31$  meV, one obtains  $D_{zz} \approx 0.6$  meV at high temperatures, where the electrons are equally distributed on each rung, i.e.  $c_l = c_r = 1/\sqrt{2}$ . This yields a characteristic linewidth of about  $\Delta H = 300$  Oe.

For the exact description of the data it was necessary to take into account the corrections due to the inter-ladder interactions. Possible exchange paths are shown in Fig. 5.8(iii). These exchange paths involve a 90°-bond geometry, which has been shown [Krug'02, Eremina'03] to produce sizable symmetric anisotropic exchange contributions, as well. For more detailed discussion of a 90°-exchange we refer to [Yushankhai'99, Tornow'99]. Considering all possible exchange paths, one obtains a maximum inter-chain *xx* component corresponding to an enhancement of the linewidth for the field applied along the crystallographic *a* direction. That allows to fit accurately the experimental data as we will show in the next chapter.

### 5.3.2. Symmetric Anisotropic Exchange in $\alpha'$ -NaV<sub>2</sub>O<sub>5</sub>

Having identified and estimated the source of the ESR line broadening in NaV<sub>2</sub>O<sub>5</sub>, we will now apply this model to the experimental data. The analysis of the angular dependencies in terms of second moments (Sec. 4.4.1) can be found in appendix C.

The leading *zz* diagonal element of the symmetric AE tensor gives rise to a 2:1 anisotropy with respect to the corresponding crystallographic *c* axis. Taking into account the corrections due to inter-ladder AE, we can fit the experimental angular dependencies of  $\Delta H$  (Fig. 5.9) deriving the ratio of two essential fit parameters  $D^{\text{inter}}/D^{\text{intra}}$  for the AE parameters between and within the ladders, respectively. Fig. 5.11 shows the temperature dependence of the ratio  $D^{\text{inter}}/D^{\text{intra}}$  together with the linewidth ratios  $\Delta H_a/\Delta H_c$ ,

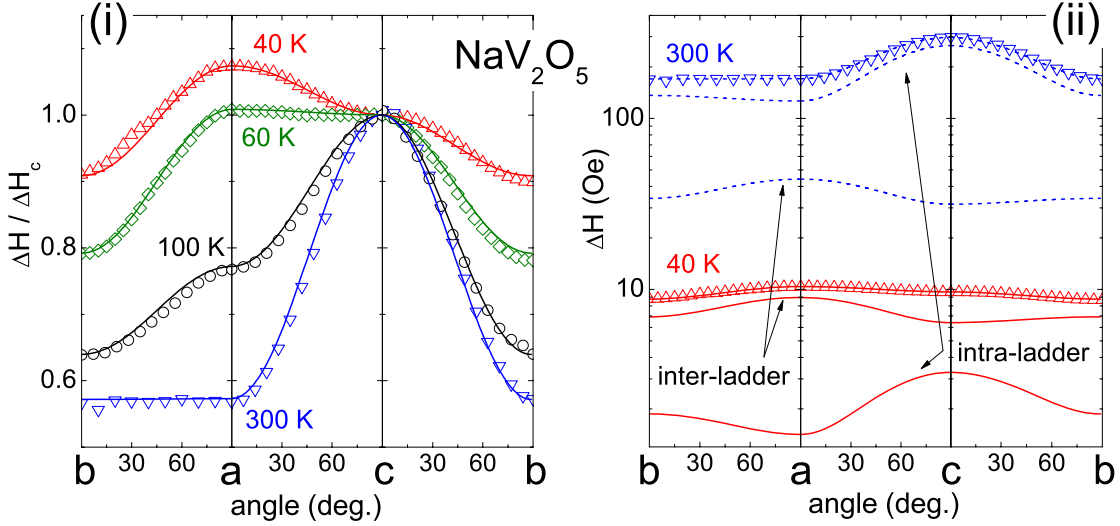


Figure 5.9.: Angular dependence of the ESR-linewidth at different temperatures. Fit curves (lines) are described in the text. **(i)**: Normalized to the linewidth for the magnetic field applied along the  $c$  axis. **(ii)**: Illustration of the contributions of intra- and inter-ladder AE to the linewidth far above (dashed blue line) and near  $T_{\text{CO}}$  (solid red line).

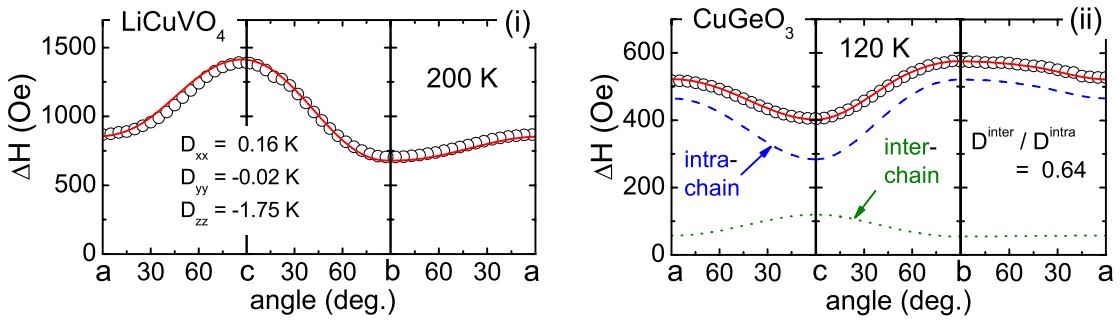


Figure 5.10.: Angular dependence of the ESR-linewidth in  $\text{LiCuVO}_4$  **(i)** and  $\text{CuGeO}_3$  **(ii)** described in terms of symmetric anisotropic exchange [Krug'02, Eremina'03]. The relevant parameters are indicated in the Figures.

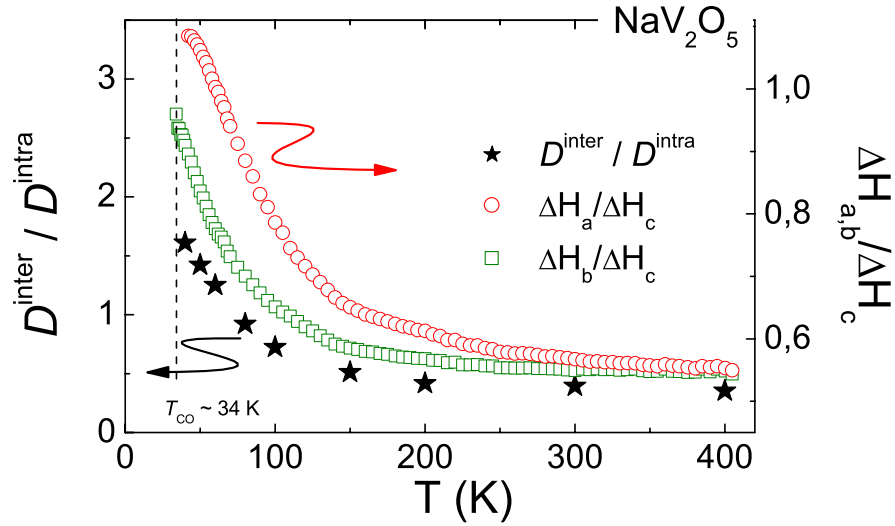


Figure 5.11.: Right ordinate: temperature dependence of the linewidth-ratio for the magnetic field applied along  $a$  or  $b$  axis normalized to  $\Delta H_c$ . Left ordinate: temperature dependent ratio of the inter- to intra-ladder AE constants obtained from the fitting of the angular dependencies of  $\Delta H$ .

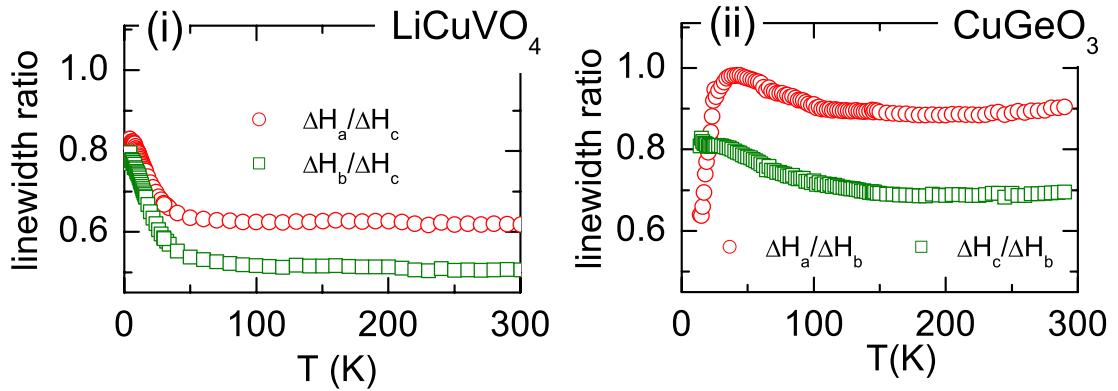


Figure 5.12.: Temperature dependence of the linewidth ratios in  $\text{LiCuVO}_4$  (i),  $\text{CuGeO}_3$  (ii) from [Krug'02, Eremina'03].

$\Delta H_b/\Delta H_c$  (remember that only the ratio of the exchange parameters can be determined from the ESR linewidth at temperatures  $T < J/k_B$  as discussed in Sec. 4.5.2). It can be clearly seen that at high temperatures ( $T > 150$  K) the dominant contribution to the line broadening is given by the intra-ladder AE. On decreasing temperature, below 150 K, the ratio strongly increases and the inter-ladder contribution becomes dominant. This can be understood taking into account the strong dependence of the AE parameters from the coefficients  $c_l, c'_l, c_r, c'_r$  which describe the electronic occupation on the vanadium sites. That means e.g. that for  $D^{\text{intra}} = D_{zz}$  (Eq. 5.4) the coefficient  $[c_l^*c'_l + c_r^*c'_r]$  is equal to 1 for the case  $V^{4.5+} - V^{4.5+}$ , and vanishes for the "zigzag" charge order ( $V^{5+} - V^{4+}$ ) realized below  $T_{\text{CO}}$ .

The observed increase of the  $D^{\text{inter}}/D^{\text{intra}}$  ratio already far above  $T_{\text{CO}}$  indicates that precursors of the developing CO set in at about 150 K, weakening considerably the intra-ladder AE. There are many evidences supporting this conclusion. In sections 5.1.2 and 5.1.3 we have shown that the elastic constants, the susceptibility, and the refractive index show an anomalous behavior already at  $T < 200$  K corresponding to the strong fluctuations in the system far above  $T_{\text{CO}}$ .

The experimentally observed linewidth is in good agreement with the theoretical prediction (5.4), as one can see in Fig. 5.9. But we would like to point out that the value of  $D_{zz} \approx 0.6$  meV may be somewhat overestimated because of the uncertainty in the used values of  $\Delta_{x^2-y^2,xy}$  and  $\Delta_{AA'}$ . Most likely, such a large linewidth results from the partly inhibited exchange narrowing in  $\text{NaV}_2\text{O}_5$ , as discussed in Sec. 4.5.1. This effect is typical for chain systems with small enough inter-chain exchange and produces a stronger broadening as compared to the predictions of the Kubo-Tomita theory. In any case, the conclusion concerning the temperature dependence of  $D^{\text{inter}}/D^{\text{intra}}$  ratio remains unchanged.

The dominance of AE in the ESR line broadening in spin chain systems is supported by the investigation of  $\text{LiCuVO}_4$  and  $\text{CuGeO}_3$ . These compounds show a similar temperature (Fig. 4.4) as well as angular dependence of the linewidth which can be accounted for using the same microscopical method as used before for  $\text{NaV}_2\text{O}_5$ . In [Krug'02] and [Eremina'03] all necessary calculations were done and it was concluded that ESR line broadening can be explained in terms of AE *only*. Two examples of angular dependencies of  $\Delta H$  with the corresponding fit curves are given in Fig. 5.10. The obtained ratios of exchange parameters and the reduced linewidths reflect the presence of fluctuations in the systems on approaching the phase transitions (Fig. 5.12), too. The estimations given in Sec. 4.4.2 and 5.3 and the similar behavior of spin relaxation on all of these compounds favor strongly a common relaxation source. In this respect  $\text{LiCuVO}_4$  plays a key role, because the DM interaction can be completely ruled out by its crystal symmetry. Therefore, we believe that the proposed symmetric anisotropic 'ring' exchange is the correct source of the immense ESR line broadening in  $\alpha'$ - $\text{NaV}_2\text{O}_5$ .

## 5.4. Summary

The anisotropy and temperature dependence of the resonance field and the width of the ESR absorption line have been investigated in the paramagnetic phase of  $\text{NaV}_2\text{O}_5$ . Analyzing the  $g$  tensor we calculated the crystal-field splittings of the  $\text{V}^{4+}$  ion and the covalence reduction of spin-orbit interaction in this system. Moreover, we have identified the symmetric anisotropic super-exchange to be the source of the immense ESR line broadening in  $\text{NaV}_2\text{O}_5$ . In this microscopic picture the dominant process consists of the simultaneous virtual hopping of electrons between the ground states and excited states of vanadium ions on neighboring rungs of the ladder involving the spin-orbit coupling on both rungs. This novel unconventional exchange process has not been considered in the discussion of ESR line broadening before. The corresponding AE parameter is found to be of the order of 1% of the isotropic exchange constant resulting in a high-temperature limit of the ESR linewidth of approximately  $10^2$  Oe. On the basis of this microscopic analysis we have shown that the ESR data can be entirely described in terms of the symmetric anisotropic exchange only. The temperature dependence of the linewidth and derived exchange parameters evidences the presence of charge fluctuations in  $\alpha'$ - $\text{NaV}_2\text{O}_5$  up to 150 K on a microscopic level.





## 6. Superexchange Competition in TiOCl

Recently, the fascinating system TiOCl came into focus as another possible candidate where orbital ordering induces a quasi-one-dimensional magnetic behavior and a spin-Peierls transition to a non-magnetic state below  $T_{c1} = 67$  K [Seidel'03]. Later on, this transition was shown to have a more complex nature. In particular, it is strongly affected by the frustrated interchain coupling, which also has to account for the first-order character of this phase transition and existence of strong fluctuations in the non ordered high-temperature phase [Hemberger'05]. This chapter concentrates on the spin relaxation mechanisms in this compound, which can be identified in the broad temperature region  $T_{c1} < T < 500$  K on the basis of ESR data.

### 6.1. Sample Characterization

Single crystals of TiOCl were prepared by chemical vapor transport. Based on the procedure described by Schäfer *et al.* [Schäfer'58], the parameters were optimized over a period of more than two years. It was found that the best results can be achieved using the starting reactants Ti, TiO<sub>2</sub> and TiCl<sub>4</sub> (acts also as a transport agent). The detailed data for temperature profiles and durations of the different transport stages can be found in [Hoinkis'07]. Typical dimensions of the obtained crystals are 4 mm×2 mm×0.1 mm. Very thin TiOCl crystals have a red color, whereas thicker ones appear black. The red color can be explained by the optical gap of  $\approx 2$  eV [Rückamp'05a]. The samples have been characterized with various experimental techniques (x-ray diffraction, scanning electron microscopy, energy dispersive x-ray analysis, Laue diffraction), evidencing the samples to be of the highest quality. Additionally, the quality of the crystals has been clearly confirmed by the susceptibility measurements which reveal a hysteresis at the first-order transition at  $T_{c1} = 67$  K which had not been reported previously (Fig. 6.3).

#### 6.1.1. Crystal Structure

The crystal structure of TiOCl belongs to the orthorhombic space group  $Pm\bar{m}n$  with  $a = 3.789(1)$  Å,  $b = 3.365(1)$  Å and  $c = 8.060(3)$  Å at room temperature. It consists of Ti-O bilayers within the  $(ab)$ -plane (see Fig. 6.1(ii)) [Beynon'93] that repeat in the  $c$  direction of the crystal. The bilayers are well separated by Cl ions mediating only a weak van der Waals interaction between successive bilayers. Within each bilayer, Ti and O form two layers of buckled chains, where Ti is always on the outer side with respect

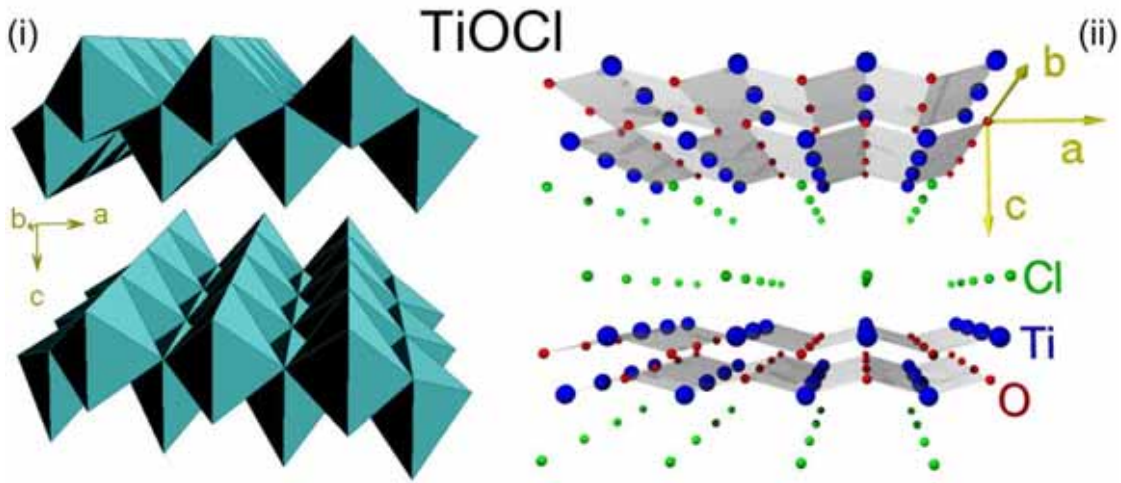


Figure 6.1.: Crystal structure of TiOCl at room temperature (space group  $Pnma$ ). Figure (i) displays the strongly distorted  $[\text{TiO}_4\text{Cl}_2]$  octahedra, Figure (ii) emphasizes the double  $[\text{TiO}]$ -layers in the  $(ab)$ -plane separated by Cl ions.

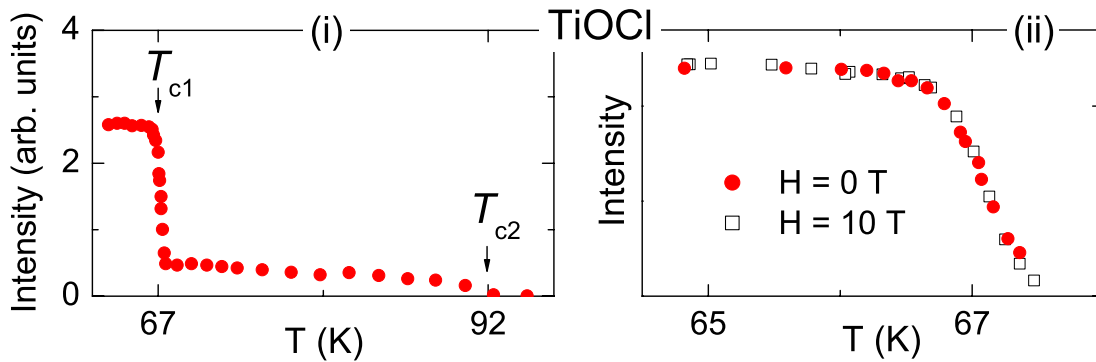


Figure 6.2.: (i): Intensities of the superlattice reflections showing up in TiOCl below  $T_{c2} \approx 92$  K observed by x-ray diffraction [Krimmel'06]. (ii): Temperature dependence of the intensity of the  $(0, 1.5, 0)$  superlattice reflection of TiOCl in the vicinity of the first phase transition around  $T_{c1} = 67$  K. Shown are measurements in a zero field (closed red circles) and in an external field of  $H = 10$  T (open black squares), respectively.

to the bilayer. The O-Ti-O bond angle is  $153^\circ$ . Each Ti ion is surrounded by a distorted octahedron of O and Cl ions (Fig. 6.1(i)). These octahedra are formed by two O ions belonging to the same Ti-O chain, two O ions belonging to neighboring chains, and two Cl which lie outside the bilayer. They are corner sharing in the  $a$  direction along the Ti-O-Ti chains and edge sharing in the  $b$  direction along the Ti-Ti chains.

At low temperatures a detailed single crystal x-ray diffraction study [Krimmel'06] observed a number of superlattice reflections along the chain direction  $(0, k + 0.5, 0)$  with  $k = 0, 1, 2$ . The strongest intensity was found for the  $(0, 1.5, 0)$ -reflection, which is characteristic for a doubling of the unit cell along the  $b$  axis. Fig. 6.2(ii) shows that the intensity of this reflection decreases strongly at  $T_{c1} = 67$  K evidencing the transition to be of first order. Above  $T_{c1} = 67$  K the  $(0, 1.5, 0)$ -reflection does not disappear (Fig. 6.2(i)), but splits into two incommensurate satellites, which can be monitored up to  $T_{c2} \approx 92$  K. Apart from the incommensurability, the structural modulation in the temperature region  $T_{c1} < T < T_{c2}$  is characterized by rather large displacements along the  $b$  axis and comparable small (about one order of magnitude weaker) amplitudes along the  $a$  axis. At  $T > T_{c2}$  the undistorted orthorhombic structure of the paramagnetic phase is completely recovered.

### 6.1.2. Magnetic and Thermal Properties

The high-temperature  $T > 130$  K part of the susceptibility data displayed in Fig. 6.3 can be fitted by a Bonner-Fisher-curve (Eq. 3.7), using the nearest-neighbor exchange  $J \approx 660$  K. That indicates the existence of one-dimensional spin-1/2 chains in TiOCl. By LDA+ $U$  and LDA+DMFT calculations it was concluded that the magnetic behavior is dominated by the direct exchange between Ti ions along the  $b$  axis and the interchain coupling effects mediated by oxygen ions along the  $a$  axis are likely to be weak [Seidel'03].

At  $T_{c1} = 67$  K a sharp drop in  $\chi(T)$  is clearly seen. In a picture based on one-dimensional spin chains, such a drop must be interpreted as a spin-Peierls transition (Sec. 3.1.1) into a nonmagnetic, dimerized ground state. This conclusion is strongly supported by the doubling of the unit cell along the  $b$  axis at  $T < T_{c1}$ . Moreover, a weak, but noticeable magnetic field effect found for this phase transition ( $\Delta T_{c1} = -0.13$  K in  $H = 10$  T [Krimmel'06]) is in accordance with the theoretical expectations.

On the other hand, the results of specific-heat measurements [Hemberger'05] depicted in Fig. 6.4 reveal that the entropy change  $\Delta S$  ( $\sim 0.01 R$ ) through this transition is surprisingly small. And also in itself the first order of the phase transition at  $T_{c1}$  contradicts with the conventional spin-Peierls scenario. In addition, a noticeable inflection point in the susceptibility and a peak in the specific heat at 91 K correspond to a second phase transition of second order, which forestalls the structural dimerization but carries the major part of the transition entropy. However, this entropy contribution  $\Delta S \sim 0.12 R$  is still vanishingly small compared to  $R \ln 2$  expected for a spin  $S = 1/2$  system, indicating the existence of strong fluctuations in a broad temperature range. This conclusion is

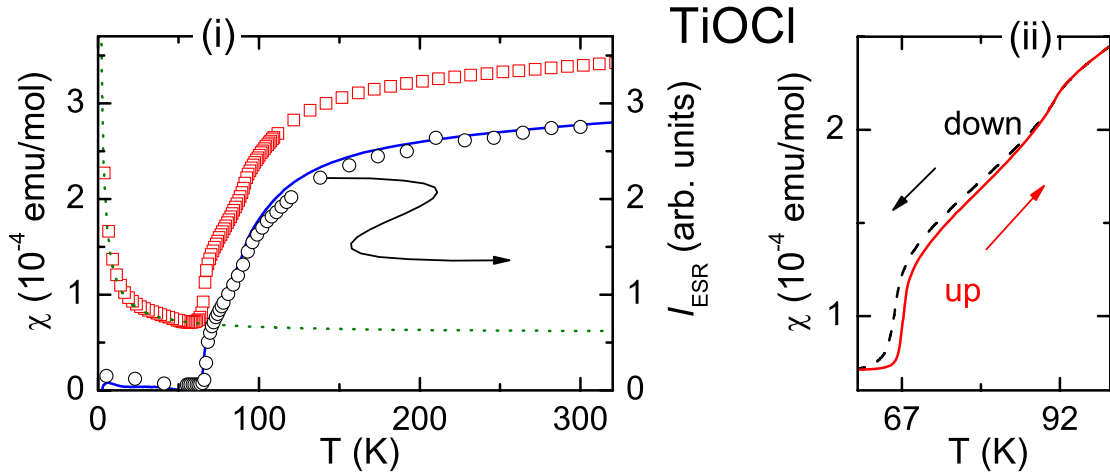


Figure 6.3.: Temperature dependence of the magnetic susceptibility of TiOCl measured by SQUID magnetometry compared to the intensity of the ESR signal. **(i)**: Raw data (red empty squares) and data (blue solid line) after subtraction of a constant offset and a Curie contribution (green dot line). The empty black circles are the  $I_{\text{ESR}}$ . **(ii)**: The cooling and heating curves without Curie subtraction in a reduced temperature range [Hoinkis'05].

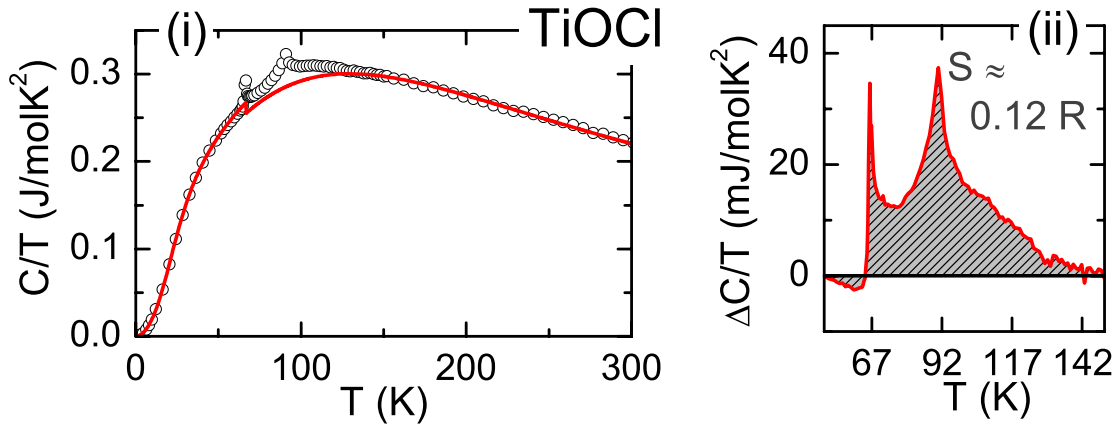


Figure 6.4.: Heat capacity of TiOCl, plotted as  $C/T$  versus  $T$ . **(i)**: Experimental data and fit of specific heat taking into account the spin- as well as the phonon contributions. **(ii)**: Difference between calculated and measured heat capacities. The area under the curve corresponds to the released entropy [Hemberger'05].

supported by Raman, NMR and infrared spectroscopy measurements discussed in the next chapter.

### 6.1.3. Fluctuations in the High-Temperature Phase

Fig. 6.5(i) shows that the temperature dependence of the phonon-mode parameters extends over a broad temperature range well above  $T_{c1}$  [Caimi'04]. The overall temperature dependence mainly develops below 200 K and tends to saturate below 100 K, indicating the presence of an extended fluctuation regime, which has been recognized in NMR data [Imai'03], as well.

The relaxation rates of  $^{35}\text{Cl}$  sites show dynamic lattice distortion with onset at 200 K, while for the  $^{46,49}\text{Ti}$  sites,  $1/T_1T$ , which probes the spin degrees of freedom, forms a maximum at about  $T^* = 135$  K (Fig. 6.5(ii)). Therefore, the interplay between the lattice and spin degrees of freedom must be already taking place at high temperatures. The temperature dependence of  $1/T_1T$  implies a pseudogap phase in the homogeneous state of the spin system with an estimated pseudogap  $\Delta_{\text{fluct}}^{(\text{NMR})}/k_B \approx 430$  K.

Additionally, the depletion of spectral weight over an energy range of the order of 400 K is very much reminiscent of a similar behavior in the Raman spectra, occurring over the same energy interval with decreasing temperature and associated with the spin-gap opening [Lemmens'04]. The resulting spin gap  $\Delta_{\text{fluct}}^{(\text{optic,Raman})}/k_B \approx 215$  K corresponds to the reduced gap ratio  $2\Delta/k_B T \sim 4.6$  and  $6.7$  for  $T_{c2}$  and  $T_{c1}$ , respectively. With respect to the mean field result 3.53 (Eq. 3.5), they are more reasonable than those obtained from NMR measurements.

Summing up, TiOCl does not display a canonical spin-Peierls behavior. Two distinct phase transitions and an incommensurate phase at intermediate temperatures arise in this structure as a result of frustration between a spin-Peierls pairing on chains of Ti atoms as driving force and elastic coupling between neighboring chains mediated by the oxygen atoms [Rückamp'05b, Schönleber'06]. The major part of the transition entropy is, however, released at higher temperatures. Strong short-range ordering fluctuations persisting in the high-temperature phase affect the magnetic, thermal and electrodynamic properties considerably already below 200 K.

## 6.2. ESR in TiOCl

The early ESR study in TiOCl [Kataev'03] revealed a strongly exchange-narrowed resonance line with  $g_{\text{eff}} \sim 2$  and suggested that there might be significant changes in the splittings of the  $d$ -orbitals between  $T_{c2}$  and room temperature, based on the temperature dependence of the anisotropic  $g$ -values.

In contrast, significant orbital fluctuations have been discarded by optical spectroscopy studies and polarization dependent ARPES measurements as discussed previously. There-

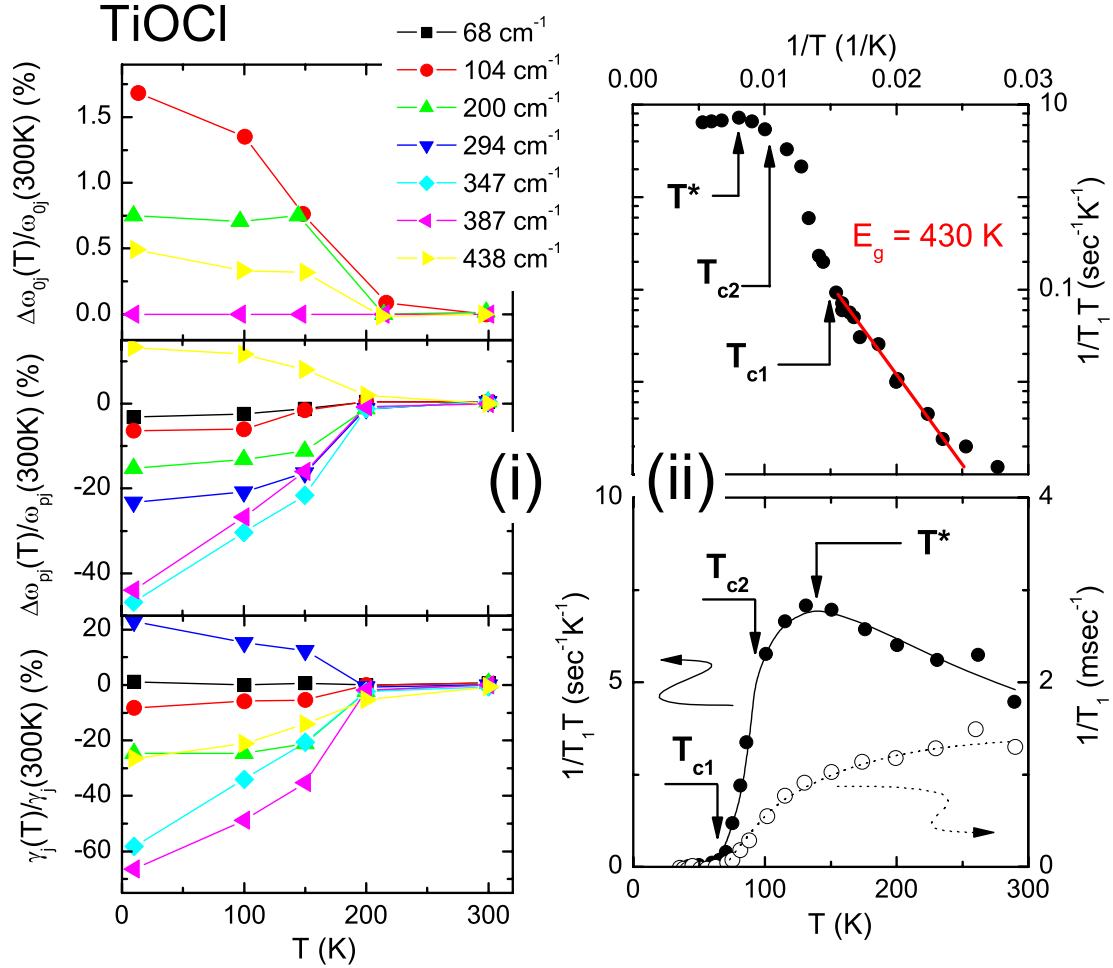


Figure 6.5.: (i): Temperature dependence along the  $a$  axis of the change with respect to 300 K for the resonance frequencies  $\omega_{0j}$  (upper frame), the oscillator strengths  $\omega_{pj}$  (middle frame), and the dampings  $\gamma_j$  (lower frame) of the phonon modes in TiOCl (identified in the legend by their respective resonance frequency in cm<sup>-1</sup>) [Caimi'04]. (ii): (lower frame)  $1/T_1$  (empty circles) and  $1/T_1T$  (filled circles) at <sup>47,49</sup>Ti sites of TiOCl measured by NMR. Solid and dashed curves are guides for eyes,  $T^* \approx 135$  K. (upper frame) The same  $1/T_1T$  data plotted in a semi-log scale. Solid line is an exponential fit with the activation energy  $E_g = 430$  K [Imai'03].

fore using ESR we reinvestigated TiOCl in detail and found temperature-independent  $g$  values up to room temperature. Moreover, we will discuss possible spin relaxation processes in this compound and analyze the temperature and angular dependence of the ESR linewidth in terms of the anisotropic exchange interactions.

### 6.2.1. Resonance Spectra and Absorption Intensity

ESR spectra obtained for TiOCl in the paramagnetic regime at different temperatures are displayed in Fig. 6.6. The spectra consist of a broad, exchange-narrowed resonance line, which is well fitted by a single Lorentzian line shape.

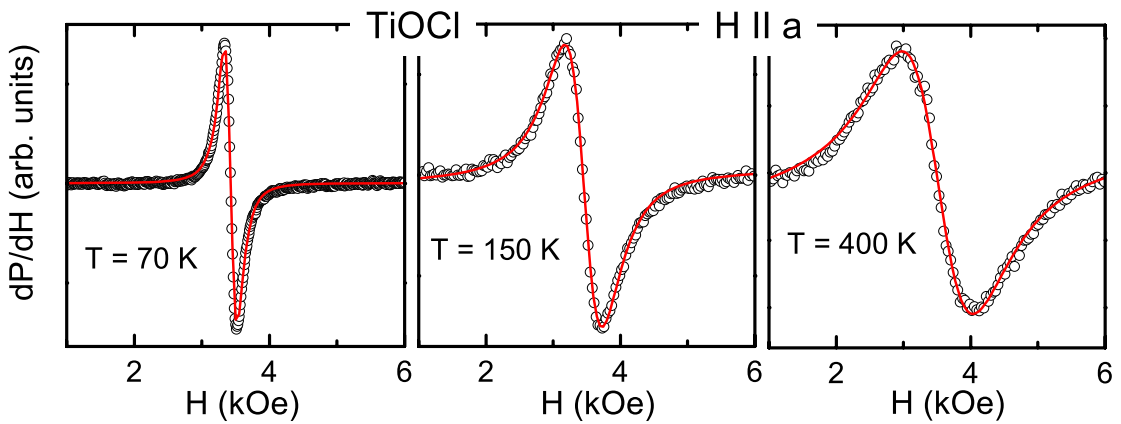


Figure 6.6.: Temperature evolution of the ESR spectrum in TiOCl for  $H \parallel a$ . Solid lines represent fits using a Lorentzian line shape.

The temperature dependence of the intensity of the ESR signal  $I_{\text{ESR}}$  is shown in Fig. 6.3(i). It is proportional to the static susceptibility (Sec. 4.2.3) and, hence, exhibits also the sharp drop at  $T_{c1}$  and the kink at  $T_{c2}$ . Note that in contrast to the static spin susceptibility  $\chi$ , the ESR signal does not contain temperature independent van Vleck contributions, showing directly the system to be non-magnetic below  $T_{c1}$ .

### 6.2.2. $g$ -Factor and ESR Linewidth

The temperature dependent ESR linewidth  $\Delta H$  at X- and Q-band frequencies is depicted in Fig. 6.7(i). It shows an anisotropic behavior with the external magnetic field  $H$  applied along the three crystallographic axes of the orthorhombic structure. Above  $T \simeq 90$  K both data sets almost coincide and the linewidth is largest when  $H \parallel a$  while the values for  $H \parallel b$  and  $H \parallel c$  are almost equal. The linewidth increases monotonously for all three directions for  $T > T_{c2}$ , however, a peculiar change from a negative to positive curvature is observed at about 250 K. Below  $T \simeq 90$  K there is a crossover of the linewidth



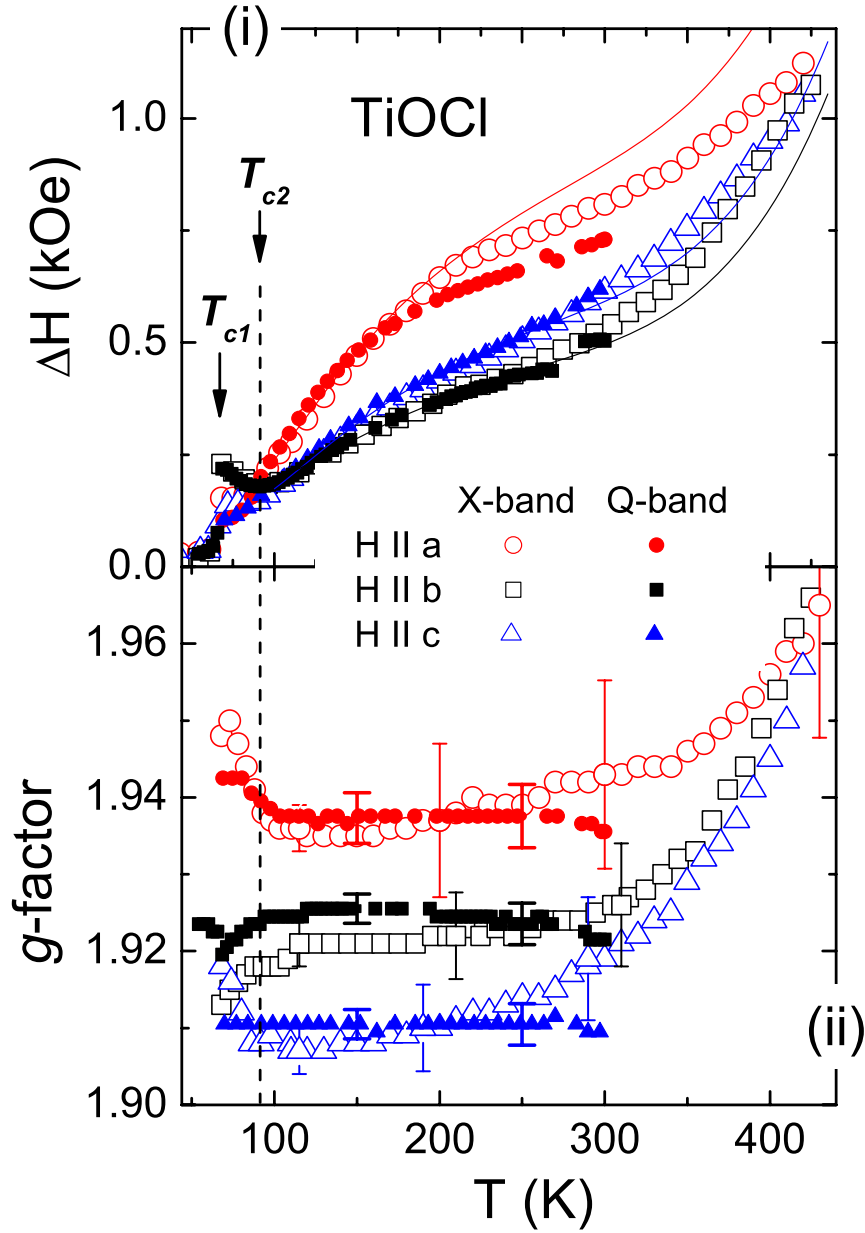


Figure 6.7.: ESR linewidth (i) and  $g$ -factor (ii) as a function of temperature for the magnetic field applied along the three crystallographic axes measured at X-band ( $\nu \approx 9.34$  GHz, the empty large symbols) and at Q-band frequency ( $\nu \approx 34$  GHz, the filled small symbols). The lines in panel (i) represent a fit by Eq. (6.9) using parameters listed in Table 6.3, the error bars in panel (ii) are given assuming the uncertainty in the resonance field as 5% of the linewidth.

data resulting in the broadest spectra for  $H\parallel b$ . Possible reasons for this effect as well as for discrepancies between X- and Q-band data will be discussed in section 6.4 in detail. On approaching the first-order transition at  $T_{c1}$ , the linewidth for all directions drops down to a value of about 50 Oe. This corresponds to the residual signal due to paramagnetic impurities which will not be further discussed. Focusing on the high-temperature behavior above 250 K we find that the anisotropy of the linewidth becomes smaller and vanishes at about 430 K.

Notably, at the same temperature the anisotropy of the effective  $g$ -factor at the X-band frequency vanishes, too (see Fig. 6.7(ii)), and we obtain  $g(430\text{ K}) \sim 1.96$  for all three directions. Concomitantly with the change of curvature of the linewidth at 250 K the temperature dependencies of the  $g$ -factor show a steep increase above 250 K, while the  $g$ -tensor is nearly constant in the temperature range  $T_{c2} < T < 250\text{ K}$ . Measurements in Q-band confirmed these findings showing an almost temperature independent  $g$  tensor below room temperature. This behavior differs from previously published results where a much larger and temperature dependent anisotropy of the  $g$ -factor was reported for  $T_{c2} < T < 300\text{ K}$  and interpreted in terms of changes of the energy splittings [Kataev'03]. Unfortunately, no spectra were shown in [Kataev'03], making it difficult to judge where this discrepancy comes from, especially, because the spectra were fitted with a single Lorentzian line shape in both cases.

Concerning the uncertainty of the obtained  $g$ -values, one has to take into account the strong increase of the linewidth with temperature, because the uncertainty of the  $g$ -value becomes larger as the order of magnitude of the linewidth becomes comparable to the resonance field of the ESR spectrum (see e.g. [Deisenhofer'02, Deisenhofer'03]). Therefore, we assume the uncertainty in the resonance field as 5% of the linewidth and obtain the error bars shown in Fig. 6.7(ii). Correspondingly, the uncertainty at the frequency  $\nu \approx 34\text{ GHz}$  is about three times smaller. Despite these error bars our  $g$ -values at room temperature  $g_a = 1.937$ ,  $g_b = 1.923$ , and  $g_c = 1.910$  differ considerably from the ones presented in [Kataev'03]. Here, we would like to emphasize that we investigated several samples, which were shown to be of very high-quality by clearly revealing the hysteresis at  $T_{c1}$  in the magnetic susceptibility.

Note that the largest discrepancy for the  $g$ -values is found for  $g_a$ , i.e. with the external field applied along the  $a$ -axis. Interestingly, for this case there is also a slight deviation in the temperature dependence of  $\Delta H_a$  in comparison to our data, suggesting that  $\Delta H_a \simeq \Delta H_b$  at room temperature, which we can exclude from our data. Hence, the given error for the  $g$ -value in [Kataev'03] might have been somewhat underestimated. Moreover, none of the calculated sets of  $g$ -values obtained by using an angular overlap model could reproduce  $g_a = 2.01$  from [Kataev'03], while the corresponding orbital energy levels seem to be in agreement with optical data [Rückamp'05b]. Instead, the values obtained from the AOM in case of isotropic  $\pi$ -interaction (model A in [Kataev'03]) describe our  $g$ -values very nicely. Therefore, we conclude that our  $g$ -factors correctly reflect the properties of TiOCl and exclude relevant changes in the crystal-field splitting

## 6. Superexchange Competition in TiOCl

Table 6.1.: Left column: Observed and calculated  $g$  tensors. Right column: Relative energies of the  $d$  orbital states in [eV] calculated by means the AOM model ( $E_{\text{AOM}}$ ), using the LDA ( $E_{\text{LDA}}$ ) [Saha-Dasgupta'04, Leonov'PR] and cluster approximations ( $E_{\text{clust}}$ ), as well as the point-charge model ( $E_{\text{pc}}$ ) [Rückamp'05a]. Experimentally ( $E_{\text{optic}}$ ) only the energies of the  $d_{x^2-y^2}$  and  $|+\rangle \equiv (d_{xz} + d_{yz})/\sqrt{2}$  levels can be determined [Rückamp'05a].

Experiment		AOM	Orbital	$E$	$E_{\text{AOM}}$	$E_{\text{clust}}$	$E_{\text{LDA}}$	$E_{\text{pc}}$	$E_{\text{optic}}$
			$d_{3z^2-r^2}$	-	<b>2.80</b>	2.11	2.27	1.28	-
$g_a$	1.937(4)	1.9366	$d_{x^2-y^2}$	$\Delta_0$	<b>1.41</b>	1.24	1.73	0.34	<b>1.5</b>
$g_b$	1.925(3)	1.9252	$ +\rangle$	$\Delta_2$	<b>0.70</b>	0.69	0.59	0.68	<b>0.65</b>
$g_c$	1.910(3)	1.9098	$ -\rangle$	$\Delta_1$	<b>0.38</b>	0.25	0.22	0.39	-
			$d_{xy}$	0	<b>0</b>	0	0	0	<b>0</b>

up to room temperature. This is in agreement with direct optical measurements of the  $d$ -level splittings [Rückamp'05a] and the fact that x-ray diffraction measurements did not detect significant changes of the crystal structure with temperature [Shaz'05].

With regard to the increase of the  $g$ -values towards higher temperatures one has to take into account the larger uncertainty due to the broadening of the line. In principle, however, such a shift could indicate a change of the local structure of the  $\text{TiO}_4\text{Cl}_2$ -octahedra. To decide about this possibility, additional structural investigations for  $T > 300$  K are desirable.

### 6.3. Crystal-Field Splittings of $\text{Ti}^{3+}$

Recalling the above discussion about the increase of uncertainty in the  $g$ -values with increasing temperatures (see Fig. 6.7(ii)), we will restrict the following evaluation to the  $g$ -values  $g_a = 1.937(4)$ ,  $g_b = 1.925(3)$ , and  $g_c = 1.910(3)$  obtained below room temperature at Q-band frequency. Note that the absence of any significant temperature dependence of the  $g$ -factor up to room temperature allows to apply the following results in this temperature range with good accuracy.

Table 6.2.: AOM parameters for the  $\text{TiO}_4\text{Cl}_2$ -octahedron in TiOCl. The bounding parameters  $e_{\sigma,\pi}$  are given in the units of [ $10^3 \text{ cm}^{-1}$ ].

$\lambda$ [ $\text{cm}^{-1}$ ]	$e_{\sigma}(\text{O}_1)$	$e_{\pi}(\text{O}_1)$	$e_{\sigma}(\text{O}_2)$	$e_{\pi}(\text{O}_2)$	$e_{\sigma}(\text{Cl})$	$e_{\pi}(\text{Cl})$	$k_x$	$k_y$	$k_z$
175	13	3.25	6.5	1.625	5	1.25	0.70	0.84	0.87

To analyze our experimental  $g$ -factors, we can again use the angular overlap model (App. B). Each  $Ti^{3+}(3d^1)$  ion is surrounded by two chlorine and four oxygen ions, building an octahedron with a strong contraction along the  $a$ -axis. According to [Schäfer'58], there are three different bond lengths: the  $Ti-O_1$  bond along the  $a$  axis  $n_{O_1} \simeq 1.95 \text{ \AA}$ , the second  $Ti-O_2$  bond in the  $(bc)$ -plane  $n_{O_2} \simeq 2.25 \text{ \AA}$  and the  $Ti-Cl$  bond in the same plane  $n_{Cl} \simeq 2.37 \text{ \AA}$ . Therefore, all other bounding parameters can be connected to the  $e_\sigma(O_1)$  as follows:

$$\begin{aligned} e_\sigma(O_2) &= \left(\frac{2.25}{1.95}\right)^{-5} e_\sigma(O_1) \approx 0.50 \cdot e_\sigma(O_1), & e_\pi(O_2) &= \frac{e_\sigma(O_2)}{4} \approx \frac{e_\sigma(O_1)}{8}, \\ e_\sigma(Cl) &= \left(\frac{2.37}{1.95}\right)^{-5} e_\sigma(O_1) \approx 0.38 \cdot e_\sigma(O_1), & e_\pi(Cl) &= \frac{e_\sigma(Cl)}{4} \approx \frac{e_\sigma(O_1)}{10}, \end{aligned}$$

and  $e_\pi(O_1) = e_\sigma(O_1)/4$ . Taking additionally into account the covalency of Ti-ligand bonds (see Table 6.2 for the used fit parameters), we are able to reproduce very well the observed anisotropy of the  $g$  tensor. The results are listed in Table 6.1 together with the predictions made in terms of the LDA+ $U$  [Saha-Dasgupta'04, Leonov'PR], the cluster and the point-charge models [Rückamp'05a]. These calculations can be compared to the experimental results obtained by optics measurements [Rückamp'05a] given in Table 6.1 as well. Two absorption peaks at  $\Delta_2 = 0.65(\pm 0.15) \text{ eV}$  and  $\Delta_0 = 1.5(\pm 0.1) \text{ eV}$  seen in those measurements were attributed to orbital excitations into the  $|+\rangle \equiv (d_{xz} + d_{yz})/\sqrt{2}$  and  $d_{x^2-y^2}$  levels, respectively.

While the energies of the transitions to the second and third excited levels can be experimentally detected, the transition to the first excited state is not directly infrared-active. But its energy is critical in order to determine, whether orbital fluctuations are a correct explanation for the interesting physics observed in  $TiOCl$ . Therefore, it is important to know the uncertainty of the calculated value  $\Delta_1^{(AOM)} = 0.38 \text{ eV}$ . In particular, because the used AOM approximation does not take properly into account the anisotropy of orbital reduction (given by the parameters  $k_i$ ) in the calculation of energy levels.

In order to do so, let us use a more simple schema and consider the local environment of the  $Ti^{3+}$  ion as a  $TiO_4Cl_2$ -octahedron with a strong tetragonal distortion along the  $a$ -axis. Then we can express the  $g$  value parallel ( $g_{\parallel}$ ) and perpendicular ( $g_{\perp}$ ) to the direction of tetragonal distortion as follows [Abragam'70]:

$$g_{\parallel} = 2 - 8 \frac{\lambda_{\parallel}}{\Delta_0}, \quad g_{\perp} = 2 - 2 \frac{\lambda_{\perp}}{\Delta'}. \quad (6.1)$$

Here  $\lambda_{\parallel}$  ( $\lambda_{\perp}$ ) and  $\Delta_0$  ( $\Delta'$ ) denote the spin-orbit (SO) coupling parameter and the relevant crystal-field splitting, respectively, for the magnetic field applied parallel (perpendicular) to the  $a$ -axis.

Identifying the experimental value of  $g_a$  with  $g_{\parallel} = 1.937(4)$  and substituting  $\lambda_{\parallel}$  by the isotropic free-ion value  $\lambda_{\text{fi}}/k_{\text{B}} = 224$  K for  $\text{Ti}^{3+}$  [Abragam'70], we derive the energy splitting between the ground state and the  $d_{x^2-y^2}$  level to be  $\Delta_0 = \Delta_{x^2-y^2} \approx 2.4(2)$  eV.<sup>1</sup> In comparison to the value  $\Delta_{x^2-y^2}^{(\text{opt})} = 1.5$  eV obtained by optical measurements [Rückamp'05a] the value derived from our  $g$ -factor is too large. Therefore, we have to take into account a covalence reduction of the spin-orbit coupling  $\lambda_{\parallel}$  [Abragam'70]. To estimate the reduction factor we use the experimental value  $\Delta_{x^2-y^2}^{(\text{opt})}$  and obtain  $\lambda_{\parallel}/k_{\text{B}} \simeq 140$  K for TiOCl, considerably smaller than the free-ion value  $\lambda_{\text{fi}}$  but in agreement with literature [Abragam'70, Kataev'03]. This large splitting allows to discard the scenario of  $d_{x^2-y^2}$  being the first excited state approximately 0.34 eV above the ground state (point-charge model), in favor of cluster calculations predicting the first excited state to be  $|-\rangle \equiv (d_{xz} - d_{yz})/\sqrt{2}$  [Kataev'03, Rückamp'05a].

To obtain lower and upper limits for the energy splittings, we can use  $\lambda_{\perp} = 140$  K and the free ion value  $\lambda_{\text{fi}} = 224$  K for the magnitude of SO coupling within the  $(bc)$ -plane. Starting with  $\lambda_{\perp} \equiv \lambda_{\parallel} = 140$  K and  $g_{\perp} = (g_b + g_c)/2 \approx 1.918(10)$  we derive  $\Delta'_{\lambda_{\parallel}} \approx 0.3$  eV for the energy splitting of the doublet  $d_{xz}, d_{yz}$  with respect to the ground state. In the real structure this doublet splits into the lower antisymmetric  $(d_{xz} - d_{yz})/\sqrt{2} \equiv |-\rangle$  (energy  $\Delta_1$ ) and higher symmetric  $(d_{xz} + d_{yz})/\sqrt{2} \equiv |+\rangle$  (energy  $\Delta_2$ ) state. Using  $2/\Delta' = 1/\Delta_1 + 1/\Delta_2$  and the experimental value  $\Delta_2 = 0.65(\pm 0.15)$  eV [Rückamp'05a], we finally obtain the lower limit  $\Delta_1^{(\lambda_{\parallel})} = 0.2(1)$  eV. Analogously, we derive the upper limit  $\Delta_1^{(\lambda_{\text{fi}})} = 0.4(1)$  eV, narrowing down the energy of the first excited state to  $\Delta_1 = 0.2 - 0.4$  eV. This is in good agreement with the other theoretical estimates listed in Table 6.1.

Thus, by means of ESR we can exclude the degeneracy of the first and second excited states in TiOCl, as indicated by band-structure results [Seidel'03, Saha-Dasgupta'04], corroborating the results obtained by optics and ARPES measurements [Rückamp'05a, Hoinkis'05].

## 6.4. Spin Relaxation in TiOCl

Having identified the character and splitting of the ground and low lying excited states via the  $g$ -factors, we will now discuss the angular and temperature dependence of the linewidth above  $T_{c1}$ , which provides information on the microscopic spin dynamics involving these energy levels. The behavior of the ESR linewidth in TiOCl can be clearly divided into the three regimes  $T < 90$  K,  $90$  K  $< T < 250$  K, and  $T > 250$  K. In the temperature range  $T_{c1} < T < 90$  K the linewidth is almost constant (for  $H \parallel a, c$ ) or decreases (for  $H \parallel b$ ) on increasing temperature. This behavior changes at about 90 K

---

<sup>1</sup> The local coordinate frame  $\{xyz\}$  is chosen so that  $z \parallel -a$ , and the  $x$  and  $y$  axes are rotated by  $45^\circ$  with respect to the  $c$  and  $b$  axis, respectively (Fig. 6.8).

together with a change of the linewidth anisotropy (see Fig. 6.11) to the monotonous increase for all directions. At high temperatures  $T > 250$  K a strong additional increase of  $\Delta H(T)$  dominates this saturation behavior (see Fig. 6.10) and the anisotropy of the line vanishes (Fig. 6.7). We attribute these different regimes to the competition of relaxation mechanisms prevailing at different temperatures, which will be discussed in detail in the following. Generally, the important mechanisms for the ESR line broadening in low-dimensional strongly correlated spin systems have been discussed in section 4.4.2. Let us now single out and estimate the relevant interactions which drive the relaxation in TiOCl:

Single-ion anisotropy is absent for  $\text{Ti}^{3+}$  ( $S=1/2$ ). Other sources of line broadening such as dipolar interaction or hyperfine coupling are negligible as a result of the large isotropic exchange  $J/k_B = 660$  K. Taking into account the average distance between the Ti-ions of about  $3.355 \text{ \AA}$  [Shaz'05] and the value of the hyperfine constant  $A_{\text{Ti}^{3+}} = 6 \cdot 10^{-4} \text{ cm}^{-1}$  [Altshuler'64] we can estimate the contribution to the linewidth from these sources as  $10^{-1}$  Oe and  $10^{-5}$  Oe, respectively. A larger contribution to the ESR linewidth could be expected for the anisotropic Zeeman interaction in case of different  $\text{Ti}^{3+}$  sites in adjacent layers [Pilawa'97]. However, this broadening strongly depends on the value of the resonance field  $H_{\text{res}}$ . At X-band frequency used in our experiment ( $H_{\text{res}} \sim 3$  kOe) the resulting contribution is less than 1 Oe for any reasonable choice of parameters (e.g. an interlayer coupling  $J_{\text{inter}} \approx 0.05 \cdot J$  [Saha-Dasgupta'04] and  $\Delta g \sim 0.3$ ).

The remaining relevant contributions stem from the anisotropic exchange interactions. Conventional estimations [Moriya'60] of their magnitude result in values at least two order of magnitudes higher as for the other sources of line broadening. Note, however, that the applicability of such estimations for low-dimensional systems like TiOCl has been questioned, recently (Sec. 2.3). Hence, one has to analyze carefully these interactions in TiOCl on a *microscopic* level. In the following it will be done for symmetric as well as antisymmetric anisotropic exchange contributions.

### 6.4.1. Symmetric Anisotropic Exchange

In section 2.3.2 we have emphasized the importance of AE for low-dimensional systems. But in order to take properly into account this relaxation source one needs a careful analysis of both the exchange geometry and the energies of the involved orbital states.

Crystal-field splittings of the relevant excited states have been already estimated above (see Sec. 6.3) and in order to illustrate the exchange geometry via these orbital levels we show the charge-distribution pictures for the pathways of AE for the intra-chain and inter-layer exchange in Figs. 6.8(i) and 6.8(ii), respectively. The inter-chain AE within one layer is not effective here because of the orthogonality of the ground-state orbital with respect to the direction of the exchange.

In analogy to the estimations made for  $\text{NaV}_2\text{O}_5$  in Sec. 5.3.1 we argue that the pathways of AE shown in Fig. 6.8 are by far the most relevant ones. The first exchange

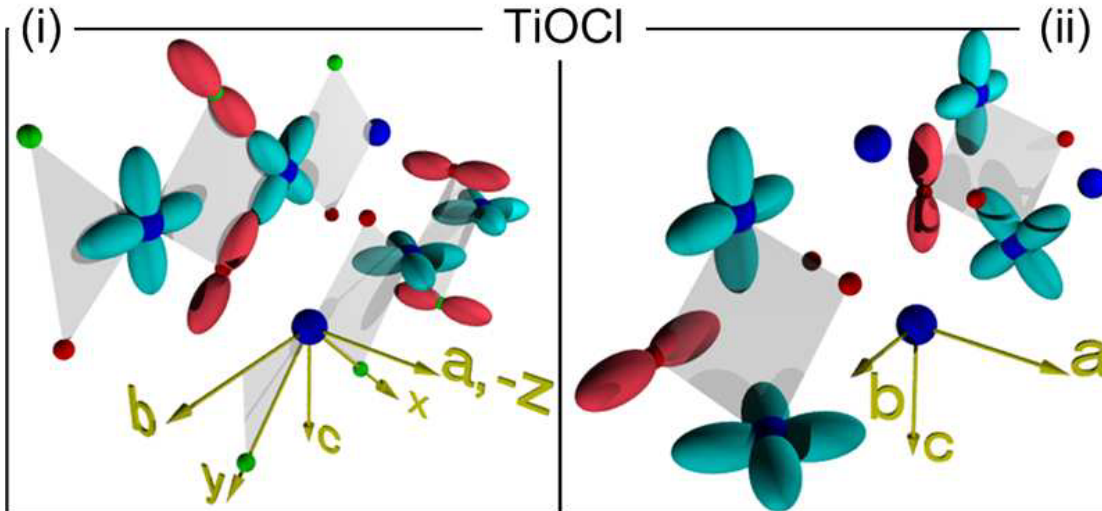


Figure 6.8.: Schematic pathway of the symmetric anisotropic exchange between Ti ions in TiOCl. Big blue spheres denote Ti ions, small red and green spheres – O and Cl ions, respectively. **(i)**: The most relevant intra-chain ( $\parallel b$ -axis) exchange paths. Left one – between the ground state  $d_{xy}$ -orbital on one site and the excited  $d_{x^2-y^2}$ -orbital on the other site, second one – between two excited  $|-\rangle$ -orbitals on both sites. **(ii)**: Two dominating exchange paths of the inter-chain AE between a Ti ion in the  $d_{xy}$ -state and the nearest-neighbor Ti ion from the adjacent chain in the excited states  $|-\rangle$  (left) or  $|+\rangle$  (right).

process between neighboring Ti ions in the chain (depicted at the left side of the panel (i)) with an electron transfer between  $d_{x^2-y^2}$  and  $d_{xy}$ -orbitals becomes important as a result of the strong  $\sigma$ -bonding between the titanium  $d$ - and the oxygen  $p$ -orbitals. The importance of the second intra-chain AE process (at the right side of the panel (i) of Fig. 6.8) via  $|-\rangle$ -orbitals is due to the small energy  $\Delta_1$  of the involved excited state. Note that only the exchange paths between the excited  $|-\rangle$ -states are shown in the second case, since the second path closing the exchange loop (see Fig. 2.12(v-vi)) is given by the hopping between the ground  $d_{xy}$ -orbitals with  $J/k_B \approx 660$  K. In Fig. 6.8(ii) the dominating exchange paths of the inter-layer AE are presented: the left one being between  $|-\rangle$  and  $d_{xy}$ -orbitals and the second between  $|+\rangle$  and  $d_{xy}$ -orbitals. These processes are of the same order of magnitude as the intra-chain exchange and cannot be neglected.

The non-zero elements of the exchange tensors can be determined via the spin-orbit operators included in this process (Sec. 2.3.2). For the first intra-chain AE process (via the  $d_{x^2-y^2}$ -orbital) the excited state is connected to the ground state  $d_{xy}$  of the same Ti ion via spin-orbit coupling with only one nonzero matrix element, namely

$\langle d_{x^2-y^2} | l_z | d_{xy} \rangle = -2i$ . Following Eq. (2.31), all AE processes via this level contribute to  $D_{zz}$  only. Taking now into account the relation for the diagonal components of the AE tensor  $\sum D_{\alpha\alpha} = 0$  (see Eq. 2.2) we obtain for this process

$$D_{zz}^{(x^2-y^2)} = -2D_{xx}^{(x^2-y^2)} = -2D_{yy}^{(x^2-y^2)}. \quad (6.2)$$

All other AE processes which make a considerable contribution to the linewidth in TiOCl involve the  $|-\rangle$  or  $|+\rangle$ -orbitals ( $|\pm\rangle \equiv \{d_{xz} \pm d_{yz}\}/\sqrt{2}$ ), which are connected to the ground state orbital  $d_{xy}$  via the matrix elements  $\langle d_{xz} | l_x | d_{xy} \rangle = i$  and  $\langle d_{yz} | l_y | d_{xy} \rangle = -i$ . The resulting nonzero elements  $D_{xx}$  and  $D_{yy}$  of the AE tensor have the same magnitude because of symmetry reasons and they have the same sign, because the expression for  $D_{\alpha\beta}$  (Eq. 2.31) depends on the square of the orbital momentum. Thus, we can write the AE tensor for these processes as  $D_{zz}^{(|-\rangle,|+\rangle)} = -2D_{xx}^{(|-\rangle,|+\rangle)} = -2D_{yy}^{(|-\rangle,|+\rangle)}$ . It becomes clear that the maximal component of the anisotropic exchange tensor is  $D_{zz}$ . Therefore, we would expect the maximal linewidth for  $H||z$  in agreement with the experimental data for  $T > 90$  K.

Consequently, we can describe the resulting angular dependence of  $\Delta H$  in terms of the moment method (see section 4.4.1 and appendix C.2)

$$\Delta H_{AE}(T, \theta) = \Delta H_{AE}(T)(1 + \cos^2\theta), \quad (6.3)$$

where  $\theta$  is the polar angle of  $H$  with respect to the  $a \equiv -z$  axis and  $\Delta H_{AE}(T)$  is proportional to the strength of the AE interaction. This parametrization does not allow to obtain the exact values of the anisotropic exchange parameters, but it is valid for all temperatures and, hence, we will apply it to describe our data using  $\Delta H_{AE}$  as a fit parameter.

Concerning the temperature dependence of the ESR linewidth produced by AE exchange interaction, clear theoretical predictions do only exist in two limiting cases:

- For the high-temperature regime  $T > J/k_B$ , the linewidth approaches the result of the Kubo-Tomita theory (Sec. 4.4.1)  $\Delta H_{AE}^{(T > J/k_B)}(T) \rightarrow \Delta H_{AE}(\infty) \propto D_{\alpha\beta}^2/J = \text{const}$ ,
- the result  $\Delta H_{AE}^{(T \ll J/k_B)}(T) \propto (\Delta H_{AE}(\infty)/J) \cdot T$  in the case  $T \ll J/k_B$  for the  $S = 1/2$  quantum antiferromagnetic chain (Sec. 4.5.2).

To model the crossover regime we will use the empirical expression (Eq. 4.28) which has already provided a successful description for several low-dimensional systems like  $\alpha'$ - $\text{NaV}_2\text{O}_5$  [Chapter 5],  $\text{CuGeO}_3$  [Eremina'03],  $\text{LiCuVO}_4$  [Krug'02] and  $\text{Na}_{1/3}\text{V}_2\text{O}_5$  [Heinrich'04]:

$$\Delta H_{AE}(T) = \Delta H_{AE}(\infty) \cdot e^{-\frac{C_1}{T+C_2}}. \quad (6.4)$$

Thus, the fit parameters to describe the contribution of the AE are  $\Delta H_{AE}(\infty), C_1, C_2$ .



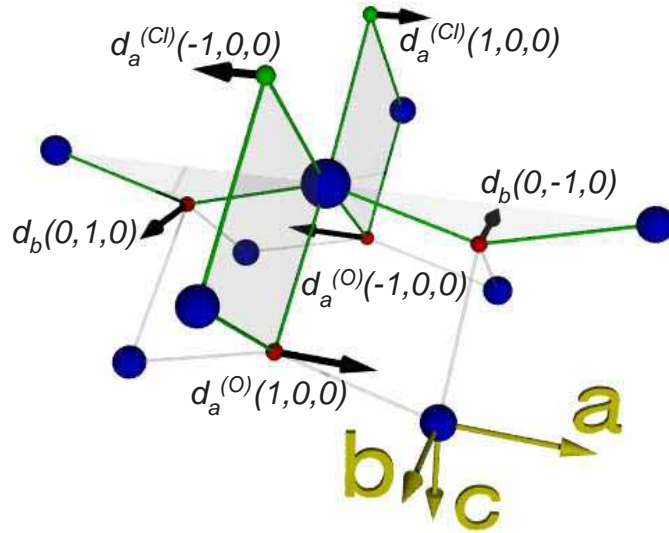


Figure 6.9.: Next-neighbor bonds of the Ti ion together with the associated parameters of the antisymmetric anisotropic exchange.  $d_b$ ,  $d_a^{(O)}$  and  $d_a^{(Cl)}$  denote the Dzyaloshinsky-Moriya parameters for the exchange along the  $a$ -axis, along the  $b$ -axis via the oxygen ion and along the  $b$ -axis via the chlorine ion, respectively. Components of the DM vectors are given in the depicted cartesian coordinate system  $\{a,b,c\}$ . Big blue spheres denote Ti ions, small red and green spheres – O and Cl ions, respectively.

#### 6.4.2. Dzyaloshinsky-Moriya Interaction

The contribution of the DM interaction to the ESR line broadening in one-dimensional systems is a heavily debated topic at the moment. The well-established approaches widely used in the 3D case fail apparently in the 1D spin systems. The right order of magnitude and the temperature dependence of this relaxation mechanism are of particular interest to understand the physics of many low-D compounds.

A general discussion of DM interaction can be found in section 2.3.1, and in that follows we will analyze its contribution into the ESR line broadening in TiOCl, using the structural data of Shaz *et al.* at room temperature [Shaz'05]. All next-neighbor bonds of the Ti ion together with the corresponding DM vectors are shown in Fig. 6.9. Only interactions of Ti ions in the same layer give rise to the antisymmetric exchange in TiOCl because of the existence of an inversion center between the Ti ions from adjacent layers. The two remaining contributions arise from the chains of the Ti ions along the  $b$  and  $a$  directions. The first one, which results in a component of  $\mathbf{d}$  in the  $a$  direction, has been considered in [Kato'05] as the dominating source of the line broadening. However, we would like to point out that there are two different bridging ions ( $\text{Cl}^-$  and  $\text{O}^{2-}$ ) leading

to DM vectors with opposite sign in this case. Although the two paths are asymmetric ( $n_{\text{Ti-Cl}} \simeq 2.393 \text{ \AA}$ ,  $n_{\text{Ti-O}} \simeq 2.187 \text{ \AA}$  at  $T = 295 \text{ K}$  [Shaz'05]) and, hence, lack inversion symmetry, one can assume that the opposite DM vectors will partially compensate each other. If we denote the respective DM parameters  $d^{(l)}$  as  $d_a^{(\text{O})}$  and  $d_a^{(\text{Cl})}$  for the exchange via the  $\text{O}^{2-}$  and  $\text{Cl}^-$  ions, respectively, only its difference  $\Delta d_a = d_a^{(\text{O})} - d_a^{(\text{Cl})}$  will give rise to the ESR line broadening and can be detected experimentally (see e.g. the discussion about the cancelation of DM interaction in  $\text{LiCuVO}_4$  [Krug'02]). Looking now at the contribution of the inter-chain DM interaction (between two neighboring  $\text{Ti}^{3+}$  sites along the  $a$  axis via the oxygen ion lying in the same ( $ac$ )-plane), we can conclude that the corresponding DM vector is pointed along the  $b$ -axis (see Fig. 6.9).

The general expression for the  $M_2$  due to the DM interaction is given in appendix C.1. In the case of TiOCl only two intra-chain and two inter-chain contributions must be taken into account by the calculation of the respective ESR line broadening. Estimation of the "geometrical factors"  $\mathbf{G}^{(l)} = [\mathbf{n}_{il} \times \mathbf{n}_{jl}]$  yields:

- (i) for the inter-chain exchange  $G_b^{(\text{O})} = \pm 0.501 \approx 1/2$ ,
- (ii)  $G_a^{(\text{O})} = \pm 0.98 \approx 1$  and  $G_a^{(\text{Cl})} = \pm 0.99 \approx 1$  for the intra-chain exchange via the  $\text{O}^{2-}$  and  $\text{Cl}^-$  ions, respectively.

Therefore, we obtain the following expression for the second moment of the DM interaction in the crystallographic system:

$$M_2^{DM}(\theta, \varphi) \propto (d_b \cdot 1/2)(1 + \sin^2\theta \cos^2\varphi) + (\Delta d_a \cdot 1)(1 + \cos^2\theta), \quad (6.5)$$

where  $\theta$  and  $\varphi$  are the polar and azimuthal angles of  $H$  with respect to the  $a$  axis. Finally, the ratios of the linewidth along the three crystallographic axes read

$$\begin{aligned} \Delta H_b : \Delta H_a : \Delta H_c &= M_2\left(\frac{\pi}{2}, 0\right) : M_2(0, \varphi) : M_2\left(\frac{\pi}{2}, \frac{\pi}{2}\right) \\ &= \frac{2 + (2\Delta d_a/d_b)^2}{1 + (2\Delta d_a/d_b)^2} : \frac{1 + 2(2\Delta d_a/d_b)^2}{1 + (2\Delta d_a/d_b)^2} : 1. \end{aligned} \quad (6.6)$$

Simplifying this expression for the case  $\Delta d_a/d_b \rightarrow 0$ , one gets  $\Delta H_b : \Delta H_a : \Delta H_c = 2 : 1 : 1$  and the angular dependence

$$\Delta H_{DM}^{(\Delta d_a/d_b \rightarrow 0)}(T, \theta, \varphi) = \Delta H_{DM}(T)(1 + \sin^2\theta \cos^2\varphi), \quad (6.7)$$

where  $\varphi$  is the azimuthal angle of  $H$  in ( $bc$ )-plane with respect to the  $b$  axis and  $\Delta H_{DM}(T)$  is proportional to the strength of the DM interaction.

Regarding the temperature dependence of  $\Delta H_{DM}$ , we will use the result obtained by Oshikawa and Affleck  $\Delta H_{DM}^{(T \ll J/k_B)}(T) \propto J^2/T^2$  obtained for the case of a staggered DM

interaction  $\mathcal{H}_{DM}^{(ij)} = \sum_i \mathbf{d}_i \cdot [\mathbf{S}_i \times \mathbf{S}_{i+1}]$  with  $\mathbf{d}_i = (-1)^i \mathbf{d}$  for  $T \ll J/k_B$  [Oshikawa'02]. Assuming that this temperature dependence also holds for a uniform DM interaction along the chain as in our case, we will apply the power law

$$\Delta H_{DM}(T) = \Delta H_{DM}(\infty) \left( \frac{J}{k_B T} \right)^2 \quad (6.8)$$

to fit the experimental data using  $\Delta H_{DM}(\infty)$  as a fit parameter. An analytical expression for the crossover behavior from this power-law (valid for  $T \ll J/k_B = 660$  K) to the constant high-temperature value of the Kubo-Tomita approach has not been derived up to now. Therefore, we extrapolate the power law up to  $T = J/k_B$  and identify  $\Delta H_{DM}(T = J/k_B) = \Delta H_{DM}(\infty)$  in order to compare the experimental values to the theoretical estimates of the Kubo-Tomita approach. We would like to recall that the ratio of  $\Delta H$  along different axes in Eq. (6.6) evaluated in the high-temperature limit does not depend on the form of the temperature dependence.

### 6.4.3. Competition of Relaxation Mechanisms

We remember that the temperature dependence of the ESR linewidth above the  $T_{c1}$  can be clearly divided into three regions:  $T_{c1} < T < 90$  K,  $90 \text{ K} < T < 250$  K and  $T > 250$  K (see Sec. 6.7). In the following we will show that the anisotropy and the temperature dependence of the linewidth for  $T_{c1} < T < 250$  K can be described as a competition of AE and DM interactions discussed above. But the change of curvature (Fig. 6.7(i)) for  $T > 250$  K clearly shows that an additional relaxation channel dominates at higher temperatures. Before we discuss the low-temperature data in detail, we shortly comment on possible reasons for this high-temperature behavior.

In order to determine the temperature dependence more accurately up to 500 K, we additionally performed measurements of crushed single crystals (see Fig. 6.10). This was necessary because of the fact that the single crystals of TiOCl are thin platelets of small mass and that the linewidth above room temperature is already very large, resulting in only very weak signals.

It turns out that the strong increase of the ESR linewidth with temperature can be very well accounted for by adding an exponential term  $\Delta H_{\text{exp}} \cdot e^{-\Delta_{ESR}/k_B T}$  to the temperature dependence of the anisotropic exchange interactions (Eqs. 6.4, 6.8):

$$\Delta H(T) = \Delta H_{AE}(\infty) \cdot e^{-\frac{c_1}{T+c_2}} + \Delta H_{DM}(\infty) \left( \frac{J}{k_B T} \right)^2 + \Delta H_{\text{exp}} \cdot e^{-\frac{\Delta_{ESR}}{k_B T}}. \quad (6.9)$$

The resulting fit is shown as a solid line in Fig. 6.10(i), yielding  $\Delta_{ESR} = 0.28$  eV. The exponential nature of the additional increase is highlighted in Fig. 6.10(ii), where the reduced linewidth data  $\Delta H_{\text{exp}}$  are plotted after subtraction of the contributions of the AE and DM interactions (dashed line in Fig. 6.10(i)).

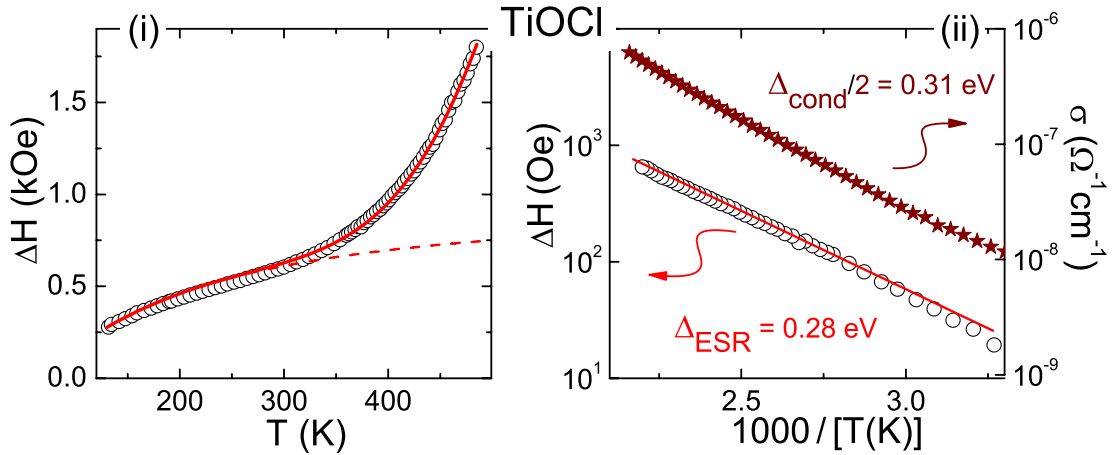


Figure 6.10.: **(i)**: Temperature dependence of the ESR linewidth for a powder sample together with a fit by Eq. (6.9). The obtained fit parameters are given in Table 6.3.  $\Delta H_{KvN}(T) = \Delta H_{AE}(T) + \Delta H_{DM}(T)$  is shown as a red dashed line. **(ii)**: Reduced contribution  $\Delta H_{exp}(T) = \Delta H(T) - \Delta H_{KvN}(T)$  compared to conductivity as Arrhenius plot.

Pointing out the similarity with the high-temperature behavior in  $\alpha'$ - $\text{NaV}_2\text{O}_5$  (compare to Eq. (5.3) and Fig. 5.6) one can state that the origin of that behavior is not clear at the moment. An additional relaxation channel via thermally activated charge carriers might cause an exponential increase of  $\Delta H(T)$ , as it has been discussed for doped manganites [Shengelaya'00], and at the metal-to-insulator transition in  $\beta$ - $\text{Na}_{1/3}\text{V}_2\text{O}_5$  [Heinrich'04]. In both cases the leading contribution to the temperature dependence is determined by the Arrhenius law of the conductivity  $e^{-\Delta_\sigma/2k_B T}$ . The corresponding temperature behavior of the dc-conductivity could be obtained from dielectric measurements (see Sec. 4.6). In an Arrhenius representation one can extract an activation energy  $\Delta_\sigma/2 \approx 0.31$  eV (see Fig. 6.10(ii)). Although this value is similar to the one obtained from the ESR linewidth, it is by far too small compared with the experimental gap value of about 2 eV observed by optical spectroscopy [Rückamp'05b]. Therefore, such a scenario appears rather unlikely. Alternatively, the exponential increase can be again interpreted in terms of a thermally activated dynamic Jahn-Teller process [Heinrich'03] or as relaxation via the first excited orbital state, whose energy has a comparable magnitude  $\Delta_1 = 0.2 - 0.4$  eV (Sec. 6.3).

Leaving the question about the nature of this divergency open, we fix now the value  $\Delta_{ESR} = 0.28$  eV and proceed to describe the anisotropic temperature dependence of the linewidth for the main orientations of the single crystal. Note that  $\Delta_{ESR}$  should not depend on the orientation of the magnetic field with respect to the crystal axes, justifying the further use of this value for the single crystal. The resulting fit curves are

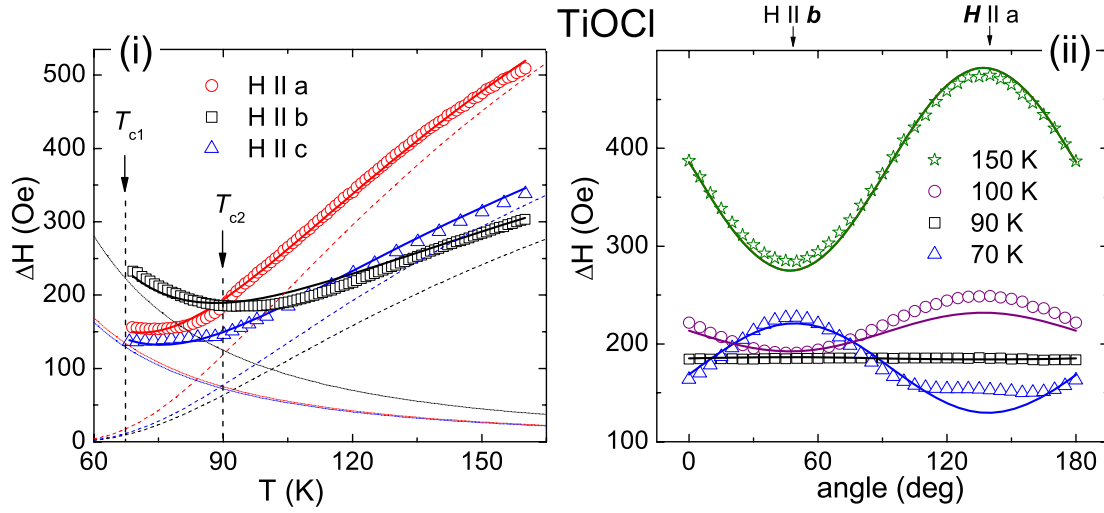


Figure 6.11.: **(i)**: Temperature dependence of the ESR linewidth in TiOCl for the magnetic field applied parallel to the three crystallographic axes. The fit curves were obtained by the sum of  $\Delta H_{AE}(T)$  and  $\Delta H_{DM}(T)$  (Eqs. 6.4, 6.8) with the parameters listed in Table 6.3. The dashed and dotted lines represent the contributions from the AE and DM interactions, respectively. **(ii)**: Angular dependence of the ESR linewidth  $\Delta H$  in TiOCl for the magnetic field applied within the  $(ab)$ -plane at different temperatures between 70 and 150 K. The solid lines represent the fit by the Eq. (6.10), where the fitting parameters are taken from Table 6.3.

Table 6.3.: Parameters determined from fits on the temperature (Figs. 6.7, 6.10, 6.11(i)) and angular (Fig. 6.11(ii)) dependencies of the linewidth by the Eq. (6.9) and (6.10), respectively. The parameters  $C_1 = 129.12$  K,  $C_2 = -38.1$  K,  $\Delta_{ESR} = 0.28$  eV,  $\Delta H_{\text{exp}} = 0.87$  MOe are assumed to be isotropic. The parameter  $S_{AE}$  used by the fit of the angular dependence of  $\Delta H$  in the  $(ab)$ -plane is equal to 1.05.

	$\Delta H_{AE}(\infty)$ [Oe]	$\Delta H_{DM}(\infty)$ [Oe]
$H \parallel a$ (single crystal)	1429	1.397
$H \parallel b$ (single crystal)	765	2.319
$H \parallel c$ (single crystal)	930	1.344
crushed single crystal	990	1.344

shown in Fig. 6.7 and the obtained fit parameters are given in Table 6.3. The agreement between fit and data below 250 K is excellent (see also Fig. 6.11(i)), but at higher temperatures deviations are clearly visible for  $H \parallel a$  and  $H \parallel b$ . The anisotropy inferred from the AE and the DM interaction below 250 K is somewhat larger than the observed one. The gradual suppression of the anisotropy with increasing temperature may result from the thermal occupation of higher lying  $d$ -levels, which is also in agreement with the disappearance of the anisotropy of the  $g$ -tensor (Fig. 6.7(ii)). A similar effect was observed at the transition from a cooperative static JT-effect to a dynamic JT-phase in (La:Sr)MnO<sub>3</sub> [Kochelaev'03].

Let us turn to the discussion of the anisotropic exchange contributions which dominate the relaxation below 250 K. Using the obtained fit parameters we additionally fitted the angular dependence of the linewidth data for the single crystal in the crystallographic ( $ab$ )-plane (Fig. 6.11(ii)) by using

$$\begin{aligned} \Delta H^{(ab)}(T, \theta) = & \Delta H_{DM}^{(H \parallel a)}(\infty) \cdot \left( \frac{J}{k_B T} \right)^2 (1 + \sin^2 \theta) + \\ & + \frac{1}{S_{AE}} \cdot \Delta H_{AE}^{(H \parallel b)}(\infty) \cdot e^{-\frac{C_1}{T+C_2}} (1 + \cos^2 \theta) + \\ & + \Delta H_{\text{exp}} \cdot e^{-\frac{\Delta E_{SR}}{k_B T}}, \end{aligned} \quad (6.10)$$

where  $\theta$  denotes the angle in the ( $ab$ )-plane with respect to the  $a$  axis. Here, we took into account only the DM contribution along the crystallographic  $b$ -axis (see Sec. 6.4.2). Concerning the AE interaction, we had to introduce the additional fit parameter  $S_{AE} \approx \Delta H_{AE}^{(H \parallel a)}(\infty) / [2 \cdot \Delta H_{AE}^{(H \parallel b)}(\infty)] = 1.05$  which indicates the deviation from the theoretically expected ratio of 1, if only the AE paths described above are taken into account (i.e.  $D_{zz} = -2D_{xx} = -2D_{yy}$ ). The fact that  $S_{AE} = 1.05$  can be explained by small contributions of the other relaxation processes. Thus, we were able to corroborate the validity of the fit parameters given in Table 6.3 by a consistent description of the temperature and angular dependence of the linewidth. Moreover, we find a good agreement of the ratios of the obtained high-temperature fit parameters for the DM interactions  $\Delta H_{DM}^{(H \parallel b)}(\infty) : \Delta H_{DM}^{(H \parallel a)}(\infty) : \Delta H_{DM}^{(H \parallel c)}(\infty) \equiv \Delta H_b^{(\text{fit})} : \Delta H_a^{(\text{fit})} : \Delta H_c^{(\text{fit})} = 1.72 : 1.04 : 1$  with the theoretically expected ratio  $2 : 1 : 1$ .

Looking at the corresponding contributions of AE and the DM interactions shown in Fig. 6.11(i), it becomes clear that the dominant relaxation mechanism for  $T > 90$  K is the AE, while the DM interaction takes over for  $T_{c1} < T < 90$  K. This competition is nicely evidenced by the corresponding orientation dependencies and the crossover at about 90 K (Fig. 6.11(ii)). However, significant contributions of the DM interactions can already be anticipated below 135 K where the linewidth for  $H \parallel b$  already becomes larger than the one for  $H \parallel c$ . Here, we have to emphasize that our analysis of the DM interaction is based on the room-temperature structure and does not take into account a possible structural phase transition at  $T_{c2}$ . Since the linewidth data does not reveal a

discontinuity at  $T_{c2}$  but a smooth crossover, we conclude that the structural changes do not significantly alter the involved relaxation processes.

## 6.5. Summary

In this chapter we have considered ESR data in TiOCl in the broad temperature range  $T_{c1} < T < 500$  K. From the  $g$  values we derived the energy of the first excited state as  $\Delta_1 = 0.2 - 0.4$  eV, in good agreement with theoretical estimations. Furthermore, we described the angular and temperature dependence of the linewidth as a competition of the anisotropic exchange interactions and an additional exponential increase for  $T > 250$  K that might be related to thermally activated lattice fluctuations. We could show that the line broadening is dominated by the symmetric anisotropic exchange for  $90 \text{ K} < T < 250 \text{ K}$  which produces the maximal linewidth along the  $a$  direction, while the antisymmetric DM interaction leads to the crossover at about 90 K with the maximal linewidth along the  $b$  direction.

## 7. Multi-Spin Chains in $\eta\text{-Na}_{9/7}\text{V}_2\text{O}_5$

While in chapter 5 charge ordering in  $\alpha'\text{-NaV}_2\text{O}_5$  was investigated, we will turn now to a related material  $\eta\text{-Na}_{9/7}\text{V}_2\text{O}_5$ . This system came recently into the focus as a unique example of a low-dimensional spin-gap system [Isobe'99]. The opening of the spin-gap below 100 K cannot be described by any known model for spin-gap systems [Duc'04]. In this chapter we will propose a model of the gapped state in this compound. Moreover, we will characterize the spin relaxation mechanisms on the basis of electron spin resonance, specific heat, susceptibility and dielectric conductivity measurements in the broad temperature range  $4\text{ K} < T < 570\text{ K}$ .

### 7.1. Crystal Structure

The crystals used in this work were prepared using the same procedure as for  $\alpha'\text{-NaV}_2\text{O}_5$ , changing accordingly the appropriate amounts of  $\text{NaVO}_3$  and  $\text{VO}_2$ . The characterization of the samples by Debye-Scherrer x-ray diffraction showed the polycrystalline material to be single phase, whereas the single crystals have a small amount (less than 0.5%) of ferromagnetic impurities.

The room-temperature structure of  $\eta\text{-Na}_{9/7}\text{V}_2\text{O}_5$  is monoclinic with space group  $P2/c$ . As depicted in Fig. 7.1 the structure consists of edge sharing  $\text{VO}_5$  pyramids with their apical oxygens pointing up and down alternately to form a zigzag chain running along the  $a$  axis. These chains exhibit a crystallographic step at every five edge-sharing  $\text{VO}_5\text{-VO}_5$  units. The zigzag chains are bridged by  $\text{VO}_4$  tetrahedra in the  $(ac)$ -plane to form the  $\text{V}_2\text{O}_5$  layers which are connected by the Na ions along the  $b$  axis. It is worth noting that the  $\text{VO}_4$  tetrahedra contain the non-magnetic  $\text{V}^{5+}$  ions bridging the chains of the magnetic vanadium ions. These chains excluding the steps are structurally similar to those of the  $\alpha'\text{-NaV}_2\text{O}_5$ , but have a larger average vanadium valence. Nine out of ten V ions are tetravalent except for two neighboring V ions on the structural step, which share one electron and, therefore, have an average valence +4.5 at high temperatures.

The low-temperature x-ray study [Duc'04] has shown a doubling of the unit cell along the  $b$  axis below 100 K suggesting charge ordering (CO) on the two  $\text{V}^{4.5+}$  sites placed on the structural step (see Fig. 7.6(ii)). But the nature of the resulting gapped state (evidenced by a drop down of the susceptibility at  $T < 100\text{ K}$  depicted in Fig. 7.3(i)) remained rather mysterious, if one takes into account the odd number of spins on each structural element. To understand the physics of this phase, it is necessary to charac-



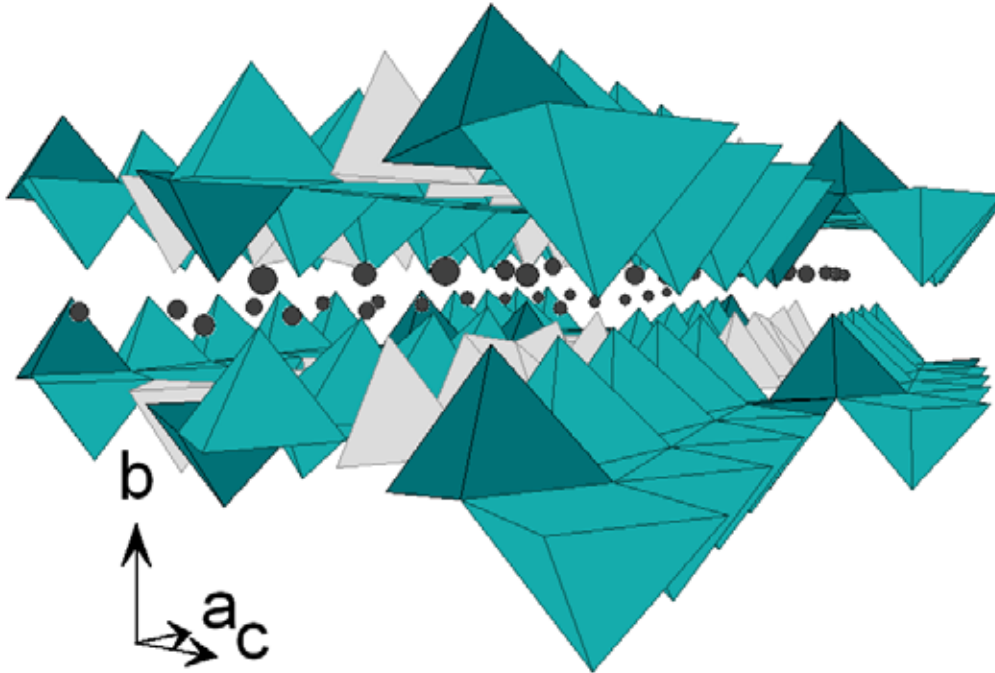


Figure 7.1.: High-temperature crystal structure of  $\eta$ - $\text{Na}_{9/7}\text{V}_2\text{O}_5$ . Dark dots denote Na ions, cyan (dark cyan) pyramids correspond to  $\text{V}^{4+}$  ( $\text{V}^{4.5+}$ ) ions surrounded by the  $\text{O}^{2-}$  ions, the light grey  $\text{VO}_4$  tetrahedra contain non-magnetic  $\text{V}^{5+}$  ions. In addition to the monoclinic coordinate system  $\{a, b, c\}$  the local coordinate system of  $\text{VO}_5$  pyramids  $\{a', b', c'\}$  (cf. Fig. 7.4) is used in the work.

terize first the system at higher temperatures. Therefore, in the next section we will discuss the spin relaxation mechanisms in  $\eta$ - $\text{Na}_{9/7}\text{V}_2\text{O}_5$  on the basis of ESR data. Then, in Sec. 7.3, we will turn to the temperature region  $30 \text{ K} < T < 100 \text{ K}$ , where charge-ordering fluctuations play an important role. Finally, specific heat and susceptibility data will be used in section 7.4 to characterize the low-temperature  $T < 30 \text{ K}$  ground state of this compound.

## 7.2. ESR in $\eta$ - $\text{Na}_{9/7}\text{V}_2\text{O}_5$

### 7.2.1. Experimental Survey

The temperature evolution as well as the angular dependence of ESR spectra at 300 K are shown in Fig. 7.2. In the whole temperature range measured,  $4 \text{ K} < T < 570 \text{ K}$ , the absorption line can be well fitted using the Lorentzian line shape. The temperature

dependent effective  $g$ -factor and the ESR linewidth  $\Delta H$  are depicted in Figs. 7.3(ii) and 7.3(iii), respectively. The previous results [Chabre'05] cover only temperature dependencies of  $\Delta H$  in two directions up to room temperature without regard to the most interesting crystallographic  $c'$  direction. At  $T > 100$  K the  $g$ -factor is nearly temperature independent and shows a pronounced anisotropy with the characteristic values  $g_b = 1.93 \pm 0.006$ ,  $g_{a'} \approx g_{c'} = 1.96 \pm 0.005$ . The CO transition affects the  $g$  tensor anisotropy, but all the changes observed lie in the experimental error which is taken as 5% of the linewidth. The intensity of the ESR signal  $I_{\text{ESR}}$  (see Fig. 7.3(i)) which is proportional to the static susceptibility [Abragam'70] shows significant deviations from the Bonner-Fisher law (Eq. 3.7) falling down below 30 K very sharply.

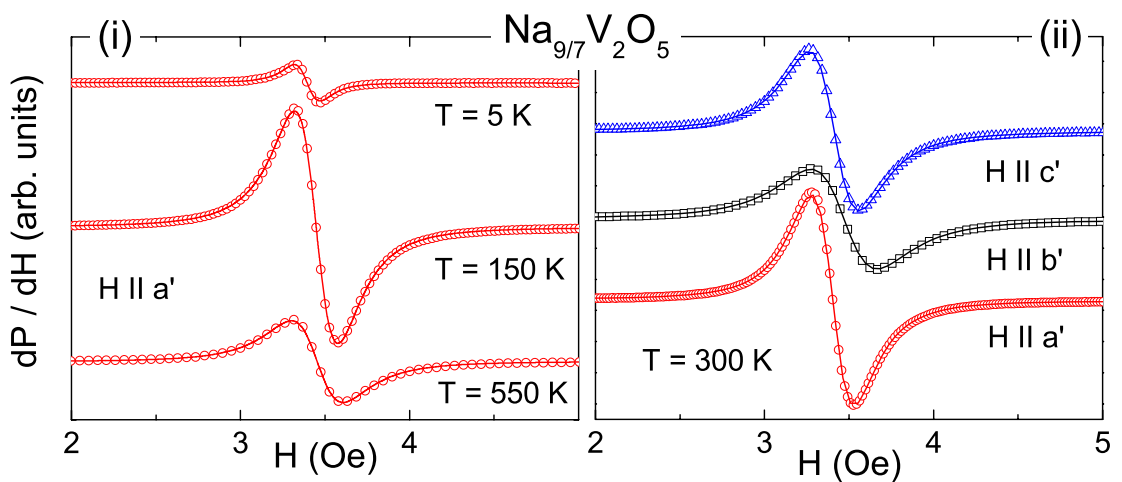


Figure 7.2.: ESR spectra of  $\eta$ - $\text{Na}_{9/7}\text{V}_2\text{O}_5$ . **(i)**: Temperature evolution of the ESR spectrum for  $H \parallel a'$ . **(ii)**: ESR spectra at room temperature for the external magnetic field parallel to the main crystallographic axes. Solid lines represent fits using Lorentzian line shape.

The linewidth shows an anisotropic behavior with the external magnetic field  $H$  applied along the three crystallographic axes as well. Above room temperature the linewidth increases monotonously for all three directions. It reveals a pronounced anisotropy with respect to the  $b'$  axis, where the linewidth is larger by a factor of about 1.5 as compared to the other two axes. Below room temperature  $\Delta H_{b'}$  increases slowly with decreasing temperature showing a smooth peak at 86 K, in accordance with previously published results [Chabre'05]. In both other crystallographic directions this peak is essentially suppressed. Moreover, the low-temperature behavior of the linewidth along the  $c'$  direction deviates strongly from the others two. It increases monotonously to low temperatures following a power law, what results in a crossover of the linewidth data at  $T \simeq 59$  K. All curves reach their maximal value around 15-23 K and fall down at lower

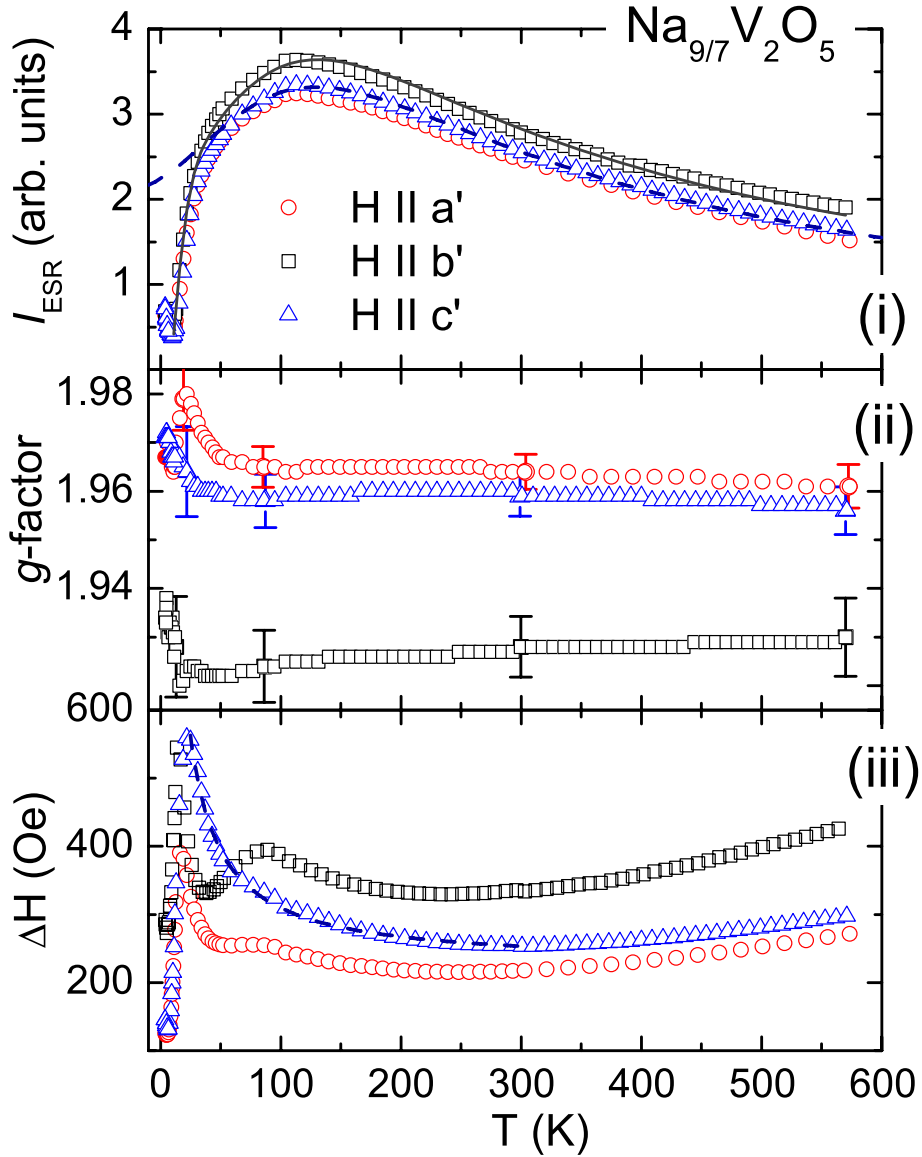


Figure 7.3.: Temperature dependence of the parameters of the ESR line in  $\text{Na}_{9/7}\text{V}_2\text{O}_5$  measured at X-band frequency ( $\nu \approx 9.3$  GHz) for the magnetic field applied along the three crystallographic axes. **(i)**: The ESR intensity  $I_{\text{ESR}}$ . The dashed blue line is a fit of  $I_{c'}$  by the Bonner-Fisher model (Eq. 3.7) with  $J = 200$  K. The solid black line fits  $I_{b'}$  by the alternating spin chain model [Johnston'00] with  $J_1/J_2 = 0.9$ . **(ii)**: The effective  $g$ -factor. The error bars are given assuming the uncertainty in the resonance field as 5% of the linewidth. **(iii)**: The ESR linewidth  $\Delta H$ . The dashed line emphasizes the  $1/T$  divergence of  $\Delta H_{c'}$ .

Table 7.1.: Left column: Observed and calculated  $\mathbf{g}$  tensors in  $\text{Na}_{9/7}\text{V}_2\text{O}_5$ . Right column: Relative energies of the  $d$  orbital states calculated by means the AOM model. For comparison the results of a LDA+ $U$  calculation for the almost isostructural compound  $\alpha'$ - $\text{NaV}_2\text{O}_5$  is given [Yaresko'00].

Experiment		AOM	Orbital state	$E_{\text{AOM}}$ [eV]	$E_{\text{LDA}+U}$ [eV]
$g_{b'}$	1.928(5)	1.926	$d_{3z^2-r^2}$	3.78	$2.2 \div 4.4$
$g_{c'}$	1.959(4)	1.960	$d_{x^2-y^2}$	2.41	$0.7 \div 4.4$
$g_{a'}$	1.964(4)	1.964	$d_{xz}$	1.03	$0.8 \div 1.8$
			$d_{yz}$	0.98	$0.7 \div 1.6$
			$d_{xy}$	0	$-0.3 \div 0.3$

temperatures. The signal at  $T < 7$  K has the Curie-like temperature dependence of the intensity and almost the same anisotropy of the linewidth and the  $g$ -factor as at high temperatures.

## 7.2.2. Splittings of Crystal-Field Levels

First, we will discuss briefly the anisotropy of the  $\mathbf{g}$  tensor. It is almost temperature independent in the measured temperature range and can be used to get information about splittings of the crystal-field levels of  $\text{V}^{4+}$  ( $3d^1$ ) ions in  $\eta$ - $\text{Na}_{9/7}\text{V}_2\text{O}_5$  in terms of the angular overlap model (appendix B).

The given anisotropy (Fig. 7.3(ii)) resembles the one in  $\alpha'$ - $\text{NaV}_2\text{O}_5$  (Fig. 5.5). Indeed, the local crystallographic environment, a  $\text{VO}_5$  pyramid, is the same in both compounds. Consequently, the  $\mathbf{g}$  tensor can be fitted using the same bounding parameters as for  $\alpha'$ - $\text{NaV}_2\text{O}_5$  (see Tables 7.1 and 7.2). The only difference is the anisotropy of the covalence reduction. In  $\alpha'$ - $\text{NaV}_2\text{O}_5$ , the distribution of electrons between two V ions in the  $(xy)$ -plane affects strongly the covalence reduction in this plane (see Table 5.2). In  $\eta$ - $\text{Na}_{9/7}\text{V}_2\text{O}_5$ , the covalence reduction is isotropic and amounts to  $k = \lambda/\lambda_{\text{fi}} = 203/248 \approx 0.82$ .

Table 7.2.: Angular overlap model parameters for the  $[\text{V}^{4+}\text{O}_5]$  complex in  $\eta$ - $\text{Na}_{9/7}\text{V}_2\text{O}_5$ .

$\lambda$ [ $\text{cm}^{-1}$ ]	$e_{\sigma}(\text{O}_3)$	$e_{\pi}(\text{O}_3)$	$e_{\sigma}(\text{O}_2)$	$e_{\pi}(\text{O}_2)$	$[10^3 \text{ cm}^{-1}]$	$k$
203	32	8	12	3		0.82

### 7.2.3. Exchange Interactions

Having got the information on the orbital level energies from the anisotropy of the  $\mathbf{g}$  tensor, we will analyze now the temperature and angular dependence of the ESR linewidth in order to determine the main spin relaxation mechanisms in  $\eta\text{-Na}_{9/7}\text{V}_2\text{O}_5$ .

The necessary estimations of all possible broadening sources have been performed already for the related compound  $\alpha'\text{-NaV}_2\text{O}_5$  (see Sec. 5.3). It was concluded that by analogy with many other low-dimensional systems with strong exchange interaction the main mechanisms of the spin relaxation are the anisotropic exchange interactions: symmetric part of the anisotropic exchange (AE) and Dzyaloshinsky-Moriya (DM) interaction.

Concerning AE interaction, we would like to point out that a step at every fifth edge-sharing  $\text{VO}_5$  unit and an additional separation of the neighboring chains by the  $\text{VO}_4$  tetrahedra presented in  $\eta\text{-Na}_{9/7}\text{V}_2\text{O}_5$  do not change significantly the exchange paths as compared to  $\alpha'\text{-NaV}_2\text{O}_5$ . The detailed description of AE in this system can be found in section 5.3. On the basis of the microscopical estimations it was concluded that symmetric exchange is the main line-broadening source at high temperatures  $T > T_{\text{CO}}$  with a characteristic linewidth of several hundreds Oersted. The exchange between the neighboring vanadium ions along the  $a'$  direction produces the linewidth along the  $b'$  direction by a factor of 2 larger as compared to the other two axes, whereas the inter-chain exchange along the crystallographic  $c$  direction reduces this anisotropy by broadening the ESR line in the  $(a'c')$  plane.

The most important difference between these two structures lies in the different average oxidation state of the  $\text{VO}_5$  pyramids. The average vanadium valence in  $\alpha'\text{-NaV}_2\text{O}_5$  is equal to +4.5, at that the electron is actually localized at the ladder rungs causing a negligible DM interaction compared to the AE. In  $\eta\text{-Na}_{9/7}\text{V}_2\text{O}_5$  only every tenth vanadium ion placed in a pyramid lacks an electron. Note that the electron in that case is always localized and at all temperatures down to the temperature where the spin dimerization takes place it has a neighboring spin. This fact allows the existence of the DM interaction in this structure which plays an important role in the relaxation at low temperatures as we will show below.

DM interaction in low-dimensional spin systems recently has come into the focus of interest and is now under heavy debate (see Sec. 2.3). In particular, the commonly used conventional relation for the DM-vector  $|d| \approx (\Delta g/g)|J|$  [Moriya'60] has been shown to overestimate its magnitude strongly. The only reliable way to determine the correct order of magnitude is the microscopical estimation using Eq. (2.23). But this procedure becomes involved for complicated exchange geometries and in the case of many competing exchange processes. The probably most evident way to determine the spin relaxation source in low-dimensional systems was recently suggested by Oshikawa and Affleck [Oshikawa'02]. It is based on the different temperature dependence of the

ESR linewidth produced by them. On quite general grounds it can be shown that the linewidth decreases in case of AE and increases in case of DM interaction with decreasing temperature at  $T < J$  (Sec. 4.5.2). Namely, for the case of DM interaction in  $S = 1/2$  antiferromagnetic chains the linewidth is given by

$$\Delta H_{\text{DM}}(T) = \frac{1}{g\mu_{\text{B}}} \frac{d^2}{J} \left[ a + b \frac{J}{T} + O\left(\frac{J^2}{T^2}\right) \right], \quad (7.1)$$

where  $a$  and  $b$  are positive constants for an antiferromagnet,  $\mu_{\text{B}}$  denotes the Bohr magneton. Note that for  $\text{TiOCl}$  (Chapter 6) only the term  $\sim 1/T^2$  was considered because it dominates the line broadening at temperatures  $T \ll J$ . In the present case, the influence of DM interaction becomes visible already at temperatures comparable with the value of the exchange integral  $J \approx 200$  K.

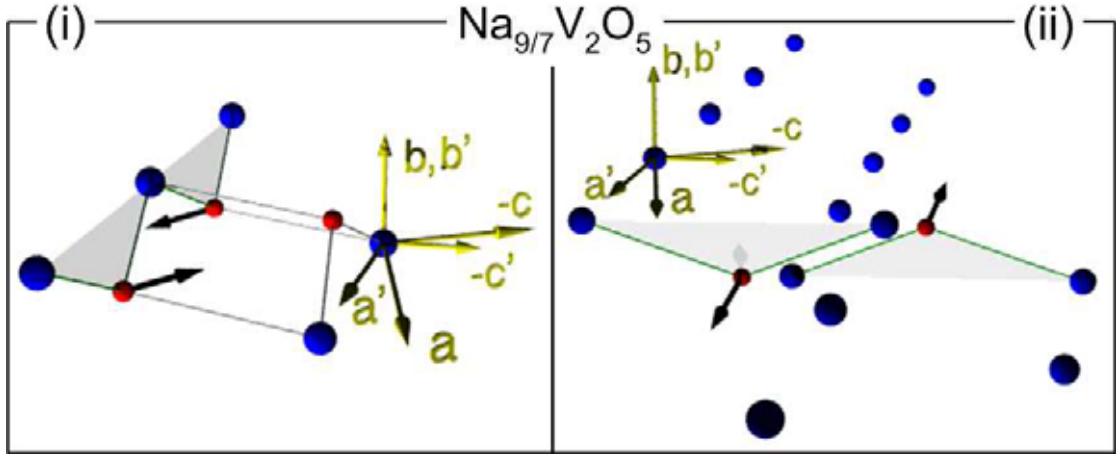


Figure 7.4.: Nearest-neighbor bonds of the vanadium ion placed (i) away from the structural step of the V-chain and (ii) on the structural step of the V-chain. The black arrows indicate the direction of the corresponding DM vectors. The blue big spheres denote V ions, the small red spheres – O ions.

As it was already mentioned above, the DM interaction has to be always present in  $\eta$ - $\text{Na}_{9/7}\text{V}_2\text{O}_5$  in contrast to  $\alpha'$ - $\text{NaV}_2\text{O}_5$ . Moreover, the CO the pattern, whatever the form it has, should not change the exchange geometry significantly because only two lattice sites near the structural steps are affected by CO. Thus,  $\eta$ - $\text{Na}_{9/7}\text{V}_2\text{O}_5$  gives a good opportunity to study the effect of DM interaction on the ESR linewidth in comparison with the system which has the same AE geometry but a suppressed antisymmetric interaction.

The double chain structure of  $\eta$ - $\text{Na}_{9/7}\text{V}_2\text{O}_5$  leads to two possible paths of the DM interaction: between the neighboring V ions along the chain (“intra-chain” exchange) and between the V ions from the neighboring chains (“inter-chain” exchange). Note,

that the antisymmetric interaction is lacking for V ions placed away from the structural step because of the existence of an inversion center between them and V ions from the neighboring chain. Only the ions placed on the structural step give a non-negligible contribution to the DM interaction. Fig. 7.4(ii) shows that the corresponding DM vector is directed along the chain direction. The geometry of the intra-chain exchange is displayed in Fig. 7.4(i).  $\mathbf{d}$  points perpendicular to the chain direction lying approximately in the  $(a'c')$ -plane.

The geometry of these interactions (bond angles and distances between the interacting ions) is almost identical, but the number of corresponding bonds is sufficiently different. The average number of intra-chain bonds is by a factor of 4 larger than the number of inter-chain bonds, what leads to the maximal broadening of the linewidth perpendicular to the chain direction. A more precise calculation gives  $\Delta H_{a'} : \Delta H_{b'} : \Delta H_{c'} \simeq 1 : 1 : 1.8$ .

#### 7.2.4. Analysis of the Linewidth

Having analyzed all essential ESR line-broadening sources we will now apply these findings and discuss the temperature as well as the angular dependence of  $\Delta H$  in order to determine the dominant source of spin relaxation in  $\eta\text{-Na}_{9/7}\text{V}_2\text{O}_5$ .

Looking at the experimental results (Fig. 7.3(iii)) it becomes clear that the anisotropy at high temperatures  $T > 200$  K is governed by the symmetric anisotropic exchange. Fig. 7.5(i) emphasizes that the anisotropy of the linewidth is temperature independent and follows the predicted anisotropy at  $T > 100$  K. Below this temperature, strong deviations are observed that indicate the influence of another spin relaxation mechanism in this temperature region.

On the basis of the previous consideration (Sec. 7.2.3) this source of line broadening can be unambiguously determined to be the antisymmetric DM interaction:

- (i) The maximum of the linewidth at  $T < 60$  K is observed approximately along the  $c'$  axes, i. e. in the direction of the DM vector. Fig. 7.5(i) clearly shows that the ratio of the linewidth  $\Delta H_{a'} : \Delta H_{b'} : \Delta H_{c'}$  approaches the theoretically expected value  $1 : 1 : 1.8$  for the line broadening due to the antisymmetric interaction.
- (ii) The characteristic temperature dependence of the DM interaction (Eq. 7.1), an increase to the lower temperatures with a power law, can be clearly seen along the  $c'$  axes, the direction most affected by this interaction. It can be well fitted by  $1/T$  down to 30 K where the spin dimerization takes place (see Fig. 7.3(iii)).

Two additional features of the temperature dependence of the linewidth are of particular interest: the peaks at about 15-23 K and 86 K. The features in  $\Delta H(T)$  below 30 K has been recently shown to be simply related to the way in which the magnetic susceptibility and the memory function depend on temperature, rather than to a specific

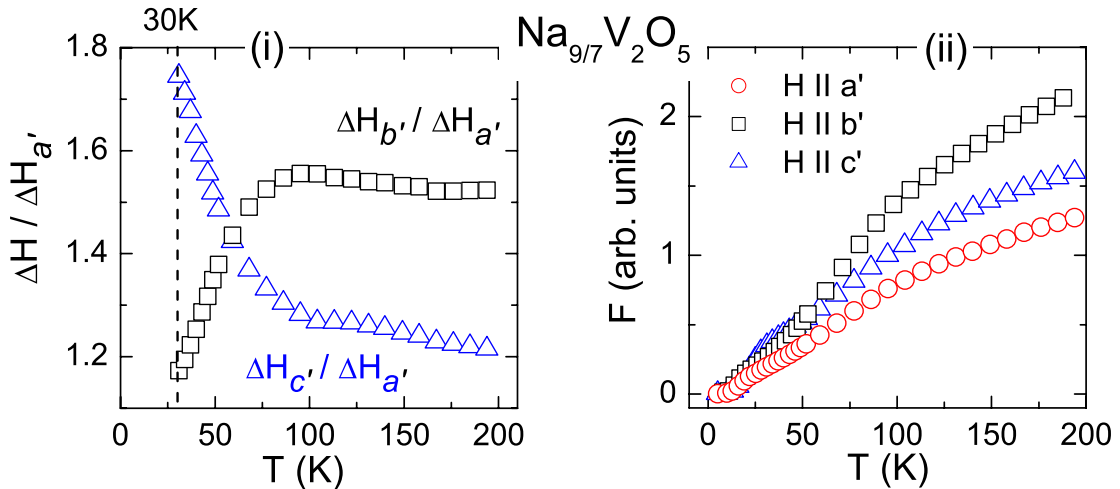


Figure 7.5.: (i): Temperature dependence of the linewidth for the magnetic field applied along the  $c'$  and  $b'$  axes normalized to  $\Delta H_{a'}$ . (ii): Temperature dependence of the memory function  $F \propto \chi_{\alpha} \cdot \Delta H_{\alpha} \cdot T$  for  $H \parallel \alpha$  ( $\alpha = \{a', b', c'\}$ ).

magnetic origin [Chabre'05]. Fig. 7.5(ii) shows that the 'memory function'<sup>1</sup> smoothes away the sharp low-temperature peak seen in  $\Delta H(T)$ . Therefore in the present work we will focus our attention only on the second feature at about 86 K. In the next section it will be shown that this feature is closely related to charge ordering in this structure.

## 7.3. Charge Fluctuations

### 7.3.1. Cross-Relaxation via a Mixed Valence Fragment $V^{4.5+\delta}-V^{4.5-\delta}$

The peak on  $\Delta H_b$  at 86 K was first observed by Chabre *et al.* [Chabre'05], where this behavior was supposed to arise due to magnetic correlations accompanying the second-order phase transition. In the following we will show that this feature can be explained by cross-relaxation of the whole spin system via  $V^{4.5+\delta}-O^{2-}-V^{4.5-\delta}$  elements placed on the structural steps.

Fig. 7.6(ii) displays the results of an x-ray analysis [Duc'04]: below  $T \sim 100$  K one can clearly see the appearance of superstructure reflections at the reduced wave vector  $\mathbf{q} = (0, 1/2, 0)$ . That indicates the occurrence of a structural phase transition resulting in the doubling of the unit cell in the  $b$  direction. This transition occurs due to CO on the two  $V^{4.5+}$  sites placed on the structural steps. At  $T < 50$  K the electron, uniformly distributed between two  $V^{4.5+}$  sites at high temperatures, undergoes a lock-in transition

<sup>1</sup> a sum of four-spin correlation functions, Eq. (4.20), calculated at a finite temperature.



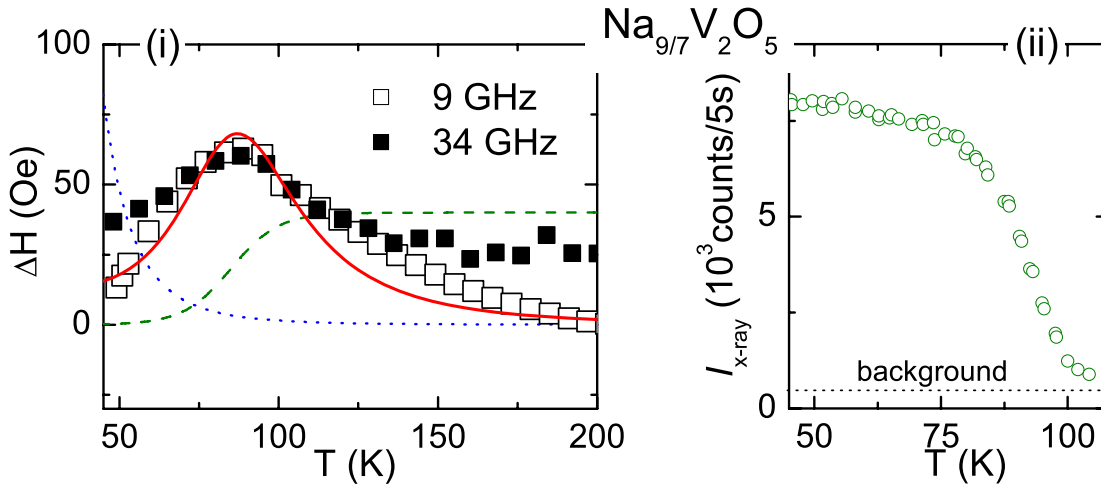


Figure 7.6.: **(i)**: Peak on the temperature dependence of the linewidth with the magnetic field  $H$  applied parallel to the  $b$  axis at X- and Q-band frequencies. Note, that the high-temperature linewidth of 332 Oe is subtracted from the experimental data. The solid red line represents the fit by the Eq. (7.6) with  $N_f \equiv 1 + \tanh \frac{T-85}{15}$  and  $T_{1f} = T^{-\alpha} \equiv T^{-5}$  functions presented by the green dash and blue dot curves, respectively. **(ii)**: Peak intensity of the symmetry equivalent  $(1\ 3.5\ \bar{4})$  superstructure reflection in  $\eta$ - $\text{Na}_{9/7}\text{V}_2\text{O}_5$  as a function of temperature taken from [Duc'04].

localizing on one of the  $\text{VO}_5$  pyramids.

An important question for describing the spin relaxation mechanism is whether electron motion in the  $\text{V}^{4.5+\delta}\text{-V}^{4.5-\delta}$  pairs is thermally activated or not. If this process is thermally activated, the position of the peak maximum should depend on frequency. But the measurements at 34 GHz (see Fig. 7.6(i)) do not reveal any changes in the position of the peak. This kind of behavior is a sure sign of a tunneling nature of the electron motion.

The Hamiltonian of such a paramagnetic center (two  $\text{VO}_5$  pyramids with a tunneling electron between them) can be written as for a dimer with a mixed valence (see, e.g., [Borras'99, Eremin'01] and therein):

$$H_0 = \frac{P^2}{M} + \frac{M\omega^2}{2}q^2 + (Vq + F)(a^+a - b^+b) + t(a^+b - b^+a). \quad (7.2)$$

Here  $q = Q_a - Q_b$  is a vibrational coordinate which describes the difference in local displacements of the surrounding ions corresponding to the localization of the electron on the left  $a$  or on the right  $b$  hand side (or, in other words, the intersite oxygen vibrations).  $V$  is the parameter of the linear vibronic interaction,  $t$  – the transfer integral and  $F$  is

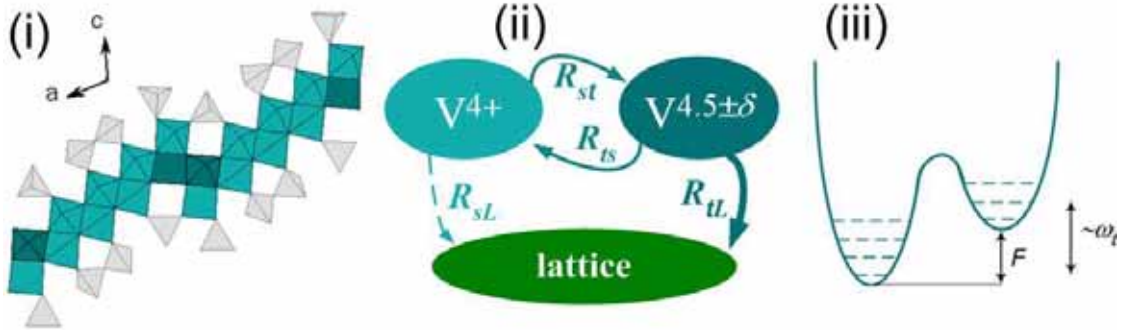


Figure 7.7.: **(i)**: Projection of the  $\eta$ - $\text{Na}_{0/7}\text{V}_2\text{O}_5$  structure onto  $(ac)$ -plane.  $\text{V}^{4.5+\delta}\text{-V}^{4.5-\delta}$  elements are shown by dark-cyan pyramids, the  $\text{V}^{4+}\text{O}_5$  pyramids are light-cyan. **(ii)**: Cross-relaxation scenario. Energy relaxation paths of the  $\text{V}^{4+}$  spins ( $s$ ) and the  $\text{V}^{4.5+\delta}\text{-V}^{4.5-\delta}$  pairs ( $t$ ). **(iii)**: Schematic drawing of the ground vibration states of an electron in a two-well potential.

the molecular field parameter which describes the difference of the crystal field energy of an extra electron on the  $a$  or  $b$  positions. The adiabatic potential

$$U(q) = \frac{M\omega^2}{2}q^2 \pm \sqrt{(Vq + F)^2 + t^2} \quad (7.3)$$

has two minima at some  $q \approx \pm q_0$  as depicted schematically in Fig. 7.7(iii). The electron can migrate from one minimum to the other. The amplitude of the migrating charge is given by

$$\delta = \frac{1}{2}[Vq_0 + F]/\sqrt{[Vq_0 + F]^2 + t^2}. \quad (7.4)$$

If the tunneling frequencies  $\omega_t = 2\sqrt{(Vq + F)^2 + t^2}/\hbar$  are in the range of the phonon spectrum, the very fast relaxation to the lattice occurs via Raman and multi-phonon processes. The corresponding relaxation time will have a power-law temperature dependence  $T_{1f} \sim T^{-\alpha}$  with  $\alpha = 5 \div 9$  [Abragam'70].

In the absence of the fast-relaxing  $\text{V}^{4.5+\delta}\text{-V}^{4.5-\delta}$  centers, the remaining  $\text{V}^{4+}$  spins placed away from structural steps relax more slowly with the relaxation time  $T_{2s}^0$  characteristic for the pure spin-spin relaxation processes. The exchange coupling  $J' \sim J$  of this subsystem to the tunneling spin will accelerate the relaxation. The effect of the additional random torque due to impurities with the fast spin-lattice relaxation rate  $R_{tL}$  on the relaxation rate of a host system (see Fig. 7.7(ii)) was investigated by Nagata *et al.* [Nagata'78]. According to that calculation the linewidth of the host system is given by

$$\Delta H_{\text{cross}} \approx \frac{32 s(s+1)}{3\gamma} \left(\frac{J'}{\hbar}\right)^2 N_f \tau_0, \quad (7.5)$$

where  $N_f$  is the concentration of the fast-relaxing spins  $s$ ,  $\gamma$  – the effective electronic gyromagnetic ratio and  $\hbar$  denotes the Plank's constant. At low temperatures the number of the fast relaxing  $\text{V}^{4.5+\delta} - \text{V}^{4.5-\delta}$  centers  $N_f$  in  $\eta\text{-Na}_{9/7}\text{V}_2\text{O}_5$  reduces exponentially. To estimate the relative number of the CO centers, the intensity of the x-ray signal  $I_{\text{x-ray}}$  represented in Fig. 7.6(ii) can be used. Approximating this temperature dependence by  $N_f(T) \equiv 1 + \tanh\frac{T-85}{15}$  and substituting the explicit temperature dependence of the relaxation time  $\tau_0 = T_{1f}$  we get finally

$$\Delta H_{\text{cross}}(T) \propto N_f \cdot T_{1f} \sim \left(1 + \tanh\frac{T-85}{15}\right) \cdot T^{-\alpha}. \quad (7.6)$$

Fig. 7.6(i) shows that this function can well describe the additional peak on the temperature dependence of  $\Delta H_{b'}$ .

Now the question arises: why does this peak show up only for the magnetic field applied along the  $b'$  direction, whereas for two other crystallographic directions it is considerably suppressed? Fig. 7.5(i) emphasizes the cancelation of the peak by dividing the linewidths by each other, what means the intensity of this peak has the same anisotropy as the main broadening source of the linewidth - anisotropic exchange interaction. In section 2.3 we have discussed that the anisotropy of exchange arises due to spin-orbit (SO) interaction. Du *et al.* [Du'95] has shown SO coupling to be the main source of the orientation dependence of the spin-lattice relaxation rate going via two-phonon Raman processes as well. Qualitatively, it can be explained as follows:

When the external magnetic field is applied along the  $b'$  direction (i. e. along the  $z$  axis of a local  $\text{VO}_5$  pyramid) SO coupling mixes to the ground  $d_{xy}$  state an excited state  $d_{x^2-y^2}$ , the state with the *same* electron spin state. Whereas if the field is applied in the perpendicular plane it adds a contribution from  $d_{xz}$  and  $d_{yz}$ , from the orbital functions with the *opposite* electron-spin state as that of the  $d_{x^2-y^2}$  contribution. Since spin-lattice relaxation requires a change in electron-spin state, relaxation in the second case will be more efficient. Hence, the relaxation time (and consequently the linewidth, see Eq. 7.6) will be larger along the  $b'$  axis as compared to the  $a'$  and  $c'$  directions, in accordance with the experimental observations.

Summing up, we have shown that the peak on the temperature dependence of the linewidth at  $T \sim 86$  K arises due to cross-relaxation of the spin system. This additional relaxation channel is given by the mixed valence elements  $\text{V}^{4.5+\delta} - \text{V}^{4.5-\delta}$  placed on the structural steps. The tunneling motion of the electron causes the very fast relaxation to the lattice, which influences the remaining spin system via the strong isotropic exchange interaction.

Having considered the influence of the CO transition on the ESR line, let us discuss now the results of specific heat and dielectric conductivity measurements, which allow to characterize this transition in more detail. It should be noted, that these measurements were performed on polycrystalline samples because of the very small mass of single crystals available. X-ray and magnetization measurements have shown these samples

to be single-phase, as also the temperature dependence of the ESR line shows all the features presented in single crystals.

### 7.3.2. Changes in Dielectric Conductivity

The results of measurements in the frequency range  $5 \text{ Hz} < \nu < 90 \text{ GHz}$  are summarized in Fig. 7.8. The behavior is dominated by charge transport, a dc conduction, approximately represented by the 5 Hz curve, and an ac contribution increasing with frequency. This contribution exhibits a weaker temperature dependence and can be ascribed to hopping transport of charge carriers. The characteristic barrier energy between these localized states can be estimated on the basis of the presented data to be

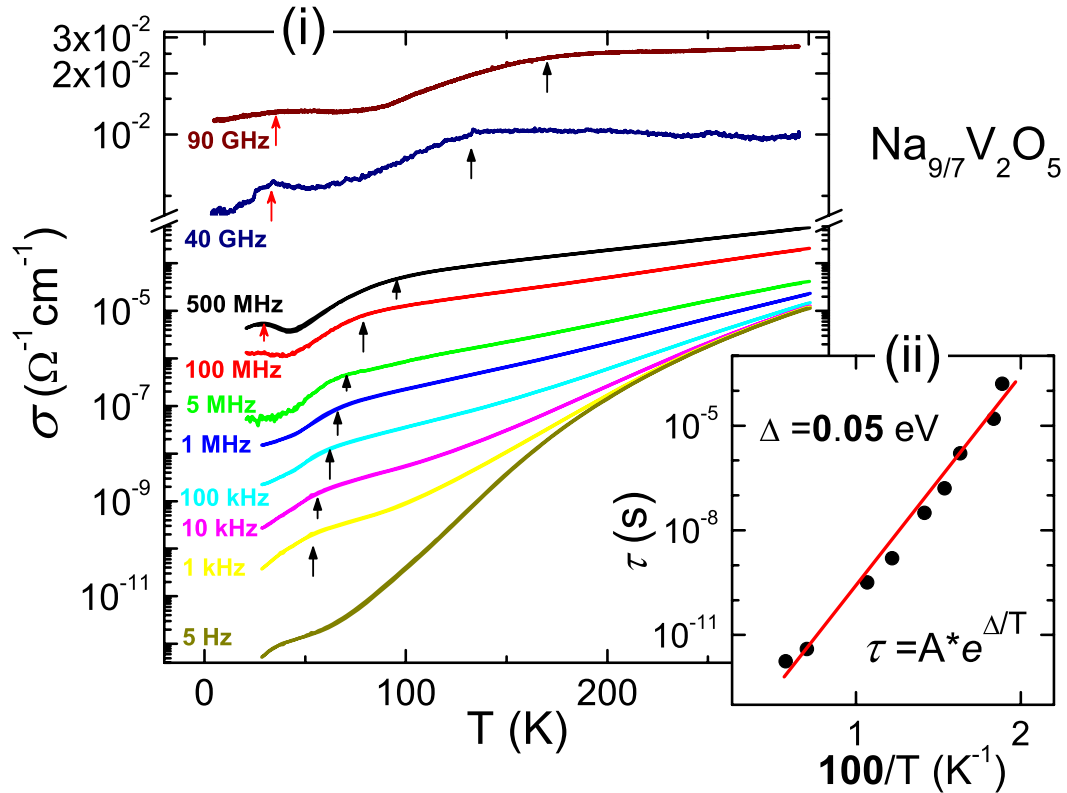


Figure 7.8.: (i): Temperature dependence of the real part of the dielectric conductivity for various frequencies in a polycrystal of  $\eta\text{-Na}_{9/7}\text{V}_2\text{O}_5$ . (ii): Temperature dependence of the relaxation time for the peak denoted by the black arrows in frame (i). The line represents the fit by an exponential function with an activation energy  $\Delta = 0.05 \text{ eV}$ .

about 0.2 eV. However, as indicated by the arrows, superimposed to these contributions there are shoulders, indicating underlying peaks. They shift towards lower temperatures with decreasing frequency. Such a peak represents a typical signature of an additional relaxation mechanism [Fichtl'05].

Most likely, this peak is related to the localization of electrons in the  $\text{V}^{4.5+\delta}\text{-V}^{4.5-\delta}$  pairs taking place in this temperature range. The motion of electrons in those pairs contributes to the ac conductivity at the frequency of their hoppings, which increases with increasing temperature. The plot of the relaxation time  $\tau = 1/2\pi\nu$  for such a peak in the Arrhenius representations would give a straight line for a purely thermally activated process. Fig. 7.8(ii) clearly shows that it is the case in  $\eta\text{-Na}_{9/7}\text{V}_2\text{O}_5$ . Moreover, the slope of  $\tau(T)$  allows to estimate the energy barrier between two  $\text{V}^{4.5+}$  ions (shown as the dark cyan pyramids in Fig. 7.1) as 0.05 eV.

Note, that at 40 GHz (the frequency used in ESR) the peak appears at  $T \sim 140$  K. At this temperature an electron still has enough energy to overcome the barrier between  $\text{V}^{4.5+\delta}\text{-V}^{4.5-\delta}$  sites. At lower temperatures only the tunneling motion is possible, in accordance with ESR data.

The appearance of the second peak denoted by the red arrows in Fig. 7.8(i) is rather unexpected. It may indicate a redistribution of charges at about 30 K (note, that also the susceptibility drops down very sharply at this temperature). But to finally decide about its origin, additional measurements at  $T < 20$  K are necessary.

Finally, we would like to point out that, in contrast to x-ray data (Fig. 7.6(ii)), the changes in dielectric conductivity become remarkable already below 150 K. That indicates the very broad temperature range of preexisting CO fluctuations in this structure. In the next section we will show how it affects the entropy released when going via this transition.

### 7.3.3. Specific Heat Measurements

Figure 7.9(i) shows the central result of this investigation, the heat capacity (given as  $C/T$ ) as function of temperature. At low temperatures  $T < 30$  K the specific heat is characteristic for a three-dimensional solid with a Debye temperature of  $\Theta_D = 152$  K. This contribution arises due to acoustical phonons and has the characteristic  $T^3$  temperature dependence of specific heat at  $T < \Theta_D/10$ .  $\Theta_D$  can be easily estimated from the linear fit of  $C/T$  vs  $T^2$  as it is shown in Fig. 7.9(ii). Using  $\Theta_D = 152$  K we can proceed with the fit of the specific heat in the complete temperature regime investigated. For the fit we will use only the experimentally determined heat-capacity values for  $100 \text{ K} < T < 300 \text{ K}$ , because in the temperature range  $50 \text{ K} < T < 100 \text{ K}$  a structural transition takes place.

As it can be seen from Figure 7.9(i), above  $T \sim 30$  K the contribution of optical phonons becomes remarkable. Introducing two modes of optical phonons, with the Einstein temperatures  $\Theta_{E_1} = 310$  K and  $\Theta_{E_2} = 850$  K, we can describe the total heat

capacity quite well. Note that the spin-chain contribution modelled by Bonner and Fisher (Sec. 3.1.2) is negligible at high temperatures. The difference between calculated and measured heat capacities clearly seen below 100 K allows to estimate the entropy  $\Delta S$  being released at the CO transition to be about  $0.16 R$ . Such a small value of the released entropy is expected, taking into account that only one electron of nine participates in the CO and that CO fluctuations extend over a very wide temperature range.

Perhaps the most striking feature of the results is a considerable linear contribution to the specific heat at low temperatures (see Fig. 7.9(ii)). Such a temperature dependence can (i) result from a residual free-electron contribution or (ii) come from the energy of the  $S = 1/2$ -chain (see Sec. 3.1.2). The first possibility may be excluded, because the dielectric measurements have shown that the electrical conductivity of the sample is negligibly small (Fig. 7.8). It is surprising because the spin structure is assumed [Duc'04] to be fully dimerised at such a low temperature. The estimations of this contribution give nevertheless  $\gamma_{\text{exp}} \approx 5 \text{ mJ/molK}^2$ , approximately 1/6 of the value predicted by the calculations of Bonner and Fisher (Eq. 3.11)

$$\gamma_{\text{Bonn}} = \frac{C(T < \frac{|J|}{10k_{\text{B}}})}{T} = \frac{0.7 R}{|J|/k_{\text{B}}} \approx \frac{5.82 \text{ J/molK}}{200 \text{ K}} \approx 29.1 \text{ mJ/molK}^2 \quad (7.7)$$

for the exchange energy of an infinite  $S = 1/2$  antiferromagnetic chain. If this contribution stems really from some kind of spin chain in this structure, the second prediction by Bonner and Fisher has to be fulfilled as well – an approximately temperature independent contribution to the susceptibility given by Eq. (3.9). In order to verify this assumption, we have to reexamine the susceptibility data published so far.

## 7.4. Exotic Low-Temperature Ground State of $\eta\text{-Na}_{9/7}\text{V}_2\text{O}_5$

The magnetic behavior of  $\eta\text{-Na}_{9/7}\text{V}_2\text{O}_5$  was first examined by Isobe *et al.* [Isobe'99]. They pointed out that such behavior of the susceptibility  $\chi(T)$  is attributable to low-dimensional systems with spin gaps. However, they failed to fit  $\chi(T)$  by theoretical equations for a spin-ladder or a dimer system. Later on, Duc *et al.* [Duc'04] have repeated that measurement supplementing it by ESR data. They claimed the susceptibility goes to zero at very low temperatures. This result was obtained by fitting the low-temperature increase of  $\chi(T)$  by a Curie-Weiss law,  $\chi_{\text{imp}} = C/(T - \theta)$ , with  $\theta = -3.35 \text{ K}$ . However, the mechanism of the gap opening remained unclear because of the odd number of spins per structural unit in  $\eta\text{-Na}_{9/7}\text{V}_2\text{O}_5$ . In this section we will show that the magnetic properties of  $\eta\text{-Na}_{9/7}\text{V}_2\text{O}_5$  can be understood in terms of a spin chain model which explains both the decrease and the low-temperature behavior of the susceptibility. Here, we would like to emphasize that we investigated several high-quality samples. In particular, a kink on  $\chi(T)$  at 102 K, observed in [Duc'04] and associated with the structural and CO transition taking place in this temperature range, turned out to be related to

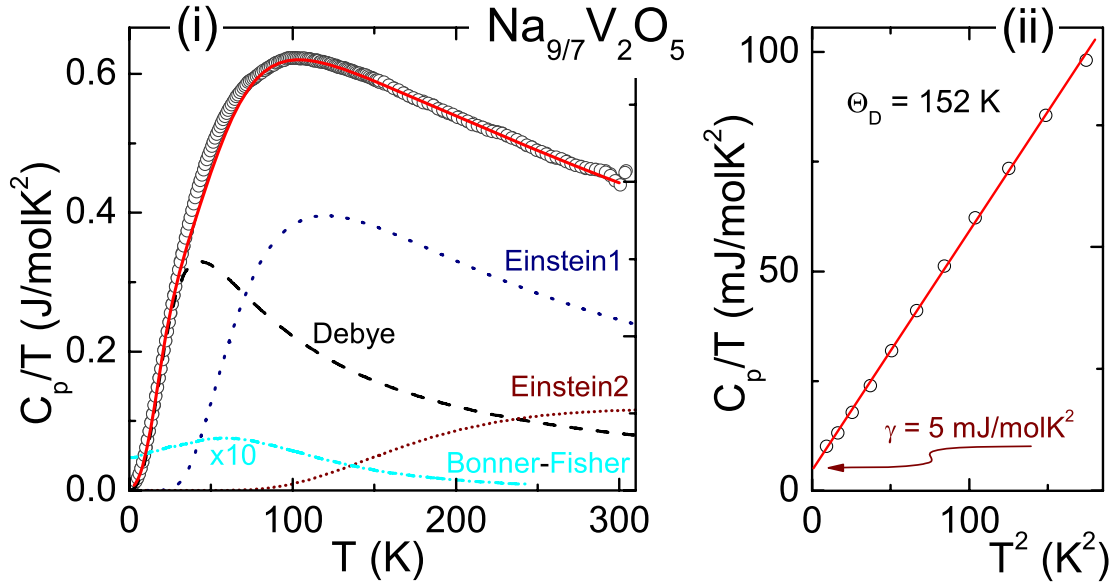


Figure 7.9.: (i): Heat capacity of  $\eta$ - $\text{Na}_{9/7}\text{V}_2\text{O}_5$  plotted as  $C/T$  vs  $T$ . The contribution of acoustical Debye-phonons is indicated by the dashed black line, contributions of two Einstein modes by the blue dot and wine short-dot lines. The expected  $S = 1/2$ -chain contribution (multiplied by a factor of 10) is shown by the cyan dash-dot line. The sum of all contributions (the red solid line) represents the best fit to the experimental results. Frame (ii) emphasizes the Debye and spin-chain contributions at low temperatures.

the presence of ferromagnetic impurities in the samples. The best samples investigated in this work do not reveal this feature.

We have carried out the measurements of the susceptibility under a magnetic field of 0.05 and 5 T. In addition, ESR data were used to characterize the magnetic properties. Fig. 7.10(iii) shows that the renormalized  $I_{\text{ESR}}(T)$  coincides with  $\chi(T)$  at high temperatures very well. Let us concentrate now on the low temperature region  $T < 20$  K where differences between the curves are clearly seen.

An increase of susceptibility to lower temperatures usually arises owing to a small amount of paramagnetic impurities present in the samples. However, in  $\eta$ - $\text{Na}_{9/7}\text{V}_2\text{O}_5$  fitting of the low-temperature data points to a Curie law  $\chi_{\text{imp}}(T) = C/T$  is possible only by introducing an additional temperature independent contribution  $\chi_0$ . There are several possible origins of such a behavior:

- (i) *Saturated ferromagnetic moments.* If the impurity spins present in the sample belong to a ferromagnetic phase, they can be responsible for a temperature independent magnetic 'background'. Their contribution can easily be determined by

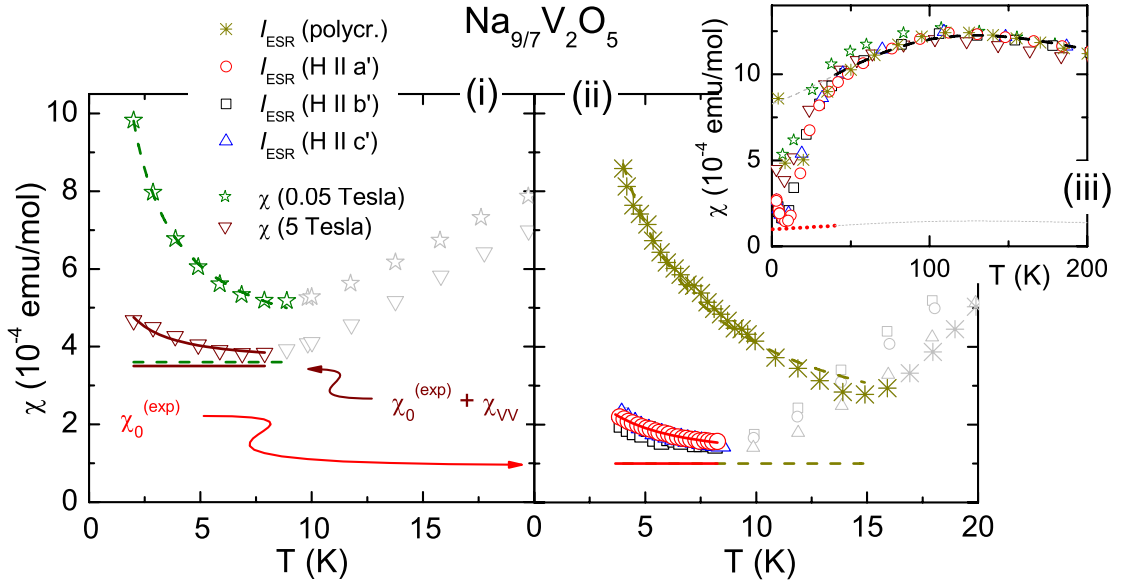


Figure 7.10.: Temperature dependence of the magnetic susceptibility  $\chi$  of  $\eta\text{-Na}_{9/7}\text{V}_2\text{O}_5$ . The lines represent fits by a sum of the Curie  $\chi_C = C/T$  and temperature independent term  $\chi_0$  and emphasize additionally the  $\chi_0$  term. The light gray symbols demonstrate the behavior of  $\chi$  at higher temperatures and are not used for the fit. **(i)**:  $\chi_{\text{SQUID}}(T)$  in a polycrystal measured by SQUID magnetometry under a magnetic field  $H = 0.05$  T (green stars) and  $H = 5$  T (dark-red triangles). **(ii)**: Intensity of the ESR signal  $I_{\text{ESR}}$  in a polycrystal (dark-yellow cross stars) and in a single crystal for the magnetic field applied along the three crystallographic axes. Frame **(iii)** shows that both  $\chi_{\text{SQUID}}$  and  $I_{\text{ESR}}$  coincide at high temperatures. The black dashed line fits  $\chi$  to the Bonner-Fisher curve (Eq. 3.7). The red dotted line is the expected contribution of multi-spin chains at low temperatures.

measurements in different magnetic fields. A hundred times larger magnetic field  $H$  reduces the susceptibility  $\chi = M/H$  of the saturated ferromagnetic moments  $M$  also by a factor of 100. Fig. 7.10(i) shows, however, that the temperature independent background is almost equal for  $\chi$  measured under  $H = 0.05$  and 5 T.

- (ii) *Pauli paramagnetism* is observed in metals and is due to the fact that conduction electrons have magnetic moments that can be aligned with the applied field. The key characteristic of Pauli paramagnetism is that the  $\chi$  value is nearly independent of temperature. But usually it has a very small value. In case of  $\eta\text{-Na}_{9/7}\text{V}_2\text{O}_5$  this contribution is negligible because of a very low conductivity of the sample (see



Fig. 7.8).

- (iii) *Van Vleck paramagnetism*  $\chi_{\text{VV}}$  is another type of paramagnetism that is also nearly independent of temperature. Van Vleck paramagnetism (see Sec. 4.2.3) is associated with thermal excitations to low-lying states. The big advantage of ESR is that the intensity of the absorption signal does not contain that contribution. As one can see in Fig. 7.10(ii) the temperature independent background in  $I_{\text{ESR}}(T)$  is indeed considerably smaller. But it is still remarkable and amounts to  $\chi_0^{(\text{exp})} \approx 1 \cdot 10^{-4}$  emu/mol.
- (iv) To all appearance, only one possible origin of this background is the *spin chain contribution* modelled by Bonner and Fisher (Sec. 3.1.2). It is predicted to be almost temperature independent and finite at zero temperature. Let us discuss it now on a more quantitative basis.

$\eta\text{-Na}_{9/7}\text{V}_2\text{O}_5$  is not a prototypical  $S = 1/2$  spin chain. Its zigzag structure and structural steps are not taken into account in the calculations by Bonner and Fisher. Nevertheless, the predicted temperature dependence of the susceptibility describes the experimental data very well. Fig. 7.3(i) displays a fit of  $I_{\text{ESR}}$  for the magnetic field applied along the  $c'$  axis by the Bonner-Fisher curve (Eq. 3.7). Even charge ordering in the pairs  $\text{V}^{4.5+\delta}\text{-V}^{4.5-\delta}$  at temperatures  $50 \text{ K} < T < 100 \text{ K}$  does not seem to affect the magnetic properties of the spin chains significantly. According to Eqs. (3.8) and (3.9), the value of  $\chi(T = 0)$  is expected to be

$$\chi_0^{(\text{Bonn})} = \frac{0.101322}{0.147} \cdot \chi_{\text{max}} \approx 0.69 \cdot \chi_{\text{max}} \approx 8.28 \cdot 10^{-4} \text{ emu/mol}, \quad (7.8)$$

where we have used the experimental value of  $\chi_{\text{max}} \approx 12 \cdot 10^{-4}$  emu/mol (Fig. 7.10(iii)).

However, at lower temperatures considerable deviations of the susceptibility from the Bonner-Fisher behavior are observable.  $\chi(T)$  decreases rapidly at  $T \sim 30 \text{ K}$  and the experimental temperature independent contribution to susceptibility  $\chi_0^{(\text{exp})}$  is only 12% of the expected value. It is useful to recall at this point that the linear contribution to the specific heat  $\gamma_{\text{exp}}$ , the second prediction made by Bonner and Fisher for a spin chain, amounts in  $\eta\text{-Na}_{9/7}\text{V}_2\text{O}_5$  to 17% of the theoretically expected value  $\gamma_{\text{Bonn}}$ .

Note, that both of these predictions were made using the high-temperature value of the exchange constant  $J$ . However, its magnitude as well as the number of spins  $N$  sharing in the thermal and magnetic properties can be different in the low-temperature phase. Both of these quantities depend only on the ratio of  $N$  and  $J$  (cf. Eqs. 3.9 and 3.11)

$$\chi_0^{(\text{Bonn})} = \frac{g^2 \mu_{\text{B}}^2}{\pi^2} \cdot \left( \frac{N}{J} \right), \quad \gamma_{\text{exp}} = 0.7 k_{\text{B}}^2 \cdot \left( \frac{N}{J} \right). \quad (7.9)$$

Therefore, only the change of this ratio can be determined comparing the expected and experimental values of  $\chi$  and  $\gamma$  in the high- and low-temperature phase of  $\eta\text{-Na}_{9/7}\text{V}_2\text{O}_5$ .

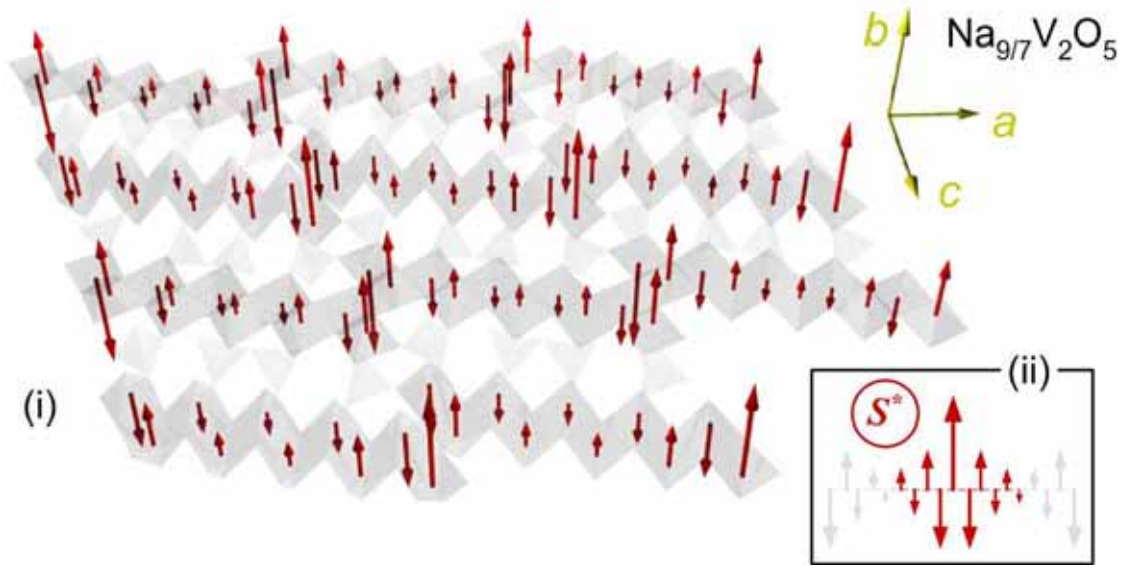


Figure 7.11.: **(i)**: Schematic spin structure of the proposed ground state in  $\eta$ - $\text{Na}_{9/7}\text{V}_2\text{O}_5$  at  $T \lesssim 10$  K. Overlap of the local antiferromagnetic spin clusters (ten lattice sites with a net magnetic moment of  $\mu_B$ ) gives rise to a spin chain with long-range AFM order. All spins (red arrows) occupy the  $\text{VO}_5$  pyramids (medium gray). These chains are separated along the  $c$  and  $b$  axes by non-magnetic  $\text{V}^{5+}\text{O}_4$  tetrahedra (light grey) and Na ions (not shown), respectively. **(ii)**: Schematic representation of the spin structure which appears near an unpaired spin. The arrows represent the average spin projections at the lattice sites.

Taking  $1/7 \approx 0.143$  as an average value between 0.12 and 0.17 obtained from the susceptibility and the specific heat data, respectively, we get

$$\frac{N^*}{J^*} = \frac{1}{7} \cdot \frac{N}{J} \quad \rightarrow \quad \frac{J^*}{J} = 7 \cdot \frac{N^*}{N}. \quad (7.10)$$

In other words, the exchange integral in the low-temperature phase  $J^*$  normalized to its high-temperature value  $J$  is by a factor of 7 larger than the respective change in the number of spins.

For example, if we assume that the spin dimerization takes place in  $\eta$ - $\text{Na}_{9/7}\text{V}_2\text{O}_5$  at  $T \sim 30$  K and only one spin survives on each structural element  $N^*/N = 1/9$ , the exchange constant between them along the chain would be  $J^* = 7/9 \cdot J$ , still comparable to the one in the non-dimerized state. Obviously, such a large value of the exchange integral is impossible if some of spins building a chain are fully dimerized and break it off.

Nevertheless, the large value of exchange integral can be understood, if we take into account the onset of the local staggered magnetization near a non-dimerized spin. The formation of such "spin clusters", shown schematically in Fig. 7.11(ii), is confirmed theoretically [Fukuyama'96] near the ends of spin chain segments in the diamagnetically diluted  $\text{CuGeO}_3$  and experimentally in the  $\text{Cu}_{1-x}\text{Mg}_x\text{GeO}_3$  [Glazkov'05] and  $\text{Pb}(\text{Ni}_{1-x}\text{Mg}_x)_2\text{V}_2\text{O}_8$  [Smirnov'02]. The spins within these clusters have nonzero average spin projections with a net magnetic moment equal to  $\mu_B$ . The length  $L$  of such a cluster (the extension of short range antiferromagnetic ordering) along the chain direction depends on temperature

$$JS^2 e^{-2L/\xi} \sim k_B T \quad (7.11)$$

and is of the order of the correlation length  $\xi$ , which is estimated to be of about ten interspin distances.

In  $\eta\text{-Na}_{9/7}\text{V}_2\text{O}_5$  each structural segment possesses an odd number of spins. Hence, one of them (every ninth one) is uncompensated and serves as an impurity spin  $S^* = 1/2$ . This magnetic moment will spread out on the neighboring spins building spin clusters. Note, that the resulting clusters overlap strongly because the characteristic magnetic correlation length is of the order of the segment length. Therefore, the order parameter has to be coherent along the whole chain (see Fig. 7.11). The magnetic and thermal properties of this effectively antiferromagnetic chain consisting of such multi-spin clusters are expected to be quantitatively different from the original chain because of the considerably smaller average magnetic moment on each site  $S_{\text{aver}} = S^*/10$ . But the exchange energy of this structure with an almost unchanged local exchange constant can still produce a linear contribution to the specific heat and a temperature independent contribution to the susceptibility. The experimental results evidence the presence of these contributions. They are about one order of magnitude smaller than the values expected for the full  $S = 1/2$  chain realized at high-temperatures, in accordance with the theoretical considerations.

The proposed multi-spin state successfully explains the puzzling controversy between the originally suggested singlet ground state and the odd number of spins per unit cell in the structure. Note that in the case observed in doped spin-Peierls and Haldane chains [Glazkov'05, Smirnov'02], these spin clusters are diluted and randomly distributed in the lattice. That gives rise to impurity induced local magnetic order and phase separation. In contrast,  $\eta\text{-Na}_{9/7}\text{V}_2\text{O}_5$  provides a regular lattice of such spin clusters, what leads to the formation of a new exotic ground state, not observed before.

## 7.5. Summary

In this chapter we have presented a detailed study of the spin-relaxation mechanisms in  $\eta\text{-Na}_{9/7}\text{V}_2\text{O}_5$ . Basing on the angular and temperature dependencies of the ESR linewidth we identify the dominant spin-relaxation mechanism at high temperatures to

be the symmetric anisotropic exchange, whereas at  $T < 60$  K it changes to the anti-symmetric anisotropic interaction. The measurements of the specific heat and dielectric conductivity allow to estimate the entropy released by the charge-ordering transition at  $60 \text{ K} < T < 100 \text{ K}$  and the energy barrier between two sites where the charge ordering takes place. Additionally, the temperature dependence of the ESR linewidth gives the possibility to address the cross-relaxation of the spin system via mixed-valence pairs  $\text{V}^{4.5+\delta}\text{-V}^{4.5-\delta}$ .

In contrast to previous studies, we present evidence that the dimerization of spins is far from complete at  $T < 10$  K, and the unpaired vanadium spins give a constant contribution to the susceptibility and a linear contribution to the specific heat. The ground state of  $\eta\text{-Na}_{9/7}\text{V}_2\text{O}_5$  can be understood in terms of "multi-spin clusters" building a linear chain along the crystallographic  $a$  axis.



## 8. Conclusions and Perspectives

The spin relaxation mechanisms were considered in three one-dimensional spin systems –  $\alpha'$ - $\text{NaV}_2\text{O}_5$ ,  $\text{TiOCl}$  and  $\eta$ - $\text{Na}_{9/7}\text{V}_2\text{O}_5$  – by using electron spin resonance spectroscopy. A close similarity of the relaxation behavior was observed and explained as due to anisotropic exchange interactions. All experimental data were successfully described on the basis of the microscopical theory of superexchange. This treatment allowed not only to determine the form but also to estimate the magnitude of the dominant exchange interaction.

Calculation of the broadening sources of the electron spin resonance line in  $\alpha'$ - $\text{NaV}_2\text{O}_5$ , using the suggested microscopical analysis, gave an unexpected result. The symmetric exchange of a particular type, with simultaneous spin-orbit coupling on both magnetic sites, was found to play the major role in spin relaxation. The corresponding exchange constant is almost two orders of magnitude larger than the one obtained from conventional estimations [Moriya'60]. Based on this result we systematically evaluated the anisotropy of the electron spin resonance linewidth in the whole paramagnetic range in terms of the symmetric anisotropic exchange only.

Having this information at hand and taking into account the recent theoretical achievements [Oshikawa'02] we were able to determine the contribution of the Dzyaloshinsky-Moriya interaction in  $\text{TiOCl}$ . We described the temperature dependence of the linewidth as due to the competition of symmetric and antisymmetric anisotropic exchange and show that the non-staggered Dzyaloshinsky-Moriya interaction broadens the linewidth towards lower temperatures as well as the staggered one. Additionally, the anisotropy of the resonance field indicates a stable orbital configuration below room temperature and allows us to estimate the energy of the first excited state, ruling out a possible degeneracy of the orbital ground state.

The universal relaxation behavior due to anisotropic exchange in spin chains enables to study more complex systems. An advanced example of application of this knowledge is given by  $\eta$ - $\text{Na}_{9/7}\text{V}_2\text{O}_5$ . The electron spin resonance data allow to address the spin-gap opening process and to investigate the cross-relaxation via the mixed-valent segments of the structure. Moreover, combining the results of specific heat, susceptibility, electron spin resonance and dielectric conductivity measurements we show that the gapped ground state can be understood in terms of multi-spin objects building up a linear chain. In spite of the small total spin, their spatial extent results in an exchange constant comparable to the one in the non-dimerized state.

An outstanding challenge for further study is given by  $\text{KCuF}_3$ . This perovskite system

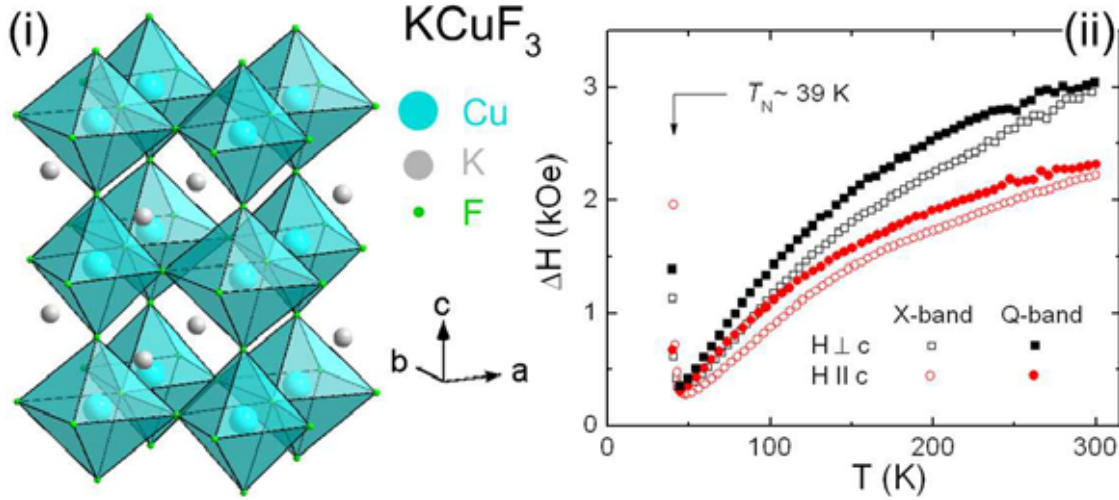


Figure 8.1.: (i): Crystal structure of  $\text{KCuF}_3$ . (ii): Temperature dependence of the ESR linewidth at X- ( $\nu \approx 9.34$  GHz) and Q-band ( $\nu \approx 34$  GHz) frequencies.

(see Fig. 8.1(i)) is presumably one of the best inorganic realizations of a one-dimensional antiferromagnetic Heisenberg chain. This fact is even more astonishing, because the effective magnetic dimensionality is a direct consequence of the orbital ordering in this compound [Kugel'72]. Recently, it has been shown by a detailed inelastic neutron scattering investigation that fingerprints of a Luttinger liquid, namely the spinon excitation continuum, exist up to temperatures of about 200 K [Lake'05]. Moreover, these specifically one-dimensional features are still observable below the antiferromagnetic ordering at  $T_N = 39$  K, indicating the strong quantum nature of magnetism in  $\text{KCuF}_3$ . Surprisingly, even the high-temperature crystal structure of this compound is not known at the moment exactly [Hidaka'98]. In this regard, the correct microscopical description of the electron spin resonance data (Fig. 8.1(ii)) may play a decisive role, resolving the up to now puzzling inconsistencies between the magnetic [Yamada'94] and crystallographic [Hidaka'98] structures and, consequently, for the whole physics related to this prototypical system.

# Appendix A. Canonical-Transformations Perturbation Method

The Hamiltonian of the electronic subsystem can be expressed as

$$\mathcal{H} = \sum \langle i\alpha|h|j\beta\rangle c_{i\alpha}^+ c_{j\beta} + \frac{1}{2} \sum \langle i\alpha_1 j\beta_2|g_{12}|k\alpha'_1 l\beta'_2\rangle c_{i\alpha}^+ c_{j\beta}^+ c_{k\alpha'} c_{l\beta'}, \quad (\text{A.1})$$

where  $i, j, k, l$  represent the lattice sites, and greek letters indicate the orbital substates of a shell.  $c_{i\alpha}^+$  is a fermion operator in the second quantization and creates an electron at the site  $i$  in the state  $\alpha$ ,  $c_{i\alpha}$  is the annihilation operator for the same electron. The localized orbitals  $\phi_{i\alpha}$  are assumed to form a complete orthogonal set.

We divide  $\mathcal{H} = \mathcal{H}_0 + V$  into the unperturbed Hamiltonian  $\mathcal{H}_0$  and the perturbation  $V$  with

$$V = \sum \langle i\alpha|\delta h|j\alpha'\rangle c_{i\alpha}^+ c_{j\alpha'} + \frac{1}{2} \sum \langle i\alpha_1 j\beta_2|\delta g_{12}|k\alpha'_1 l\beta'_2\rangle c_{i\alpha}^+ c_{j\beta}^+ c_{l\beta'} c_{k\alpha'}, \quad (\text{A.2})$$

where

$$\delta h = h - \tilde{h}, \quad \langle i\alpha|\tilde{h}|j\alpha'\rangle = \delta_{i\alpha, j\alpha'} \sum \delta_{\bar{\alpha}\bar{\beta}} \frac{\langle i\beta|h|j\beta\rangle}{2[\bar{\beta}]}, \quad (\text{A.3})$$

and

$$\delta g_{12} = g_{12} - \tilde{g}_{12}, \quad (\text{A.4})$$

$$\langle i\alpha_1 j\beta_2|\tilde{g}_{12}|k\alpha'_1 l\beta'_2\rangle = \delta_{i\alpha, k\alpha'} \delta_{j\beta, l\beta'} \sum \delta_{\bar{\alpha}\bar{\tau}} \delta_{\bar{\beta}\bar{\tau}} \langle i\tau'_1 j\tau_2|g_{12}^{\alpha\beta}|i\tau'_1 j\tau_2\rangle, \quad (\text{A.5})$$

$$g_{12}^{\alpha\beta} = \frac{g_{12} (1 - \mathcal{P}_{12})}{2[\bar{\beta}] (2[\bar{\alpha}] - \delta_{\bar{\alpha}, \bar{\beta}})}. \quad (\text{A.6})$$

Here  $[\bar{\alpha}]$ ,  $[\bar{\beta}]$  are the orbital degeneracy or the number of states in the subshell (so that the subshell  $\bar{\alpha}$  is complete when the number of electrons is equal to  $2[\bar{\alpha}]$ ). The operator  $\mathcal{P}_{12}$  exchanges two electrons, and the eigenvalues of  $\mathcal{H}_0$  are the average energies of the electrons in the Hartree-Fock approximation.

The perturbation  $V$  can be rewritten as a sum of two terms  $V = V^{(1)} + V^{(2)}$ .  $V^{(2)}$  is the part of the Hamiltonian with nonzero matrix elements between the excited (with electron transfer) and ground (with some electron excitations on the same site) state configurations. In other words, using the definitions introduced in Fig. A.1,  $V_{mm'}^{(2)} \equiv V_{ll'}^{(2)} \equiv 0, V_{ml}^{(2)} \neq 0$ . Note that the energy scheme pointed out in Fig. A.1 corresponds to



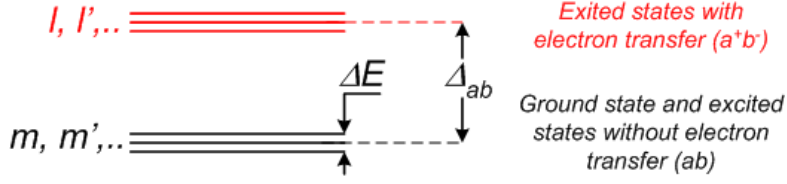


Figure A.1.: Sketchy energy schema supposed in our analysis. Possible on-site excitations (denoted by  $m, m', ..$ ) have a much smaller energy compared to the excitation with transfer to the neighboring site (denoted by  $l, l', ..$ ).

the large energy distance between the excited and ground states  $\Delta_{ab}$  with respect to the energy splitting of each of them  $\Delta E \ll \Delta_{ab}$ , what is usually very well fulfilled in real systems. The case  $\Delta E \sim \Delta_{ab}$  is briefly discussed in chapter 2.2.4.

Hoppings of electrons to the other site can be described by

$$V^{(2)} = \sum t_{i\alpha, j\beta} c_{i\alpha}^+ c_{j\beta}, \quad (\text{A.7})$$

where  $t_{i\alpha, j\beta}$  are the transfer integrals determined by

$$t_{i\alpha, j\beta} = \langle i\alpha | h | j\beta \rangle + \sum \frac{n_{\bar{\tau}}}{2[\bar{\tau}]} \langle i\alpha_1 l \tau_2 | g_{12} (1 - \mathcal{P}_{12}) | j\beta_1 l \tau_2 \rangle. \quad (\text{A.8})$$

Here  $n_{\bar{\tau}}$  is the number of electrons in the shell  $\bar{\tau}$ .

The operator  $V^{(1)}$  contains all interactions which do not change the number of electrons on site. Therefore, it acts within quasi-degenerate states of excited and ground-state configurations:  $V_{ml}^{(1)} \equiv 0, V_{mm'}^{(1)} \neq 0, V_{ll'}^{(1)} \neq 0$ . The most important of them are the Coulomb interaction and the crystal field:

$$V^{(1)} = \frac{1}{2} \sum \langle i\alpha_1 i\beta_2 | \delta g_{12} | i\alpha'_1 i\beta'_2 \rangle c_{i\alpha}^+ c_{i\beta}^+ c_{i\beta'} c_{i\alpha'} + \langle i\alpha | \delta h | i\alpha' \rangle c_{i\alpha}^+ c_{i\alpha'}. \quad (\text{A.9})$$

Here we would like to emphasize, that in an excited state (with changed number of electrons on the site) the crystal field can be much larger than in the ground state.

In order to take into account the electron transfers we employ the canonical Schrieffer-Wolff transformations: i. e. we transform the initial Hamiltonian  $\mathcal{H}$  by using an unitary operator  $e^{-S} = \sum_{n=0}^{\infty} \frac{1}{n!} S^n$  into the effective exchange Hamiltonian

$$\mathcal{H}_{\text{eff}} = e^{-S} \mathcal{H} e^S = \mathcal{H} + [\mathcal{H}, S] + \frac{1}{2} [[\mathcal{H}, S], S] + \frac{1}{6} [[[\mathcal{H}, S], S], S] + \dots = \sum_{n=0}^{\infty} \frac{1}{n!} [\mathcal{H}, S]^{(n)}. \quad (\text{A.10})$$

The Hamiltonian  $\mathcal{H}_{\text{eff}}$  describes all effects of spin exchange between different sites. By a peculiar choice of the  $S$  matrix we can cancel all hopping terms of this Hamiltonian

$(\mathcal{H}_{\text{eff}})_{lm} \equiv 0$ , thereby describing the effects of the electron transfer as a perturbation to the ground state energy of localized spin. This approximation assumes naturally that  $V^{(2)}, V^{(1)} \ll \Delta_{ab}$ , what is usually well fulfilled.

For determination of the  $S$ -matrix we perform the following iteration procedure

$$S = S^{(1)} + S^{(2)} + S^{(3)} + S^{(4)} + S^{(5)}, \quad (\text{A.11})$$

where the indices 1, 2, .. correspond to the order of perturbation theory. By this transformation the hopping terms  $V_{ml}^{(2)}$  vanish in the new basis if:

$$\begin{aligned} [\mathcal{H}_0, S^{(1)}] &= -V^{(2)}, \\ [\mathcal{H}_0, S^{(2)}] &= -[V^{(1)}, S^{(1)}], \\ [\mathcal{H}_0, S^{(3)}] &= -[V^{(1)}, S^{(2)}] - \frac{1}{3}[[V^{(2)}, S^{(1)}], S^{(1)}], \\ [\mathcal{H}_0, S^{(4)}] &= -[V^{(1)}, S^{(3)}] - \frac{1}{3}[[V^{(2)}, S^{(1)}], S^{(2)}] - \frac{1}{3}[[V^{(2)}, S^{(2)}], S^{(1)}], \\ [\mathcal{H}_0, S^{(5)}] &= -[V^{(1)}, S^{(4)}] - \frac{1}{3}[[V^{(2)}, S^{(1)}], S^{(3)}] - \frac{1}{3}[[V^{(2)}, S^{(3)}], S^{(1)}] - \\ &\quad - \frac{1}{3}[[V^{(2)}, S^{(2)}], S^{(2)}] + \frac{1}{45}[[[[V^{(2)}, S^{(1)}], S^{(1)}], S^{(1)}], S^{(1)}]. \end{aligned} \quad (\text{A.12})$$

These equations give us the following expressions for the matrix  $S$ :

$$\begin{aligned} S_{ml}^{(1)} &= -\frac{V_{ml}^{(2)}}{E_m^{(0)} - E_l^{(0)}} \equiv -\frac{V_{ml}^{(2)}}{\Delta_{ml}}, \\ S_{ml}^{(2)} &= -\frac{[V^{(1)}, S^{(1)}]_{ml}}{\Delta_{ml}} = \frac{1}{\Delta_{ml}} \left[ \sum_{m'} \frac{V_{mm'}^{(1)} V_{m'l}^{(2)}}{\Delta_{m'l}} - \sum_{l'} \frac{V_{ml'}^{(2)} V_{l'l}^{(1)}}{\Delta_{ml'}} \right], \\ S_{ml}^{(3)} &= \frac{1}{\Delta_{ml}} \left[ -\sum_{m'm''} \frac{V_{mm'}^{(1)} V_{m'm''}^{(1)} V_{m''l}^{(2)}}{\Delta_{m'l} \Delta_{m''l}} - \sum_{l'l''} \frac{V_{ml''}^{(2)} V_{l'l''}^{(1)} V_{l'l}^{(1)}}{\Delta_{ml'} \Delta_{ml''}} + \right. \\ &\quad \left. + \sum_{l'm'} \frac{1}{\Delta_{m'l'}} \left( \frac{1}{\Delta_{ml'}} + \frac{1}{\Delta_{m'l}} \right) V_{mm'}^{(1)} V_{m'l'}^{(2)} V_{l'l}^{(1)} + \right. \\ &\quad \left. + \frac{1}{3} \sum_{nl'} \left( \frac{2}{\Delta_{ml'} \Delta_{nl}} - \frac{1}{\Delta_{l'n} \Delta_{nl}} - \frac{1}{\Delta_{ml'} \Delta_{l'n}} \right) V_{ml'}^{(2)} V_{l'n}^{(2)} V_{nl}^{(2)} \right], \dots \end{aligned} \quad (\text{A.13})$$

Putting the relations (A.11-A.12) into the Eq. (A.10), one gets for the effective exchange operator

$$\mathcal{H}_{\text{eff}} = \mathcal{H}_0 + V^{(1)} + \frac{1}{2}[V^{(2)}, S] - \frac{1}{24}[[[V^{(2)}, S], S], S] + \frac{1}{144}[[[[[V^{(2)}, S], S], S], S], S]. \quad (\text{A.14})$$

This is the most general form of the interaction Hamiltonian including all terms up to the sixth order of the perturbation theory.

Eq. (A.14) is very convenient for estimations of exchange integrals. In order to demonstrate it, we will give the corresponding expression for the integral of isotropic exchange  $\mathcal{H}_{\text{iso}} = J(\mathbf{S}_a \cdot \mathbf{S}_b)$

$$J = \frac{1}{2S_a S_b} \left[ \sum J_{\eta\zeta} + \sum J_{\eta\zeta}(\mu) + \sum J_{\eta\zeta}(\nu) \right] \quad (\text{A.15})$$

between two magnetic ions in the ground states with the maximal spin values.  $J_{\eta\zeta}$  are the individual channel contributions for pairs of half-filled orbitals  $\eta$  and  $\zeta$  of the ions  $a$  and  $b$ , respectively (see Fig. 2.2). The exchange integrals  $J_{\eta\zeta}(\mu)$  and  $J_{\eta\zeta}(\nu)$  may be called correlation integrals, since they depend on the spatial distribution of the electrons of vacant ( $\mu$ ) and filled shells ( $\nu$ ) of interacting ions. After substituting necessary terms instead of  $V^{(1)}$  (Eq. A.9) and  $V^{(2)}$  (Eq. A.7) into (Eq. A.14), the quantities  $J_{\eta\zeta} = J_{\eta\zeta}(a \rightarrow b) + J_{\zeta\eta}(b \rightarrow a)$  read [Eremin'90]

$$\begin{aligned} J_{\zeta\eta}(b \rightarrow a) = & -\frac{1}{2} \langle \eta_1 \zeta_2 | g_{12} | \zeta_1 \eta_2 \rangle + |B_{\zeta\eta}|^2 \Delta_{\zeta\eta} - \sum_{\kappa\rho} M_{\eta\kappa} \langle \zeta_1 \kappa_2 | g_{12} | \eta_1 \rho_2 \rangle M_{\rho\zeta} - \\ & - \sum_{\kappa} \left[ \langle \zeta_1 \eta_2 | g_{12} | \kappa_1 \eta_2 \rangle M_{\kappa\zeta} - M_{\zeta\kappa} \langle \kappa_1 \eta_2 | g_{12} | \eta_1 \zeta_2 \rangle \right] - \sum_{\kappa\rho} M_{\zeta\kappa} M_{\rho\zeta} \langle \eta_1 \kappa_2 | g_{12} | \rho_1 \eta_2 \rangle + \\ & + \sum_{\kappa} M_{\eta\kappa} M_{\kappa\zeta} B_{\zeta\eta} (\Delta_{\zeta\eta} + \Delta_{\kappa\zeta} + \Delta_{\kappa\eta}) + \\ & + \sum_{\kappa\rho} M_{\eta\kappa} M_{\kappa\zeta} M_{\zeta\rho} M_{\rho\eta} \left[ \frac{\Delta_{\kappa\zeta} \Delta_{\rho\zeta}}{\Delta_{\zeta\eta}} + \frac{(\Delta_{\rho\eta} + \Delta_{\kappa\zeta})(\Delta_{\rho\zeta} + \Delta_{\kappa\eta})}{2\Delta_{\eta\kappa\rho\zeta}} \right] - \\ & - \sum_{\kappa\rho} M_{\eta\kappa} M_{\kappa\zeta} M_{\zeta\rho} M_{\rho\eta} \frac{(\Delta_{\rho\eta} + \Delta_{\kappa\zeta})(\Delta_{\rho\zeta} + \Delta_{\kappa\eta})}{2|\Delta_{\eta\kappa\rho\zeta}|^2} \langle \kappa_1 \rho_2 | \delta g_{12} | \rho_1 \kappa_2 \rangle. \end{aligned} \quad (\text{A.16})$$

This expression includes all types of contributions: direct exchange, indirect Yamashita-Kondo's exchange, Kramers's exchange, Anderson's superexchange (see chapter 2.1.2). The introduced dimensionless quantities  $M_{\eta\kappa} = t_{\eta\kappa}/\Delta_{\eta\kappa}$  and  $B_{\zeta\eta}$  can be expressed in terms of overlap integrals  $S_{\eta\kappa}$  and covalence parameters  $\gamma_{\eta\kappa}$  by the following relations:

$$\begin{aligned} M_{\eta\kappa} &= -\left( \gamma_{\eta\kappa} + \frac{S_{\eta\kappa}}{2} \right), \\ B_{\zeta\eta} &= -\left( \gamma_{\zeta\eta} + \frac{S_{\zeta\eta}}{2} \right) + \frac{1}{2} \sum_{\kappa} \frac{|\Delta_{\kappa\zeta}|}{|\Delta_{\zeta\eta}|} \left( \gamma_{\zeta\kappa} + \frac{3}{4} S_{\zeta\kappa} \right) S_{\kappa\eta} + \frac{1}{2} \sum_{\kappa} S_{\zeta\kappa} \left( \gamma_{\kappa\eta} + \frac{3}{4} S_{\kappa\eta} \right) \frac{|\Delta_{\kappa\eta}|}{|\Delta_{\zeta\eta}|}. \end{aligned} \quad (\text{A.17})$$

All parameters entering into these expressions can be determined from the experimental data obtained by electron-nuclear double resonance and optic measurements. Formulas for estimates of  $J_{\eta\zeta}(\mu)$  and  $J_{\eta\zeta}(\nu)$  are given in [Eremin'83].

The term corresponding to the Anderson's model of exchange interaction (chapter 2.2.1) can be written in accordance with (A.16) as

$$\mathcal{H}_{\text{iso}}(b \rightarrow a) = \sum \frac{t_{\kappa\eta'} c_{\kappa}^+ a_{\eta'} \cdot t_{\zeta\kappa'} b_{\zeta}^+ c_{\kappa'} \cdot t_{\rho\zeta'} c_{\rho}^+ b_{\zeta'} \cdot t_{\eta\rho'} a_{\eta}^+ c_{\rho'}}{\Delta_{\kappa\eta'} \Delta_{\kappa\kappa'} \Delta_{\kappa\zeta'}}. \quad (\text{A.18})$$

The shell of the intervening diamagnetic ions (e.g.  $\text{O}^{2-}$ ,  $\text{F}^-$ ) is assumed to be fully filled, i.e. in the initial ground state there are always two electrons with opposite spins on the  $p$  (or  $s$ ) orbital of the ligand ion. Therefore, the following relations can be used to simplify the Hamiltonian (A.18):

$$c_{\kappa}^+ c_{\kappa'} = \delta_{\kappa\kappa'}, \quad c_{\kappa}^+ c_{\rho}^+ c_{\rho'} c_{\kappa'} = \delta_{\kappa\kappa'} \delta_{\rho\rho'} - \delta_{\kappa\rho'} \delta_{\rho\kappa'}. \quad (\text{A.19})$$

The result is given by

$$\mathcal{H}_{\text{iso}}(b \rightarrow a) = \frac{1}{\Delta_{ca}^2 \Delta_{ab}} \sum t_{\kappa\eta'} t_{\zeta\kappa} t_{\rho\zeta'} t_{\eta\rho} \cdot a_{\eta'} b_{\zeta}^+ b_{\zeta'} a_{\eta}^+, \quad (\text{A.20})$$

where  $\Delta_{ab}(\Delta_{ca})$  denote the energy of the electron transfer between the magnetic ions (between the diamagnetic and magnetic ions). That energy can be factored out, because it is large with respect to the distance between the orbital levels. Obviously, the electron does not change its spin at hopping that results in additional conditions:  $s_{\eta'} = s_{\zeta}$  and  $s_{\eta} = s_{\zeta'}$ . Then, using the usual relations between the spin operators  $s^{(z)}$ ,  $s^{\pm} \equiv s^{(x)} \pm i s^{(y)}$  and the Fermi operators  $a_{s^{(z)}}^+$ ,  $a_{s^{(z)}}$ :

$$s^{(z)} = \frac{1}{2} (a_{\uparrow}^+ a_{\uparrow} - a_{\downarrow}^+ a_{\downarrow}), \quad s^+ = a_{\uparrow}^+ a_{\downarrow}, \quad s^- = a_{\downarrow}^+ a_{\uparrow}, \quad (\text{A.21})$$

and  $a_{\uparrow}^+ a_{\uparrow} + a_{\downarrow}^+ a_{\downarrow} = 1$ , we obtain finally

$$\mathcal{H}_{\text{iso}}(b \rightarrow a) = \frac{1}{\Delta_{ca}^2 \Delta_{ab}} \sum t_{\eta\rho} t_{\rho\zeta'} t_{\zeta\kappa} t_{\kappa\eta'} \left( -\frac{1}{2} + 2(\mathbf{s}_a \cdot \mathbf{s}_b) \right), \quad (\text{A.22})$$

in accordance with the classical Anderson's result [Anderson'55]. The values of hopping integrals entering this expression can be estimated, e. g., using the LDA+U approach [Yaresko'02] or from magnetic susceptibility data.

Use of the perturbation theory allows to describe the anisotropy of exchange interaction, too. The spin-orbit (SO) interaction (2.17) which provides coupling to the lattice is going into the effective exchange Hamiltonian (A.14) as an additional on-site perturbation  $V^{(1)} = \mathcal{H}_{LS}$  beside four hopping terms  $V^{(2)}$ . The resulting expressions corresponding to the fifth

$$\mathcal{H}_{\text{eff}}^{(5)} \propto \sum_{m'} \left( \mathcal{H}_{\text{eff}}^{(4, \text{hop})} \right)_{mm'} \cdot \frac{V_{m'm}^{(1)}}{\Delta_{mm'}} = \sum_{lnl'm'} \frac{V_{ml}^{(2)} V_{ln}^{(2)} V_{nl'}^{(2)} V_{l'm'}^{(2)}}{\Delta_{ml} \Delta_{ln} \Delta_{nl'}} \cdot \frac{V_{m'm}^{(1)}}{\Delta_{mm'}}, \quad (\text{A.23})$$

and the sixth orders of perturbation theory

$$\mathcal{H}_{\text{eff}}^{(6)} \propto \sum_{m'm''l'l'n} \frac{V_{mm'}^{(1)}}{\Delta_{mm'}} \cdot \frac{V_{m'l}^{(2)} V_{ln}^{(2)} V_{n'l'}^{(2)} V_{l'm''}^{(2)}}{\Delta_{m'l} \Delta_{ln} \Delta_{n'l'}} \cdot \frac{V_{m''m}^{(1)}}{\Delta_{mm''}}. \quad (\text{A.24})$$

give the Hamiltonians of antisymmetric and symmetric parts of anisotropic exchange, respectively (see chapter 2.3).

## Appendix B. Angular Overlap Model and the Program Package CAMMAG

The conceptual framework of AOM is a simple molecular orbital approach which is now most widely used to discuss the general chemistry of the transition metals. This describes the metal-ligand bonding in terms of covalent  $\sigma$  and  $\pi$  bonding interactions, rather than using the electrostatic perturbations of crystal-field theory. It may be argued that the AOM is superior to the crystal-field theory because its basis – that weak covalent interactions between the ligand orbitals and metal  $d$  orbitals cause properties such as color – is closer to physical reality than is the electrostatic basis that underlies the crystal-field theory. But it is important to recognize that the AOM involves severe approximations [Figgis'00] as well and was never meant to be a quantitative method of *calculating* physically real values of the energy levels in transition-metal complexes. The resulting parameters are always derived from experiment.

The major advantage of an approach such as the AOM, which parameterizes the ligand field in terms of *individual* metal-ligand interactions, is that it can readily be used to form the basis of a general computer program to calculate properties derived from the energy levels and wavefunctions of a metal complex. This would be much harder using a global crystal-field model, for which the ligand-field parameters are a function of the symmetry of the complex, which is often, formally at least, low.

The first ligand-field program to be widely used, *CAMMAG*, was developed by Gerloch and co-workers [Gerloch'72]. Basically, the positions and the orientations of the ligands in the complex are defined using information from the crystal-structure analysis. To each ligand a set of bonding parameters is assigned. These, together with the  $d$  configuration of the metal and appropriate Racah and spin-orbit coupling parameters, are used to calculate the energy levels and associated wavefunctions of the metal in the complex. The energy levels can be compared with the observed electronic spectrum of the complex. The wavefunctions are used to estimate the molecular  $g$  values and their orientations both in a defined molecular coordinate system and with respect to the crystal axes. If desired, the molecular and crystal magnetic susceptibilities may also be calculated at specified temperatures.

This program represents a powerful tool for the interpretation of the ESR data: it allows to calculate the relative energies of all crystal-field levels of a transition metal

ion using the anisotropy of its  $g$  factor, exclusively. As it was mentioned already the parameters CAMMAG takes use of are:

- (i) Structural data for the local environment of the magnetic ion,
- (ii) Racah parameters  $B$  and  $C$ ,
- (iii) SO coupling constant  $\lambda$ ,
- (iv) Orbital reduction factors  $k_i$  ( $i = \{x, y, z\}$ ),
- (v) Bounding parameters  $e_\sigma$  and  $e_\pi$ .

The typical values of the Racah parameters and  $\lambda$  for every ion can be taken e. g. from [Abragam'70]. But reduction of the SO coupling due to the covalency of the metal-ligand bondings as well as the reduction factors  $k_i$  are in fact used as fitting parameters. Keeping in mind other parameters –  $e_\sigma$  and  $e_\pi$  (formally, individual for every ligand ion!) it becomes obvious that additional restrictions are required to be imposed, or the system will be underdetermined. Here we can use an important advantage of the AOM: all bounding parameters in the framework of this model are universal for the particular type of the bond and can be transferred from one situation to another. Only one correction must be made for differences in the metal-ligand bond length. Experiments [Minomura'61] as well as theoretical considerations [Smith'69, Berrejo'83] suggest that

$$e_\sigma \sim r^{-x}, \quad (4 < x < 6). \quad (\text{B.1})$$

Another restriction gives  $e_\pi$  in relation to  $e_\sigma$ . For  $\pi$ -bonding it is common to use [Glaum'96, Figgis'00]

$$e_\pi \approx 0.25 \cdot e_\sigma. \quad (\text{B.2})$$

This program is used to calculate the energy of the orbital states for all systems discussed in the present work.

## Appendix C. Kubo-Tomita Approach and Method of Moments

Here we will outline the approach used to analyze the angular dependence of the ESR linewidth in the high-temperature approximation. It is based on the Kubo-Tomita formula introduced in section 4.4.1

$$\Delta H = \frac{1}{g\mu_B} \frac{M_2}{J} \quad \text{with} \quad M_2 = -\frac{\text{Sp}([\mathcal{H}_{\text{int}}, S^+][\mathcal{H}_{\text{int}}, S^-])}{\text{Sp}[S^+, S^-]}. \quad (\text{C.1})$$

This approach allows to calculate  $\Delta H$  in case of strong exchange narrowing ( $\mathcal{H}_{\text{iso}} \gg \mathcal{H}_{\text{int}}$ ) at temperatures  $T > J/k_B$ . The linewidth depends only on the value of the second moment of the absorption line  $M_2$  which can be estimated by using Eq. (C.1). These calculations are rather straightforward but somewhat tedious. Therefore, in the following we will give only the final expressions obtained for the cases of dominant relaxation via symmetric as well as antisymmetric anisotropic exchange interactions.

### C.1. Second Moment of Dzyaloshinsky-Moriya Interaction

Within the coordinate system, where the  $\tilde{z}$  axis is determined by the external magnetic field  $H$ , the second moment due to DM interaction is calculated as

$$M_2^{\text{DM}} = \frac{2}{3}S(S+1) \left[ (\tilde{d}_x)^2 + (\tilde{d}_y)^2 + 2(\tilde{d}_z)^2 \right]. \quad (\text{C.2})$$

After transformation into the crystallographic system  $(x, y, z) \parallel (a, b, c)$  one gets

$$M_2^{\text{DM}} = \frac{2}{3}S(S+1) \left[ d_x^2 (1 + \sin^2\theta \cos^2\varphi) + d_y^2 (1 + \sin^2\theta \sin^2\varphi) + d_z^2 (1 + \cos^2\theta) + d_x d_y \sin 2\varphi \sin^2\theta + d_x d_z \sin 2\theta \cos^2\varphi + d_y d_z \sin 2\theta \sin^2\varphi \right], \quad (\text{C.3})$$

where  $\theta$  and  $\varphi$  are the polar and azimuth angles of the  $\tilde{z} \parallel H$  direction with respect to the crystallographic system. Note that the isotropic  $g$  value was assumed for this transformation. For the calculation of the linewidth, each bond of the ion of interest has to be considered by applying Eq. (C.3), then the sum of the second moments is substituted into Eq. (C.1).



## C.2. Second Moment of Symmetric Anisotropic Exchange

Here we give the explicit expression for the second moment  $M_2$  of symmetric anisotropic exchange in a spin chain with equivalent magnetic sites. In coordinates  $\tilde{x}, \tilde{y}, \tilde{z}$ , where the  $\tilde{z}$ -axis is defined by the direction of the applied magnetic field  $\mathbf{H}$ ,  $M_2$  reads [Soos'77, Pilawa'97]:

$$M_2^{\text{AE}} = 2 \frac{S(S+1)}{3} \left\{ f_1 (2\tilde{D}_{zz} - \tilde{D}_{xx} - \tilde{D}_{yy})^2 + f_2 \cdot 10(\tilde{D}_{xz}^2 + \tilde{D}_{yz}^2) + f_3 [(\tilde{D}_{xx} - \tilde{D}_{yy})^2 + 4\tilde{D}_{xy}^2] \right\}. \quad (\text{C.4})$$

The factor 2 appeared due to the summation over nearest-neighbors. The symbols  $f_1$ ,  $f_2$ , and  $f_3$  denote the so-called spectral-density functions, as introduced by Pilawa [Pilawa'97].  $f_1$  corresponds to the secular part, whereas  $f_2$  and  $f_3$  correspond to non-secular parts. On the one hand these factors account for the reduction of the nonsecular parts in the case that the Zeeman energy is large compared to the exchange energy. On the other hand they include the possible effect of spin diffusion which enhances the secular part.

On transformation of the anisotropic exchange parameters to the crystallographic coordinates  $(x, y, z)$  one obtains in equation (C.4):

$$[2\tilde{D}_{zz} - \tilde{D}_{xx} - \tilde{D}_{yy}]^2 = [D_{zz}(3 \cos^2 \beta - 1) + D_{xx}(3 \sin^2 \beta \cos^2 \alpha - 1) + D_{yy}(3 \sin^2 \beta \sin^2 \alpha - 1)]^2,$$

$$\tilde{D}_{xz}^2 + \tilde{D}_{yz}^2 = [(D_{xx} \cos^2 \alpha + D_{yy} \sin^2 \alpha - D_{zz}) \cos \beta \sin \beta + 2D_{yz} \cos 2\beta \sin \alpha]^2 + [(D_{yy} - D_{xx}) \sin \beta \cos \alpha \sin \alpha]^2,$$

$$[(\tilde{D}_{xx} - \tilde{D}_{yy})^2 + 4\tilde{D}_{xy}^2] = [D_{xx}(\cos^2 \beta \cos^2 \alpha - \sin^2 \alpha) + D_{yy}(\cos^2 \beta \sin^2 \alpha - \cos^2 \alpha) + D_{zz} \sin^2 \beta]^2 + (D_{yy} - D_{xx})^2 \cos^2 \beta \sin^2 2\alpha.$$

Here it has been taken into account that the  $g$  factor is usually anisotropic and therefore

$$\cos \alpha = \frac{A}{\sqrt{A^2 + B^2}}, \quad \cos \beta = \frac{C}{\sqrt{A^2 + B^2 + C^2}},$$

where

$$A = g_{xx} \sin \theta \cos \varphi, \quad B = g_{yy} \sin \theta \sin \varphi, \quad C = g_{zz} \cos \theta.$$

This describes the full angular dependence of the second moment dependent on polar angle  $\theta$  and azimuth angle  $\varphi$ .

# Bibliography

- [Abragam'70] A. Abragam and B. Bleaney, *Electron paramagnetic resonance of transition ions*, Clarendon, Oxford (1970).
- [Altshuler'64] S. A. Altshuler and B. M. Kozyrev, *Electron paramagnetic resonance*, Acad. Press, New York (1964).
- [Anderson'53] P. W. Anderson and P. R. Weiss, *Exchange narrowing in paramagnetic resonance*, Reviews of Modern Physics **25**, 269-276 (1953).
- [Anderson'55] P. W. Anderson, H. Hasegawa, *Considerations on double exchange*, Physical Review **100**, 675-681 (1955).
- [Anderson'59] P. W. Anderson, *New approach to the theory of superexchange interactions*, Physical Review **115**, 2-13 (1959).
- [Anderson'63] P. W. Anderson, *Theory of magnetic exchange interactions - exchange in insulators and semiconductors*, Solid State Physics **14**, 99-214 (1963).
- [Attfield'06] J. P. Attfield, *Charge ordering in transition metal oxides*, Solid State Sciences **8**, 861-867 (2006).
- [Barnes'81] S.E. Barnes, *Theory of electron spin resonance of magnetic ions in metals*, Advances in Physics **30**, 801-938 (1981).
- [Barnes'94] T. Barnes and J. Riera, *Susceptibility and excitation spectrum of  $(VO)_2P_2O_7$  in ladder and dimer-chain models*, Physical Review B **50**, 6817 (1994).
- [Baxter'71] R. J. Baxter, *One-Dimensional Anisotropic Heisenberg Chain*, Physical Review Letters **26**, 834-834 (1971).
- [Bencini'90] A. Bencini and D. Gatteschi, *EPR of Exchange Coupled Systems*, Springer, Berlin (1991).
- [Benner'83] H. Benner, M. Brodehl, H. Seitz, and J. Wiese, *Influence of nondiagonal dynamic susceptibility on the EPR signal of Heisenberg magnets*, Journal of Physics C: Solid State Physics **16**, 6011-6030 (1983).
- [Bernert'01] A. Bernert, T. Chatterji, P. Thalmeier, P. Fulde, *Structure determination, valence, and superexchange in the dimerized low temperature phase of  $\alpha'$ - $NaV_2O_5$*  European Physical Journal B **21**, 535-546 (2001).

- [Beynon'93] R. Beynon and J. Wilson, *TiOCl, TiOBr - are these RVB  $d^1$ ,  $S=1/2$  materials? The results of scandium substitution set in the context of other  $S=1/2$  systems of current interest for high-temperature superconductivity and the metal-insulator transition*, Journal of Physics: Condensed Matter **5**, 1983-2000 (1993).
- [Berrejo'83] M. Berrejo, L. Pueyo, *On the  $R_{ML}$  dependence of  $10Dq$* , Journal of Chemical Physics **78**, 854-857 (1983).
- [Bethe'31] H. A. Bethe, *Zur Theorie der Metalle. I. Eigenwerte und Eigenfunktionen der linearen Atomkette*, Zeitschrift für Physik **71**, 205-226 (1931).
- [Blasse'65] G. Blasse, *Antiferromagnetism of the spinel  $LiCuVO_4$* , Journal of Physics and Chemistry of Solids, **27**, 612-613 (1965).
- [Bleaney'52] B. Bleaney, K. D. Bowers, *Anomalous Paramagnetism of Copper Acetate*, Proceedings of the Royal Society **A214**, 451-465 (1952).
- [Bloch'46] F. Bloch, *Nuclear Induction*, Physical Review **70**, 460-474 (1946).
- [Bockrath'99] M. Bockrath, D. H. Cobden, J. Lu, A. G. Rinzler, R. E. Smalley, T. Balents, P. L. McEuen, *Luttinger-liquid behaviour in carbon nanotubes*, Nature **397**, 598-601 (1999).
- [Bonner'64] J. C. Bonner and M. E. Fisher, *Linear Magnetic Chains with Anisotropic Coupling*, Physical Review **135**, A640 (1964).
- [Bonner'82] J. C. Bonner and H. W. J. Blöte, *Excitation spectra of the linear alternating anti-ferromagnet*, Physical Review B **25**, 6959 (1982).
- [Borras'99] J. J. Borras-Almenar, E. Coronado, S. M. Ostrovsky, A. V. Paliy, B. S. Tsukerblat, *Localisation vs. delocalisation in the dimeric mixed-valence clusters in the generalised vibronic model. Magnetic manifestations*, Chemical Physics **240**, 149-161 (1999).
- [Bulaevskii'78] L. N. Bulaevskii, A. I. Buzdin, D. I. Khomskii, *Spin-Peierls transition in magnetic field*, Solid State Communications **27**, 5-10 (1978).
- [Boucher'96] J. P. Boucher and L. P. Regnault, *The inorganic spin-Peierls compound  $CuGeO_3$* , Journal de Physique I France **6**, 1939-1966 (1996).
- [Braden'96] M. Braden, G. Wilkendorf, J. Lorenzana, M. Ain, G. J. McIntyre, M. Behruzi, G. Heger, G. Dhahenne, and A. Revcolevschi, *Structural analysis of  $CuGeO_3$ : Relation between nuclear structure and magnetic interaction*, Physical Review B **54**, 1105-1116 (1996).
- [Braden'98] M. Braden, B. Hennion, W. Reichardt, G. Dhahenne, and A. Revcolevschi, *Spin-Phonon Coupling in  $CuGeO_3$* , Physical Review Letters **80**, 3634-3637 (1998).
- [Bray'75] J. W. Bray, H. R. Hart, Jr., L. V. Interrante, I. S. Jacobs, J. S. Kasper, G. D. Watkins, S. H. Wee, J. C. Bonner, *Observation of a Spin-Peierls Transition in a Heisenberg Antiferromagnetic Linear-Chain System*, Physical Review Letters **35**, 744-747 (1975).

- 
- [vanBodegom'81] B. van Bodegom, B. C. Larson, and H. A. Mook, *Diffuse x-ray and inelastic neutron scattering study of the spin Peierl's transition in N-methyl-N-ethyl-morpholinium bistetracyanoquinodimethane [MEM (TCNQ)<sub>2</sub>]*, Physical Review B **24**, 1520-1523 (1981).
- [Carpy'75] A. Carpy and J. Galy, *Affinement de la structure cristalline du bronze  $\alpha'$  -  $\text{NaV}_2\text{O}_5$*  Acta Crystallographica Section B **31**, 1481-1482 (1975).
- [Caimi'04] G. Caimi, L. Degiorgi, N. N. Kovaleva and P. Lemmens, F. C. Chou, *Infrared optical properties of the spin-1/2 quantum magnet  $\text{TiOCl}$* , Physical Review B **69**, 125108 (2004).
- [Chabre'05] F. Chabre, A. M. Ghorayeb, P. Millet, V. A. Pashchenko, and A. Stepanov, *Low-temperature behavior of the ESR linewidth in a system with a spin gap:  $\eta - \text{Na}_{1.286}\text{V}_2\text{O}_5$* , Physical Review B **72**, 012415 (2005).
- [Chen'95] C. H. Chen and S-W. Cheong, *Lattice fluctuations well above the spin-Peierls transition in the linear-chain system  $\text{CuGeO}_3$* , Physical Review B **51**, 6777-6779 (1995).
- [Cheung'78] T. T. P. Cheung, Z. G. Soos, R. E. Dietz, and F. R. Merrit, *Temperature Dependence of Exchange Narrowing in the One-Dimensional Antiferromagnet  $\text{N}(\text{CH}_3)_4\text{MnCl}_3$  (TMMC)*, Physical Review B **17**, 1266-1276 (1978).
- [Choukroun'01] J. Choukroun, J.-L. Richard, and A. Stepanov, *High-Temperature Electron Paramagnetic Resonance in Magnets with the Dzyaloshinskii-Moriya Interaction*, Physical Review Letters **87**, 127207 (2001).
- [Choukroun'03] J. Choukroun, J.-L. Richard, and A. Stepanov, *Electron paramagnetic resonance in weakly anisotropic Heisenberg magnets with a symmetric anisotropy*, Physical Review B **68**, 144415 (2003).
- [Craco'06] L. Craco, M. S. Laad, E. Müller-Hartmann, *Metallizing the Mott insulator  $\text{TiOCl}$  by electron doping*, Journal of Physics: Condensed Matter **18**, 10943-10953 (2006).
- [Cross'79] M. C. Cross, D. S. Fisher, *A new theory of the spin-Peierls transition with special relevance to the experiments on  $\text{TTFCuBDT}$* , Physical Review B **19**, 402-419 (1979).
- [Dagotto'96] E. Dagotto and T. M. Rice, *Surprises on the way from one- to two-dimensional quantum magnets: The ladder materials*, Science **271**, 618-623 (1996).
- [Damascelli'00] A. Damascelli, C. Presura, and D. van der Marel, J. Jegoudez and A. Revcolevschi, *Optical spectroscopic study of the interplay of spin and charge in  $\alpha'$ - $\text{NaV}_2\text{O}_5$* , Physical Review B **61**, 2535-2552 (2000).
- [Deisenhofer'02] J. Deisenhofer, M. V. Eremin, D. Zakharov, V. A. Ivanshin, R. Eremina, H.-A. Krug von Nidda, A. A. Mukhin, A. M. Balbashov, and A. Loidl, *Crystal field and Dzyaloshinsky-Moriya interaction in orbitally ordered  $\text{La}_{0.95}\text{Sr}_{0.05}\text{MnO}_3$ : an ESR study*, Physical Review B **65**, 104440 (2002); cond-mat/0108515.
- [Deisenhofer'03] J. Deisenhofer, B. I. Kochelaev, E. Shilova, A. M. Balbashov, A. Loidl, and H.-A. Krug von Nidda, *Orbital order parameter in  $\text{La}_{0.95}\text{Sr}_{0.05}\text{MnO}_3$  probed by electron spin resonance*, Physical Review B **68**, 214427 (2003).

- [Deisenhofer'05] J. Deisenhofer, *Order and disorder in manganites: electron spin resonance*, PhD thesis, Universität Augsburg, Augsburg (2005).
- [Dietz'71] R. E. Dietz, F. R. Merritt, R. Dingle, D. Hone, B. G. Silbernagel and P. M. Richards, *Exchange narrowing in one-dimensional systems*, Physical Review Letters **26**, 1186-1188 (1971).
- [Du'95] J.-L. Du, G. R. Eaton, S. S. Eaton, *Temperature, orientation, and solvent dependence of electron spin-lattice relaxation rates for nitroxyl radicals in glassy solvents and doped solids*, Journal of Magnetic Resonance **A115**, 213-221 (1995); *Temperature and orientation dependence of electron-spin relaxation rates for bis(diethylthiocarbamate)copper(II)*, Journal of Magnetic Resonance **A117**, 67-72 (1995).
- [Duc'04] F. Duc, P. Millet, S. Ravy, A. Thiollet, F. Chabre, A. M. Ghorayeb, F. Mila, A. Stepanov, *Low-temperature superstructure and charge-ordering effect in  $\eta - Na_{1.286}V_2O_5$* , Physical Review B **69**, 094102 (2004).
- [Dyson'55] F. J. Dyson, *Electron Spin Resonance Absorption in Metals. I. Experimental*, Physical Review **98**, 337-348 (1955); *Electron Spin Resonance Absorption in Metals. II. Theory of Electron Diffusion and the Skin Effect*, Physical Review **98**, 349-359 (1955).
- [Dzialoshinski'58] I. Dzialoshinski, *A thermodynamic theory of "weak" ferromagnetism of anti-ferromagnetics*, Journal of Physics and Chemistry of Solids **4**, 241-255 (1958).
- [Eggert'94] S. Eggert, I. Affleck, M. Takahashi, *Susceptibility of the spin 1/2 Heisenberg antiferromagnetic chain*, Physical Review Letters **73**, 332-335 (1994).
- [Emin'91] D. Emin, *Orbital magnetism of singlet large bipolarons*, Physical Review B **43**, 2633-2636 (1991).
- [Eremin'72] M. V. Eremin, A. A. Kornienko, A. M. Leushin, *Theory of exchange interaction*, Fizika Tverdogo Tela **14**, 378-381 (1972).
- [Eremin'77] M. V. Eremin, Y. V. Rakitin, *Channel Model in Isotropic Exchange Theory*, Physica Status Solidi (b) **80**, 579-587 (1977); *Channel Model in Isotropic Exchange Theory (II)*, **82**, 221-228 (1978); *Channel Model in Isotropic Exchange Theory (III)*, **85**, 783-788 (1978).
- [Eremin'80] M. V. Eremin, Yu. V. Rakitin, *On Kinetic Exchange Theory*, Physica Status Solidi (b) **97**, 51-62 (1980);
- [Eremin'81] M. V. Eremin, Yu. V. Rakitin, *Kinetic Exchange at low charge transfer energies*, Journal of Physics C: Solid State Physics **14**, 247-253 (1981).
- [Eremin'82a] M. V. Eremin, Yu. V. Rakitin, *Interference of superexchange interactions*, Journal of Physics C: Solid State Physics **15**, L259-L261 (1982).
- [Eremin'82b] M. V. Eremin, *Two-bridge mechanism of indirect exchange*, Fizika Tverdogo Tela **24**, 3216-3222 (1982).

- [Eremin'83] M. V. Eremin,  $V^{2+}$ ,  $Mn^{2+}$ ,  $Ni^{2+}$  exchange interactions in cubic crystalline fields, *Fizika Tverdogo Tela* **25**, 1754-1760 (1983).
- [Eremin'85] M. V. Eremin, *Theory of exchange interaction of magnetic ions in dielectrics*, *Spectroscopy of Crystals*, pp. 150-172, Nauka, Moskau (1985).
- [Eremin'90] M. V. Eremin, *Effect of charge-transfer processes on the electronic structure of centers with unfilled d and f shells*, *Optics and Spectroscopy (USSR)* **68**, 502-504 (1990).
- [Eremin'01] M. V. Eremin, S. I. Nikitin, S. Yu. Prosvirnin, N. I. Silkin, R. V. Yusupov, *Optical studies of  $Cr^{3+}Cr^{2+}$  pair center in  $KZnF_3$  crystal*, *Solid State Communications* **117**, 297-301 (2001).
- [Eremin'05] M. V. Eremin, D. V. Zakharov, R. M. Eremina, J. Deisenhofer, H.-A. Krug von Nidda, G. Obermeier, S. Horn, and A. Loidl, *Unconventional anisotropic superexchange in  $\alpha'$ - $NaV_2O_5$* , *Physical Review Letters* **96**, 027209 (2006).
- [Eremin'UP] M. V. Eremin *et al.*, unpublished.
- [Eremina'03] R. M. Eremina, M. V. Eremin, V. N. Glazkov, H.-A. Krug von Nidda, and A. Loidl, *Anisotropic exchange interactions in  $CuGeO_3$  probed by electron spin resonance spectroscopy*, *Physical Review B* **68**, 014417 (2003).
- [Eskes'90] H. Eskes, L. H. Tjeng, and G. A. Sawatzky, *Cluster-model calculation of the electronic structure of  $CuO$ : A model material for the high- $T_c$  superconductors*, *Physical Review B* **41**, 288-299 (1990).
- [Estes'78] W. E. Estes, D. P. Gavel, W. E. Hatfield, D. J. Hodgson, *Magnetic and structural characterization of dibromo- and dichlorobis(thiazole)copper(II)*, *Inorganic Chemistry* **17**, 1415-1421 (1978).
- [Fabricius'98] K. Fabricius, A. Klümper, U. Löw, B. Büchner, T. Lorenz, G. Dhalenne, A. Revcolevschi, *Reexamination of the microscopic couplings of the quasi-one-dimensional antiferromagnet  $CuGeO_3$* , *Physical Review B* **57**, 1102-1107 (1998).
- [Ferguson'71] J. Ferguson, H. J. Guggenheim, E. R. Krausz, *Optical absorption by Cu-Mn pairs in  $KZnF_3$* , *Journal of Physics C: Solid State Physics* **4**, 1866-1873 (1971).
- [Fichtl'05] R. Fichtl, V. Tsurkan, P. Lunkenheimer, J. Hemberger, V. Fritsch, H.-A. Krug von Nidda, E.-W. Scheidt, A. Loidl, *Orbital freezing and orbital glass state in  $FeCr_2S_4$* , *Physical Review Letters* **94**, 027601 (2005).
- [Figgis'00] B. N. Figgis and M. A. Hitchman, *Ligand Field Theory and Its Applications*, Wiley-VCH, New York (2000).
- [Fischer'99] M. Fischer, P. Lemmens, G. Els, and G. Guntherodt, E. Ya. Sherman, E. Morre, C. Geibel, and F. Steglich, *Spin-gap behavior and charge ordering in  $\alpha'$ - $NaV_2O_5$  probed by light scattering*, *Physical Review B* **60**, 7284-7294 (1999).

- [Freeman'61] A. J. Freeman, R. E. Watson, *Theory of Direct Exchange in Ferromagnetism*, Physical Review **124**, 1439-1454 (1961).
- [Freeman'62] A. J. Freeman, R. K. Nesbet, R. E. Watson, *Two-Electron Heisenberg Exchange Interaction between Neighboring Atoms*, Physical Review **125**, 1978-1981 (1962).
- [Fujii'97] Y. Fujii, H. Nakao, T. Yosihama, M. Nishi, K. Nakajima, K. Kakurai, M. Isobe, Y. Ueda and Hiroshi Sawa, *New inorganic spin-Peierls compound  $\text{NaV}_2\text{O}_5$  evidenced by x-ray and neutron scattering*, Journal of the Physical Society of Japan **66**, 326-329 (1997).
- [Fukuyama'96] H. Fukuyama, T. Tanimoto, M. Saito, *Antiferromagnetic long range order in disordered spin-Peierls systems*, Journal of the Physical Society of Japan **65**, 1182-1185 (1996).
- [Garivullina'72] R. L. Garivullina, M. V. Eremin, A. M. Leushin, *Direct exchange interaction between ions with unfilled 3d-shells*, Fizika Tverdogo Tela **14**, 382-391 (1972).
- [Gerloch'72] M. Gerloch, *Magnetism and Ligand-Field Analysis*, Chapman-Hall, London (1972).
- [Glazkov'05] V. N. Glazkov, A. I. Smirnov, H.-A. Krug von Nidda, A. Loidl, K. Uchinokura, T. Masuda, *Field-controlled phase separation at the impurity-induced magnetic ordering in the spin-Peierls magnet  $\text{CuGeO}_3$* , Physical Review Letters **94**, 057205 (2005).
- [Glaum'96] R. Glaum, M. A. Hitchman, *On the Bonding Behaviour of Transition Metal Ions in Inorganic Solids – Optical and E.P.R. Spectroscopic Studies on Anhydrous Phosphates and Phosphate-Silicates of  $\text{Tr}^{3+}$* , Australian Journal of Chemistry **49**, 1221-1228 (1996).
- [Golubchik'97] S. A. Golubchik, M. Isobe, A. N. Ivlev, B. N. Mavrin, M. N. Popova, A. B. Sushkov, Y. Ueda and A. N. Vasil'ev, *Raman, infrared and optical spectra of the spin-Peierls compound  $\text{NaV}_2\text{O}_5$* , Journal of the Physical Society of Japan **66**, 4042-4046 (1997).
- [Gondaira'66] K.-I. Gondaira and Y. Tanabe, *A note on the theory of superexchange interaction*, Journal of the Physical Society of Japan **21**, 1527-1548 (1966).
- [Goto'03] T. Goto and B. Lüthi, *Charge ordering, charge fluctuations and lattice effects in strongly correlated electron systems*, Advances in Physics **52**, 67-118 (2003).
- [Grenier'01] B. Grenier, O. Cepas, L. P. Regnault, J. E. Lorenzo, T. Ziman, P. J. Boucher, A. Hiess, T. Chatterji, J. Jegoudez, A. Revcolevshi, *Charge ordering and spin dynamics in  $\text{NaV}_2\text{O}_5$* , Physical Review Letters **86**, 5966-5969 (2001).
- [Grenier'02] S. Grenier, A. Toader, J. E. Lorenzo, Y. Joly, B. Grenier, S. Ravy, L. P. Regnault, H. Renevier, J. Y. Henry, J. Jegoudez, and A. Revcolevschi, *X-ray anomalous scattering investigations on the charge order in  $\alpha'$ - $\text{NaV}_2\text{O}_5$* , Physical Review B, **65**, 180101(R) (2002).
- [Griffiths'63] R. B. Griffiths, *Magnetization Curve at Zero Temperature for the Antiferromagnetic Heisenberg Linear Chain*, Physical Review **133**, A768-A775 (1963).

- 
- [Griffith'71] J. S. Griffith, *The Theory of Transition Metal Ions*, Cambridge University Press, Cambridge (1971).
- [Gros'05] C. Gros and G. Y. Chitov, *The spin-SAF transition in  $\text{NaV}_2\text{O}_5$  induced by spin-pseudospin coupling*, Europhysics Letters **69**, 447-453 (2005).
- [Goodenough'58] J. B. Goodenough, *Theory of the Role of Covalence in the Perovskite-Type Manganites  $[\text{La}, \text{M(II)}]\text{MnO}_3$* , Physical Review **100**, 564-573 (1955); *An interpretation of the magnetic properties of the perovskite-type mixed crystals  $\text{La}_{1-x}\text{Sr}_x\text{CoO}_{3-\lambda}$* , Journal of Physics and Chemistry of Solids **6**, 287-297 (1958).
- [Grüner'94] G. Grüner, *Density Waves in Solids*, Addison-Wesley Publishing Company, New York (1994).
- [Haldane'83] F. D. M. Haldane, *Continuum dynamics of the 1D Heisenberg anti-ferromagnet – identification with the  $O(3)$  non-linear sigma-model*, Physics Letters A **93**, 464-468 (1983); *Nonlinear Field Theory of Large-Spin Heisenberg Antiferromagnets: Semiclassically Quantized Solitons of the One-Dimensional Easy-Axis Néel State*, Physical Review Letters **50**, 1153-1156 (1983).
- [Harris'63] E. A. Harris and J. Owen, *Biquadratic exchange between  $\text{Mn}^{2+}$  ions in  $\text{MgO}$* , Physical Review Letters **11**, 9-10 (1963).
- [Hase'93] M. Hase, I. Terasaki and K. Uchinokura, *Observation of the spin-Peierls transition in linear  $\text{Cu}^{2+}$  ( $\text{spin}-1/2$ ) chains in an inorganic compound  $\text{CuGeO}_3$* , Physical Review Letters **70**, 3651-3654 (1993).
- [Heinrich'03] M. Heinrich, H.-A. Krug von Nidda, A. Krimmel, A. Loidl, R. M. Eremina, A. D. Ineev, B. I. Kochelaev, A. V. Prokofiev, and W. Aßmus, *Structural and magnetic properties of  $\text{CuSb}_2\text{O}_6$  probed by ESR*, Physical Review B **67**, 224418 (2003).
- [Heinrich'04] M. Heinrich, H.A. Krug von Nidda, R. M. Eremina, A. Loidl, Ch. Helbig, G. Obermeier, and S. Horn, *Spin dynamics and charge order in  $\beta - \text{Na}_{1/3}\text{V}_2\text{O}_5$* , Physical Review Letters **93**, 116402 (2004).
- [Heisenberg'28] W. Heisenberg, *Zur Theorie des Ferromagnetismus*, Zeitschrift für Physik **49**, 619-636 (1928).
- [Heitler'27] W. Heitler and F. London, *Wechselwirkung neutraler Atome und homöopolare Bildung nach der Quantenmechanik*, Zeitschrift für Physik **44**, 455-472 (1927).
- [Hemberger'98] J. Hemberger, M. Lohmann, M. Nicklas, A. Loidl, M. Klemm, G. Obermeier and S. Horn, *Thermodynamic, transport and magnetic properties of  $\alpha' - \text{NaV}_2\text{O}_5$* , Europhysics Letters **42**, 661-666 (1998).
- [Hemberger'05] J. Hemberger, M. Hoinkis, M. Klemm, M. Sing, R. Claessen, S. Horn, and A. Loidl, *Heat capacity of the quantum magnet  $\text{TiOCl}$* , Physical Review B **72**, 012420 (2005).



- [Hennessey'73] M. J. Hennessey, C. D. McElwee, and P. M. Richards, *Effect of Interchain Coupling on Electron-Spin Resonance in Nearly One-Dimensional Systems*, Physical Review B **7**, 930-947 (1973).
- [Hidaka'98] M. Hidaka, T. Eguchi, I. Yamada, *New superlattice crystal structure in  $KCuF_3$  revealed by x-ray diffraction experiments*, Journal of the Physical Society of Japan **67**, 2488-2494 (1998).
- [Hoinkis'05] M. Hoinkis, M. Sing, J. Schafer, M. Klemm, S. Horn, H. Benthien, E. Jeckelmann, T. Saha-Dasgupta, L. Pisani, R. Valenti, and R. Claessen, *Electronic structure of the spin-1/2 quantum magnet  $TiOCl$* , Physical Review B **72**, 125127 (2005).
- [Hoinkis'07] M. Hoinkis, *Phase transitions in low-dimensional transition metal compounds*, PhD thesis, Universität Augsburg, Augsburg (2007).
- [Huber'99] D. L. Huber, G. Alejandro, A. Caneiro, M. T. Causa, F. Prado, M. Tovar, S. B. Os-eroff, *EPR linewidths in  $La_{1-x}Ca_xMnO_3$ :  $0 < x < 1$* , Physical Review B **60**, 12155 (1999).
- [Hybertsen'92] M. S. Hybertsen, E. B. Stechel, W. M. C. Foulkes, and M. Schluter, *Model for low-energy electronic states probed by x-ray absorption in high- $T_c$  cuprates*, Physical Review B **45**, 10032-10050, (1992).
- [Ikebe'71] M. Ikebe and M. Date, *Electron Spin Resonance in One Dimensional Antiferromagnet  $KCuF_3$* , Journal of the Physical Society of Japan **30**, 93-100 (1971).
- [Imai'03] T. Imai, F. C. Chou, *Novel spin-gap behavior in layered  $S = 1/2$  quantum spin system  $TiOCl$* , cond-mat/0301425.
- [Ishii'03] H. Ishii, H. Kataura, H. Shiozawa, H. Yoshioka, H. Otsubo, Y. Takayama, T. Miyahara, S. Suzuki, Y. Achiba, M. Nakatake, T. Narimura, M. Higashiguchi, K. Shimada, H. Namatame, M. Taniguchi, *Direct observation of Tomonaga-Luttinger-liquid state in carbon nanotubes at low temperatures*, Nature **426**, 540-544 (2003).
- [Ising'25] E. Ising, *Beitrag zur Theory des Ferromagnetismus*, Zeitschrift für Physik **31**, 253-258 (1925).
- [Isobe'96] M. Isobe and Y. Ueda, *Magnetic susceptibility of quasi-one-dimensional compound  $\alpha'$ - $NaV_2O_5$  possible spin-Peierls compound with high critical temperature of 34 K*, Journal of the Physical Society of Japan **65**, 1178-1181 (1996).
- [Isobe'99] M. Isobe, Y. Ueda, Y. Oka, T. Yao, *Crystal structure and magnetic properties of  $Na_9V_{14}O_{35}$ : sodium-vanadium bronze  $\eta$ - $Na_xV_2O_5$* , Journal of Solid State Chemistry **145**, 361-365 (1999).
- [Johnston'00] D. C. Johnston, R. K. Kremer, M. Troyer, X. Wang, A. Klümper, S. L. Budko, A. F. Panchula, and P. C. Canfield, *Thermodynamics of spin  $S=1/2$  antiferromagnetic uniform and alternating-exchange Heisenberg chains*, Physical Review B **61**, 9558-9606 (2000).

- 
- [Karpenko'76] B. V. Karpenko, *Some new aspects of the theory of the double exchange mechanism*, Journal of Magnetism and Magnetic Materials **3**, 267-274 (1976).
- [Kataev'03] V. Kataev, J. Baier, A. Moller, L. Jongen, G. Meyer, and A. Freimuth, *Orbital order in the low-dimensional quantum spin system TiOCl probed by ESR*, Physical Review B **68**, 140405(R) (2003).
- [Kato'05] C. Kato, Y. Kobayashi, M. Sato, *ESR Studies on Quasi One-Dimensional Spin System TiOBr*, Journal of the Physical Society of Japan **74**, 473-477 (2005).
- [Kawamori'02] A. Kawamori, J. Yamauchi and H. Ohta, *ESR in the 21st Century: Basics and Applications to Material, Life and Earth Sciences*, Elsevier, Amsterdam (2002).
- [Keffer'62] F. Keffer, *Moriya Interaction and the Problem of the Spin Arrangements in  $\beta$ -MnS*, Physical Review **126**, 896-900 (1962).
- [Kegler'01] Ch. Kegler, N. Büttgen, H.-A. Krug von Nidda, A. Krimmel, L. Svistov, B. I. Kochelaev, A. Loidl, A. Prokofiev, and W. Aßmus, *Magnetic resonance on LiCuVO<sub>4</sub>*, European Physical Journal B **22**, 321-326 (2001).
- [Kegler'06] C. Kegler, N. Büttgen, H.-A. Krug von Nidda, A. Loidl, R. Nath, A. V. Mahajan, A. V. Prokofiev, and W. Aßmus, *NMR study of lineshifts and relaxation rates of the one-dimensional antiferromagnet LiCuVO<sub>4</sub>*, Physical Review B **73**, 104418 (2006).
- [Kramers'34] H. A. Kramers, *L'interaction entre les atomes magnétogènes dans un cristal paramagnétique*, Physica **1**, 182-192 (1934).
- [Krimmel'06] A. Krimmel, J. Strempler, B. Bohnenbuck, B. Keimer, M. Hoinkis, M. Klemm, S. Horn, A. Loidl, M. Sing, R. Claessen, and M. v. Zimmermann, *Incommensurate structure of the spin-Peierls compound TiOCl in zero and finite magnetic fields*, Physical Review B **73**, 172413 (2006).
- [Kochelaev'03] B. I. Kochelaev, E. Shilova, J. Deisenhofer, H.-A. Krug von Nidda, A. Loidl, A. A. Mukhin and A. M. Balbashov, *Phase Transitions and Spin Relaxation in La<sub>0.95</sub>Sr<sub>0.05</sub>MnO<sub>3</sub>*, Modern Physics Letters B **17**, 459-467 (2003).
- [Kubo'54] R. Kubo and K. Tomita, *A general theory of magnetic resonance absorption*, Journal of the Physical Society of Japan **9**, 888-919 (1954).
- [Kubo'61] R. Kubo, in *Fluctuation, relaxation and resonance in Magnetic systems*, ed. by D. ter Haar, Oliver and Boyd, Edinburgh, p. 23 (1961).
- [Kugel'72] K. I. Kugel, D. I. Khomskii, *Superexchange ordering of degenerate orbitals and magnetic structure of dielectrics with Jahn-Teller ions*, Journal of Experimental and Theoretical Physics Letters **15**, 629-632 (1972).
- [Krug'97] H.-A. Krug von Nidda, *Electron spin resonance in strongly correlated Cer-compounds*, PhD thesis, TU Darmstadt, Darmstadt (1997).

- [Krug'02] H.-A. Krug von Nidda, L. E. Svistov, M. V. Eremin, R. M. Eremina, A. Loidl, V. Kataev, A. Validov, A. Prokofiev, and W. Aßmus, *Anisotropic exchange in  $\text{LiCuVO}_4$  probed by ESR*, Physical Review B **65**, 134445 (2002).
- [Kuntscher'06] C. A. Kuntscher, S. Frank, A. Pashkin, M. Hoinkis, M. Klemm, M. Sing, S. Horn, R. Claessen, *Possible pressure-induced insulator-to-metal transition in low-dimensional  $\text{TiOCl}$* , Physical Review B **74**, 184402 (2006).
- [Lafontaine'89] M. A. Lafontaine, M. Leblanc, and G. Ferey, *New refinement of the room-temperature structure of  $\text{LiCuVO}_4$* , Acta Crystallographica Section C **45**, 1205-1206 (1989).
- [Lagendijk'77] A. Lagendijk, H. D. Raedt, *Self-consistent diffusion coefficients in nearly-one-dimensional paramagnets*, Physical Review B **16**, 293-296 (1977).
- [Lake'05] B. Lake, D. A. Tennant, C. D. Frost, S. E. Nagler, *Quantum criticality and universal scaling of a quantum antiferromagnet*, Nature Materials **4**, 329-334 (2005).
- [Lee'06] S. Lee, J. G. Park, D. T. Adroja, D. Khomskii, S. Streltsov, K. A. McEwen, H. Sakai, K. Yoshimura, V. I. Anisimov, D. Mori, R. Kanno, R. Ibberson, *Spin gap in  $\text{Tl}_2\text{Ru}_2\text{O}_7$  and the possible formation of haldane chains in three-dimensional crystals*, Nature Materials **5**, 471-476 (2006).
- [Lemmens'04] P. Lemmens, K. Y. Choi, G. Caimi, L. Degiorgi, N. N. Kovaleva, A. Seidel, and F. C. Chou, *Giant phonon softening in the pseudogap phase of the quantum spin system  $\text{TiOCl}$* , Physical Review B **70**, 134429 (2004).
- [Leonov'PR] I. Leonov, private communication.
- [Lohmann'97] M. Lohmann, A. Loidl, M. Klemm, G. Obermeier and S. Horn, *ESR study of the spin-peierls transition in  $\text{NaV}_2\text{O}_5$* , Solid State Communications **104**, 649-652 (1997).
- [Lohmann'00] M. Lohmann, H.-A. Krug von Nidda, M. V. Eremin, A. Loidl, G. Obermeier and S. Horn, *Charge Order in  $\text{NaV}_2\text{O}_5$  Studied by EPR*, Physical Review Letters **85**, 1742-1745 (2000).
- [Lunkenheimer'00] P. Lunkenheimer, U. Schneider, R. Brand, A. Loidl, *Glassy dynamics*, Contemporary Physics, **41**, 15-36 (2000).
- [Luther'98] S. Luther, H. Nojiri, M. Motokawa, M. Isobe, Y. Ueda, *Direct Observation of the Spin Gap in  $\text{NaV}_2\text{O}_5$  by Submillimeter Wave ESR*, Journal of the Physical Society of Japan **67**, 3715-3717 (1998).
- [Luttinger'63] J. M. Luttinger, *An exactly soluble model of a many-fermion system*, Journal of Mathematical Physics **4**, 1154-1162 (1963).
- [Maeda'03] Y. Maeda and M. Oshikawa, *Numerical analysis of electron-spin resonance in the spin-1/2 XY model*, Physical Review B **67**, 224424 (2003).

- 
- [Mazurenko'02] V. V. Mazurenko, A. I. Lichtenstein, M. I. Katsnelson, I. Dasgupta, T. Saha-Dasgupta, and V. I. Anisimov, *Nature of insulating state in  $\text{NaV}_2\text{O}_5$  above charge-ordering transition: A cluster dynamical mean-field study*, Physical Review B **66**, 081104 (2002).
- [Mermin'66] N. D. Mermin, H. Wagner, *Absence of Ferromagnetism or Antiferromagnetism in One- or Two-Dimensional Isotropic Heisenberg Models*, Physical Review Letters **17**, 1133-1136 (1966).
- [Minomura'61] S. Minomura, H. G. Drickamer, *Effect of Pressure on the Spectra of Transition Metal Ions in  $\text{MgO}$  and  $\text{Al}_2\text{O}_3$* , Journal of Chemical Physics **35**, 903-907 (1961).
- [Mori'62] H. Mori and K. Kawasaki, *Theory of Dynamical Behaviors of Ferromagnetic Spins*, Progress of Theoretical Physics **27**, 529-570 (1962); Progress of Theoretical Physics **28**, 971-570 (1962).
- [Moriya'60] T. Moriya, *New Mechanism of Anisotropic Superexchange Interaction*, Physical Review Letters **4**, 228-230 (1960); *Anisotropic Superexchange Interaction and Weak Ferromagnetism*, Physical Review **120**, 91-98 (1960).
- [Moskvin'77] A. S. Moskvin, I. G. Bostrem, *Some peculiarities of exchange interaction in orthoferrite-orthochromites*, Fizika Tverdogo Tela **19**, 1616-1626 (1977).
- [Musin'76] R. N. Musin and P. V. Schastnev, *Calculation of quantum-chemical intermolecular integrals using truncated Gaussian expansion of atomic orbitals*, Journal of Structural Chemistry **17**, 343-346 (1976); *Calculation of exchange interactions of atoms in paired orbital approximation. 1.*, Journal of Structural Chemistry **17**, 356-361 (1976); *Calculation of exchange interactions of atoms in paired orbital approximation. 2.*, Journal of Structural Chemistry **17**, 362-67 (1976).
- [Nagata'72] K. Nagata and Y. Tazuke, *Short range order effects on EPR frequencies in Heisenberg linear chain antiferromagnets*, Journal of the Physical Society of Japan **32**, 337-345 (1972).
- [Nagata'78] K. Nagata, T. Nishino, T. Hirose, T. Komatsubara *EPR in the impure Heisenberg Linear Chain  $\text{CsMn}_{1-x}\text{Co}_x\text{Cl}_3 \cdot 2\text{H}_2\text{O}$* , Journal of the Physical Society of Japan **44**, 813-818 (1978).
- [Nishimoto'98] S. Nishimoto and Y. Ohta, *Optical conductivity of the trellis-lattice  $t$ - $J$  model: charge fluctuations in  $\text{NaV}_2\text{O}_5$* , Journal of the Physical Society of Japan **67**, 3679-3682 (1998); *A model study of the low-energy charge dynamics of  $\text{NaV}_2\text{O}_5$* , Journal of the Physical Society of Japan **67**, 4010-4013 (1998).
- [Nojiri'00] H. Nojiri, S. Luther, M. Motokawa, M. Isobe and Y. Ueda, *High frequency ESR investigation on dynamical charge disproportionation and spin gap excitation in  $\text{NaV}_2\text{O}_5$* , Journal of the Physical Society of Japan **69**, 2291-2298 (2000).
- [Ohama'97] T. Ohama, H. Yasuoka, M. Isobe and Y. Ueda, *The  $d$  orbital character in the spin-Peierls system  $\text{NaV}_2\text{O}_5$* , Journal of the Physical Society of Japan **66**, 3008-3011 (1997).

- [Ohama'99] T. Ohama, H. Yasuoka, M. Isobe, and Y. Ueda, *Mixed valency and charge ordering in  $\alpha'$ - $\text{NaV}_2\text{O}_5$* , Physical Review B **59**, 3299-3302 (1999).
- [Oshikawa'02] M. Oshikawa and I. Affleck, *Low-temperature electron spin resonance theory for half-integer spin antiferromagnetic chains*, Physical Review Letters **82**, 5136-5139 (1999); *Electron spin resonance in  $S=1/2$  antiferromagnetic chains*, Physical Review B **65**, 134410 (2002).
- [Owen'72] J. Owen and E. A. Harris, *Pair Spectra and Exchange Interaction*, in: Electron Paramagnetic Resonance. Ed. Geschwind, Plenum Press (1972).
- [Pake'73] G. E. Pake and T. L. Estle, *The physical principles of electron paramagnetic resonance*, Benjamin Inc., New York (1973).
- [Peierls'55] R. E. Peierls, *Quantum theory of solids*, Oxford University Press, Oxford (1955).
- [Pilawa'97] B. Pilawa, *Anisotropy of the electron spin-resonance linewidth of  $\text{CuGeO}_3$* , Journal of Physics: Condensed Matter **9**, 3779-3792 (1997).
- [Pratt'55] G. W. Pratt, *Antiferromagnetism*, Physical Review **97**, 926-932 (1955).
- [Pytte'74] E. Pytte, *Peierls instability in Heisenberg chains*, Physical Review B **10**, 4637-4642 (1974).
- [Quirion'98] G. Quirion, F. S. Razavi, B. Dumoulin, M. Poirier, A. Revcolevschi, and G. Dhahlenne, *Ultrasonic study of the spin-Peierls system  $\text{CuGeO}_3$  under pressure*, Physical Review B **58**, 882-886 (1998).
- [Rado'63] Rado and Suhl eds., *Magnetism I*, vol. 1, Academic Press (1963).
- [Reiter'75] G. F. Reiter, J. P. Boucher, *Theory of exchange narrowing in one and two dimensions*, Physical Review B **11**, 1823-1829 (1975).
- [Rückamp'05a] R. Rückamp, E. Benckiser, M. W. Haverkort, H. Roth, T. Lorenz, A. Freimuth, L. Jongen, A. Moller, G. Meyer, P. Reutler, B. Buchner, A. Revcolevschi, S.-W. Cheong, C. Sekar, G. Krabbes and M. Grüninger, *Optical study of orbital excitations in transition-metal oxides*, New Journal of Physics **7**, 144 (2005); cond-mat/0503405.
- [Rückamp'05b] R. Rückamp, J. Baier, M. Kriener, M. W. Haverkort, T. Lorenz, G. S. Uhrig, L. Jongen, A. Moller, G. Meyer, and M. Grüninger, *Zero-Field Incommensurate Spin-Peierls Phase with Interchain Frustration in  $\text{TiOCl}$* , Physical Review Letters **95**, 097203 (2005).
- [Saha-Dasgupta'04] T. Saha-Dasgupta, R. Valenti, H. Rosner and C. Gros,  *$\text{TiOCl}$ , an orbital-ordered system?*, Europhysics Letters **67**, 63-69 (2004).
- [Sawa'02] H. Sawa, E. Ninomiya, T. Ohama, H. Nakao, K. Ohwada, Y. Murakami, Y. Fujii, Y. Noda, M. Isobe, Y. Ueda, *Low-temperature structure of the quarter-filled ladder compound  $\alpha'$ - $\text{NaV}_2\text{O}_5$* , Journal of the Physical Society of Japan **71** 385-388 (2002).

- [Schastnev'75] P. V. Schastnev and K. M. Salikhov, *Spin polarization and exchange interaction for multielectron systems*, Theoretical and Experimental Chemistry **9**, 223-229 (1975).
- [Schäfer'58] H. Schäfer, F. Wartenpfehl, E. Weise, *Über Titanchloride. V. Titan(III)-oxychlorid*, Zeitschrift für anorganische und allgemeine Chemie **295**, 268-280 (1958).
- [Schönleber'06] A. Schönleber, S. van Smaalen, L. Palatinus, *Structure of the incommensurate phase of the quantum magnet TiOCl*, Physical Review B **73**, 214410 (2006).
- [Schwenk'99] H. Schwenk, S. Zherlitsyn, B. Luthi, E. Morre and C. Geibel, *Elastic constants and charge ordering in  $\alpha'$ - $\text{NaV}_2\text{O}_5$* , Physical Review B **60**, 9194-9197 (1999).
- [Seidel'03] A. Seidel, C. A. Marianetti, F. C. Chou, G. Ceder, and P. A. Lee,  *$S = 1/2$  chains and spin-Peierls transition in TiOCl*, Physical Review B **67**, 020405(R) (2003).
- [Seo'98] H. Seo and H. Fukuyama, *Charge Ordering and Spin Gap in  $\text{NaV}_2\text{O}_5$* , Journal of the Physical Society of Japan **67**, 2602-2605 (1998).
- [Shaz'05] M. Shaz, S. van Smaalen, L. Palatinus, M. Hoinkis, M. Klemm, S. Horn, and R. Claessen, *Spin-Peierls transition in TiOCl*, Physical Review B **71**, 100405(R) (2005).
- [Shengelaya'00] A. Shengelaya, G.-M. Zhao, H. Keller, and K. A. Müller, B. I. Kochelaev, *EPR in  $\text{La}_{1-x}\text{Ca}_x\text{MnO}_3$ : Relaxation and bottleneck*, Physical Review B **61**, 5888-5890 (2000).
- [Slichter'96] C. P. Slichter. *Principles of magnetic resonance*, vol. 1 of *Springer Series in Solid-State Science*. Springer-Verlag, Berlin (1996).
- [Smirnov'99] A. I. Smirnov, M. N. Popova, A. B. Sushkov, and S. A. Golubchik, D. I. Khomskii and M. V. Mostovoy, A. N. Vasilev, M. Isobe and Y. Ueda, *High-frequency dielectric and magnetic anomaly at the phase transition in  $\text{NaV}_2\text{O}_5$* , Physical Review B **59**, 14546-14551 (1999).
- [Smirnov'02] A. I. Smirnov, V. N. Glazkov, H.-A. Krug von Nidda, A. Loidl, L. N. Demianets, A. Ya. Shapiro, *Paramagnetic and antiferromagnetic resonances in the diamagnetically diluted Haldane magnet  $\text{PbNi}_2\text{V}_2\text{O}_8$* , Physical Review B **65**, 174422 (2002).
- [Smith'69] D. W. Smith, *Dependence of  $10Dq$  on the MetalLigand Distance in NiO*, Journal of Chemical Physics **50**, 2784-2784 (1969).
- [Smolinski'98] H. Smolinski, C. Gros, W. Weber, U. Peuchert, G. Roth, M. Weiden and C. Geibel,  *$\text{NaV}_2\text{O}_5$  as a Quarter-Filled Ladder Compound*, Physical Review Letters **80**, 5164-5167 (1998).
- [Soos'77] Z. G. Soos, K. T. McGregor, T. T. P. Cheung, and A. J. Silverstein, *Antisymmetric and anisotropic exchange in ferromagnetic copper(II) layers*, Physical Review B **16**, 3036-3048 (1977).
- [Suaud'00] N. Suaud, M.-B. Lepetit, *Ab initio evaluation of local effective interactions in  $\alpha'$ - $\text{NaV}_2\text{O}_5$* , Physical Review B **62**, 402-409 (2000).

- [Thalmeier'98] P. Thalmeier, P. Fulde, *Charge ordering and spin-Peierls transition in  $\alpha'$ - $\text{NaV}_2\text{O}_5$* , Europhysics Letters **44** 242-248 (1998).
- [Tomonaga'50] S. Tomonaga, *Remarks on Bloch's method of sound waves applied to many-fermion problems*, Progress of Theoretical Physics **5** 544-569 (1950).
- [Tornow'99] S. Tornow, O. Entin-Wohlman, and A. Aharony, *Anisotropic superexchange for nearest and next-nearest coppers in chain, ladder, and lamellar cuprates*, Physical Review B **60**, 10206-10215 (1999).
- [Troyer'94] M. Troyer, H. Tsunetsugu, D. Würtz, *Thermodynamics and spin gap of the Heisenberg ladder calculated by the look-ahead Lanczos algorithm*, Physical Review B **50**, 13515-13527 (1994).
- [Vasilev'97] A. N. Vasilev, A. I. Smirnov, M. Isobe and Y. Ueda, *Electron spin resonance in the spin-Peierls compound  $\text{NaV}_2\text{O}_5$*  Physical Review B **56**, 5065-5068 (1997).
- [Vasilev'99] A. N. Vasil'ev, *Quasi-one-dimensional antiferromagnet  $\text{LiCuVO}_4$* , Journal of Experimental and Theoretical Physics Letters **69**, 876-880 (1999).
- [Vasilev'01] A. N. Vasilev, L. A. Ponomarenko, H. Manaka, I. Yamada, M. Isobe, and Y. Ueda, *Magnetic and resonant properties of quasi-one-dimensional antiferromagnet  $\text{LiCuVO}_4$* , Physical Review B **64**, 024419 (2001).
- [vanVleck'48] J. H. Van Vleck, *The dipolar broadening of magnetic resonance lines in crystals*, Physical Review **74**, 1168-1183 (1948).
- [Völenkle'67] H. Völenkle, A. Wittmann, and H. Nowotny, *Zur Kristallstruktur von  $\text{CuGeO}_3$* , Monatshefte für Chemie **98**, 1352-1357 (1967).
- [Voronkova'83] V. K. Voronkova, M. V. Eremin, L. V. Mosina, Yu. V. Yablokov, *Unusually large values of the E.P.R. spectra fine structure parameter of  $\text{Cu(II)}$  dimers with two-bridge exchange mechanisms*, Molecular Physics **50**, 379-388 (1983).
- [vonSchnering'98] H. G. von Schnering, Y. Grin, M. Kaupp, M. Somer, R. Kremer, O. Jepsen, T. Chatterji und M. Weiden, *Redetermination of the crystal structure of sodium vanadate,  $\alpha'$ - $\text{NaV}_2\text{O}_5$* , Zeitschrift für Kristallographie **213**, 246-246 (1998).
- [Walstedt'01] R. E. Walstedt and S.-W. Cheong, *Covalency in  $\text{La}_2\text{CuO}_4$ : A study of  $^{17}\text{O}$  hyperfine couplings in the paramagnetic phase*, Physical Review B **64** 014404 (2001).
- [White'94] S. R. White, R. M. Noack, D. J. Scalapino, *Resonating Valence Bond Theory of Coupled Heisenberg Chains*, Physical Review Letters **73**, 886-889 (1994).
- [Wigner'34] E. Wigner, *On the interaction of electrons in metals*, Physical Review **46**, 1002-1011 (1934).
- [Yamada'89] I. Yamada, H. Fujii, and M. Hidaka, *Experimental evidence of the Dzyaloshinsky-Moriya antisymmetric exchange interaction in the one-dimensional Heisenberg antiferromagnet  $\text{KCuF}_3$ : EPR measurements*, Journal of Physics: Condensed Matter **1**, 3397-3408 (1989).

- 
- [Yamada'94] I. Yamada, N. Kato, *Multi-sublattice magnetic structure of  $KCuF_3$  caused by the antisymmetric exchange interaction: antiferromagnetic resonance measurement*, Journal of the Physical Society of Japan **63**, 289-297 (1994).
- [Yamada'98] I. Yamada, H. Manaka, H. Sawa, M. Nishi, M. Isobe and Y. Ueda, *Temperature and Angular Dependence of Electron Paramagnetic Resonance Line in  $\alpha'$ - $NaV_2O_5$* , Journal of the Physical Society of Japan **67**, 4269-4278 (1998).
- [Yaresko'00] A. N. Yaresko, V. N. Antonov, H. Eschrig, P. Thalmeier, P. Fulde, *Electronic structure and exchange coupling in  $\alpha'$ - $NaV_2O_5$* , Physical Review B **62**, 15538-15546 (2000).
- [Yaresko'02] A. Yaresko, R. Hayn, A. Perlov, H. Rosner, P. Thalmeier, *Calculation of exchange integrals in transition metals oxides using the LDA+U approach*, Physica B **312-313**, 619 (2002).
- [Yamashita'58] J. Yamashita, J. Kondo, *Superexchange Interaction*, Physical Review **109**, 730-741 (1958).
- [Yosida'96] K. Yosida, *Theory of Magnetism*, Springer, Berlin (1996).
- [Yushankhai'99] V. Yu. Yushankhai and R. Hayn, *Anisotropic superexchange of a  $90^\circ$  Cu-O-Cu bond*, Europhysics Letters **47**, 116-121 (1999).
- [Zavoiski'45] E. Zavoiski, *Paramagnetic relaxation in solutions in perpendicular fields*, Journal of Experimental and Theoretical Physics **15**, 344-350 (1945).
- [Zener'51] C. Zener, *Interaction between the d-Shells in the Transition Metals. II. Ferromagnetic Compounds of Manganese with Perovskite Structure*, Physical Review **82**, 403-405 (1951).
- [Zvyagin'01] A. A. Zvyagin, *Temperature dependence of the electron paramagnetic resonance linewidth in  $NaV_2O_5$* , Physical Review B **63**, 172409 (2001).
- [Zvyagin'05] S. A. Zvyagin, A. K. Kolezhuk, J. Krzystek, and R. Feyerherm, *Electron Spin Resonance in Sine-Gordon Spin Chains in the Perturbative Spinon Regime*, Physical Review Letters **95**, 017207 (2005).





## List of Publications

- *Anisotropic Exchange in Spin Chains*  
D. V. Zakharov, M. V. Eremin, H.-A. Krug von Nidda, J. Deisenhofer, R. M. Eremina, A. Loidl,  
submitted for the proceedings of the Les Houches/PITP summer school "Quantum Magnetism" (2007).
- *Spin dynamics in the low-dimensional magnet  $TiOCl$*   
D. V. Zakharov, J. Deisenhofer, H.-A. Krug von Nidda, P. Lunkenheimer, J. Hemberger, M. Hoinkis, M. Klemm, M. Sing, R. Claessen, M. V. Eremin, S. Horn, and A. Loidl,  
Physical Review B **73**, 094452 (2006).
- *Unconventional anisotropic superexchange in  $\alpha'$ - $NaV_2O_5$*   
M. V. Eremin, D. V. Zakharov, R. M. Eremina, J. Deisenhofer, H.-A. Krug von Nidda, G. Obermeier, S. Horn, and A. Loidl,  
Physical Review Letters **96**, 027209 (2006).
- *Electron spin resonance of the low-dimensional spin-system  $Sr_2V_3O_9$*   
V. A. Ivanshin, V. Yushankhai, J. Sichelschmidt, D. V. Zakharov, E. E. Kaul, and C. Geibel,  
Journal of Magnetism and Magnetic Materials **272-276P2**, 960 (2004).
- *Nature of the EPR Line Asymmetry in  $La_{0.70}Ca_{0.25}Ba_{0.05}MnO_3$*   
D. V. Zakharov, D. G. Zverev, V. V. Izotov,  
Journal of Experimental and Theoretical Physics Letters **78**, 6, 402 (2003).
- *ESR study of the anisotropic exchange in the quasi one-dimensional antiferromagnet  $Sr_2V_3O_9$*   
V. A. Ivanshin, V. Yushankhai, J. Sichelschmidt, D. V. Zakharov, E. E. Kaul, and C. Geibel,  
Physical Review B **68**, 064404 (2003).
- *Crystal Field, Dzyaloshinsky-Moriya interaction and orbital order in  $La_{0.95}Sr_{0.05}MnO_3$  probed by ESR*

## *Bibliography*

---

J. Deisenhofer, M. Eremin, D. V. Zakharov, V. A. Ivanshin, R. M. Eremina, H.-A. Krug von Nidda, A. A. Mukhin, A. M. Balbashov, and A. Loidl, *Physical Review B* **65**, 104440 (2002).

# Acknowledgements

As everybody who did PhD in the ESR group Augsburg I would like to thank first of all Hans-Albrecht. For 1001 small and big things... May God grant you strength to carry that all you loaded on yourself!

It was a pleasure to work these three years on the chair of Alois Loidl. I really enjoyed researching there and I will definitely miss the atmosphere you create.

I kindly acknowledge my chief Mikhail Eremin, for making a reality of my work in Germany, for contributing to the biggest part of my knowledge, for always being an example of a true scientist...

My fourth supervisor, Jochen, I can't thank you enough for always being there to help, to motivate and to discuss about physics and all around it. I will never forget your cynical words but kind deeds, anarchical altruism, straightforwardness, unquenchable enthusiasm and thirst for knowledge. I hope we will meet ourselves in Kazan, but anyway.. see you on Skype!

My best thanks, of course, to the whole group of EP5, DAAD and everyone who helped this work to see the light of the day.



# Curriculum Vitae

**Name** Dmitry Zakharov  
**Date of Birth** 13.02.1981  
**Place of Birth** Kazan/Russia  
**Nationality** Russian

**09/1988 - 06/1998** Primary & Grammar School  
at Gymnasium #36 Kazan/Russia

**09/1998 - 06/2004** Study of Physics at the University of Kazan/Russia  
**04/2002 - 12/2005** Research Assistant at the University of Kazan/Russia  
**06/2002** Bachelor Thesis:  
“Crystal Field and Dzyaloshinsky-Moriya Interaction  
in  $\text{La}_{0.95}\text{Sr}_{0.05}\text{MnO}_3$  probed by ESR”  
**06/2004** Master Thesis:  
“Estimation of Anisotropic Exchange Parameters  
in Some Transition Metal Oxides  
from the Angular Dependence of the ESR Linewidth”

**10/2004 - present** Post-Graduate Study at the University of  
Augsburg/Germany and Kazan/Russia







